


1-1-2014

Precursors And Processes For The Growth Of Metallic First Row Transition Metal Films By Atomic Layer Deposition

Lakmal Charidu Kalutarage
Wayne State University,

Follow this and additional works at: http://digitalcommons.wayne.edu/oa_dissertations

 Part of the [Chemistry Commons](#), [Film and Media Studies Commons](#), and the [Nanoscience and Nanotechnology Commons](#)

Recommended Citation

Kalutarage, Lakmal Charidu, "Precursors And Processes For The Growth Of Metallic First Row Transition Metal Films By Atomic Layer Deposition" (2014). *Wayne State University Dissertations*. Paper 891.

This Open Access Dissertation is brought to you for free and open access by DigitalCommons@WayneState. It has been accepted for inclusion in Wayne State University Dissertations by an authorized administrator of DigitalCommons@WayneState.

**PRECURSORS AND PROCESSES FOR THE GROWTH OF METALLIC FIRST ROW
TRANSITION METAL FILMS BY ATOMIC LAYER DEPOSITION**

by

LAKMAL CHARIDU KALUTARAGE

DISSERTATION

Submitted to the Graduate School

of Wayne State University,

Detroit, Michigan

in partial fulfillment of the requirements

for the degree of

DOCTOR OF PHILOSOPHY

2014

MAJOR : CHEMISTRY (Inorganic)

Approved by:

Advisor

Date

© COPYRIGHT BY

Lakmal Charidu Kalutarage

2014

All Rights Reserved

DEDICATION

I dedicate my dissertation to my parents for their love and support and to my lovely wife, Buddhima Mahanama, who supported me in numerous ways throughout these years.

ACKNOWLEDGEMENTS

Pursuing a Ph.D. is the most challenging task I have encountered so far in my life. There are numerous people who were behind me offering their support to me during this period. First and foremost, I would like to extend my sincere thanks to my advisor, Dr. Charles H. Winter, for his guidance and support throughout the years, and introducing me to the ALD community. I was able to gather valuable experiences on the deposition of thin films in his laboratory and these experiences laid the foundation for my future career. I would also like to thank my dissertation committee members, Dr. Matthew Allen, Dr. Colin Poole, and Dr. Charles Dezelah for their time and valuable suggestions.

Working in a laboratory requires a lot of support from coworkers. My coworkers have supported me in numerous ways. Many thanks go to Dr. Mahesh Karunaratne for teaching me laboratory techniques and giving me valuable chemistry lessons. I would like to thank Dr. Hiran Perera for his support and friendship throughout these years. Thank you, Dr. Christopher Snyder, for the time spent discussing chemistry problems that inspired me to come up with new ideas. I am also grateful to other past and present Winter group members for their support in various ways.

I would like to thank Dr. Mary Jane Heeg and Dr. Philip Martin for solving X-ray crystal structures, Dr. Bashar Kesbati for help with NMR spectroscopy, and Dr. Mike Mei for assistance with SEM and XRD. Also, I would like to thank Nestor Ocampo for assistance with computer related issues, science stores, academic, and non-academic staff members in the department of chemistry for offering their assistance.

I wish to thank my parents and siblings who have consistently guided, motivated, and supported me towards achieving my goals. Without their inspiration and encouragement I would not be where I am at today. Finally, I give endless appreciation and thanks to my wife, Buddhima Mahanama, who gave courage and love to succeed in my journey. Without her support and motivation this dissertation would not have been possible.

TABLE OF CONTENTS

Dedication	ii
Acknowledgements.....	iii
List of Tables	vii
List of Figures	ix
List of Abbreviations	xvi
CHAPTER 1 – Introduction.....	1
CHAPTER 2 – Volatile and Thermally Stable Mid to Late Transition Metal Complexes Containing α -Imino Alkoxide Ligands	24
CHAPTER 3 – Synthesis and Structure of Volatile and Thermally Stable Mid to Late First Row Transition Metal Complexes Containing α -Imino Ketonate and α -Imino Enolate Ligands	52
CHAPTER 4 – Synthesis, Structure, and Solution Reduction Reactions of Volatile and Thermally Stable Mid to Late First Row Transition Metal Complexes Containing Hydrazone Ligands	87
CHAPTER 5 – Volatility and High Thermal Stability in Mid to Late First Row Transition Metal Complexes Containing 1,2,5-Triazapentadienyl Ligands	113
CHAPTER 6 – Low Temperature Atomic Layer Deposition of Copper Films Using Borane Dimethylamine as the Reducing Co-Reagent	131
CHAPTER 7 – Low Temperature Thermal Atomic Layer Deposition of Ni, Co, Fe, Mn, and Cr Metal Thin Films Using Borane Dimethylamine as the Reducing Co-Reagent.....	160
CHAPTER 8 – Synthesis and Structure of Volatile and Thermally Stable Molybdenum(II)	

and Tungsten(II) Complexes Containing N, O Donor Ligands.....	181
CHAPTER 9 – Conclusions and Future Directions.....	211
References.....	216
Abstract.....	233
Autobiographical Statement.....	236

LIST OF TABLES

Table 1. Reduction potentials.....	13
Table 2. Experimental crystallographic data for 10–12, 14, and 15	28
Table 3. Selected bond lengths (Å) and angles (°) for 10–12, 14, and 15	29
Table 4. Volatility and thermal stability data for 1–15	36
Table 5a. Experimental crystallographic data for 16–18 and 20	62
Table 5b. Experimental crystallographic data for 21–24	63
Table 6. Selected bond lengths (Å) and angles (°) for 16, 17, 20, and 21	64
Table 7. Selected bond lengths (Å) and angles (°) for 18 and 19	65
Table 8. Selected bond lengths (Å) and angles (°) for 22–24	66
Table 9. Selected bond lengths (Å) and angles (°) for 18	72
Table 10. Selected bond lengths (Å) and angles (°) for 19	73
Table 11. Volatility and thermal stability data for 16–25	76
Table 12. Experimental crystallographic data for 27, 31, 32, and 34–36	92
Table 13a. Selected bond lengths (Å) for 27, 31, 32, and 34–36	93
Table 13b. Selected bond angles (°) for 27, 31, 32, and 34–36	94
Table 14. Volatility and thermal stability data for 26–36	99
Table 15. Reactivity of 27 and 29 toward reducing agents in tetrahydrofuran: a, ambient temperature; b, upon reflux	102
Table 16. Experimental crystallographic data for 42 and 43	116
Table 17. Selected bond lengths (Å) and angles (°) for 42, and 43	117
Table 18. Volatility and thermal stability data for 37–45	121

Table 19. Atomic concentrations of Cu, C, N, O, and B obtained by XPS after 120 s of Ar ion sputtering on the indicated substrates	140
Table 20a. Experimental crystallographic data for 47, 49, 50, and 52	191
Table 20b. Experimental crystallographic data for 53, 56, 57, and 59	192
Table 21. Selected bond lengths (Å) and angles (°) for 47, 49, 50, 52, and 53	193
Table 22a. Selected bond lengths (Å) for 56, 57, and 59	194
Table 22b. Selected bond angles (°) for 56, 57, and 59	195
Table 23. Volatility and thermal stability data for 47–59	201

LIST OF FIGURES

Figure 1. Comparison of the conformality and coverage of a film deposited by CVD, PVD, and ALD	4
Figure 2. (a) Evaporative PVD (b) Sputter PVD	5
Figure 3. Deposition of M by CVD from precursor ML_n	7
Figure 4. Steps in the ALD cycle in the deposition of Al_2O_3 from trimethylaluminum and water	9
Figure 5. Plot of growth rate versus precursor pulse length	10
Figure 6. A plot of growth rate versus temperature	11
Figure 7. Perspective view of 10 with thermal ellipsoids at the 50% probability level.....	30
Figure 8. Perspective view of 11 with thermal ellipsoids at the 50% probability level.....	31
Figure 9. Perspective view of 12 with thermal ellipsoids at the 50% probability level.....	32
Figure 10. Perspective view of 14 with thermal ellipsoids at the 50% probability level.....	33
Figure 11. Perspective view of 15 with thermal ellipsoids at the 50% probability level.....	34
Figure 12. TGA of 1–3	37
Figure 13. TGA of 4, 5, and 9	37
Figure 14. Powder XRD spectrum of Ni produced upon treatment of 2 with $BH_3(NHMe_2)$ in tetrahydrofuran at $23\text{ }^\circ C$	38
Figure 15. Powder XRD spectrum of Co produced upon treatment of 3 with $BH_3(NHMe_2)$ in tetrahydrofuran at $23\text{ }^\circ C$	39
Figure 16. Perspective view of 17 with thermal ellipsoids at the 50% probability level.....	67
Figure 17. Perspective view of 18 with thermal ellipsoids at the 50% probability level.....	68
Figure 18. Perspective view of 20 with thermal ellipsoids at the 50% probability level.....	69
Figure 19. Perspective view of 22 with thermal ellipsoids at the 50% probability level.....	70
Figure 20. Perspective view of 24 with thermal ellipsoids at the 50% probability level.....	71

Figure 21. TGA of 16 , 18 , and 19 (top), TGA of 20–25 (bottom)	77
Figure 22. DTA of 20–22 and 24	78
Figure 23. Powder XRD spectrum of Co produced upon treatment of 17 with $\text{BH}_3(\text{NHMe}_2)$ in tetrahydrofuran at $23\text{ }^\circ\text{C}$	79
Figure 24. Perspective view of 27 with thermal ellipsoids at the 50% probability level.....	95
Figure 25. Perspective view of 32 with thermal ellipsoids at the 50% probability level.....	96
Figure 26. Perspective view of 35 with thermal ellipsoids at the 50% probability level.....	97
Figure 27. TGA plots of 26–28 and 30	100
Figure 28. TGA plots of 31–36	100
Figure 29. DTA plots of 26–28 and 30	101
Figure 30. (a) Powder XRD spectrum of the Co powder obtained from the reaction between 27 and N_2H_4 . (b) Powder XRD spectrum of the Co powder obtained from the reaction between 27 and $\text{BH}_3(\text{SMe}_2)$ after annealing at $600\text{ }^\circ\text{C}$ for 4 hours under argon	103
Figure 31. Perspective view of 42 with thermal ellipsoids at the 50% probability level.....	118
Figure 32. Perspective view of 43 with thermal ellipsoids at the 50% probability level.....	119
Figure 33. TGA plots of 37–40	122
Figure 34. TGA plots of 42–45	122
Figure 35. Powder XRD spectrum of Ni metal produced upon treatment of 42 with hydrazine.....	123
Figure 36. Surface SEM views of ALD Cu after the nucleation step	134
Figure 37. Growth rate as a function of the pulse length of 46 at a substrate temperature of $150\text{ }^\circ\text{C}$ on Ru	136
Figure 38. Growth rate as a function of the pulse length of $\text{BH}_3(\text{NHMe}_2)$ at a substrate temperature of $150\text{ }^\circ\text{C}$ on Ru	136
Figure 39. Growth rate as a function of deposition temperature in the binary process on Ru.....	137

Figure 40. Film thickness as a function of the number of deposition cycles at a growth temperature of 150 °C on Ru	138
Figure 41a. XPS spectra of 25 nm Cu films deposited at 150 °C on Ru	139
Figure 41b. High-resolution XPS multiplex of Cu 2p region.....	139
Figure 42. Powder XRD spectrum of a Cu film after annealing for 3 h at 300 °C.....	141
Figure 43. AFM images of Cu film surfaces deposited at 120 and 160 °C on Ru	142
Figure 44a. Growth rate as a function of the pulse length of 46 at a substrate temperature of 150 °C on Pd.....	144
Figure 44b. Growth rate as a function of the pulse length of 46 at a substrate temperature of 150 °C on Pt	144
Figure 45a. Growth rate as a function of the pulse length of formic acid at a substrate temperature of 150 °C on Pd.....	145
Figure 45b. Growth rate as a function of the pulse length of formic acid at a substrate temperature of 150 °C on Pt	145
Figure 46a. Growth rate as a function of the pulse length of BH ₃ (NHMe ₂) at a substrate temperature of 150 °C on Pd.....	146
Figure 46b. Growth rate as a function of the pulse length of BH ₃ (NHMe ₂) at a substrate temperature of 150 °C on Pt	146
Figure 47a. Growth rate as a function of deposition temperature on Pd in the ternary process	147
Figure 47b. Growth rate as a function of deposition temperature on Pt in the ternary process	148
Figure 48a. Film thickness as a function of the number of deposition cycles at a growth temperature of 150 °C on Pd.....	149
Figure 48b. Film thickness as a function of the number of deposition cycles at a growth temperature of 150 °C on Pt	149
Figure 49a. XPS spectra of 20 nm Cu films deposited at 150 °C.....	151
Figure 49b. High-resolution XPS multiplex of Cu 2p region.....	151
Figure 50. AFM images of Cu films surfaces deposited at 140 and 160 °C on Pd	153

Figure 51. AFM images of Cu films surfaces deposited at 140 and 160 °C on Pt	154
Figure 52. Sheet resistivity as a function of the number of deposition cycles at a growth temperature of 150 °C on Pd.....	155
Figure 53. SEM views of Cu films deposited at 150 °C on Pd substrate (top) and Pt substrate (bottom) after 50 cycles	156
Figure 54. Growth rate as a function of the pulse length of 9 at a substrate temperature of 180 °C.....	163
Figure 55. Growth rate as a function of the pulse length of $\text{BH}_3(\text{NHMe}_2)$ at a substrate temperature of 180 °C.....	163
Figure 56. Growth rate of Cr as a function of deposition temperature	164
Figure 57. Cr film thickness as a function of the number of deposition cycles at a deposition temperature of 180 °C	164
Figure 58. XPS survey scan of an 8 nm thick Cr film deposited at 170 °C.....	165
Figure 59. High resolution XPS scan of the Cr 2p region of an 8 nm thick Cr film deposited at 170 °C	165
Figure 60. AFM images of an 8 nm thick Cr film deposited at 170 (top) and 180 °C (bottom)	166
Figure 61. Growth rate as a function of the pulse length of 2 at a substrate temperature of 180 °C.....	167
Figure 62. Growth rate as a function of the pulse length of 3 at a substrate temperature of 180 °C.....	167
Figure 63. Growth rate as a function of the pulse length of $\text{BH}_3(\text{NHMe}_2)$ at a substrate temperature of 180 °C for the Ni deposition.....	168
Figure 64. Growth rate as a function of the pulse length of $\text{BH}_3(\text{NHMe}_2)$ at a substrate temperature of 180 °C for the Co deposition.....	168
Figure 65. Growth rate of Ni as a function of deposition temperature	169
Figure 66. Growth rate of Co as a function of deposition temperature	169
Figure 67. Ni film thickness as a function of the number of deposition cycles at a deposition temperature of 180 °C	170

Figure 68. Co film thickness as a function of the number of deposition cycles at a deposition temperature of 180 °C	170
Figure 69. XPS survey scans of an 8 nm thick Ni film deposited at 180 °C	171
Figure 70. High resolution XPS scan of the Ni 2p region of an 8 nm thick Ni film deposited at 180 °C	171
Figure 71. XPS survey scan of a 7 nm thick Co film deposited at 180 °C	172
Figure 72. High resolution XPS scan of the Co 2p region of a 7 nm thick Co film deposited at 180 °C	172
Figure 73. AFM images of an 8 nm thick Ni film deposited at 170 (top) and 190 °C (bottom)	173
Figure 74. AFM images of a 7 nm thick Co film deposited at 170 (top) and 190 °C (bottom)	174
Figure 75. Growth rate as a function of the pulse length of 7 at a substrate temperature of 180 °C.....	175
Figure 76. Growth rate as a function of the pulse length of 8 at a substrate temperature of 225 °C.....	176
Figure 77. XPS survey scan of a 4 nm thick Fe film deposited at 180 °C.....	176
Figure 78. High resolution XPS scan of the Fe 2p region of a 4 nm thick Fe film deposited at 180 °C	177
Figure 79. XPS survey scan of a 10 nm thick Mn film deposited at 225 °C	177
Figure 80. High resolution XPS scan of the Mn 2p region of a 10 nm thick Mn film deposited at 225 °C.....	178
Figure 81. Perspective view of 47 with thermal ellipsoids at the 50% probability level.....	196
Figure 82. Perspective view of 53 with thermal ellipsoids at the 50% probability level.....	197
Figure 83. Perspective view of 56 with thermal ellipsoids at the 50% probability level.....	198
Figure 84. Perspective view of 57 with thermal ellipsoids at the 50% probability level.....	199
Figure 85. TGA plots of 47–50	202
Figure 86. TGA plots of 53–55	202

LIST OF ABBREVIATIONS

acac.....	acetylacetonate
AFM.....	Atomic Force Microscopy
ALD.....	Atomic Layer Deposition
at. %.....	atomic %
Cp.....	Cyclopentadienyl
CVD.....	Chemical Vapor Deposition
DAD.....	diazadiene
dmamp.....	1-dimethylamino-2-methylpropanoate
dmap.....	3-dimethylamino-2-butoxide
DTA.....	Differential Thermal Analysis
hfac.....	1,1,1,5,5,5-hexafluoroacetylacetonato
IR.....	Infrared Spectroscopy
ITRS.....	International Technology Roadmap for Semiconductors
MOSFET.....	Metal Oxide Semiconductor Field Effect Transistor
NMR.....	Nuclear Magnetic Resonance
PEALD.....	Plasma-Enhanced Atomic Layer Deposition
PVD.....	Physical Vapor Deposition
SEM.....	Scanning Electron Microscopy
TGA.....	Thermogravimetric Analysis
tmhd.....	2,2,6,6-tetramethylheptanedionato
XPS.....	X-Ray Photoelectron Spectroscopy

CHAPTER 1

Introduction

1.1 Miniaturization of Microelectronic Devices

Deposition of thin film materials in microelectronic devices is a vital step in device manufacturing. Many kinds of materials with specific properties need to be deposited in various parts of electronic devices. With technological innovations, the materials thicknesses in electronic devices are becoming smaller. This miniaturization trend was first identified by Gordon Moore in 1965, who predicted that the number of transistors in an integrated circuit should double every 18 to 24 months.¹ Continuing reduction of dimensions in microelectronic device manufacturing will require the growth of conformal thin films with thicknesses ranging from a few atomic layers to tens of nanometers in the near future.¹ The *International Technology Roadmap for Semiconductors* (ITRS) predicts a reduction in feature size to 10 nm in 2015.² When moving to small feature sizes, the thicknesses of the materials layers are also getting thinner and the aspect ratios increase, thus, posing a major technical challenge for electronic device producers. Continuing reduction of feature dimensions and increased aspect ratios lead to two major problems: (1) the thin film materials used in traditional devices may not function as they did before with larger dimensions and (2) the need to develop new deposition technologies to grow ultra thin films because traditional deposition methods may not provide required conformality and/or meet device standards. In order to address these problems, the microelectronics industry is seeking new materials and new deposition techniques.

1.2 Materials Containing Transition Metals

Thin films of the metallic first row transition metals have many important current and future applications. Currently, Cu is used as interconnect material instead of Al due to its lower resistivity and higher resistance toward electromigration.³ Cu is deposited in trenches and vias through a two-step process that involves the deposition of a thin, conformal Cu seed layer by physical vapor deposition (PVD), followed by the electrodeposition of Cu fill.⁴ This Cu seed layer must have adequate conformality and coverage to ensure that the electroplated Cu fill gives a complete coverage and absence of voids along the feature sidewalls, which cause interconnect resistance to be higher than desired. Currently, this Cu seed layer deposited by PVD, affords poor conformality and step coverage in high aspect ratio features in future microelectronics devices. For future microelectronics devices featuring high aspect ratio trenches and vias, much thinner and highly conformal Cu seed layers are required. However, Cu does not adhere well to silicon surfaces, making the creation of a continuous Cu seed layer difficult, especially in high aspect ratio features. Therefore, other metal seed layers for Cu metallization, including Ru, Co, and Cr have been investigated.⁶

Another problem of using Cu as an interconnect material is the diffusion of Cu into SiO₂ layers and Si substrates due to the high temperatures used in device fabrication. Therefore, a barrier layer is required between the Cu layer and the Si substrate. This barrier layer must stop the diffusion of Cu at deposition temperatures long enough for device manufacturing and should be unreactive with both Cu and Si, while demonstrating good adhesion to both Cu and Si. Furthermore, this barrier layer should tolerate thermal and mechanical stress encountered during the device fabrication process. In order to reduce the electrical resistivity of the interconnect stacks (Cu fill/Cu seed layer/seed layer for Cu/barrier layer/substrate), future barrier layers

should be ≤ 5 nm.^{2,3} Currently, nitride-based barrier layers including TaN and WN_x ($x = 0.5-1$) are used as Cu diffusion barriers.⁵ However nitride-based barrier materials tend to be ineffective as Cu diffusion barriers when approaching ≤ 5 nm thicknesses.^{3,4} In order to overcome this problem, considerable efforts have been made toward the identification of alternative barrier materials. New proposed barrier materials include very thin films (≤ 5 nm) of Mn,⁷ Ru, and Cr.⁸ Recently, it has been shown that annealing of 150 nm thick Cu/Mn alloy films (Cu/Mn:90/10) on SiO_2 at temperatures between 250 and 450 °C leads to the formation of 2–8 nm thick $MnSi_xO_y$ layers between Cu and SiO_2 .⁷ Importantly, the $MnSi_xO_y$ layer acts as a Cu diffusion barrier, even at 450 °C up to 100 h. Therefore, this work suggests that very thin $MnSi_xO_y$ layers can be used as future Cu diffusion barriers. However, these Cu/Mn alloy films have been deposited by sputtering (a PVD method), which affords poor conformal coverage in high aspect ratio features in future microelectronic devices.⁴

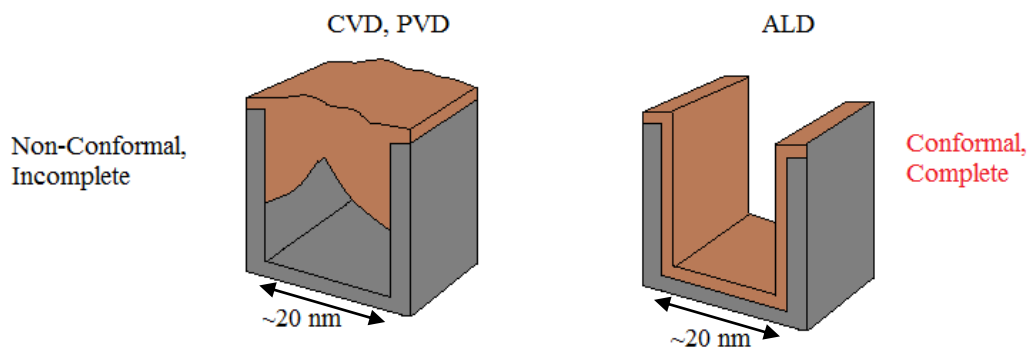
In addition, several other applications require the growth of transition metal films. One such application is in the metal-oxide-semiconductor (MOS) transistors used in microelectronics devices. These transistors consist of three electrodes, namely, source, drain, and gate. In these transistors NiSi and $CoSi_2$ are used as source and drain contact materials. NiSi and $CoSi_2$ are fabricated by the growth of Ni or Co metal films on silicon contacts followed by thermal annealing.⁹ Migration of Si and Ni or Co atoms at high temperature creates NiSi or $CoSi_2$ layers. Another application is in the magnetoresistive random access memory (MRAM) devices used to store data. The storage performance of these devices is highly dependent on material properties and microstructure of the thin films. Therefore, thin film materials are required to be deposited as thin as a few atomic layers and must be highly conformal. Technological innovations have led to use of thin, conformal layers of magnetic metals including Ni, Co, or Fe in MRAM devices.¹⁰

Recently, Cu nanocrystals (2.9–3.4 nm) grown by atomic layer deposition (ALD) on silica have shown high activity for the water gas shift reaction ($\text{CO} + \text{H}_2\text{O} \rightarrow \text{H}_2 + \text{CO}_2$) and performed better than Pt nanocrystals on silica supports.¹¹ More applications of first row transition metal thin films will be discussed in Section 1.4.

1.3 Deposition Techniques

Deposition of thin film materials in current electronic devices is performed by vapor deposition techniques, including physical vapor deposition (PVD), chemical vapor deposition (CVD), and atomic layer deposition (ALD).¹² These deposition techniques have been used to deposit conformal thin films in device features. However, when the thicknesses become a few atomic layers to a few nanometers in future electronic devices, CVD and PVD techniques do not allow the deposition of conformal thin films, as illustrated in Figure 1.

Figure 1. Comparison of the conformality and coverage of a film deposited by CVD, PVD, and ALD.

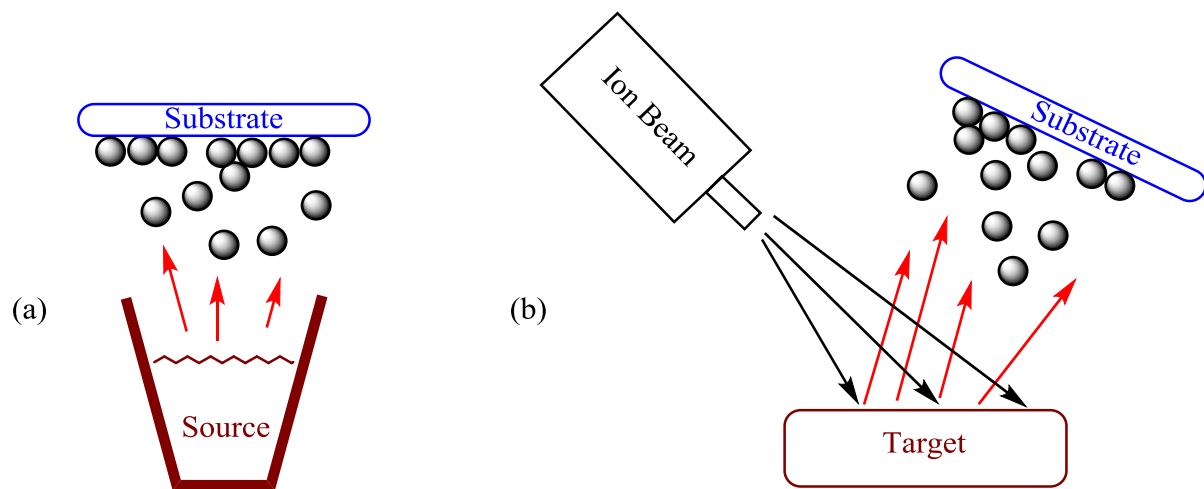


1.3.1 Physical Vapor Deposition

In PVD, surface atoms are removed from a source material and deposited on the surface of the substrate. Removal of atoms can be carried out by thermal heating of the source or high energy particle bombardment by electrons, atoms, or ions in a vacuum.¹³ The process of the removal of atoms by heating is called evaporation. In evaporation, the material is heated to its melting point, and the standard evaporation process is illustrated in Figure 2a. Evaporation can

be divided into two classes: (1) quasi-equilibrium evaporation and (2) non-equilibrium evaporation.¹³ The quasi-equilibrium evaporation process occurs when a material (liquid) has a nearly steady equilibrium with its vapor in a heated cell. Then the vapor is transferred through a small aperture and a tunnel to the cooled substrate where the deposition occurs. On the other hand, in non-equilibrium evaporation a liquid material is evaporated in an open vessel where equilibrium is not present because of low vapor pressure of the material in a large volume. The evaporated material is then transferred through a chamber to the cooled substrate for the deposition.

Figure 2. (a) Evaporative PVD (b) Sputter PVD.¹³

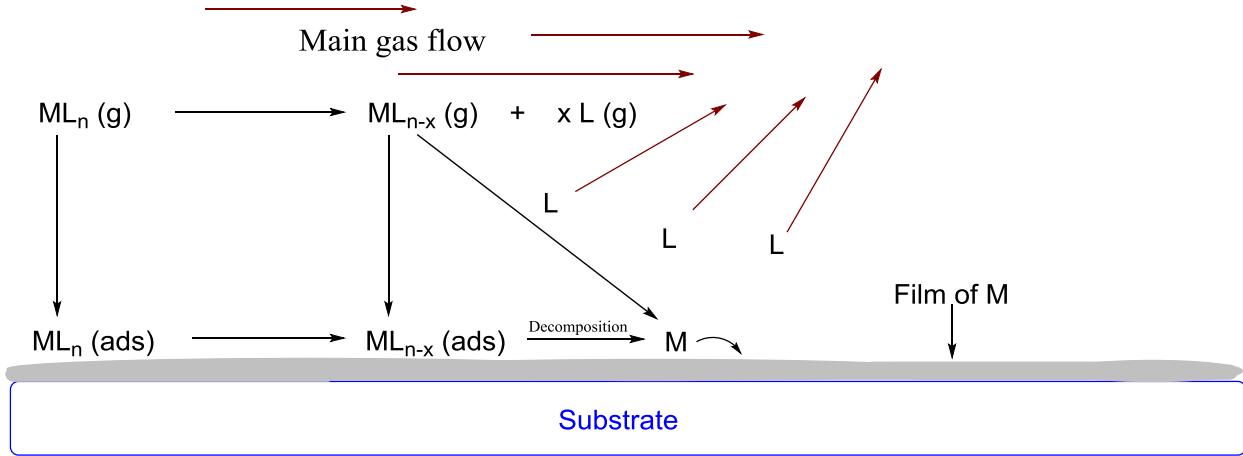


The removal of atoms by particle bombardment is called sputtering (Figure 2b). The kinetics of the particle emission process differs between the sputter method and the evaporation method. In the evaporation method, atoms are emitted because the heating of the material provides enough energy for the atoms to go into the vapor phase. However, in sputtering, atoms are emitted from a source material target by bombardment with high energy particles such as inert gas ions, other ions, neutral atoms, molecules, or photons. Then the ejected atoms are directed to a substrate, where the deposition occurs.¹³

PVD techniques allow the deposition of materials at high deposition rates. However, the evaporation method is directional and leads to columnar type growth because of the low probability of collisions of in-flight atoms.¹³ In contrast, growth by sputtering occurs at higher pressures, leading to scattering of in-flight atoms because of collisions. Therefore, high distribution over the substrate (step-coverage) can be achieved by sputter growth, which gives the ability to deposit materials in three-dimensional structures.¹³ However, many PVD processes afford poor step-coverage and non-conformal films in high aspect ratio structures in electronic devices.¹³

1.3.2 Chemical Vapor Deposition

In CVD, one or more gaseous precursor compounds is introduced into a heated reaction chamber.¹⁴ These precursors can undergo complex reactions (reduction, oxidation, and decomposition) in the gas phase or on the substrate surface leading to the growth of films (Figure 3). Introduced precursor molecules can adsorb onto the surface or chemically react with functional groups on the surface. Then these molecules can undergo various reactions to form a film. Desired product molecules/atoms generated from gas phase reactions also can be incorporated in to the growing film. The precursors are introduced using inert gases such as helium, nitrogen, or argon, which help to remove gaseous byproducts and excess precursor molecules.

Figure 3. Deposition of M by CVD from precursor ML_n .

A good CVD precursor should have acceptable volatility, reactivity, and thermal stability at the desired delivery temperatures.^{14d} Precursors must be pure when they sublime into the reaction chamber to avoid the presence of unwanted elements in the growing film. The precursors must have sufficient reactivity in order to react on the substrate surface, but preferably not in the gas phase. Gas phase reactions may lead to non-conformal, rough films. Gas phase reactions can be minimized by decreasing the pressure of the reaction chamber. Low pressure decreases the collisions between gaseous molecules, which reduces gas phase reactions.^{14c} The ability of a precursor to adsorb onto the substrate or react with the substrate surface can be measured by the sticking probability (S_r). S_r is the fraction of incident flux of molecules that adsorb onto or react with the surface reaction sites. Highly reactive precursors with S_r value close to 1 tend to stick to the surface so that they do not move on the surface leading to non-conformal films with rough surfaces. On the other hand, less reactive precursors with low S_r values may move on the substrate surface before adsorbing onto or reacting with surface reaction sites, to afford smooth conformal films.

Although CVD- and PVD-based techniques are currently used to deposit thin film materials in semiconductor industry, deposition of conformal thin films in high aspect ratio

features may be difficult in future electronic devices. Consequently, a deposition technique that can deposit conformal thin films in high aspect ratio features is required. ALD is the method of choice to overcome this problem because ALD inherently offers conformal thin films in high aspect ratio features and high accuracy of thicknesses.

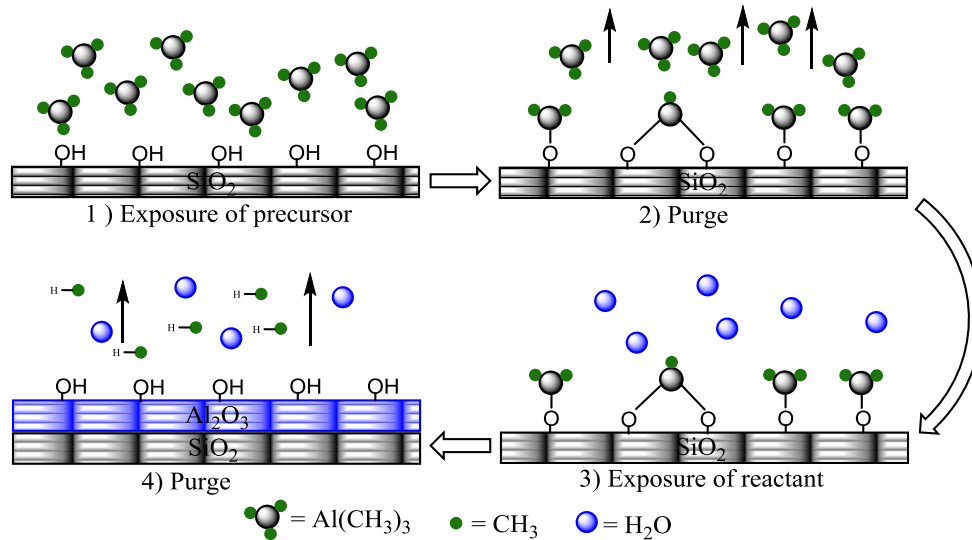
1.3.3 Atomic Layer Deposition

ALD was originally called atomic layer epitaxy (ALE), and was developed by Suntola and Antson in the 1970s.¹⁵ ALD was first developed for the deposition of thin layers in thin film electroluminescent (TFEL) large-area flat panel displays. However, ALD techniques have been improved based on the needs of the semiconductor industry. Because ALD is capable of producing conformal thin films in high aspect ratio features, interest in ALD in the microelectronics industry has been increased over the years.

ALD allows the deposition of ultra-thin conformal films with accurate thickness control due to the self-limiting growth mechanism.¹⁵ Unlike chemical vapor deposition (CVD), gas phase reactions in ALD are eliminated by keeping the precursors separated from each other in the gas phase. In the ALD process, precursor gases are pulsed alternatively into the deposition chamber where adsorption or surface reactions take place on the hot substrate surface.¹⁵ The deposition chamber is purged with a flow of inert gas between alternative precursor pulses. An ALD cycle consists of four steps: (1) exposure of the first precursor to the substrate surface, (2) inert gas purge to remove unreacted precursor and products, (3) exposure of second precursor to produce desired thin film material, and (4) inert gas purge to remove gaseous reaction byproducts. Figure 4 illustrates the steps in the deposition of Al_2O_3 from trimethylaluminum (TMA) as the aluminum source and water as the oxidizing agent. In the purge step, excess precursors and the by-product methane are removed from the reaction chamber. Under optimized

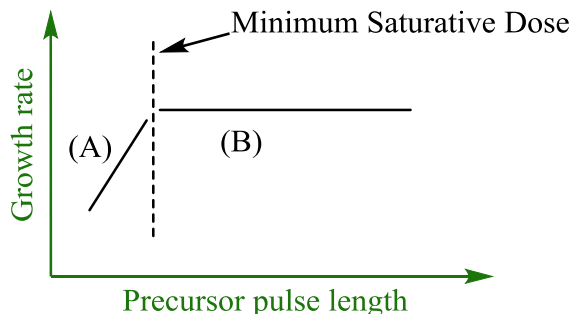
experimental conditions, the growth rate remains constant, thereby allowing film thickness to be determined by the number of deposition cycles.¹⁵

Figure 4. Steps in the ALD cycle in the deposition of Al_2O_3 from trimethylaluminum and water.



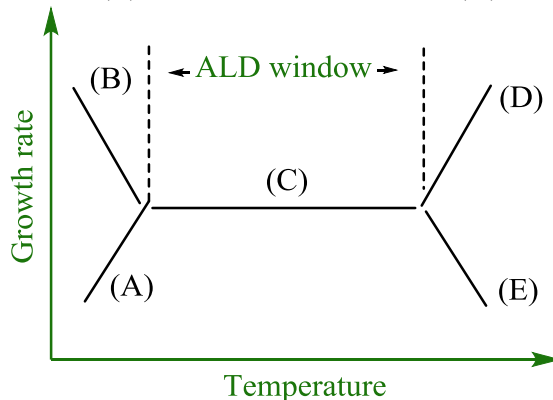
In principle, one cycle of an ALD process generates one atomic layer of the desired material.¹⁵ The number of precursor molecules introduced to the reaction chamber can be varied by changing the precursor pulse length or the partial pressure of the precursor inside the reaction chamber. Once all of the surface reaction sites ($-\text{OH}$ groups in Figure 4) are saturated, regardless of the number of precursor molecules introduced to the substrate surface, there is no place for a reaction to occur, which leads to termination of the growth process. This is known as self-limited growth. If a process exhibits a self-limited growth, the growth rate is not dependent on the precursor dose after the minimum precursor dose is given (Figure 5).

Figure 5. Plot of growth rate versus precursor pulse length. Region A: Sub-saturative regime. Region B: Surface sites are saturated and film growth is self-limited.



Usually film growth processes are temperature dependent.¹⁵ However, an ALD process can give a constant film growth over a temperature range. This temperature range is called the ALD window (Figure 6).¹⁵ In this temperature range the number of molecules that adsorb to the substrate surface is a constant. At low temperatures, a lower growth rate than the growth rate in ALD window can be observed due to not having sufficient energy to overcome the activation barrier of the reaction. Alternatively, at low temperatures, higher growth rates can also be achieved due to precursor condensation. If the deposition temperature exceeds the decomposition temperature of the precursors, higher growth rate may result due to CVD-like growth. Also, at the high temperatures substrate deactivation can occur due to the loss of reactive sites from the substrate surface. Having a temperature range which has a constant growth rate is advantageous. However, it is not necessary to have an ALD window to follow an ALD mechanism, if self-limited growth behavior is demonstrated at one temperature.

Figure 6. A plot of growth rate versus temperature. (A): Insufficient reactivity, (B): Precursor condensation, (C): ALD window. (E): Substrate deactivation, (D): Precursor self-decomposition.



The ALD technique offers many advantages over other vacuum-based deposition techniques.¹⁵ With ALD, high thickness control can be achieved. The control of precursor flux and flow rates are not critical for the growth rate if self-limited behavior is observed. Furthermore, films deposited by ALD are uniform over a large area of the substrate, allowing easy scale-up in industry. Also, highly conformal and pinhole-free dense films can be achieved even in high aspect ratio features. ALD also offers the possibility of deposition at low temperatures. However, low temperature depositions may be disadvantageous, because at low temperatures poorly crystalline or amorphous films may result. Another disadvantage of ALD is that low growth rates lead to long deposition times. Nevertheless, ALD can afford conformal films in high aspect ratio features that other current methods are not capable of offering, which is a major incentive to use in device manufacturing.

Thermal and plasma are the two types of ALD processes.¹⁶ In thermal ALD, heat is used to induce surface reactions and growth occurs thermodynamically. On the other hand, in plasma enhanced ALD (PEALD), high energy radicals are used as co-reagents. Plasma sources can include O₂, N₂, NH₃, H₂, and H₂O vapor. Due to the high reactivity of plasma sources, low temperature deposition can be performed and high growth rates are usually obtained. However,

in plasma processes, radical recombination reactions can occur, leading to loss of reactive species in deep features which results in lower growth. Consequently, films deposited in high aspect ratio features may be non-conformal. PEALD may also result in rough film due to substrate damage. Therefore, the microelectronics industry prefers to use thermal ALD processes over PEALD, where possible.

1.4 Late First row Transition Metal ALD Precursors and Processes

ALD precursors must be thermally stable on the surface of the substrate at the deposition temperature, or else non-self-limited, CVD-like growth occurs through precursor decomposition.^{12a,12c,17} In addition, the metal precursor should be highly reactive toward a second precursor (H₂, hydrazines, silanes, H₂O, O₂, O₃, NH₃, others) to afford the desired thin film material. Other important characteristics of ALD precursors include sufficient volatility to allow rapid reaction with the surface reactive sites. The steric bulk of ligands should be minimized to afford maximum density of precursor-derived molecules on the surface, which will lead to maximum film growth rate. The absence of undesired elements in the precursors is also required. Moreover, film growth byproducts should be volatile in order to reduce impurities in the film.

Metallic first row transition metal thin films need to be deposited by ALD to meet future conformality and film thickness uniformity requirements in microelectronics.² In order to achieve these conformality and uniformity requirements, depositions should be done ≤ 150 °C, since low temperature reduces surface mobility of atoms and minimizes the tendency of the metal atoms to form islands at low thicknesses and rough films at higher thicknesses.

To date, only the growth of Cu thin films and noble metal thin films is well developed, due to the positive reduction potential of the M(II) ions and the availability of sufficiently strong reducing agents that can reduce M(II) precursors to their zero valent state.^{18,19} The difficulty in

reducing transition metals M(II) to the metals M(0) is governed by the reduction potentials listed in Table 1.^{20a} The potentials become generally more negative in going from Ni(II) to Cr(II), and the ALD growth becomes more difficult as the E° values decrease. Thermal ALD processes for Ni to Cr are poorly developed or unknown, due to the lack of suitable reactive co-reagents that can reduce the metal precursors in positive oxidation states to the metal(0) oxidation state.¹⁸ Consequently, PEALD or high temperature thermal ALD have been used to deposit Ni, Co, Fe, and Mn films, while deposition of Cr has not been achieved by any kind of ALD method.¹⁸ The following sections describe the current state of the literature of late first row transition metal ALD precursors and processes.

Table 1. Reduction potentials.

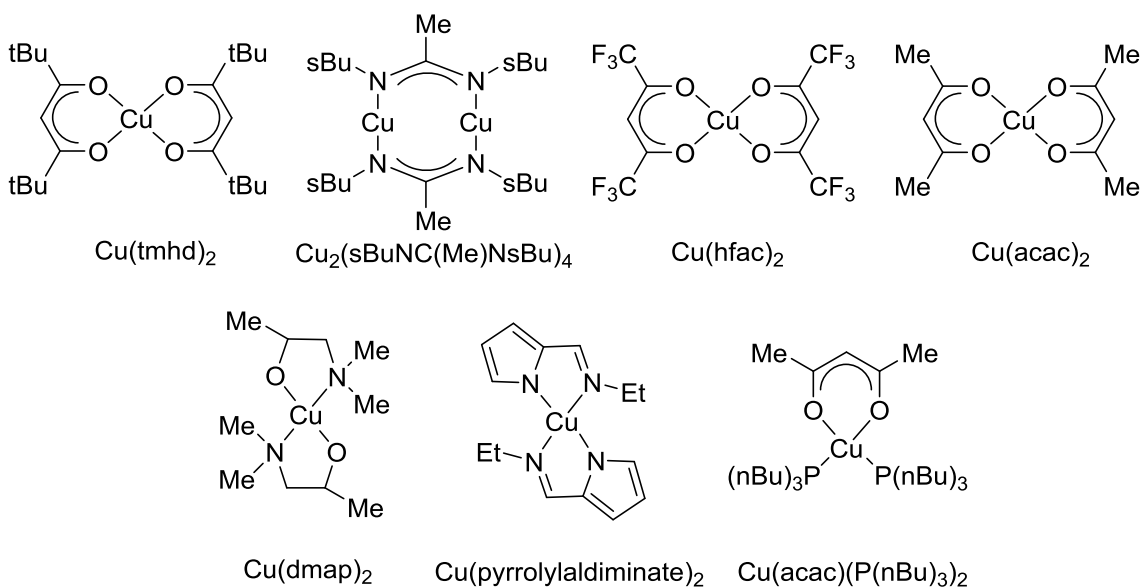
$M^{2+} + 2e^- \leftrightarrow M$	E° (V)
Cu	0.3419
Ni	-0.257
Co	-0.280
Fe	-0.447
Mn	-1.185
Cr	-0.913

1.4.1 Copper Metal Films by ALD

Cu has replaced aluminum as interconnect materials in integrated circuits, due to its low resistivity and high resistance for electromigration.³ Cu precursors that have been reported in the literature for the ALD growth of Cu films are shown in Chart 1. The deposition of Cu metals has been performed by indirect and direct ALD. In indirect ALD, CuO, Cu₂O, and Cu₃N have been

deposited first by ALD and then are reduced by reducing co-reagents.¹⁷ This section will be mainly focused on direct Cu depositions, which do not require prior deposition of Cu oxides or nitrides.

Chart 1. Cu ALD precursors.



Direct Cu ALD processes include $\text{Cu}(\text{tmhd})_2$ and H_2 between 190 and 260 °C,^{22a} $\text{Cu}_2(\text{sBuNC}(\text{Me})\text{NsBu})_4$ and H_2 between 150 and 250 °C,^{22b} $\text{Cu}(\text{hfac})_2$ and isopropanol at 300 °C,^{22c} CuCl and H_2 between 360 and 410 °C,^{22d} and CuCl and Zn between 440 and 500 °C.^{22e} In these processes, high deposition temperatures are required because of the low reactivity of the Cu precursors toward reducing co-reagents at lower temperatures. In the process that uses CuCl and Zn, temperatures of 400 °C are required to avoid condensation of CuCl and Zn due to their low volatilities.

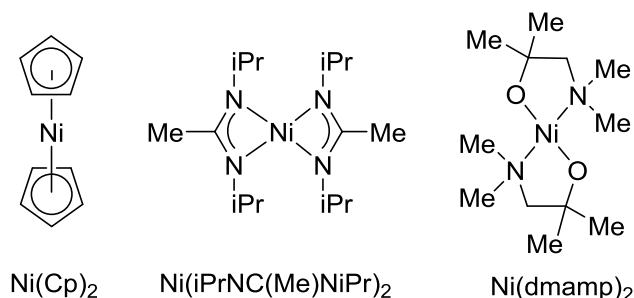
A remarkable achievement in ALD of Cu was reported using the precursors $\text{Cu}(\text{dmap})_2$ and ZnEt_2 .²³ This process demonstrated the deposition of Cu films within the ALD window of 100–120 °C and the films were high pure, low resistive Cu. However, zinc incorporation was observed above 130 °C, which reduces the viability of this process in device fabrication.

Recently, Winter et al. reported a low temperature Cu ALD process that employs $\text{Cu}(\text{dmap})_2$, formic acid, and hydrazine.²⁴ In this process, $\text{Cu}(\text{dmap})_2$ is unreactive toward hydrazine, but can be transformed to Cu(II) formate upon treatment with formic acid. Cu(II) formate is then readily reduced to Cu metal by hydrazine. Much more detail discussion about ALD Cu is described in Chapter 7.

1.4.2 Nickel Metal Films by ALD

Alloy films containing Ni (NiSi , Ni_3N) are used as contact materials in metal oxide semiconductor field effect transistor (MOSFET) devices.²⁵ The volatile precursors that have been reported for Ni ALD include $\text{Ni}(\text{dmamp})_2$,²⁶ $\text{Ni}(\text{tmhd})_2$,²⁷ $\text{Ni}(\text{Cp})_2$,²⁸ $\text{Ni}(\text{EtCp})_2$,²⁸ $\text{Ni}(\text{Cp})(\text{allyl})$,²⁹ $\text{Ni}(\text{tBuNC}(\text{nBu})\text{NtBu})_2$,³⁰ $\text{Ni}(\text{OC}(\text{CF}_3)\text{CHC}(\text{Me})\text{NH})_2$,³¹ and $\text{Ni}(\text{tBu}_2\text{DAD})_2$.³² The precursors that have been used to date for the ALD growth of Ni films are shown in Chart 2.

Chart 2. Ni ALD precursors.



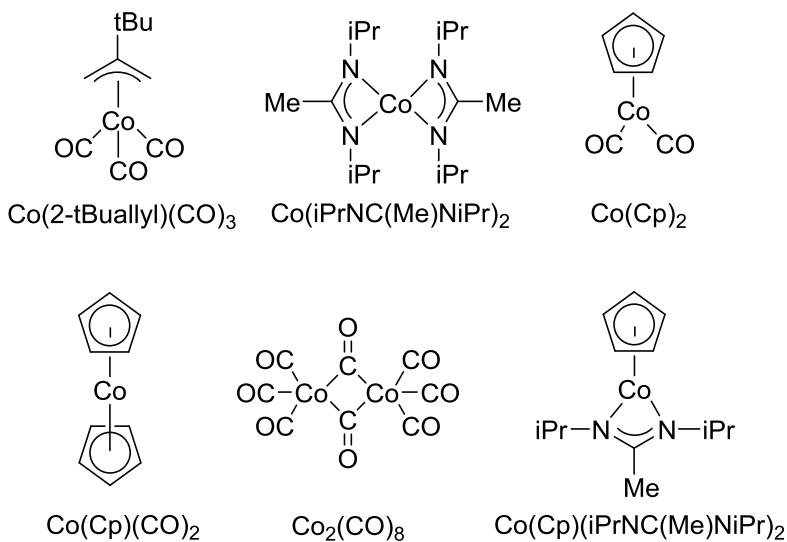
The thermal ALD growth of Ni metal films is not well developed. An indirect Ni ALD process has been reported using $\text{Ni}(\text{Cp})_2$ and water at 165 °C on TiN substrate. The resultant NiO film was then treated with an H_2 plasma to afford Ni metal films.³³ Gordon reported an ALD process using $\text{Ni}(\text{iPrNC}(\text{Me})\text{NiPr})_2$ and H_2 that affords Ni metal films at a growth temperature of 250 °C.^{22b} However, the deposition temperature is higher than the thermal decomposition temperature of $\text{Ni}(\text{iPrNC}(\text{Me})\text{NiPr})_2$ which suggest a CVD process. Another thermal Ni ALD process was reported using $\text{Ni}(\text{dmamp})_2$ and H_2 with temperatures between 200 and 240 °C.³⁴

These growth temperatures are also above the decomposition temperature of $\text{Ni}(\text{dmamp})_2$, and therefore the process may occur by CVD-like growth. The PEALD growth of Ni thin films and nanorods has been demonstrated using $\text{Ni}(\text{dmamp})_2$ and H_2 or ammonia plasma with substrate temperatures between 200 and 250 °C.^{34b-e} The growth rate was about 1.0-1.6 Å/cycle within this temperature range with using H_2 plasma.

1.4.3 Cobalt Metal Films by ALD

Co films are used in magnetoresistive devices, integrated circuits, and lithium batteries.³⁵ The volatile Co precursors that have been reported for Co ALD include $\text{Co}(\text{tmhd})_2$,³⁶ $\text{Co}_2(\text{CO})_8$,³⁷ $\text{Co}(\text{Cp})(\text{iPrNC}(\text{nBu})\text{NiPr})$,³⁸ $\text{Co}(\text{Cp})_2$,³⁷ $\text{Co}(\text{Cp})(\text{CO})_2$,³⁷ $\text{Co}(\text{Cp})(\text{allyl})$,³⁹ and $\text{Co}(\text{tBu}_2\text{DAD})_2$.³² The precursors that have been used to date for the ALD growth of Co films are shown in Chart 3.

Chart 3. Co ALD precursors.



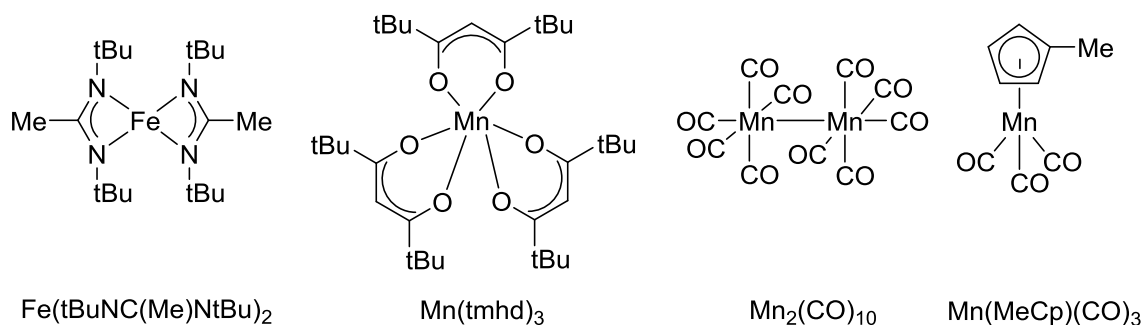
There have been few reports of the thermal ALD growth of Co metal films. An ALD process that have used $\text{Co}(\text{2-tBuallyl})(\text{CO})_3$ and 1,1-dimethylhydrazine has reported the growth of Co metal films at a substrate temperature of 140 °C.³⁹ However, the basic ALD growth parameters of this process were not reported. Another ALD process using the precursors

$\text{Co}(\text{iPrNC}(\text{Me})\text{NiPr})_2$ and H_2 afforded Co metal films at a growth temperature of $350\text{ }^\circ\text{C}$.^{22b} However, the growth rate was low ($0.12\text{ \AA}/\text{cycle}$) and the deposition temperature was higher than the Co precursor decomposition temperature, which suggest CVD-like growth. Another report described the thermal Co ALD growth using the same precursors, $\text{Co}(\text{iPrNC}(\text{Me})\text{NiPr})_2$ and H_2 , at a substrate temperature of $300\text{ }^\circ\text{C}$.⁴⁰ PEALD of Co metal thin films have been reported using precursors $\text{Co}(\text{Cp})(\text{CO})_2$, $\text{Co}(\text{Cp})_2$, $\text{Co}_2(\text{CO})_8$, and $\text{Co}(\text{Cp})(\text{iPrNC}(\text{Me})\text{NiPr})$.^{37,38} The reducing agents ammonia, H_2 , or N_2 plasmas were employed and growth temperatures were between 75 and $175\text{ }^\circ\text{C}$. These processes have growth rates up to $1.5\text{ \AA}/\text{cycle}$.

1.4.4 Iron, Manganese, and Cr Metal Films by ALD

Fe and Cr metal thin films are important because of their magnetic, electrical, optical, and catalytic applications.⁴¹ Cr films are also proposed as Cu seed layers for Cu metallization in electronic devices.^{6,41} Mn containing thin films (MnSi_xO_y) can be used as Cu barrier layers.⁷ Metalorganic Fe and Mn precursors that have been used to date for the ALD growth of metallic films are shown in Chart 4. To date, the deposition of Cr films by CVD or ALD has not been demonstrated. The volatile precursors for this group include $\text{Fe}(\text{tmhd})_3$,⁴² $\text{Fe}_2(\text{OtBu})_6$,⁴³ $\text{Fe}(\text{Cp})_2$,⁴⁴ $\text{Fe}(\text{tBu}_2\text{DAD})_2$,³² $\text{Mn}(\text{EtCp})_2$,⁴⁵ $\text{Mn}(\text{tmhd})_3$,⁴⁶ $\text{Mn}_2(\text{CO})_{10}$,⁴⁷ $\text{Mn}(\text{MeCp})_2$,⁴⁷ $\text{Mn}(\text{iPrNC}(\text{nBu})\text{NiPr})_2$,⁴⁸ and $\text{Mn}(\text{tBu}_2\text{DAD})_2$,³² $\text{Cr}(\text{B}_3\text{H}_8)_2$,⁴⁹ $\text{Cr}(\text{iPrNC}(\text{CH}_3)\text{NiPr})_3$,⁵⁰ $\text{Cr}(\text{tBuNC}(\text{CH}_3)\text{NtBu})_2(\text{X})$ ($\text{X} = \text{pyrazolate, 1,2,4-triazolate}$),⁵⁰ and $\text{Cr}(\text{tBu}_2\text{DAD})_2$.³²

Chart 4. Fe and Mn ALD precursors.



The reductions of Fe, Mn, and Cr in +2 or +3 oxidation states to their zero valent states are difficult. As summarized in Table 1, compared to the similar ions of Cu, Ni, and Co, the +2 ions of Fe, Mn, and Cr have very negative reduction potentials. Therefore, little progress has been made with the thermal ALD growth of metallic films of these elements. The ALD growth of Fe metal films has been reported using $\text{Fe}(\text{tBuNC}(\text{Me})\text{NtBu})_2$ and H_2 at a deposition temperature of 250 °C.^{22b} The ALD growth of Fe metal films on aerogels has been reported, but no details were given.⁵¹ The thermal ALD growth of Mn metal films has not been reported to date, due to the extremely negative reduction potential of the Mn(II) ion (Table 1). The PEALD growth of Cu/Mn metal alloy films was reported, using $\text{Cu}(\text{dmamp})_2$, $\text{Mn}(\text{tmhd})_3$, and H_2 plasma with substrate temperatures between 100 and 180 °C.⁵² However, the surfaces of the films were rough and the roughness increased with deposition temperature. To date, there are no thermal or plasma ALD processes for the deposition of Cr metal thin films.

1.5 Overview of Ligands Used in Metal Precursors

Anionic and neutral ligands have been used to design ALD precursors. Anionic ligands that have been used in ALD precursors include alkoxides such as dmap and dmamp, β -diketonates such as acac, tmhd, and hfac, amidinates such as $i\text{PrNC}(\text{Me})\text{NiPr}$, $\text{tBuNC}(\text{Me})\text{NtBu}$, and $s\text{BuNC}(\text{Me})\text{NsBu}$, pyrrolylaldiminates, β -diketiminates, 2-tBuallyl, Cp and alkyl-substituted Cp, and halides. Neutral ligands that have been used in precursor development include phosphines such as $\text{P}(\text{nBu})_3$, vinyltrimethylsilane, and carbonyl. Precursors that have neutral ligands tend to have low thermal stability, since loss of the neutral ligand often provides low temperature decomposition pathways. Consequently, such ligand loss limits the upper temperature of self-limited ALD growth. Moreover, chelating anionic ligands can provide highly thermally stable precursors. The purpose of the ligands in the precursor is to provide the highest

volatilities, the highest possible decomposition temperatures, and reactivity toward the reducing co-reagent to provide the desired metal film. As noted above, metallic transition metal films generally need to be grown at low temperatures (≤ 150 °C) to obtain smooth, continuous films. Thermal stabilities of the precursors above 200 °C are highly desirable to ensure that the precursors can be heated at delivery temperatures for extended periods of time without decomposition, and self-limited ALD growth can occur over a wide window. High volatility of precursors is extremely important, since the lowest deposition temperature is usually higher than the precursor delivery temperature, in order to avoid condensation on the substrate and reactor walls. First row transition metal precursors containing many β -diketonate ligands are oligomeric due to the smaller sizes of the ligands, which lead to low volatilities. Although monomeric β -diketonate complexes have been synthesized using bulky substituents on the ligand back bone, these complexes have low volatilities due to the high molecular weight of the precursors.⁵³ Complexes containing β -diketiminatate ligands tend to form monomeric complexes due to the large size of the ligand, however, many have low thermal stabilities.⁵⁴ Amidinate precursors have been used in ALD to deposit metallic films, however, many have low thermal stabilities.^{38,22b} The reported Cu and Ni precursors with alkoxide ligands have high volatilities.¹⁸ However, due to the presence of accessible β -hydrogen atoms, they can have low thermal stabilities. Moreover, due to their small size, alkoxide ligands do not form volatile and stable complexes with larger ions, such as Co(II), Fe(II), Mn(II), and Cr(II).

Numerous metalorganic precursors have been made in the past using the above mentioned and some other ligand systems. Nevertheless most of precursors suffer from low thermal stability, low volatility, or low reactivity. In order to obtain high thermal stability, conjugated ligands without β -H atoms are desirable. Volatility can be increased by avoiding

phenyl groups and other aromatic groups. However, when the ligand becomes too small it cannot saturate the coordination sphere of the metal center, which may lead to the formation of dimeric compounds. Therefore new ligands should be designed by considering all of the above ideas. This thesis demonstrates attempts to make novel transition metal precursors from newly designed ligands.

1.6 Reducing Co-reagents

One of the major problems in the ALD of first row transition metal films is the lack of powerful reducing co-reagents that can convert a metal precursor (usually in a positive oxidation state) to its metallic form. Based on the reduction potentials listed in Table 1, some of the metal ions have very negative reduction potentials, making them hard to reduce to their metallic form. Among the first row transition metals, Cu(II) is the most easily reduced to its metallic form, because the Cu(II) ion has a positive reduction potential. Consequently, the growth of Cu metal films is the best developed among the first row transition metals. In the deposition of Cu metal films, many different reducing co-reagents have been used such as H_2 ,^{22a,22b,22d} isopropanol,^{22c} Zn,^{22e} $ZnEt_2$,²³ hydrazine,²⁴ and formic acid.^{22f} As described in the Section 1.4.1, some of these reducing agents afforded low temperature thermal growth of high purity, low resistivity Cu films.^{23,24} Although Cu(II) is reduced by the above mentioned reducing agents, other first row transition metal ions including Ni(II), Co(II), Fe(II), Mn(II), and Cr(II), cannot be reduced by these reducing agents at the low temperatures due to the high reduction potentials of M(II) ions. Although ALD growth of Ni, Co, and Fe films has been reported using H_2 , the depositions have been performed at above 200 °C, because H_2 does not react with first row transition metal precursors below 200 °C.^{22b} Also, thermal ALD growth of Ni, Co, Fe, and Mn has not been reported with reducing agents other than H_2 . Due to the lack of reactivity of available reducing

co-reagents PEALD processes have been used to deposit Ni,^{33,34b-e} Co,^{37,38} and Mn⁵² films. As noted above, due to the possibility of substrate damage and low conformal coverage in high aspect ratio features, plasma processes may not be acceptable for the deposition of metallic transition metal films in microelectronics devices. Unlike the deposition of other first row transition metal films, Cr films have not been deposited either by any ALD or CVD method.

Thermal ALD growth of metallic Ni, Co, Fe, Mn, and Cr films requires the identification of highly reactive co-reagents that are capable of reducing these metal ions to their metallic states. Main group element hydrides are potentially promising reducing co-reagents, since they should transfer hydride from the main group element to the transition metal. Boranes and related compounds containing B–H bonds may be promising ALD co-reagents, and have proven successful in the solution growth of metallic transition metal nanoparticles.⁵⁵ There are many commercially available and volatile borane adducts in the form of BH₃(L) (L = THF, various amines, other donor ligands). The transition metal hydrides formed from H atoms transfer from B atoms are known to be unstable leading to the rapid elimination of H₂ to afford the metals.⁵⁶

1.7 Molybdenum and Tungsten Oxides

Chapter 8 describes the synthesis and characterization of Mo and W complexes as potential precursors for the deposition of MoO_x and WO_x films, respectively. Metal oxides can be used as insulators, semiconductors, conductors, superconductors, catalysts, and gas sensors.^{12a} Metal oxide films can be deposited by ALD through treatment of the metal source precursors with H₂O, H₂O₂, O₂, or O₃.⁶ H₂O has been used for the deposition of most oxide films, whereas O₃ is used with less reactive precursors due to its high oxidizing power.^{12a} Many metal oxides have been deposited by ALD, including ZrO₂,^{12a} HfO₂,^{12a} ZnO,^{12a} SnO₂,^{12a} Al₂O₃,⁵⁷ and Ta₂O₅.⁵⁸ The Mo and W oxides MoO₃ and WO₃ have are of great interest due to their optical and

electronic properties.⁵⁹ MoO₃ films have been deposited by various methods, including ALD,^{60a} thermal evaporation,^{60b} sputtering,^{60c} CVD,^{60d} electrodeposition,^{60e} flash evaporation,^{60f} and photochemical metal-organic deposition,^{60g} whereas, WO₃ films have been deposited by ALD,^{61a},^{61b} CVD,^{61c} plasma enhanced CVD,^{61d} and sputtering.^{61e} In nearly all metal oxide thin films, the metal is in the highest common oxidation state, irrespective of the metal precursor oxidation state.

Recently, the Winter group reported the deposition of W₂O₃ films by ALD from W₂(NMe₂)₆ and water.⁶² Interestingly, this ALD process led to the deposition of W₂O₃ (not WO₃) with retention of the oxidation state of the metal precursor.⁶² Importantly, W₂O₃ is a largely unprecedented oxide.^{61a-c} Reasons for the formation of W₂O₃ include the low deposition temperatures (≤ 220 °C), high reactivity of the precursor toward water, and the low oxidizing power of water.⁶² These results suggest that similar ALD processes with other low or mid-valent metal precursors that are volatile, thermally stable, and highly reactive toward water should afford the corresponding metal oxides with same oxidation state as the precursor. The deposition of low-valent metal oxide or nitride materials, where the oxidation state of the metal in the thin film is the same as that of the precursors, is very rare.⁶² The depositions of SnO,^{63a} PbO,^{63b} and Ta₃N₄^{63c} films, which have the same oxidation state as the metal precursor, have been reported by CVD.

1.8 Thesis Problem

As noted above, metal films deposited by ALD have high demand in microelectronics manufacturing because ALD offers highly conformal films and high thickness control. However, there is much room for improvement in first row transition metal ALD. As mentioned above, thermal ALD growth of Ni, Co, Fe, Mn, and Cr are poorly developed or unknown. The major

reasons include lack of suitable metal precursors and powerful reducing co-reagents. As a result, highly volatile, thermally stable, and reactive metal precursors should be designed and synthesized. Also, screening of the reducing power of available reducing co-reagents should be carried out.

The deposition of low-valent metal oxides, where the oxidation state of the metal in the thin film is the same as that of the precursors, is very rare. These largely unprecedented mid-valent metal oxides may have important uses compared to existing oxides. Based on the discussion in Section 1.7, divalent Mo and W ALD precursors that are volatile, highly reactive toward an oxygen precursor, and thermally stable, should afford metal oxides, MoO and WO, respectively, where the metal is in the +2 oxidation state.

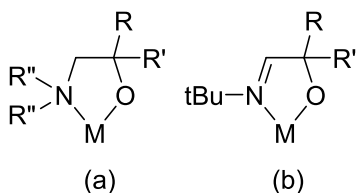
The goals and the focus of this thesis are the design and synthesis of new transition metal precursors, screening of reducing co-reagents, and deposition of transition metal thin films by ALD. The new metal precursors are expected to be highly volatile, thermally stable, and reactive toward the co-reagents. The structure and properties of the new complexes will be evaluated by NMR, IR, melting point determinations, elemental analyses, X-ray crystal structure determinations, and magnetic moment calculations. The volatility and the thermal stability will be assessed by preparative sublimations, thermogravimetric analysis (TGA)/differential thermal analysis (DTA), and solid state decomposition temperature determinations. ALD growth studies will be performed using the newly synthesized metal precursors and appropriate co-reagents. The film compositions and morphologies will be assessed by X-ray photoelectron spectroscopy (XPS), X-ray diffraction (XRD), atomic force microscopy (AFM), scanning electron microscopy (SEM), and four-point probe resistivity.

CHAPTER 2

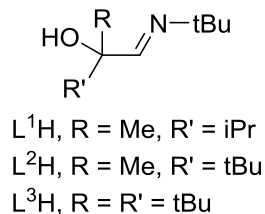
Volatile and Thermally Stable Mid to Late Transition Metal Complexes Containing α -Imino Alkoxide Ligands

2.1 Introduction

There is considerable interest in the growth of metallic first row transition metal thin films by atomic layer deposition (ALD), in view of their applications in microelectronics and other devices.⁶⁴ ALD of these metals requires precursors that combine volatility, thermal stability at the deposition temperature, and high reactivity toward a second reagent to afford the metallic film.^{12c,12d,15a} While several low temperature (< 200 °C) thermal ALD processes have been reported for Cu,^{23,24} analogous growth of the other first row transition metals remains scantily documented.^{22a,34a,39,40} Alloy films, such as Cu/Mn for fabrication of ultrathin, conformal Mn-Si-O Cu diffusion barriers,⁷ require Cu, Mn, and other precursors with similar chemistry and deposition temperatures, as well as a common co-reagent that can reduce all metal precursors equally well (E° Cu(II) = 0.3419 V; Mn(II) = -1.185 V²⁰). Such precursors do not currently exist.¹⁸ Cu⁶⁴ and Ni⁶⁵ complexes containing β -amino alkoxide ligands (Chart 5, (a)) are widely used precursors for the growth of Cu and Ni films by ALD and chemical vapor deposition (CVD).^{23,24,34} However, volatile β -amino alkoxide complexes are unknown for the other first row transition metals, presumably because these ligands cannot saturate the coordination spheres of the larger metal(II) ions. Moreover, there is a lack of volatile, strong reducing agents that can transform first row transition metal(II) ions to the metals at low temperatures.¹⁸

Chart 5. β -Amino alkoxide (a) and α -imino alkoxide (b) ligands.

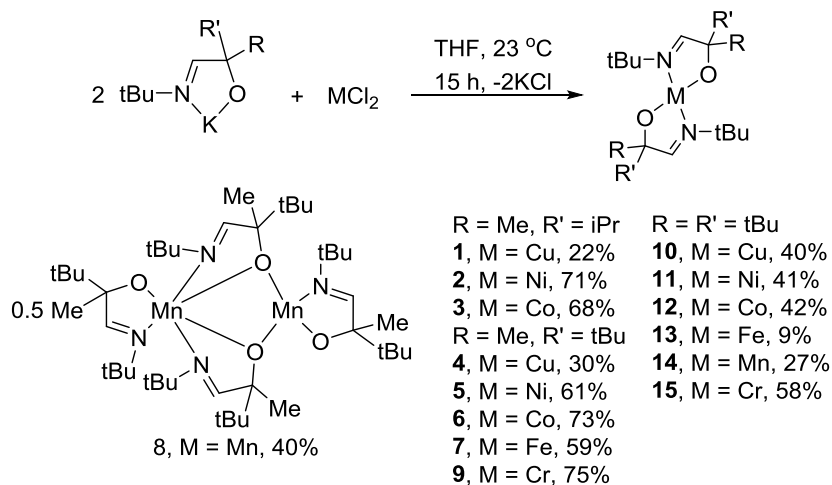
In this chapter the synthesis, structure, volatility, and thermal stability of a series of Cu(II), Ni(II), Co(II), Fe(II), Mn(II), and Cr(II) complexes that contain α -imino alkoxide ligands (Chart 5, (b) and Chart 6) are described. These complexes exhibit good volatilities, high thermal stabilities, and high reactivities toward reducing agents, and thus have excellent properties for use as ALD precursors. Additionally, it was found that $\text{BH}_3(\text{NHMe}_2)$ can reduce Cu, Ni, Co, Fe, and Cr α -imino alkoxide precursors to their corresponding zero valent metals. This work therefore demonstrates a general new class of ALD precursors as well as a strong reducing agent that can be used for the ALD growth of metal films from metal ions with negative E° values.

Chart 6. Chemical structures of L^1H – L^3H .

2.2 Results and Discussion

Synthetic Aspects. The α -imino alcohols (Chart 6) were prepared and characterized as described in the Experimental Section. Treatment of the alcohols with KH in tetrahydrofuran, followed by addition of anhydrous MCl_2 , afforded **1–15** after workup by sublimation (Scheme 1). Similar treatment of FeCl_2 , MnCl_2 , and CrCl_2 with KL^1 did not afford isolable products.

Scheme 1. Synthesis of 1–15.



These complexes were characterized by spectral and analytical methods, and by X-ray crystallography. The Ni complexes **2**, **5**, and **11** are diamagnetic, and the ^1H NMR spectrum of **11** showed the expected two singlets in a 2:1 ratio for the ligand tBu groups. The ^1H NMR spectra of **2** and **5**, by contrast, revealed sets of resonances for two diastereomers in 1:1 ratios, due to the presence of a chiral center in each ligand. The remaining complexes are paramagnetic and exhibited very broad resonances in their ^1H NMR spectra. Solid state and solution magnetic moment data suggested that **1**, **4**, **9**, **10**, and **15** are square planar in both media, which was corroborated by X-ray structural data for **1**, **10**, and **15**. Magnetic data showed that **3**, **7**, **13**, and **14** are tetrahedral in the solid state and in solution, which fit the crystal structures of **3** and **14**. Magnetic data suggest that **6** and **12** are square planar in the solid state, but are tetrahedral in solution.

X-Ray Crystal Structures. Among **1–9**, only low resolution X-ray crystal structures could be obtained for **1–3** and **8**, due to the diastereomeric mixtures and difficulty in growing single crystals. However, high quality X-ray crystal structures of **10–12**, **14**, and **15** were determined. A low resolution X-ray crystal structure of **8** showed a dimer with the atom

connectivity shown in Scheme 1. The X-ray crystal structures of **10–12**, **14**, and **15** are shown in Figures 7–11, respectively. Complex **14** is a tetrahedral monomer, with κ^2 -coordination of the α -imino alkoxide ligands. The Mn–O and Mn–N bond lengths are 1.963(1) and 1.967(1) Å and 2.205(1) and 2.216(1) Å, respectively. The intraligand O–Mn–N angles are 79.30(4) and 79.68(4)°, while the corresponding interligand angles are 121.00(4) and 115.02(5)°. The O–Mn–O and N–Mn–N angles are 139.12(5) and 131.18(5)°, respectively. Within the MnC₂NO ligand cores, the C–N, C–C, and C–O bond lengths are 1.263(2) and 1.267(2), 1.517(2), and 1.382(2) and 1.390(2) Å, respectively. These values are consistent with C–N double bonds, C–C and C–O single bonds. By contrast, **10–12**, and **15** are square planar monomers, with κ^2 -coordination of the α -imino alkoxide ligands. The M–O and M–N bond lengths fall in the range of 1.8274(8) to 1.9474(6) and 1.9466(10) to 2.1141(17) Å, respectively. The M–O and M–N bond lengths of **10** and **11** are similar to the those of reported β -amino alkoxide complexes.^{59,60} β -Amino alkoxide structures for Co(II), Fe(II), Mn(II), and Cr(II) are not reported even though heteroleptic structures with monodentate aromatic alkoxide ligands are widely explored.⁶⁶ The intraligand O–M–N angles are between 80.59(7) and 85.14(4)°, while the corresponding interligand angles fall in the range of 94.89(4) to 99.40(7)°. The O–M–O and N–M–N angles are between 179.56(10) and 180.00(14)°, respectively, which demonstrate almost perfect square planar geometries. The C–N, C–C, and C–O bond lengths within the ligand core bonds fall near the corresponding bond lengths of **14**, which reveal structurally similar ligands.

Table 2. Experimental crystallographic data for **10–12, 14, and 15.**

	10	11	12	14	15
Formula	C ₂₈ H ₅₆ CuN ₂ O ₂	C ₂₈ H ₅₆ NiN ₂ O ₂	C ₂₈ H ₅₆ CoN ₂ O ₂	C ₂₈ H ₅₆ MnN ₂ O ₂	C ₂₈ H ₅₆ CrN ₂ O ₂
FW	516.29	512.42	511.70	507.71	504.76
Space group	P2 ₁ /n	P1	P1	P2 ₁ 2 ₁ 2 ₁	P1
a (Å)	10.1813(9)	7.7457(10)	7.7400(7)	9.1671(5)	7.7205(8)
b (Å)	10.3444(9)	9.8404(12)	9.8222(9)	16.1500(9)	9.8256(11)
c (Å)	14.0839(12)	10.4432(13)	10.4549(9)	20.4953(11)	10.5948(12)
V (Å ³)	1436.0(2)	719.34(16)	718.79(11)	3034.3(3)	733.64(14)
Z	2	1	1	4	1
T (K)	100(2)	100(2)	100(2)	100(2)	100(2)
λ (Å)	0.71073	0.71073	0.71073	0.71073	0.71073
ρ _{calc} (g cm ⁻³)	1.194	1.183	1.147	1.098	1.154
μ ((mm ⁻¹))	0.786	0.702	0.621	0.455	0.419
R(F) ^a (%)	4.12	2.52	2.63	2.49	3.03
Rw(F) ^b (%)	13.01	8.85	9.29	8.19	9.20

^aR(F) = $\Sigma||F_o| - |F_c||/\Sigma|F_o|$. ^bRw(F) = $[\Sigma w(F_o^2 - F_c^2)^2/\Sigma w(F_o^2)^2]^{1/2}$.

Table 3. Selected bond lengths (Å) and angles (°) for **10–12, 14, and 15.**

	10	11	12	14	15
M–O	1.8756(13)	1.8419(8)	1.8274(8)	1.9633(10)	1.9426(16)
		1.8428(8)	1.8279(8)	1.9672(10)	1.9474(16)
M–N	2.0526(15)	1.9409(10)	1.9664(9)	2.2053(12)	2.1098(17)
		1.9466(10)	1.9670(9)	2.2157(13)	2.1141(17)
C–O	1.387(2)	1.3865(14)	1.3956(13)	1.3818(17)	1.386(2)
		1.3924(14)	1.4014(13)	1.3904(16)	
C–N	1.268(3)	1.2811(14)	1.2760(14)	1.2632(19)	1.278(3)
		1.2785(14)	1.2785(14)	1.267(2)	
C _{core} –C _{core}	1.510(3)	1.4930(17)	1.4924(16)	1.517(2)	1.506(3)
		1.4963(16)	1.5004(16)		1.523(3)
N–M–O	83.37(6)	85.02(4)	84.27(4)	79.30(4)	80.59(7)
	96.63(6)	85.14(4)	84.33(4)	79.68(4)	80.78(7)
		94.89(4)	95.69(4)	115.02(5)	99.23(7)
		94.94(4)	95.71(4)	121.00(4)	99.40(7)
N–M–N	180.00(14)	179.86(5)	179.83(6)	131.18(5)	179.67(10)
O–M–O	180.00(9)	179.92(6)	179.88(6)	139.12(5)	179.56(10)

Figure 7. Perspective view of **10** with thermal ellipsoids at the 50% probability level.

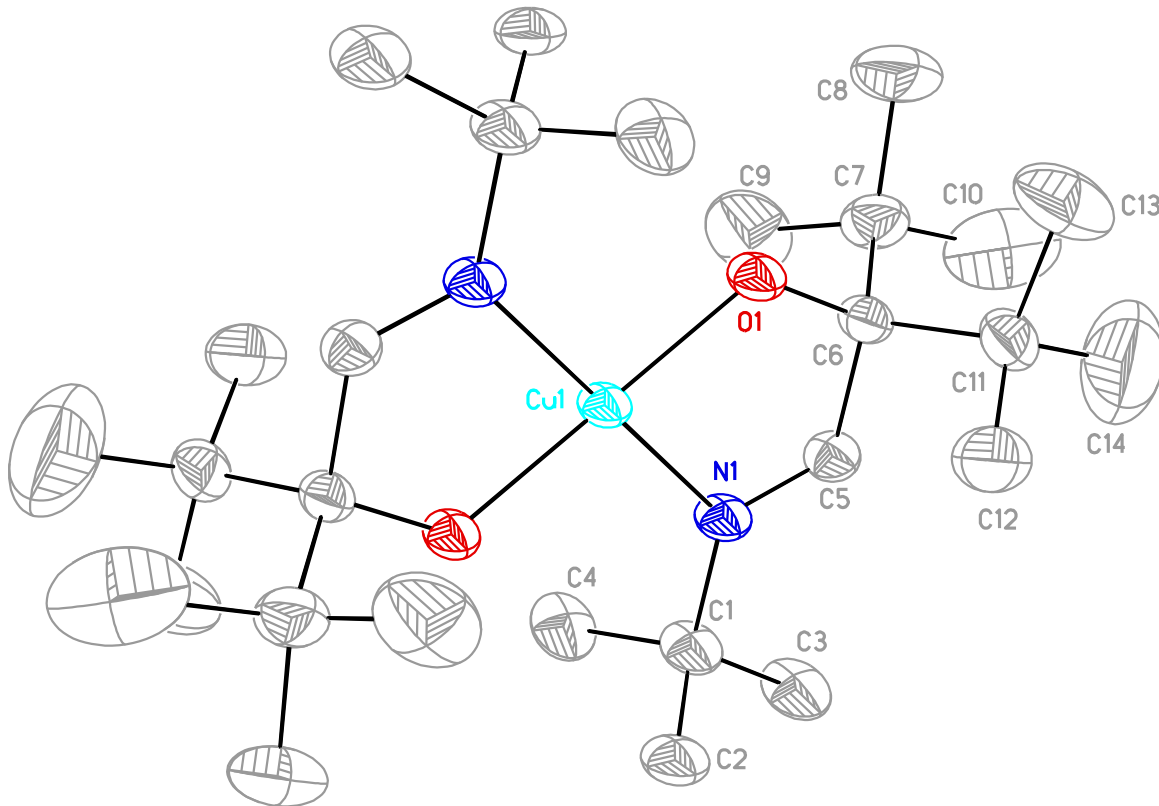


Figure 8. Perspective view of **11** with thermal ellipsoids at the 50% probability level.

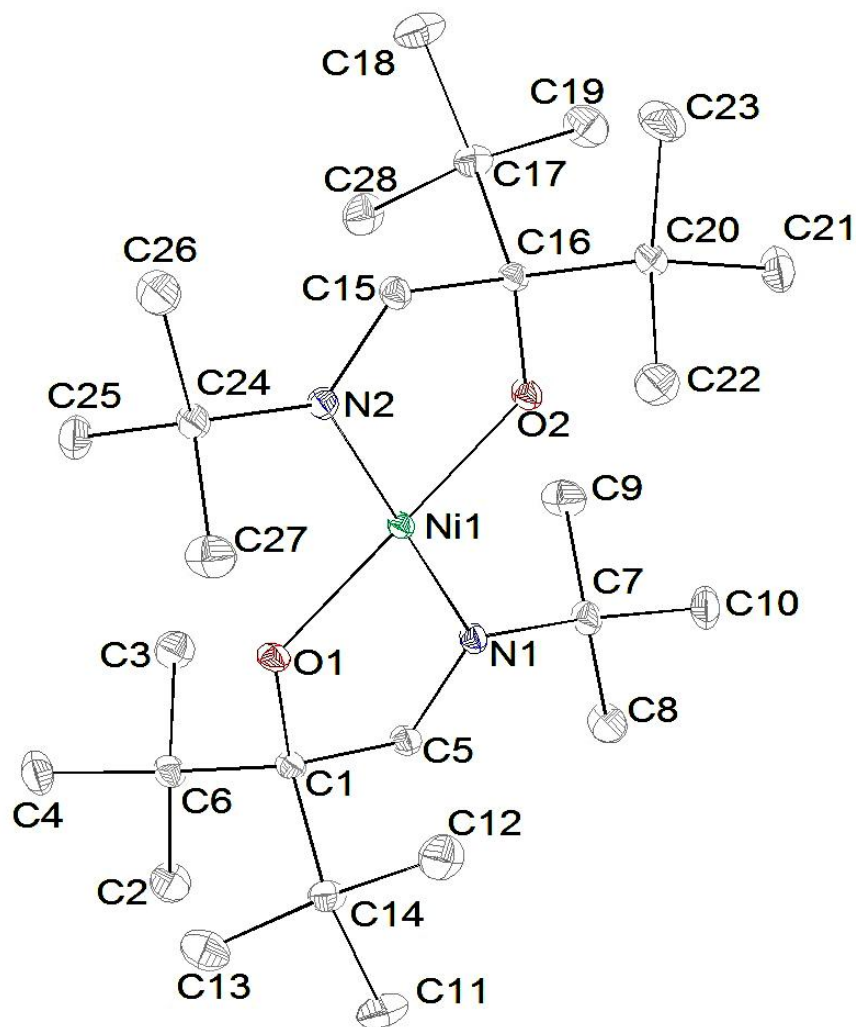


Figure 9. Perspective view of **12** with thermal ellipsoids at the 50% probability level.

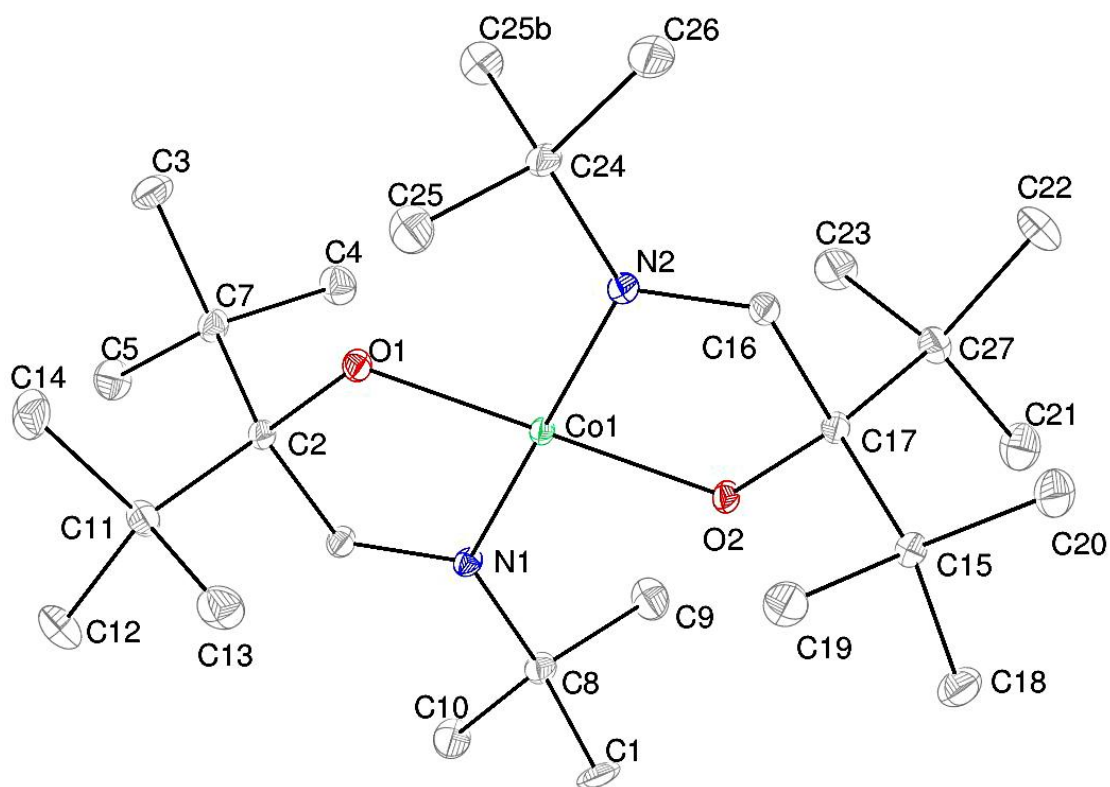


Figure 10. Perspective view of **14** with thermal ellipsoids at the 50% probability level.

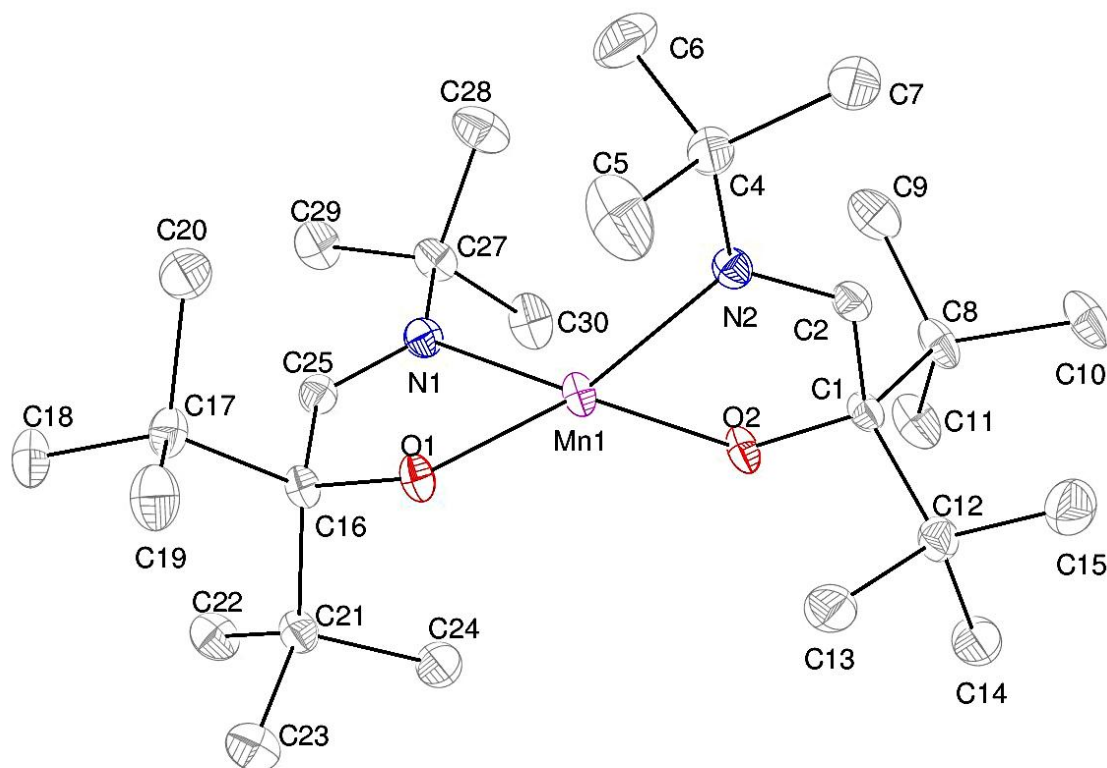
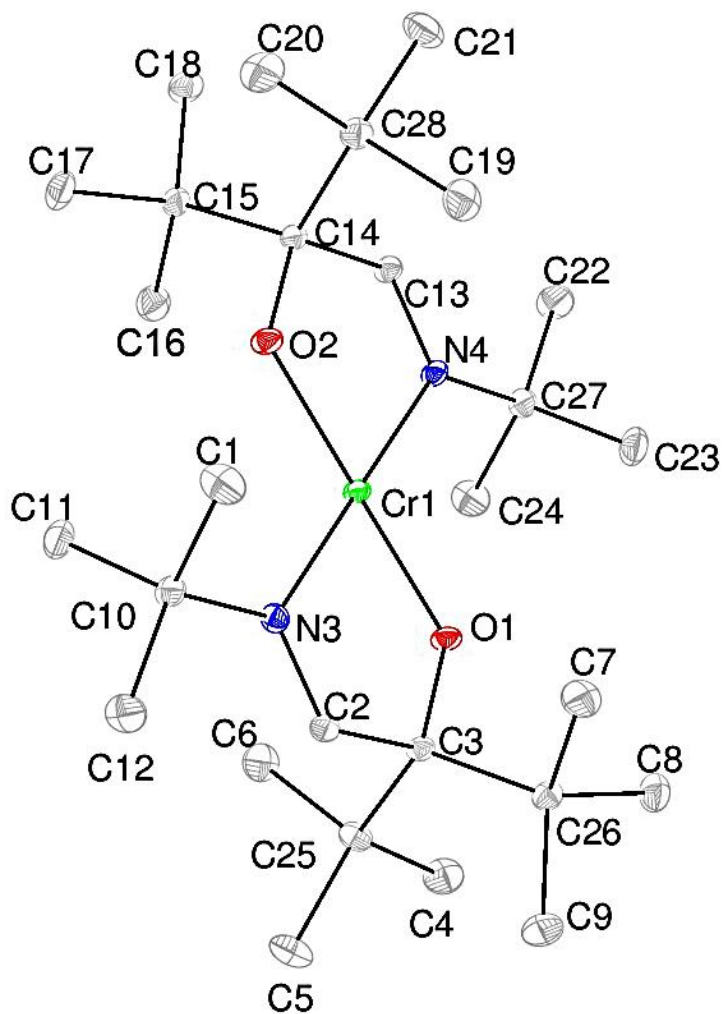


Figure 11. Perspective view of **15** with thermal ellipsoids at the 50% probability level.



Evaluation of Thermal Stability, Volatility, and Reactivity Toward Co-Reagents.

The suitability of **1–15** for use as ALD precursors was assessed by preparative sublimation experiments, solid state decomposition point measurements, and TGA. Table 4 lists thermal properties of **1–15**. These complexes sublime on ~0.5 g scales in ~3 hours with < 5% nonvolatile residues between 90 and 160 °C at 0.05 Torr (Table 4). These preparative sublimation temperatures are approximately the same as those required for precursor delivery in the ALD reactors,²⁴ and thus constitute useful data. The sublimation temperature of **8** is higher than those of the others because of its dimeric structure. This complex is a dimer because the size of the ligand (L^2) is not big enough to saturate the coordination sphere of Mn(II) ion. In contrast, **14** is a monomer because the larger size of the ligand saturates the coordination sphere of Mn(II) ion so that dimerization is avoided. If available, monomeric precursors are preferred over dimers in ALD because high molecular weight precursors tend to have low volatilities. For comparison, monomeric **14** sublimates at 130 °C/0.05 Torr, but undergoes thermal decomposition at 200 °C. Accordingly, **8** has more useful properties, in spite of its dimeric structure. Cu complexes **1**, **4**, and **10** are less volatile than $Cu(dmap)_2$, have similar decomposition temperatures to $Cu(dmap)_2$, and pose no advantage over $Cu(dmap)_2$ for use in ALD.^{23,24,64} The decomposition temperatures of the other complexes are above 200 °C (Table 4), which should permit self-limited ALD growth at < 200 °C. TGA curves for selected precursors are shown in Figures 12 and 13, which show single weight losses due to the sublimation without a prominent decompositions. Successful TGA curves for the other precursors were not obtained because of the higher sensitivity of these precursors to brief air exposure required during the analyses.

Table 4. Volatility and thermal stability data for **1–15**.

	R	R'	Metal	Sublimation temperature (°C/0.05 Torr)	Melting point (°C)	Solid state decomposition temperature (°C)
1	iPr	Me	Cu	105	134–136	183
2			Ni	90	125–127	216
3			Co	90	96–98	234
4	tBu	Me	Cu	130	163–165	203
5			Ni	120	175–177	231
6			Co	115	84–86	232
7			Fe	85	112–114	246
8			Mn	160	221–223	259
9			Cr	115	173–175	230
10	tBu	tBu	Cu	135	183–185	185
11			Ni	140	195–197	215
12			Co	135	144–146	220
13			Fe	130	125–127	201
14			Mn	130	149–151	<200
15			Cr	140	202–204	270

Figure 12. TGA of 1–3.

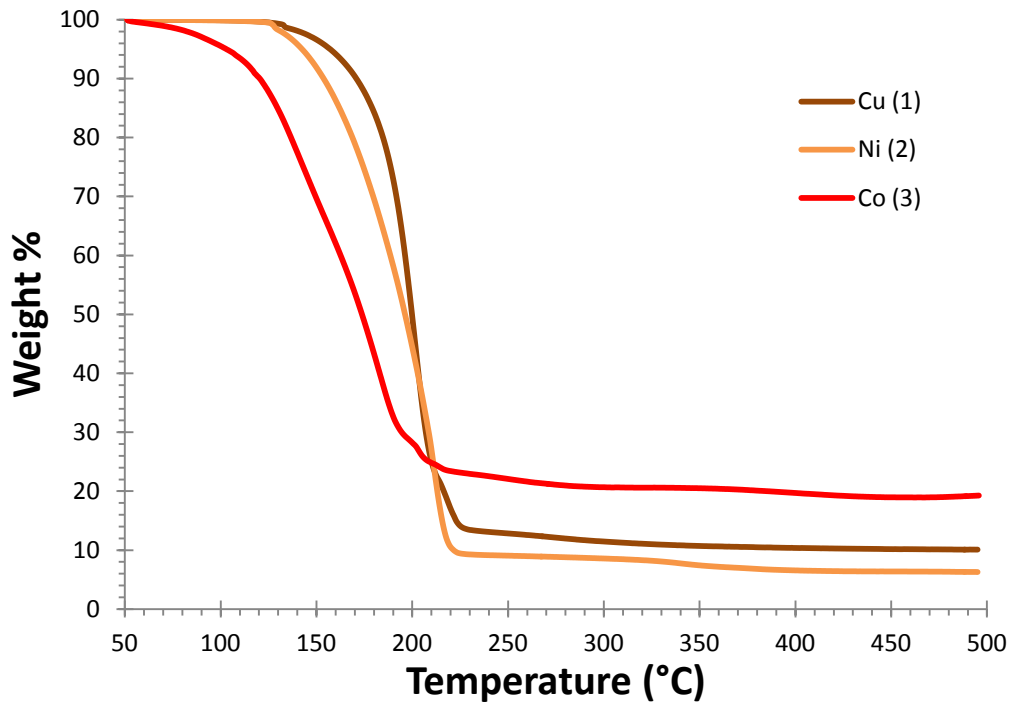
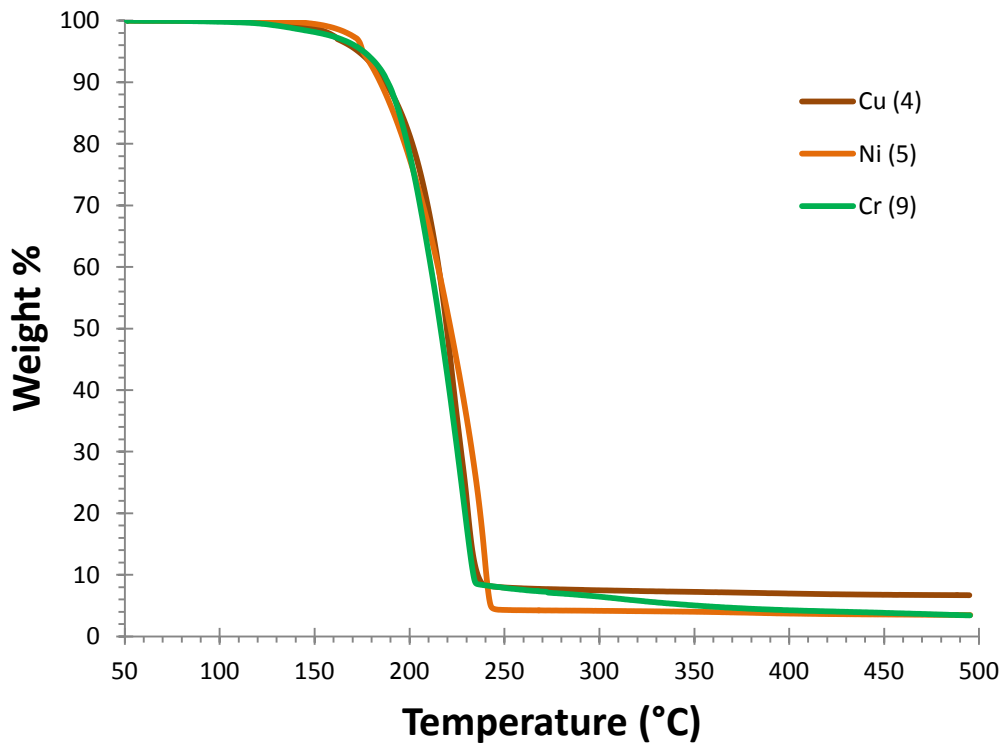


Figure 13. TGA of 4, 5, and 9.



Previous reports have shown that solution reactions between metal precursors and reducing agents are useful in screening precursor pairs for transition metal ALD processes.^{23,24,67} Therefore, **1–6**, **8**, and **10–12** were treated with anhydrous hydrazine and $\text{BH}_3(\text{NHMe}_2)$ in tetrahydrofuran at 23 °C. All of the Cu precursors were reduced by hydrazine and $\text{BH}_3(\text{NHMe}_2)$ in < 0.25 h giving Cu powders, which were confirmed by powder XRD. Metallic black powders were observed with both reducing agents with Ni and Co precursors in < 0.25 h. These precipitates stuck to the magnetic stir bar and powder XRD spectra indicated crystalline Ni and Co (Figures 14 and 15). Treatment of **8** with $\text{BH}_3(\text{NHMe}_2)$ afforded a black powder only upon reflux, and no precipitates were observed with hydrazine.

Figure 14. Powder XRD of Ni produced upon treatment of **2** with $\text{BH}_3(\text{NHMe}_2)$ in tetrahydrofuran at 23 °C. The reference spectrum for Ni metal is overlaid (JCPDS 04-0850).

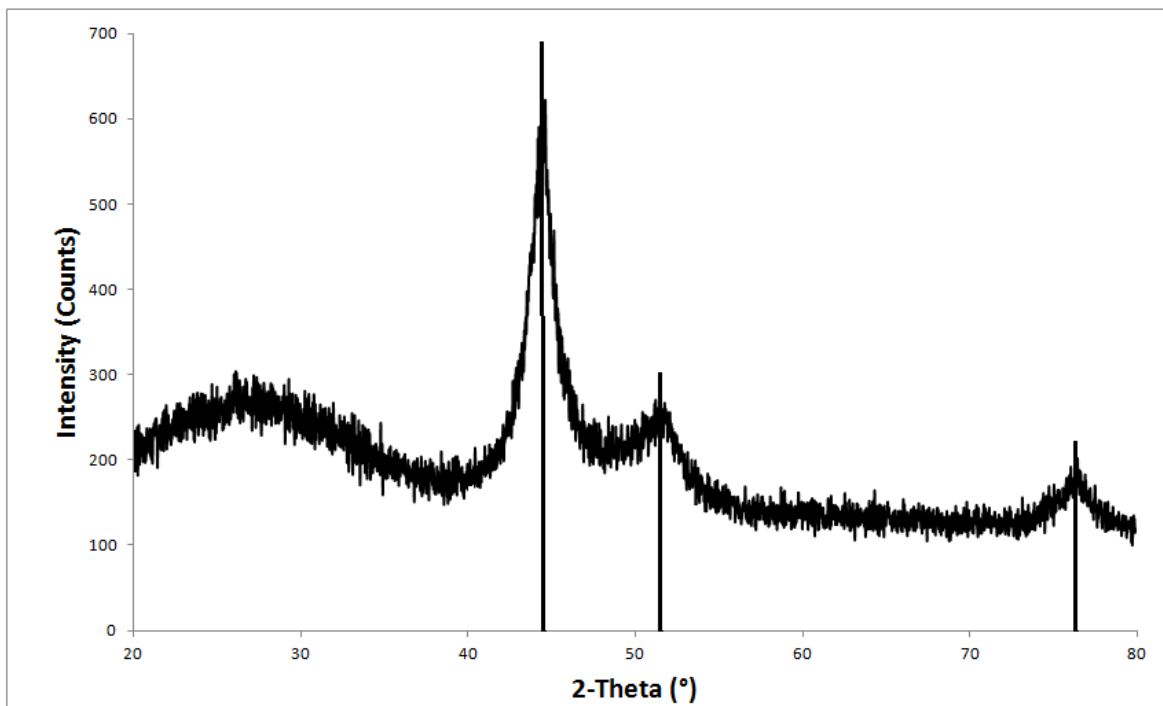
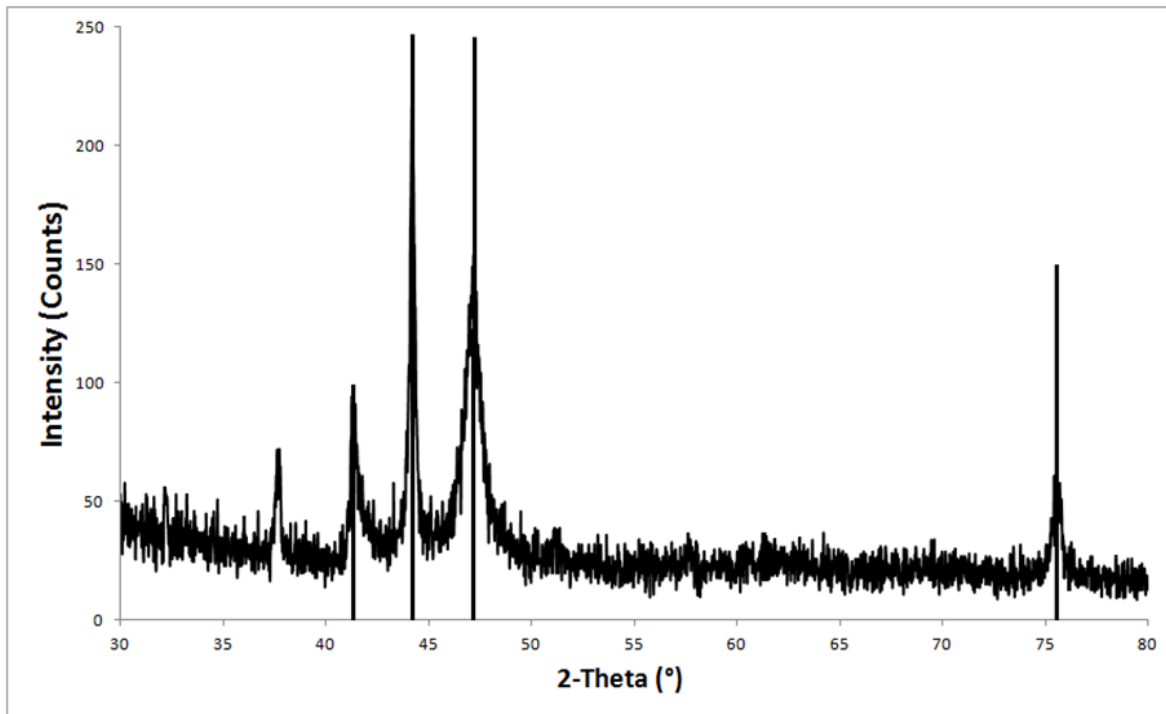


Figure 15. Powder XRD of Co produced upon treatment of **3** with $\text{BH}_3(\text{NHMe}_2)$ in tetrahydrofuran at 23 °C. The reference spectrum for Co metal is overlaid (JCPDS 05-0727).



Encouraged by the solution reactivity results, film depositions with **2**, **3**, and **7–9** and $\text{BH}_3(\text{NHMe}_2)$ were carried out. Self-limiting behavior was observed for **2**, **3**, and **7–9**, with growth rates of about 0.09 (Ni), 0.07 (Co), 0.07 (Fe), 0.10 (Mn), and 0.08 (Cr) Å/cycle at temperatures of 180 (Ni, Co, Fe, Cr) or 225 °C (Mn). XPS confirmed deposition of metallic Ni, Co, Fe, and Cr, but films derived from **8** revealed MnO_x , which likely arises from post-deposition oxidation of Mn upon exposure to air.⁶⁸ The detailed deposition results will be discussed in Chapter 8.

Precursor Properties of 1–15. Complexes **1–15** display good volatilities and high thermal stabilities, and **1–6**, **8**, and **10–12** react with $\text{BH}_3(\text{NHMe}_2)$ co-reagents to provide corresponding metal powders. These properties suggest that **1–15** may be good precursors for use in ALD metal film growth.^{12,15} Importantly, **1–15** contain similar ligands, and are reduced by $\text{BH}_3(\text{NHMe}_2)$ to corresponding metals. Such similar chemistry also should make **1–15** promising

precursors for the ALD growth of metal alloy films, such as Cu/Mn alloys for self-forming barrier layers,⁷ since ALD growth of metal alloys requires overlap of the ALD windows for the separate metals.^{12,15} The properties of **1–15** can be compared with related complexes that have been evaluated for their potential to serve as ALD precursors. The Winter group has reported carbohydrazide complexes $M(\text{OC}(\text{tBu})\text{NNMe}_2)_2$ ($M = \text{Cu}, \text{Ni}, \text{Co}$), which sublime between 70 and 80 °C at 0.05 Torr, and have solid state decomposition temperatures of 255 (Cu), 245 (Co), and 325 °C (Ni).⁶⁹ These complexes have higher volatilities than **1–15** and have higher thermal stabilities than **1–15**. However, Cr(II), Fe(II), and Mn(II) carbohydrazides are not volatile.⁶⁹ The β -amino alkoxide complexes $M(\text{OCRR}'\text{CH}_2\text{NR}'')_2$ ($M = \text{Cu}, \text{Ni}$) have been reported as ALD and CVD precursors. $\text{Cu}(\text{OCHMeCH}_2\text{NMe}_2)_2$ ^{23,24} sublimes at 70–90 °C/0.05 Torr and analogous $\text{Ni}(\text{OCMe}_2\text{CH}_2\text{NMe}_2)_2$ ^{26,28b} and $\text{Ni}(\text{OCMeEtCH}_2\text{NMe}_2)_2$ ^{34a,d} sublime at 90 and 35 °C/0.05 Torr, respectively. Although these precursors have high volatilities, they decompose below 200 °C.^{23,24,26,28b,34a,d} β -Amino alkoxide complexes for Co(II), Fe(II), Mn(II), and Cr(II) have not been reported, possibly because the small size of the ligands cannot saturate the coordination spheres of these metal ions. β -Diketonate complexes are related to alkoxide precursors and Cu(II), Ni(II), Co(III), and Mn(III) complexes have been reported. $\text{Cu}(\text{tmhd})_2$,^{70a} $\text{Cu}(\text{acac})_2$,^{70b} $\text{Ni}(\text{tmhd})_2$,²⁷ $\text{Co}(\text{tmhd})_3$,^{70c} and $\text{Mn}(\text{tmhd})_3$ ^{70d} complexes are volatile and sublime at 120-140, 138, 165, 110, and 90 °C/0.05 Torr, respectively.

2.3 Conclusions

A new class of ALD precursors containing α -imino alkoxide ligands has been synthesized, characterized, and their volatility, thermal stability, and reactivity were assessed. These complexes have useful ALD precursor properties and they react with $\text{BH}_3(\text{NHMe}_2)$ to afford corresponding metal powders in solution, which may lead to viable ALD processes. α -

Imino alkoxide ligands are large enough to saturate the coordination spheres of the larger ions, such as Co(II), Fe(II), Mn(II), and Cr(II), which is not possible with β -amino alkoxide ligands. Moreover, the monomeric and dimeric nature of the complexes can be tuned by changing the size of the ligand.

2.4 Experimental Section

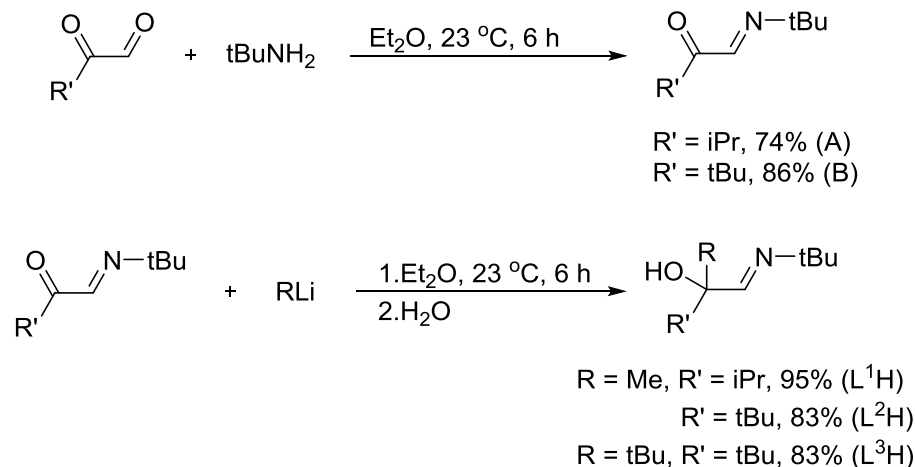
General Considerations. All manipulations were carried out under Ar using either Schlenk or glove box techniques, except that the ligands were prepared under ambient atmosphere. Tetrahydrofuran was distilled from sodium benzophenone ketyl. Hexane was distilled from P_2O_5 . Anhydrous transition metal chlorides ($CrCl_2$, $MnCl_2$, $FeCl_2$, $CoCl_2$, $NiCl_2$ and $CuCl_2$) were obtained from Strem Chemicals Inc. and used as received. $NiCl_2 \cdot CH_3CN$ was prepared according to a literature procedure.⁷¹ Potassium hydride (30 wt% dispersion in mineral oil; washed with hexane before use), *tert*-butyl amine, methyl lithium, and *tert*-butyl lithium were purchased from Sigma-Aldrich. Pinacolone and SeO_2 were purchased from Alfa Aesar. 3-methylbutanal was purchased from Acros Organics. 3-Methyl-2-oxobutanal⁷² and 3,3-dimethyl-2-oxobutanal⁷³ were prepared using published procedures.

1H and $^{13}C\{^1H\}$ NMR spectra were obtained at 400 and 100 MHz in C_6D_6 and were referenced to the residual proton and the ^{13}C resonances of the solvents. Melting points were obtained on a Thermo Scientific Mel-Temp 3.0 digital melting point apparatus and are uncorrected. TGA were carried out with a TA SDT-2960 TGA/DTA instrument at a rate of 10 $^{\circ}C/min$.

Preparation of 1-(*tert*-butylimino)-3-methylbutan-2-one (A). A 100 mL round bottomed flask was charged with a magnetic stir bar, 3-methyl-2-oxobutanal (1.00 g, 9.99 mmol), and diethyl ether (20 mL). To this stirred solution at ambient temperature was slowly

added *tert*-butyl amine (1.1 mL, 10 mmol), and the solution was stirred for 6 h. The resultant yellow solution was washed with water (5 mL) and organic layer was separated. The organic layer was dried over anhydrous Na_2SO_4 and the volatile components were removed under reduced pressure. Compound A was obtained as a light yellow oil that distilled at 60 °C/0.05 Torr (1.147 g, 74%): ^1H NMR (C_6D_6 , 23 °C, δ) 7.45 (s, 1H, *CHN*), 3.67 (sep, 1H, $J = 8.0$ Hz, *CH(CH}_3)_2*), 1.08 (d, 6H, $J = 8.0$ Hz, *CH(CH}_3)_2*), 0.96 (s, 9H, *C(CH}_3)_3*); $^{13}\text{C}\{^1\text{H}\}$ NMR (C_6D_6 , 23 °C, ppm) 205.00 (s, CO), 153.93 (s, CN), 58.07 (s, *C(CH}_3)_3*), 34.12 (s, *CH(CH}_3)_2*), 28.79 (s, *C(CH}_3)_3*), 18.52 (s, *CH(CH}_3)_2*).

Preparation of 1-(*tert*-butylimino)-3,3-dimethylbutan-2-one (B). A 100 mL round bottomed flask was charged with a magnetic stir bar, 3,3-dimethyl-2-oxobutanal (1.00 g, 8.77 mmol) and diethyl ether (20 mL). To this stirred solution at ambient temperature was slowly added *tert*-butyl amine (0.90 mL, 8.8 mmol), and the solution was stirred for 6 h. The resultant yellow solution was washed with water (5 mL) and organic layer was separated. The organic layer was dried over anhydrous Na_2SO_4 and the volatile components were removed under reduced pressure. Compound B was obtained as a light yellow oil upon distillation at 65 °C/0.05 Torr (1.276 g, 86%): ^1H NMR (C_6D_6 , 23 °C, δ) 7.48 (s, 1H, *CHN*), 1.32 (s, 9H, *C(CH}_3)_3*), 0.95 (s, 9H, *C(CH}_3)_3*); $^{13}\text{C}\{^1\text{H}\}$ NMR (C_6D_6 , 23 °C, ppm) 205.45 (s, CO), 153.76 (s, CN), 58.16 (s, *C(CH}_3)_3*), 43.88 (s, *C(CH}_3)_3*), 28.64 (s, *C(CH}_3)_3*), 27.13 (s, *C(CH}_3)_3*); ESI-HRMS: calcd for $\text{C}_{10}\text{H}_{20}\text{NO}$ ($[\text{M} + \text{H}]^+$) 170.1545; found 170.1549.



Preparation of 1-(*tert*-butylimino)-2,3-dimethylbutan-2-ol (L¹H). A 100 mL round bottomed flask was charged with a magnetic stir bar, 1-(*tert*-butylimino)-3-methylbutan-2-one (1.00 g, 6.44 mmol), and diethyl ether (20 mL). To this stirred solution at 0 °C was slowly added a 1.6 M solution of methyl lithium in diethyl ether (4.4 mL, 7.5 mmol), and the solution was stirred for 6 h at ambient temperature. Water (5 mL) was added to the resultant yellow solution at 0 °C, and the mixture was transferred to a separatory funnel. The diethyl ether layer was extracted with the water, and the organic layer was separated and then extracted with another 5 ml water portion of water. The organic layer was separated and then dried over anhydrous Na₂SO₄. The volatile components were then removed under reduced pressure. L¹H was isolated as a light yellow oil upon vacuum distillation of the crude product at 55 °C/0.05 Torr (1.048 g, 95%): ¹H NMR (C₆D₆, 23 °C, δ) 7.34 (s, 1H, CHN), 4.59 (s, broad, 1H, OH), 1.62 (septet, 1H, J = 8.0 Hz, CH(CH₃)₂), 1.15 (s, 3H, CCH₃), 1.03 (s, 9H, C(CH₃)₃), 1.00 (d, 3H, J = 8.0 Hz, CHCH₃), 0.82 (d, 3H, J = 8 Hz, CHCH₃); ¹³C{¹H} NMR (C₆D₆, 23 °C, ppm) 162.10 (s, CHN), 73.86 (s, COH), 56.01 (s, C(CH₃)₃), 36.14 (s, CH(CH₃)₂), 29.65 (s, C(CH₃)₃), 23.95 (s, CCH₃) (s, CH(CH₃)₂), 17.55 (s, CH(CH₃)₂), 16.80 (s, CH(CH₃)₂); ESI-HRMS calcd for C₁₀H₂₂NO [M + H]⁺ 172.1701; found 172.1701.

Preparation of 1-(*tert*-Butylimino)-2,3,3-trimethylbutan-2-ol (L²H). In a fashion similar to the preparation of L¹H, treatment of 1-(*tert*-butylimino)-3,3-dimethylbutan-2-one (1.00 g, 5.91 mmol) in diethyl ether (20 mL) with a 1.6 M solution of methyl lithium in diethyl ether (4.1 mL, 6.5 mmol) for 6 h at ambient temperature afforded L²H (0.908 g, 83%) as a light yellow oil upon vacuum distillation at 60 °C /0.05 Torr: ¹H NMR (C₆D₆, 23 °C, δ) 7.57 (s, 1H, CHN), 4.96 (s, broad, 1H, OH), 1.19 (s, 3H, CCH₃), 1.02 (s, 9H, C(CH₃)₃), 0.98 (s, 9H, C(CH₃)₃); ¹³C{¹H} NMR, (C₆D₆, 23 °C, ppm) 161.38 (s, CHN), 75.53 (s, COH), 56.09 (s, C(CH₃)₃), 37.58 (s, C(CH₃)₃), 29.58 (s, C(CH₃)₃), 25.60 (s, C(CH₃)₃), 21.26 (s, CCH₃); ESI-HRMS calcd for C₁₁H₂₄NO [M + H]⁺ 186.1858; found 186.1857.

Preparation of 3-(*tert*-Butylimino)methyl)-2,2,4,4-tetramethylpentan-3-ol (L³H). In a fashion similar to the preparation of L¹H, treatment of 1-(*tert*-butylimino)-3,3-dimethylbutan-2-one (1.00 g, 5.91 mmol) in diethyl ether (20 mL) with a 1.7 M solution of *tert*-butyl lithium in pentane (3.8 mL, 6.5 mmol) for 6 h at ambient temperature afforded L³H (1.113 g, 83%) as a light yellow oil upon vacuum distillation at 65 °C /0.05 Torr: ¹H NMR (C₆D₆, 23 °C, δ) 7.79 (s, 1H, CHN), 4.99 (s, 1H, OH), 1.11 (s, 18H, C(CH₃)₃), 1.03 (s, 9H, C(CH₃)₃); ¹³C{¹H} NMR (C₆D₆, 23 °C, ppm) 161.07 (s, CHN), 78.78 (s, COH), 56.36 (s, C(CH₃)₃), 47.65 (s, C(CH₃)₃), 40.30 (s, C(CH₃)₃), 29.50 (s, C(CH₃)₃), 28.90 (s, C(CH₃)₃), 26.38 (s, C(CH₃)₃). ESI-HRMS calcd for C₁₄H₃₀NO [M + H]⁺ 228.2327; found 228.2332.

Preparation of Cu(L¹)₂ (1). A 100 mL Schlenk flask was charged with a magnetic stir bar, 1-(*tert*-butylimino)-2,3-dimethylbutan-2-ol (1.00 g, 5.84 mmol), and tetrahydrofuran (30 mL). To this stirred solution at ambient temperature was slowly added potassium hydride (0.257 g, 6.42 mmol), and the solution was stirred for 4 h. This solution was then slowly added dropwise with a cannula to a stirred suspension of anhydrous CuCl₂ (0.390 g, 2.92 mmol) in

tetrahydrofuran (40 mL) at $-78\text{ }^{\circ}\text{C}$. The resultant dark purple-brown solution was stirred for 15 h at ambient temperature. The volatile components were then removed under reduced pressure, and the resultant dark purple powder was dissolved in hexane (60 mL). The resultant solution was filtered through a 1-cm pad of Celite on a coarse glass frit, and hexane was then removed under reduced pressure. Purple crystals of **1** were obtained by sublimation at $105\text{ }^{\circ}\text{C}/0.05\text{ Torr}$ (0.791 g, 22%): mp $134\text{--}136\text{ }^{\circ}\text{C}$; $\mu_{\text{eff}} = 1.70$ and $1.78\ \mu_{\text{B}}$ in the solid state and in benzene solution, respectively. Anal. Calcd for $\text{C}_{20}\text{H}_{40}\text{CuN}_2\text{O}_2$: C, 59.45; H, 9.98; N, 6.93. Found: C, 59.50; H, 9.81; N, 6.87.

Preparation of $\text{Ni}(\text{L}^1)_2$ (2**).** In a fashion similar to the preparation of **1**, treatment of anhydrous $\text{NiCl}_2 \cdot \text{CH}_3\text{CN}$ (0.490 g, 2.92 mmol) in tetrahydrofuran (40 mL) with a solution of potassium 1-(*tert*-butylimino)-2,3-dimethylbutan-2-olate (prepared from 1-(*tert*-butylimino)-2,3-dimethylbutan-2-ol (1.00 g, 5.84 mmol) and potassium hydride (0.257 g, 6.42 mmol) in tetrahydrofuran (30 mL)) for 15 h at ambient temperature afforded **2** (0.810 g, 71%) as pale red crystals upon sublimation at $90\text{ }^{\circ}\text{C}/0.05\text{ Torr}$: mp $125\text{--}127\text{ }^{\circ}\text{C}$; $^1\text{H NMR}$ (C_6D_6 , $23\text{ }^{\circ}\text{C}$, δ) Isomer 1: 10.91 (s, 1H, CHN), 1.74 (septet, 1H, $J = 8.0\text{ Hz}$, $\text{CH}(\text{CH}_3)_2$), 1.58 (s, 9H, $\text{C}(\text{CH}_3)_3$), 1.31 (d, 3H, $J = 8.0\text{ Hz}$, $\text{C}(\text{CH}_3)_2$), 1.05 (d, 3H, $J = 8.0\text{ Hz}$, $\text{C}(\text{CH}_3)_2$), 0.94 (s, 3H, CCH_3), Isomer 2: 10.60 (s, 1H, CHN), 1.74 (septet, 1H, $J = 8.0\text{ Hz}$, $\text{CH}(\text{CH}_3)_2$), 1.55 (s, 9H, $\text{C}(\text{CH}_3)_3$), 1.22 (d, 3H, $J = 8.0\text{ Hz}$, $\text{C}(\text{CH}_3)_2$), 1.01 (d, 3H, $J = 8\text{ Hz}$, $\text{C}(\text{CH}_3)_2$), 0.93 (s, 3H, CCH_3); $^{13}\text{C}\{^1\text{H}\}\text{ NMR}$, (C_6D_6 , $23\text{ }^{\circ}\text{C}$, ppm) Isomer 1: 157.61 (s, CHN), 67.60 (s, CO), 66.91 (s, $\text{C}(\text{CH}_3)_3$), 58.64 (s, $\text{CH}(\text{CH}_3)_2$), 50.55 (s, CCH_3), 36.30 (s, $\text{C}(\text{CH}_3)_3$), 17.71 (s, $\text{CH}(\text{CH}_3)_2$), 17.43 (s, $\text{CH}(\text{CH}_3)_2$), Isomer 2: 155.03 (s, CHN), 66.91 (s, CO), 63.90 (s, $\text{C}(\text{CH}_3)_3$), 56.25 (s, $\text{CH}(\text{CH}_3)_2$), 47.65 (s, CCH_3), 35.69 (s, $\text{C}(\text{CH}_3)_3$), 17.61 (s, $\text{CH}(\text{CH}_3)_2$), 17.13 (s, $\text{CH}(\text{CH}_3)_2$). Anal. Calcd for $\text{C}_{20}\text{H}_{40}\text{NiN}_2\text{O}_2$: C, 60.17; H, 10.10; N, 7.02. Found: C, 60.52; H, 10.26; N, 6.89.

Preparation of $\text{Co}(\text{L}^1)_2$ (3). In a fashion similar to the preparation of **1**, treatment of anhydrous CoCl_2 (0.376 g, 2.92 mmol) in tetrahydrofuran (40 mL) with a solution of potassium 1-(*tert*-butylimino)-2,3-dimethylbutan-2-olate (prepared from 1-(*tert*-butylimino)-2,3-dimethylbutan-2-ol (1.00 g, 5.84 mmol) and potassium hydride (0.257 g, 6.42 mmol) in tetrahydrofuran (30 mL)) for 15 h at ambient temperature afforded **3** (0.791 g, 68%) as green crystals upon sublimation at 90 °C/0.05 Torr: mp 96-98 °C; $\mu_{\text{eff}} = 3.78$ and $3.94 \mu_{\text{B}}$ in the solid state and in benzene solution, respectively. Anal. Calcd for $\text{C}_{20}\text{H}_{40}\text{CoN}_2\text{O}_2$: C, 60.13; H, 10.09; N, 7.07. Found: C, 60.38; H, 10.22; N, 6.85.

Preparation of $\text{Cu}(\text{L}^2)_2$ (4). In a fashion similar to the preparation of **1**, treatment of anhydrous CuCl_2 (0.363 g, 2.70 mmol) in tetrahydrofuran (40 mL) with a solution of potassium 1-(*tert*-butylimino)-2,3,3-trimethylbutan-2-olate (prepared from 1-(*tert*-butylimino)-2,3,3-trimethylbutan-2-ol (1.00 g, 5.40 mmol) and potassium hydride (0.238 g, 5.94 mmol) in tetrahydrofuran (30 mL)) for 15 h at ambient temperature afforded **4** (0.350 g, 30%) as purple crystals upon sublimation at 130 °C /0.05 Torr: mp 163–165 °C; $\mu_{\text{eff}} = 1.79$ and $1.75 \mu_{\text{B}}$ in the solid state and in benzene solution, respectively. Anal. Calcd for $\text{C}_{22}\text{H}_{44}\text{CuN}_2\text{O}_2$: C, 61.15; H, 10.26; N, 6.48. Found: C, 61.05; H, 9.98; N, 6.51.

Preparation of $\text{Ni}(\text{L}^2)_2$ (5). In a fashion similar to the preparation of **1**, treatment of anhydrous $\text{NiCl}_2 \cdot \text{CH}_3\text{CN}$ (0.456 g, 2.70 mmol) in tetrahydrofuran (40 mL) with a solution of potassium 1-(*tert*-butylimino)-2,3,3-trimethylbutan-2-olate (prepared from 1-(*tert*-butylimino)-2,3,3-trimethylbutan-2-ol (1.00 g, 5.40 mmol) and potassium hydride (0.238 g, 5.94 mmol) in tetrahydrofuran (30 mL)) for 15 h at ambient temperature afforded **5** (0.702 g, 61%) as pale red crystals upon sublimation at 120 °C/0.05 Torr: mp 175–177 °C; $^1\text{H NMR}$ (C_6D_6 , 23 °C, δ) Isomer 1: 10.23 (s, 1H, CHN), 1.47 (s, 9H, $\text{C}(\text{CH}_3)_3$), 1.15 (s, 3H, CCH_3), 1.10 (s, 9H, $\text{C}(\text{CH}_3)_3$);

Isomer 2: 10.03 (s, 1H, CHN), 1.45 (s, 9H, C(CH₃)₃), 1.10 (s, 3H, CCH₃), 1.05 (s, 9H, C(CH₃)₃); ¹³C{¹H} NMR (C₆D₆, 23 °C, ppm) Isomer 1: 164.94 (s, CHN), 65.55 (s, CO), 58.01 (s, C(CH₃)₃), 46.26 (s, C(CH₃)₃), 33.94 (s, CCH₃), 26.62 (s, C(CH₃)₃); Isomer 2: 163.12 (s, CHN), 65.11 (s, CO), 56.12 (s, C(CH₃)₃), 44.88 (s, C(CH₃)₃), 33.56 (s, CCH₃), 26.54 (s, C(CH₃)₃); Anal. Calcd for C₂₂H₄₄NiN₂O₂: C, 61.84; H, 10.38; N, 6.56. Found: C, 61.92; H, 10.28; N, 6.44.

Preparation of Co(L²)₂ (6). In a fashion similar to the preparation of **1**, treatment of anhydrous CoCl₂ (0.350 g, 2.70 mmol) in tetrahydrofuran (40 mL) with a solution of potassium 1-(*tert*-butylimino)-2,3,3-trimethylbutan-2-olate (prepared from 1-(*tert*-butylimino)-2,3,3-trimethylbutan-2-ol (1.00 g, 5.40 mmol) and potassium hydride (0.238 g, 5.94 mmol) in tetrahydrofuran (30 mL)) for 15 h at ambient temperature afforded **6** (0.800 g, 73%) as orange crystals upon sublimation at 115 °C/0.05 Torr: mp 84–86 °C; $\mu_{\text{eff}} = 1.85$ and $4.06 \mu_{\text{B}}$ in the solid state (orange) and in benzene solution (green), respectively. Anal. Calcd for C₂₂H₄₄CoN₂O₂: C, 61.81; H, 10.37; N, 6.55. Found: C, 62.51; H, 10.37; N, 6.44.

Preparation of Fe(L²)₂ (7). In a fashion similar to the preparation of **1**, treatment of anhydrous FeCl₂ (0.342 g, 2.70 mmol) in tetrahydrofuran (40 mL) with a solution of potassium 1-(*tert*-butylimino)-2,3,3-trimethylbutan-2-olate (prepared from 1-(*tert*-butylimino)-2,3,3-trimethylbutan-2-ol (1.00 g, 5.40 mmol) and potassium hydride (0.238 g, 5.94 mmol) in tetrahydrofuran (30 mL)) for 15 h at ambient temperature afforded **7** (0.676 g, 59%) as purple crystals upon sublimation at 85 °C/0.05 Torr: mp 112–114 °C; $\mu_{\text{eff}} = 5.10$ and $5.23 \mu_{\text{B}}$ in the solid state and in benzene solution, respectively. Anal. Calcd for C₂₂H₄₄FeN₂O₂: C, 62.25; H, 10.45; N, 6.60. Found: C, 62.02; H, 10.37; N, 6.56.

Preparation of Mn₂(L²)₄ (8). In a fashion similar to the preparation of **1**, treatment of anhydrous MnCl₂ (0.340 g, 2.70 mmol) in tetrahydrofuran (40 mL) with a solution of potassium

1-(*tert*-butylimino)-2,3,3-trimethylbutan-2-olate (prepared from 1-(*tert*-butylimino)-2,3,3-trimethylbutan-2-ol (1.00 g, 5.40 mmol) and potassium hydride (0.238 g, 5.94 mmol) in tetrahydrofuran (30 mL)) for 15 h at ambient temperature afforded **8** (0.457 g, 40%) as off-white crystals upon sublimation at 160 °C /0.05 Torr: mp 221–223 °C; $\mu_{\text{eff}} = 7.92$ and $8.07 \mu_{\text{B}}$ in the solid state and in benzene solution, respectively. Anal. Calcd for $\text{C}_{22}\text{H}_{44}\text{MnN}_2\text{O}_2$: C, 62.39; H, 10.47; N, 6.61. Found: C, 62.22; H, 10.32; N, 6.40.

Preparation of $\text{Cr}(\text{L}^2)_2$ (9**).** In a fashion similar to the preparation of **1**, treatment of anhydrous CrCl_2 (0.332 g, 2.70 mmol) in tetrahydrofuran (40 mL) with a solution of potassium 1-(*tert*-butylimino)-2,3,3-trimethylbutan-2-olate (prepared from 1-(*tert*-butylimino)-2,3,3-trimethylbutan-2-ol (1.00 g, 5.40 mmol) and potassium hydride (0.238 g, 5.94 mmol) in tetrahydrofuran (30 mL)) for 15 h at ambient temperature afforded **9** (0.852 g, 75%) as pale green crystals upon sublimation at 115 °C/0.05 Torr: mp 173–175 °C; $\mu_{\text{eff}} = 4.75$ and $4.91 \mu_{\text{B}}$ in the solid state and in benzene solution, respectively. Anal. Calcd for $\text{C}_{22}\text{H}_{44}\text{CrN}_2\text{O}_2$: C, 62.82; H, 10.54; N, 6.66. Found: C, 62.96; H, 10.35; N, 6.43.

Preparation of $\text{Cu}(\text{L}^3)_2$ (10**).** In a fashion similar to the preparation of **1**, treatment of anhydrous CuCl_2 (0.296 g, 2.20 mmol) in tetrahydrofuran (40 mL) with a solution of potassium 3-((*tert*-butylimino)methyl)-2,2,4,4-tetramethylpentan-3-olate (prepared from 3-((*tert*-butylimino)-methyl)-2,2,4,4-tetramethylpentan-3-ol (1.00 g, 4.40 mmol) and potassium hydride (0.194 g, 4.84 mmol) in tetrahydrofuran (30 mL)) for 15 h at ambient temperature afforded **10** (0.454 g, 40%) as purple crystals upon sublimation at 135 °C/0.05 Torr: mp 183–185 °C; $\mu_{\text{eff}} = 1.82$ and $1.79 \mu_{\text{B}}$ in the solid state and in benzene solution, respectively. Anal. Calcd for $\text{C}_{28}\text{H}_{52}\text{CuN}_2\text{O}_2$: C, 65.14; H, 10.93; N, 5.43. Found: C, 65.09; H, 10.81; N, 5.35.

Preparation of Ni(L³)₂ (11). In a fashion similar to the preparation of **1**, treatment of anhydrous NiCl₂•CH₃CN (0.371 g, 2.20 mmol) in tetrahydrofuran (40 mL) with a solution of potassium 3-((*tert*-butylimino)methyl)-2,2,4,4-tetramethylpentan-3-olate (prepared from 3-((*tert*-butylimino)-methyl)-2,2,4,4-tetramethylpentan-3-ol (1.00 g, 4.40 mmol) and potassium hydride (0.194 g, 4.84 mmol) in tetrahydrofuran (30 mL)) for 15 h at ambient temperature afforded **11** (0.585 g, 52%) as pale red crystals upon sublimation at 140 °C /0.05 Torr: mp 195–197 °C; ¹H NMR (C₆D₆, 23 °C, δ) 10.93 (s, 1H, CHN), 1.41 (s, 18H, C(CH₃)₃), 1.39 (s, 9H, C(CH₃)₃); ¹³C{¹H} NMR (C₆D₆, 23 °C, ppm) 162.54 (s, CHN), 66.60 (s, CO), 65.41 (s, C(CH₃)₃), 61.29 (s, C(CH₃)₃), 33.59 (s, C(CH₃)₃), 29.91 (s, C(CH₃)₃); Anal. Calcd for C₂₈H₅₂N₂NiO₂: C, 65.75; H, 11.04; N, 5.48. Found: C, 65.53; H, 10.96; N, 5.25.

Preparation of Co(L³)₂ (12). In a fashion similar to the preparation of **1**, treatment of anhydrous CoCl₂ (0.286 g, 2.20 mmol) in tetrahydrofuran (40 mL) with a solution of potassium 3-((*tert*-butylimino)methyl)-2,2,4,4-tetramethylpentan-3-olate (prepared from 3-((*tert*-butylimino)-methyl)-2,2,4,4-tetramethylpentan-3-ol (1.00 g, 4.40 mmol) and potassium hydride (0.194 g, 4.84 mmol) in tetrahydrofuran (30 mL)) for 15 h at ambient temperature afforded **12** (0.470 g, 42%) as orange crystals upon sublimation at 135 °C/0.05 Torr: mp 144–146 °C; $\mu_{\text{eff}} = 1.79$ and 3.98 μ_{B} in the solid state (orange) and in benzene solution (green), respectively. Anal. Calcd for C₂₈H₅₂CoN₂O₂: C, 65.72; H, 11.03; N, 5.47. Found: C, 66.11; H, 11.41; N, 5.30.

Preparation of Fe(L³)₂ (13). In a fashion similar to the preparation of **1**, treatment of anhydrous FeCl₂ (0.279 g, 2.20 mmol) in tetrahydrofuran (40 mL) with a solution of potassium 3-((*tert*-butylimino)methyl)-2,2,4,4-tetramethylpentan-3-olate (prepared from 3-((*tert*-butylimino)-methyl)-2,2,4,4-tetramethylpentan-3-ol (1.00 g, 4.40 mmol) and potassium hydride (0.194 g, 4.84 mmol) in tetrahydrofuran (30 mL)) for 15 h at ambient temperature afforded **13**

(0.101 g, 9%) as purple crystals upon sublimation at 130 °C/0.05 Torr: mp 125–127 °C; $\mu_{\text{eff}} = 4.81$ and $4.87 \mu_{\text{B}}$ in the solid state and in benzene solution, respectively. Anal. Calcd for $\text{C}_{28}\text{H}_{52}\text{FeN}_2\text{O}_2$: C, 66.12; H, 11.10; N, 5.51. Found: C, 67.07; H, 11.30; N, 5.36.

Preparation of $\text{Mn}(\text{L}^3)_2$ (14). In a fashion similar to the preparation of **1**, treatment of anhydrous MnCl_2 (0.276 g, 2.20 mmol) in tetrahydrofuran (40 mL) with a solution of potassium 3-((*tert*-butylimino)methyl)-2,2,4,4-tetramethylpentan-3-olate (prepared from 3-((*tert*-butylimino)-methyl)-2,2,4,4-tetramethylpentan-3-ol (1.000 g, 4.40 mmol) and potassium hydride (0.194 g, 4.84 mmol) in tetrahydrofuran (30 mL)) for 15 h at ambient temperature afforded **14** (0.150 g, 27%) as off-white crystals upon sublimation at 130 °C/0.05 Torr: mp 149–151 °C; $\mu_{\text{eff}} = 5.83$ and $5.89 \mu_{\text{B}}$ in the solid state and in benzene solution, respectively. Anal. Calcd for $\text{C}_{28}\text{H}_{52}\text{MnN}_2\text{O}_2$: C, 66.24; H, 11.12; N, 5.52. Found: C, 66.41; H, 11.15; N, 5.28.

Preparation of $\text{Cr}(\text{L}^3)_2$ (15). In a fashion similar to the preparation of **1**, treatment of anhydrous CrCl_2 (0.271 g, 2.20 mmol) in tetrahydrofuran (40 mL) with a solution of potassium 3-((*tert*-butylimino)methyl)-2,2,4,4-tetramethylpentan-3-olate (prepared from 3-((*tert*-butylimino)-methyl)-2,2,4,4-tetramethylpentan-3-ol (1.00 g, 4.40 mmol) and potassium hydride (0.194 g, 4.84 mmol) in tetrahydrofuran (30 mL)) for 15 h at ambient temperature afforded **14** (0.652 g, 58%) as pale green crystals upon sublimation at 140 °C/0.05 Torr: mp 202–204 °C; $\mu_{\text{eff}} = 5.01$ and $4.95 \mu_{\text{B}}$ in the solid state and in benzene solution, respectively. Anal. Calcd for $\text{C}_{28}\text{H}_{52}\text{CrN}_2\text{O}_2$: C, 66.63; H, 11.18; N, 5.55. Found: C, 66.87; H, 10.87; N, 5.33.

Following sections describe the general procedures for sublimation, thermal decomposition, and solution screening studies. In the rest of this dissertation, these studies were carried out as explained below.

Sublimation Studies. For the sublimation experiments, 2.5 cm diameter, 30 cm long glass tubes were employed. One end of the tube was sealed and the other end was equipped with a vacuum adapter with a 24/40 male glass joint. In an argon-filled glove box, the compound to be sublimed (~ 0.5 g) was loaded into a 1.0 x 4.0 cm glass tube and this tube was placed at the sealed end of the glass sublimation tube. The sublimation tube was fitted with a 24/40 vacuum adapter, and then was inserted into a horizontal Buchi Kugelrohr oven such that about 15 cm of the tube was situated in the oven. A vacuum of 0.05 Torr was established, and the oven was heated to the indicated temperature. The compounds sublimed to the cool zone just outside of the oven. The percent recovery was obtained by weighing the sublimed product. The percent nonvolatile residue was calculated by weighing the 1.0 x 4.0 cm glass tube at the end of the sublimation.

Thermal Decomposition Studies. In an argon-filled dry box, a melting point capillary tube was charged with 1-2 mg of a sample and the end of the tube was sealed with a small amount of stopcock grease. The capillary tube was then removed from the dry box, and the end was flame sealed. The capillary tube was transferred to an Electrothermal Model 9200 melting point apparatus, and was then heated at 5 °C/min starting at 25 °C. Samples were visually observed for discoloration or other evidence of decomposition.

General Procedure for Solution Reduction Reactions. A 100 mL Schlenk flask was charged with a magnetic stir bar, metal precursor (0.100 g), and tetrahydrofuran (10 mL). To each stirred solution at ambient temperature was slowly added a reducing agent (5 equivalents), and solution was stirred for 1 hour. Solutions that did not afford black powders or black solutions after 1 hour at ambient temperature were refluxed for 1 hour.

CHAPTER 3

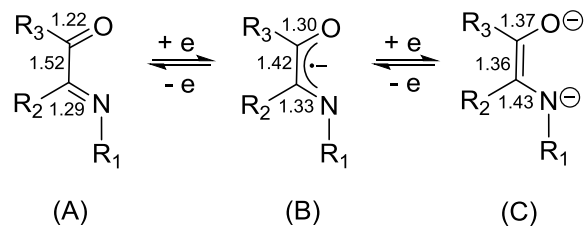
Synthesis and Structure of Volatile and Thermally Stable Mid to Late First Row Transition Metal Complexes Containing α -Imino Ketonate and α -Imino Enolate Ligands

3.1 Introduction

Transition metal complexes containing diazadienyl ligands are widely explored,³² while their oxygen containing analogs, α -imino ketonate complexes, are quite undeveloped.⁷⁴ Homoleptic complexes containing α -imino ketonate ligands are limited to one Ni(II) and one Co(II) complex containing a phenyl group on the carbonyl carbon atom,⁷⁴ although some heteroleptic complexes are reported with various types of bulky substituents.⁷⁵ Due to the presence of phenyl substituents in the ligands, the reported α -imino ketonate complexes should not have appreciable volatility.

The Winter group has previously reported the synthesis of transition metal diazadienyl complexes by treating diazadienyl radical anions with transition metal chlorides.³² However, attempts to make Cu complexes failed because the ligand radical anion reduces Cu(II) to Cu(0), instead of making a Cu complex. In response to this problem, in this dissertation work, α -imino ketonate ligands were synthesized, which have an oxygen donor atom instead of a nitrogen donor atom in the diazadienyl ligand. The oxygen atom is less basic than the nitrogen atom and may lower the reducing power of the ligand. The α -imino ketone ligand can exist in three possible forms as shown in Chart 7.⁷⁴ Form A is the neutral ligand. α -Imino ketones can be reduced by one electron (π -radical monoanion) or two electrons (closed shell dianion) which are represented by forms B and C respectively.⁷⁴

Chart 7. Different redox states of α -imino ketonate ligand with their characteristic bond distances (\AA).⁷⁴



Due to the redox active nature of α -iminoketone ligands, they may catalyze bond formation or cleavage reactions through a redox process. A publication has shown that palladium complexes containing α -iminoketonate ligands are capable of catalyzing olefin polymerizations.⁷⁶ This report discusses the tuning of the R groups to obtain the desired electronic and steric properties for the catalytic activity of the palladium complexes. Another publication shows Co-Cl bond formation reactions through a Co(III) complex containing α -iminophenolate ligands, due to the redox active nature of α -iminophenolate ligands.⁷⁷

Chapter 2 described the synthesis and characterization of first row late transition metal complexes and the evaluation of their properties to use as ALD precursors. In order to explore novel classes of potential ALD precursors, complexes with α -imino ketonate ligand systems were synthesized and their properties were assessed. In this chapter, the syntheses of the complexes containing new α -imino ketonate ligands are discussed. Moreover, attempts to make complexes with ligands containing an iPr substituent on carbonyl carbon led to a new class of transition metal complexes. The radical anion formed during the treatment of the ligand with lithium metal is basic enough to abstract an acidic α -H (α to carbonyl) from the iPr group of a nearby ligand molecule as shown in Scheme 2. Then, the negative charge formed at the α -C of the carbonyl group is delocalized through C-C-O bonds as shown in Scheme 2, leading to an enolate moiety in the ligand. This type of ligands can be named as α -imino enolate ligands.

During the course of the syntheses of α -imino enolate complexes, KH was used to deprotonate the ligand. The α -imino enolate ligand is analogous to α -imino alkoxide ligands, and complexes containing α -imino enolate ligands are not previously reported. The chemical structures of α -imino ketone ligands and α -imino enol ligand are shown in Chart 8.

Scheme 2. Formation of α -imino enolate complexes.

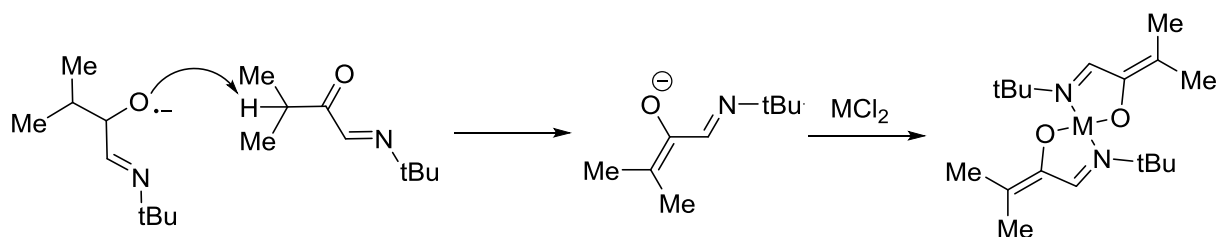
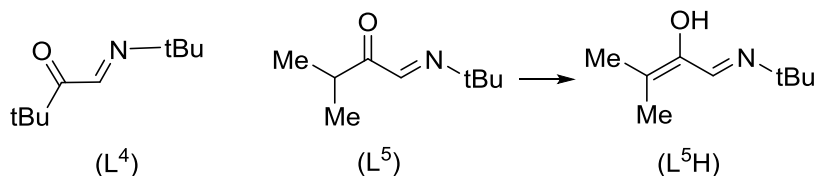


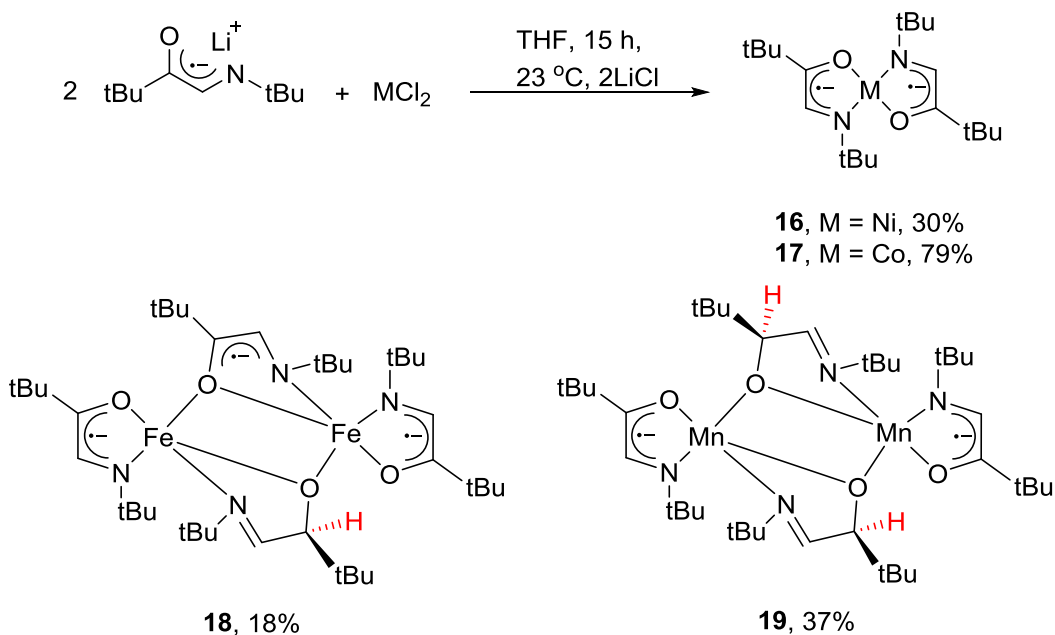
Chart 8. Chemical structures of α -imino ketone (L^4 and L^5) and α -imino enol ligand precursors (L^5H).



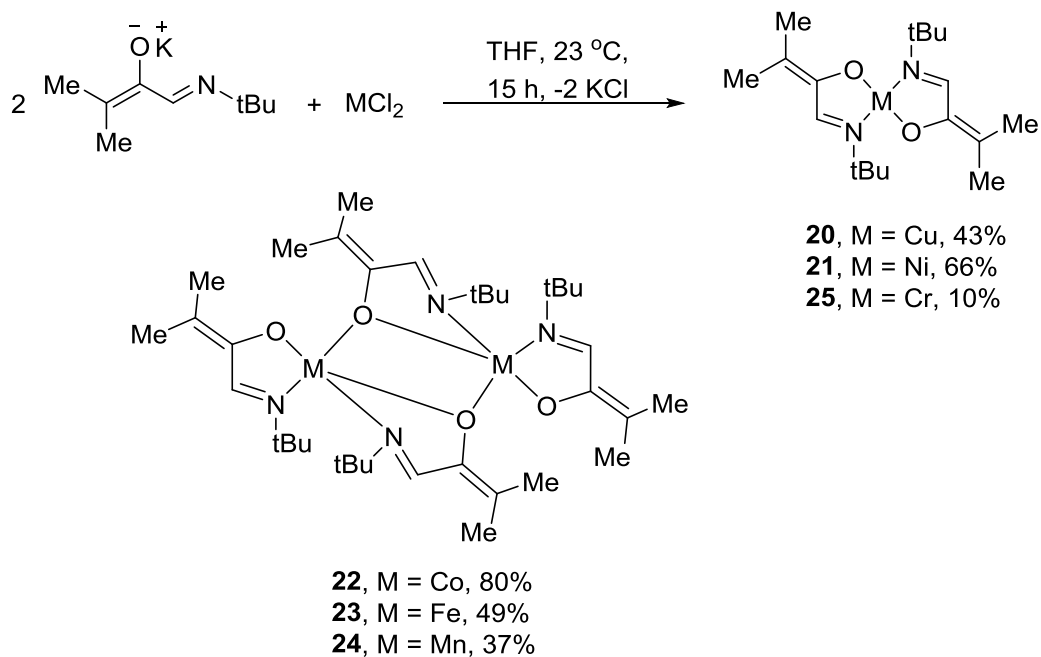
3.2 Results and Discussion

Synthetic Aspects. The α -imino ketone ligand precursors L^4 and L^5 were synthesized and characterized as described in the Experimental Section upon treatment of *tert*-butyl or isopropyl glyoxal with selenium dioxide followed by the treatment with *tert*-butyl amine. The lithium salt LiL^4 was prepared by treatment of L^4 with lithium in tetrahydrofuran. Similarly, KL^5 was prepared by treatment of L^5 with potassium hydride in tetrahydrofuran. These solutions were then treated directly with anhydrous MCl_2 ($M = Cu, Ni, Co, Fe, Mn, \text{ or } Cr$) as illustrated in Schemes 3 and 4 to afford complexes **16–25** as crystalline solids by either sublimation or crystallization in hexane at $-23\text{ }^\circ\text{C}$. Treatment of LiL^4 with $CuCl_2$ resulted in the precipitation of Cu metal and treatment with $CrCl_2$ did not afford isolable products.

Scheme 3. Synthesis of 16–19.



Scheme 4. Synthesis of 20–25.



The structures of **16–25** were assigned by spectral and analytical data. In addition, X-ray crystal structure determinations were carried out for **16–18** and **20–24**. Complex **16** is the only

diamagnetic species in the ketonate series and resonances for the ligand substituents were observed in the ^1H NMR and ^{13}C NMR spectra. According to the X-ray crystal structure, **16** adopts tetrahedral geometry around the metal center, which should lead to a paramagnetic species having two unpaired electrons. These two unpaired electrons are antiferromagnetically coupled to two unpaired electrons of radical anion ligand, making **16** a diamagnetic species which is NMR active. The magnetic moment for **17** ($1.79 \mu_B$) is very close to that of expected for high-spin Co(II) ion that is antiferromagnetically coupled to two unpaired electrons of radical anion L^4 ligands (Chart 7, form B). Complexes **18** and **19** exist as dimers and solid-state magnetic moments for **18** and **19** are 4.82 and $5.96 \mu_B$, respectively. Very similar values for **17–19** were measured in benzene solution using the Evans method, suggesting similar molecular structures in the solid state and solution.

The existence of the ligand L^5 in the enolate form was substantiated by the bond lengths and angles obtained from X-ray crystal structures of **16–20** and the NMR of Ni complex (**21**). As expected, a C=C double bond was present outside of the ligand core based on bond lengths and angles obtained from the X-ray crystal structures. ^1H and ^{13}C NMR ligand resonances observed for **21** suggest that the Ni center is a spin-paired, diamagnetic d^8 Ni(II) center. ^1H NMR spectra displayed two distinct peaks for two chemically nonequivalent CH_3 groups in **21** that were chemically equivalent (Me groups of iPr) in the original ligand precursor. Moreover, the septet corresponding to the iPr-H in the ligand was not present in the ^1H NMR spectrum of **21**. The ^{13}C NMR spectrum of **21** displayed two resonances indicating the presence of sp^2 hybridized carbons for the external double bond. Both the ^1H and ^{13}C NMR spectra suggest that the ligand exists in the enolate form. Complexes **20** and **22–25** are paramagnetic and displayed very broad peaks in ^1H NMR spectra. Also, complexes **20** and **22–25** displayed similar solid state and solution state

magnetic moment values, suggesting that they adopt similar structures in both states. The solid and solution state magnetic moment (μ_{eff}) values of **20** are 1.88 and 1.80 μ_B , respectively, which are close to the spin only value for a d^9 Cu(II) center with one unpaired electron ($\mu_{\text{eff}} = 1.73 \mu_B$). Complexes **22–24** displayed solid state magnetic moment values of 6.83, 7.21, and 8.45 μ_B , respectively, and exist as dimers based on X-ray crystal structures as described later, suggesting that the unpaired electrons of both metal centers are antiferromagnetically coupled. Complex **25** displayed solid and solution state magnetic moment values of 4.80 and 4.98 μ_B , respectively, which can be attributed to a Cr(II) center with four unpaired electrons ($\mu_{\text{eff}} = 4.90 \mu_B$).

X-Ray Crystal Structures. The X-ray crystal structures of **16–18** and **20–24** were obtained to establish the solid state configurations and to assess the bonding modes of the α -imino ketonate and α -imino enolate ligands. Experimental crystallographic data are summarized in Table 5, and selected bond lengths and angles are presented in Tables 6 (**16**, **17**, **20**, and **21**), 7 (**18** and **19**), and 8 (**22–24**). Representative perspective views of **17**, **18**, **20**, **22**, and **24** are given in Figures 16–20, respectively. A low resolution X-ray crystal structure of **19** demonstrates a dimeric Mn complex. The spectral and analytical data for **25** are similar to those of **20** and **21**, which suggest structurally similar, square planar monomeric complex.

Complexes **16** and **17** adopt tetrahedral geometry around the metal center, with κ^2 -N,O coordination of the ligands. The ligand core C–O, C–C, and C–N bond distances of **16** and **17** fall between 1.290(3) and 1.298(3), 1.390(4) and 1.405(4), and 1.328(4) and 1.342(4) Å, respectively. These bond distances are similar to those expected for form B (Chart 7), which are π -radical mono-anionic ligands. The intraligand N–M–O angles of **16** and **17** fall in the range of 82.41(8) and 83.62(10)°, and the interligand N–M–O angles fall in the range of 115.92(9) and

118.87(10)°. The N–M–N and O–M–O angles of **16** and **17** are in between 123.10(9) and 135.75(9)°.

Complexes **18** and **19** demonstrate dimeric structures and an unusual structure in some of the ligands (Schemes 3 and 4). Two of the ligands are coordinated to metal centers in terminal κ^2 -fashion and the other two ligands are coordinated in bridging $\mu\text{-}\kappa^1:\kappa^2$ -fashion. The oxygen atoms in both bridging ligands are bonded to both metal centers. Selected bond lengths and angles of **18** and **19** are listed in Tables 9 and 10, respectively. The terminal ligand core C–O, C–C, and C–N bond distances of **18** and **19** are in between 1.270(8) and 1.290(3), 1.326(10) and 1.407(4), and 1.268(9) and 1.397(8) Å, respectively, which are closer to the values (form B, Chart 7) obtained for **16** and **17**. However, some of the bridging ligands of **18** (Figure 17) and **19** have different bond lengths and angles that would suggest they have different structures from α -imino ketonate ligand. One of the bridging ligands of **18** has ligand core C₂₁–O₃, C₂₁–C₂₂, and C₂₂–N₃ (Figure 17) bond distances of 1.329(4), 1.453(4), and 1.299(4) Å, respectively, which are closer to the values of terminal ligand bond distances. On the other hand, the other bridging ligand has ligand core C₁₁–O₂, C₁₁–C₁₂, and C₁₂–N₂ (Figure 17) bond distances of 1.404(3), 1.505(4), and 1.272(4) Å, respectively. These bond distances are almost similar to the expected bond distances for C–O (1.43 Å) and C–C (1.54 Å) single and C=N (1.21 Å) double bonds.^{13b} Moreover, tetrahedral geometry can be seen around C₁₁ atom (C₁₂–C₁₁–O₂, 109.9(2); C₁₃–C₁₁–O₂, 111.5(2); C₁₂–C₁₁–C₁₃, 110.9(2)° (Figure 17)). The above mentioned bond distances and angles suggest that there is an H atom on C₁₁ which was not present in the ligand precursor (L⁴) (Figure 17, Scheme 3). Similar bond distances and angles were observed for the both bridging ligands in **19**, implying that two H atoms are abstracted by the carbon atom that is bonded to the oxygen atom (Scheme 3).

The experimental data other than X-ray crystal structures are not available to establish this H abstraction phenomenon. Because of their paramagnetic nature, NMR spectra of **18** and **19** cannot be taken to assign resonances for the new H atoms, and the frequency of newly formed C–H bonds in infrared spectrum could not be resolved. Computational calculations might provide more insight to this H abstraction process and the oxidation states of the metal centers. A detailed discussion of the H abstraction phenomenon can be found later in this discussion.

Complexes **20** and **21** have remarkably similar molecular structures. In these structures, asymmetric unit contains two independent half-molecules, both occupying inversion centers. Complexes **20** and **21** are four-coordinate monomeric structures with square planar geometry around the metal centers with κ^2 -N,O coordination of the α -imino enolate ligand. In both complexes oxygen and nitrogen donor atoms of the two ligands are coordinated in a trans fashion, with N–M–N' and O–M–O' angles of 180.00°. The intraligand and interligand N–M–O angles fall between 83.47(5) and 85.13(4)°, and 94.87(4) and 96.53(5)°, respectively. The C–N bond distances of the α -imino enolate ligand core in **20** and **21** range between 1.286(2) and 1.2955(15) Å, which are between the distances expected for C–N single (1.46 Å) and C=N double bonds (1.21 Å).^{20b} The ligand core C–C and C–O bond lengths lie between 1.4463(16) and 1.451(2) Å, and 1.335(2) and 1.3387(14) Å, respectively, which are also in between the distances expected for C–C and C–O single and double bonds. These C–C and C–O bond lengths suggest that the negative charge is delocalized through the ligand core bonds. The external C–C bond that contains a ligand core carbon atom has bond lengths between 1.357(2) and 1.3619(16) Å, which is very close to the length of a C=C double bond. The M–N distances (**20**, 2.0304(14) and 2.0332(14); **21**, 1.9304(10) and 1.9347(10) Å) are longer than the M–O distances (**20**, 1.8838(12) and 1.8849(12); **21**, 1.8407(8) and 1.8421(8) Å), and these M–N and

M–O lengths are consistent with a slightly anionic imino nitrogen atom and an anionic oxygen atom, respectively. However it is important to note that previously reported Cu β -amino alkoxide complexes with similar geometry and bonding mode have slightly shorter Cu–O distances (Cu(OCMe₂CH₂NMe₂)₂,^{64d} 1.863(1) and Cu(OCHMeCH₂NMe₂)₂,^{64a} 1.865(3) Å) than those of **20** (1.8838(12) and 1.8849(12) Å). This difference in Cu–O distances are likely due to the delocalization of the negative charge over the ligand core atoms in **20**, resulting in longer Cu–O distances in **20** relative to the previously reported Cu complexes. The Cu–N bond distances (2.0304(14) and 2.0332(14) Å) of **20** are slightly shorter than those of the previously reported complexes Cu(OCHMeCH₂NMe₂)₂^{64d} (2.052(3) Å) and Cu(OCMe₂CH₂NMe₂)₂^{64a} (2.058(1) Å), likely due to the presence of a slight negative charge on the imino nitrogen atom in **20** rendering the nitrogen atom more electronegative, thereby, decreasing the Cu–N bond distance. Similar trends were observed with Ni–O and Ni–N bond lengths in **21** relative to the previously reported Ni β -amino alkoxide complexes Ni(OCHMeCH₂NMe₂)₂,^{65b} Ni(OCMe₂CH₂NMe₂)₂, and Ni(OCMe₂CH₂NEt₂)₂.^{65a}

Complexes **22–24** exist as dinuclear complexes in which each metal atom is bonded to the nitrogen and oxygen donor atoms of one of the terminal ligands in κ^2 -fashion and to one nitrogen atom and two oxygen atoms of two bridging ligands in μ - κ^1 : κ^2 -fashion. The metal centers of **22** and **23** can be approximated as exhibiting distorted trigonal bipyramidal geometries. The axial positions are occupied by two oxygen atoms, one from a κ^2 and one from a μ - κ^1 : κ^2 ligand, while the equatorial positions are occupied by two nitrogen atoms from one κ^2 and one μ - κ^1 : κ^2 ligand and one oxygen atom from the other μ - κ^1 : κ^2 ligand. The calculated index of trigonality of each metal center is close to 1 suggesting that metal centers display a trigonal bipyramidal geometry. The X-ray structure of **24** indicates the presence of two independent half-

dimers in the asymmetric unit. Each dimer occupies an inversion center. The M–O bond distances of the bridging ligands (**22**, 2.0214(19), 2.0331(19), and 2.1096(19) Å; **23**, 2.083(3), 2.087(3), 2.094(3), and 2.096(3) Å; **24**, 2.1068(11), 2.1116(11), and 2.1467(11) Å) are longer than those of the terminal ligands (**22**, 1.9472(19), and 1.955(2) Å; **23**, 1.974(3) and 1.978(3) Å; **24**, 2.0131(11) and 2.0237(12) Å), possibly because oxygen atoms of the bridging ligands are bonded to both metal centers. Also, the same trend was observed for the ligand core C–O bond distances. In **22** and **23**, the N–M–O (M = Co and Fe) bite angles of the bridging ligands (**22**, 76.64(9), 76.71(9), 76.72(8), and 77.08(9)°; **23**, 75.73(14), 76.14(12), 76.18(14), and 76.26(13)°) are smaller than those of the terminal ligands (**22**, 80.86(10), 81.38(8), 81.83(9), and 81.91(8)°; **23**, 77.73(13), 77.78(12), 78.79(12), and 79.33(12)°). The bite angles of the bridging ligands in **22** and **23** are also smaller than those of **20** and **21**. In contrast, the bite angles of the bridging ligands of **24** (80.86(4), 81.16(4), 112.67(5), and 116.55(4)°) are larger than those of the terminal ligands (77.55(5) and 77.77(5)°). Additionally, all the other bond lengths and angles are similar to those of **20** and **21**.

Table 5a. Experimental crystallographic data for **16–18** and **20**.

	16	17	18	20
Formula	C ₂₀ H ₃₈ NiN ₂ O ₂	C ₂₀ H ₃₈ CoN ₂ O ₂	C ₄₀ H ₇₆ Fe ₂ N ₄ O ₄	C ₁₈ H ₃₄ CuN ₂ O ₂
FW	397.23	397.45	788.75	374.01
Space group	P12 ₁ /c1	P2 ₁ /c	p1bar	p1bar
a (Å)	18.0679(16)	17.9016(11)	9.5801(6)	9.7332(3)
b (Å)	12.2068(8)	12.0248(7)	21.1047(12)	10.2853(3)
c (Å)	10.4202(9)	10.4070(6)	11.3029(7)	11.7988(4)
V (Å ³)	2298.2(3)	2240.1(2)	2231.0(2)	976.17(5)
Z	4	4	2	2
T (K)	200(2)	100(2)	100(2)	100(2)
λ (Å)	0.71073	0.71073	0.71073	0.71073
ρ _{calc} (g cm ⁻³)	1.148	1.178	1.174	1.272
μ (mm ⁻¹)	0.858	0.780	0.690	1.129
R(F) ^a (%)	4.34	5.59	4.52	3.09
Rw(F) ^b (%)	10.26	11.55	11.51	8.37

$$^a R(F) = \frac{\sum ||F_o| - |F_c||}{\sum |F_o|}$$

$$^b R_w(F) = \left[\frac{\sum w(F_o^2 - F_c^2)^2}{\sum w(F_o^2)^2} \right]^{1/2}$$

Table 5b. Experimental crystallographic data for **21–24**.

	21	22	23	24
Formula	C ₁₈ H ₃₄ NiN ₂ O ₂	C ₃₆ H ₆₄ Co ₂ N ₄ O ₄	C ₃₆ H ₆₄ Fe ₂ N ₄ O ₄	C ₃₆ H ₆₄ Mn ₂ N ₄ O ₄
FW	367.17	734.77	728.61	726.79
Space group	p1bar	p1bar	p1bar	p1bar
a (Å)	9.7399(7)	10.4367(9)	10.495(3)	10.4823(7)
b (Å)	10.2627(8)	20.0010(17)	20.441(6)	10.5255(6)
c (Å)	11.6485(9)	21.4342(19)	21.557(7)	19.4788(12)
V (Å ³)	967.47(13)	4054.4(6)	4178.0(2)	1996.8(2)
Z	2	4	4	2
T (K)	100(2)	100(2)	200(2)	100(2)
λ (Å)	0.71073	0.71073	0.71073	0.71073
ρ _{calc} (g cm ⁻³)	1.260	1.204	1.158	1.209
μ (mm ⁻¹)	1.013	0.857	0.732	0.671
R(F) ^a (%)	2.60	5.26	7.05	3.37
Rw(F) ^b (%)	7.15	10.82	18.30	7.72

$$^a R(F) = \frac{\sum ||F_o| - |F_c||}{\sum |F_o|}$$

$$^b Rw(F) = [\sum w(F_o^2 - F_c^2)^2 / \sum w(F_o^2)^2]^{1/2}$$

Table 6. Selected bond lengths (Å) and angles (°) for **16**, **17**, **20**, and **21**.

	16	17	20	21
M–O	1.9295(18)	1.947(2)	1.8838(12)	1.8407(8)
	1.9303(19)	1.951(2)	1.8849(12)	1.8421(8)
M–N	1.899(2)	1.910(2)	2.0332(14)	1.9304(10)
	1.907(2)	1.919(3)	2.0304(14)	1.9347(10)
C–O	1.290(3)	1.290(4)	1.335(2)	1.3387(14)
	1.294(3)	1.298(3)	1.336(2)	1.3372(14)
C–N	1.331(3)	1.328(4)	1.287(2)	1.2955(15)
	1.325(3)	1.342(4)	1.286(2)	1.2913(15)
C–C _{core}	1.390(4)	1.405(4)	1.451(2)	1.4469(16)
	1.399(4)	1.399(4)		1.4463(16)
C=C	-	-	1.359(2)	1.3619(16)
			1.357(2)	1.3610(16)
N–M–O	118.44(9)	118.87(10)	96.53(5)	94.95(4)
	115.92(9)	117.54(10)	83.47(5)	94.87(4)
	82.61(8)	83.58(10)		85.13(4)
	82.41(8)	83.62(10)		85.05(4)
N–M–N	135.75(9)	135.45(11)	180.0	180.00(6)
O–M–O	128.60(8)	123.10(9)	180.00(13)	180.00(12)

Table 7. Selected bond lengths (Å) and angles (°) for **18** and **19**.

	18		19	
	Terminal	Bridging	Terminal	Bridging
M–O	2.0231(19)	2.0184(17)	2.075(5)	2.093(4)
	2.0957(19)	2.0334(17)	2.130(4)	2.062(5)
		2.0693(19)		2.086(4)
		2.1943(18)		2.116(4)
M–N	2.161(2)	2.308(2)	2.143(5)	2.324(5)
	2.048(2)	2.087(2)		2.256(5)
C–O	1.290(3)	1.329(4)	1.270(8)	1.366(8)
	1.289(3)	1.404(3)	1.279(7)	1.403(6)
C–N	1.322(4)	1.272(4)	1.397(8)	1.253(8)
	1.332(4)	1.299(4)	1.268(9)	1.286(8)
C–C _{core}	1.394(4)	1.505(4)	1.326(10)	1.547(9)
	1.407(4)	1.453(4)	1.446(10)	1.459(9)
N–M–O	77.10(8)	75.53(7)	77.83(19)	73.89(19)
	78.39(8)	76.63(8)	76.6(2)	74.77(18)
N–M–N ^a	148.70(8)		131.52(18)	
	103.77(8)		129.8(2)	
O–M–O ^b	92.22(7)		169.91(18)	
	119.43(8)		99.72(19)	
	156.47(7)		101.71(15)	
	168.63(7)		168.48(16)	

^aN_{terminal}–M–N_{bridging}. ^bO_{terminal}–M–O_{bridging}

Table 8. Selected bond lengths (Å) and angles (°) for **22–24**.

	22^a		23^a		24	
	Terminal	Bridging	Terminal	Bridging	Terminal	Bridging
M–O	1.955(2)	2.0214(19)	1.974(3)	2.094(3)	2.0237(12)	2.1068(11)
	1.9472(19)	2.1096(19)	1.978(3)	2.096(3)	2.0161(11)	2.1467(11)
		2.0331(2)		2.083(3)		2.1116(11)
			2.087(3)			
M–N	2.113(2)	2.126(2)	2.200(3)	2.188(4)	2.2624(13)	2.2260(14)
	2.117(2)	2.120(3)	2.186(4)	2.178(4)	2.2600(13)	2.2403(14)
C–O	1.328(3)	1.350(4)	1.326(5)	1.351(5)	1.3248(19)	1.3492(19)
		1.345(3)	1.315(5)	1.352(6)	1.3275(19)	1.3541(18)
C–N	1.286(3)	1.279(4)	1.280(5)	1.290(6)	1.286(2)	1.283(2)
	1.282(3)	1.280(4)	1.279(5)	1.288(6)		
C–C _{core}	1.460(4)	1.450(4)	1.465(6)	1.445(7)	1.464(2)	1.464(2)
	1.471(4)	1.457(4)	1.459(6)	1.444(6)		1.462(2)
C=C	1.360(4)	1.347(4)	1.354(6)	1.354(7)	1.367(2)	1.354(2)
	1.358(4)	1.351(4)	1.360(6)	1.356(6)		1.352(2)
N–M–O	81.83(9)	76.72(8)	77.78(12)	76.18(14)	77.55(5)	112.67(5)
	81.91(8)	77.08(9)	77.73(13)	75.73(14)	77.77(5)	74.78(4)
						116.55(4)
						75.13(4)
N–M–N ^b	118.22(9)		107.68(14)		114.56(5)	
	110.07(9)		132.70(15)		114.76(5)	
O–M–O ^c	99.24(8)		178.16(12)		177.46(4)	
	104.26(8)		99.61(13)		100.71(4)	
	174.74(8)		173.15(15)		176.82(4)	
	178.02(8)		107.38(15)		102.08(4)	

^aAsymmetric unit contains two molecules; only data for molecule with M1-M2 are listed. ^bN_{terminal}-M-N_{bridging}. ^cO_{terminal}-M-O_{bridging}

Figure 16. Perspective view of **17** with thermal ellipsoids at the 50% probability level.

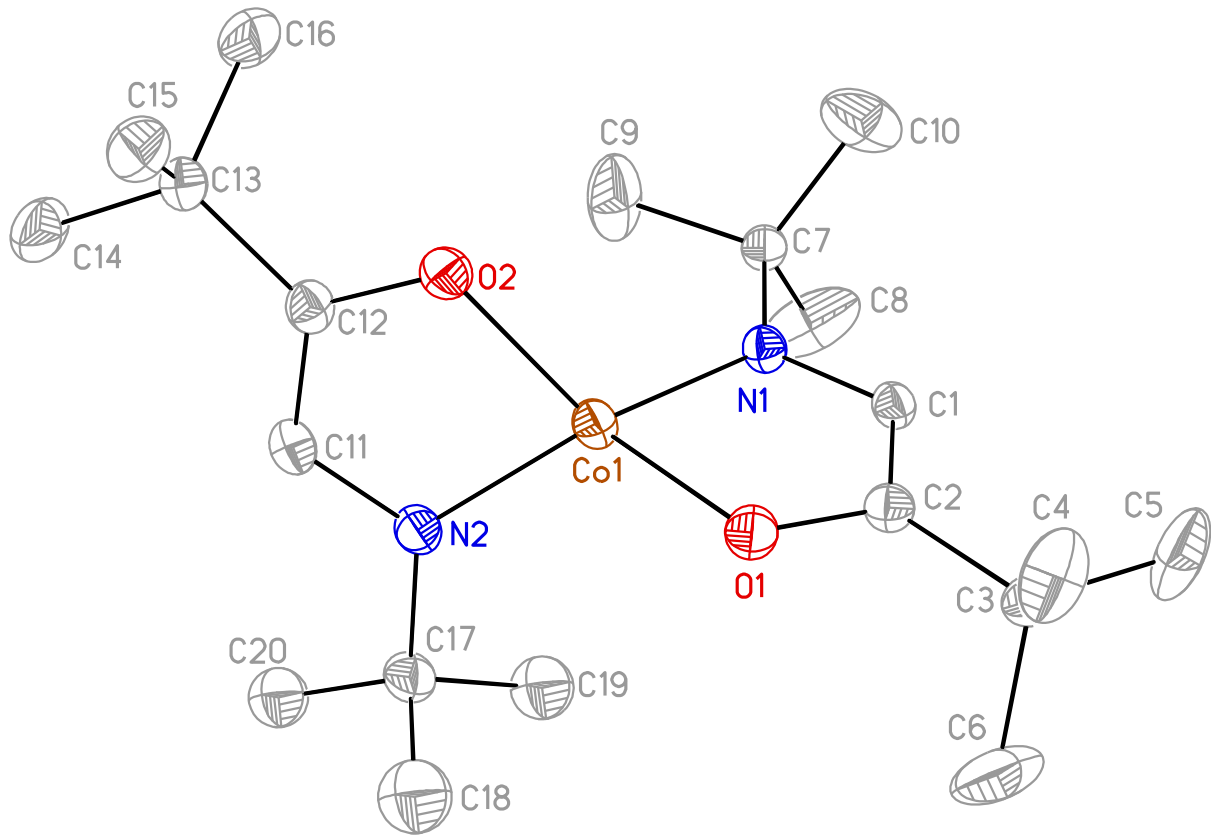


Figure 17. Perspective view of **18** with thermal ellipsoids at the 50% probability level.

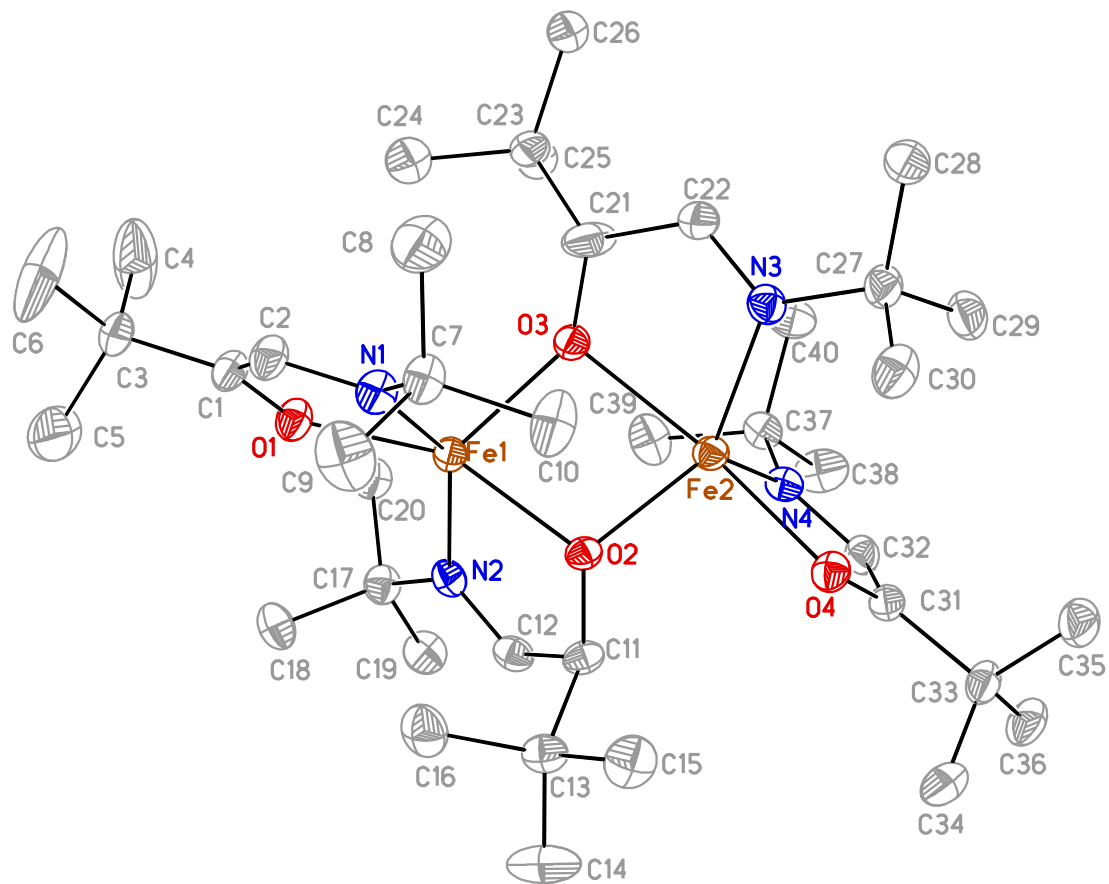


Figure 18. Perspective view of **20** with thermal ellipsoids at the 50% probability level.

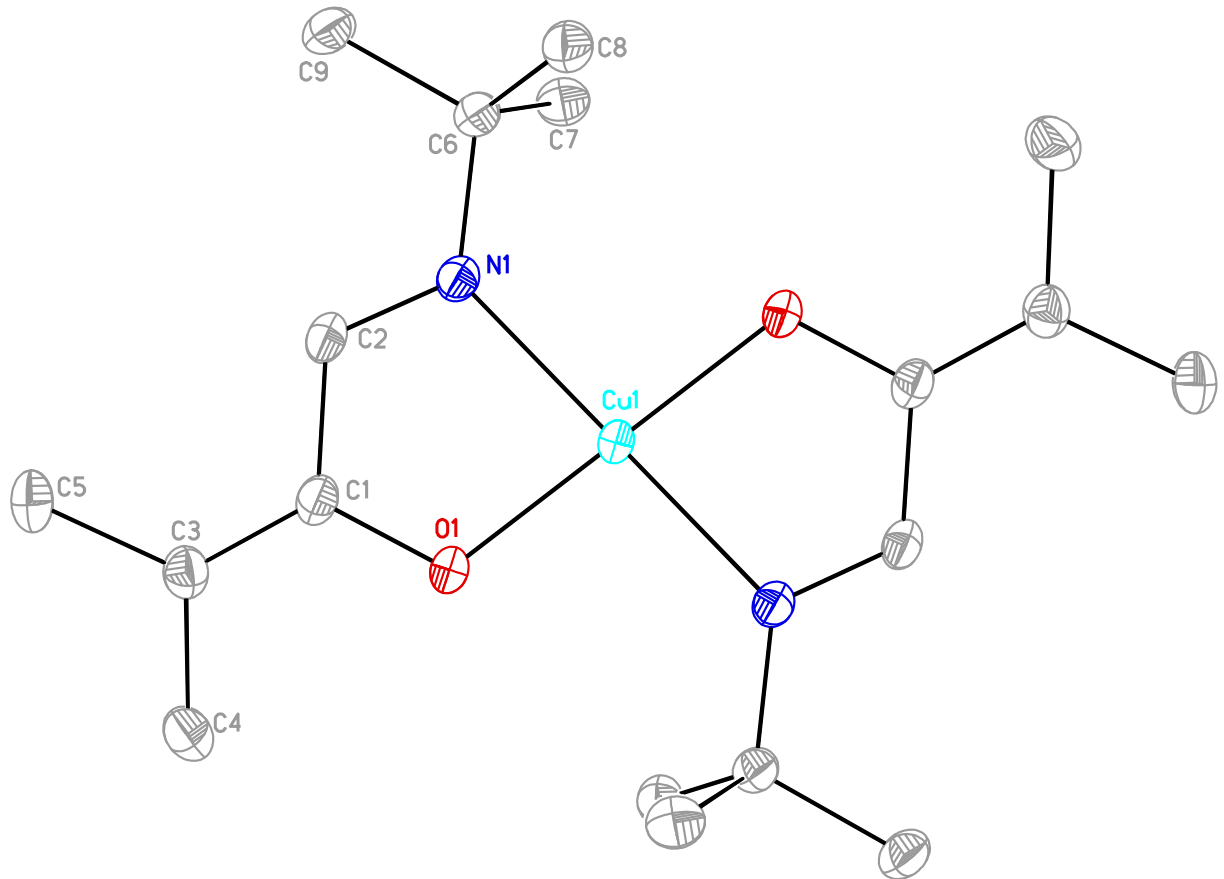


Figure 19. Perspective view of **22** with thermal ellipsoids at the 50% probability level.

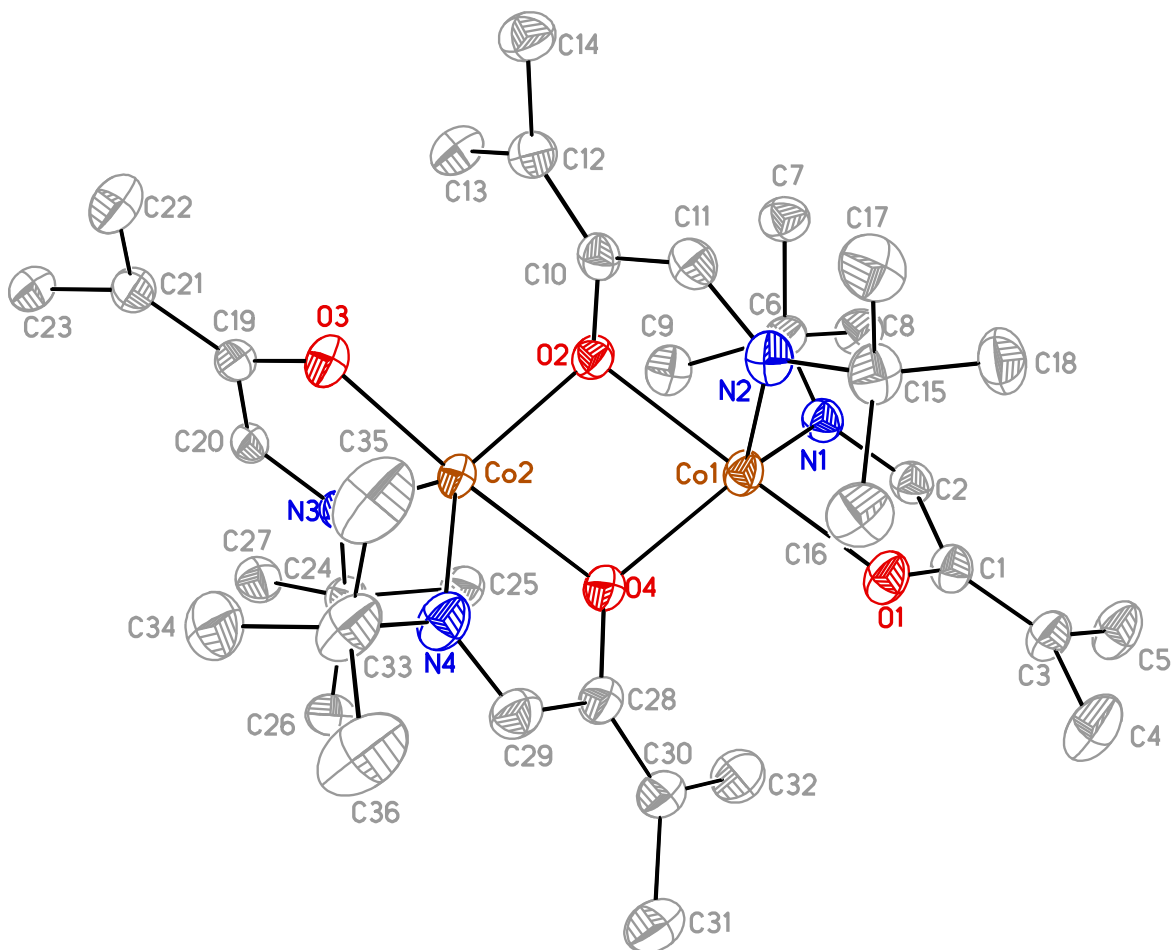


Figure 20. Perspective view of **24** with thermal ellipsoids at the 50% probability level.

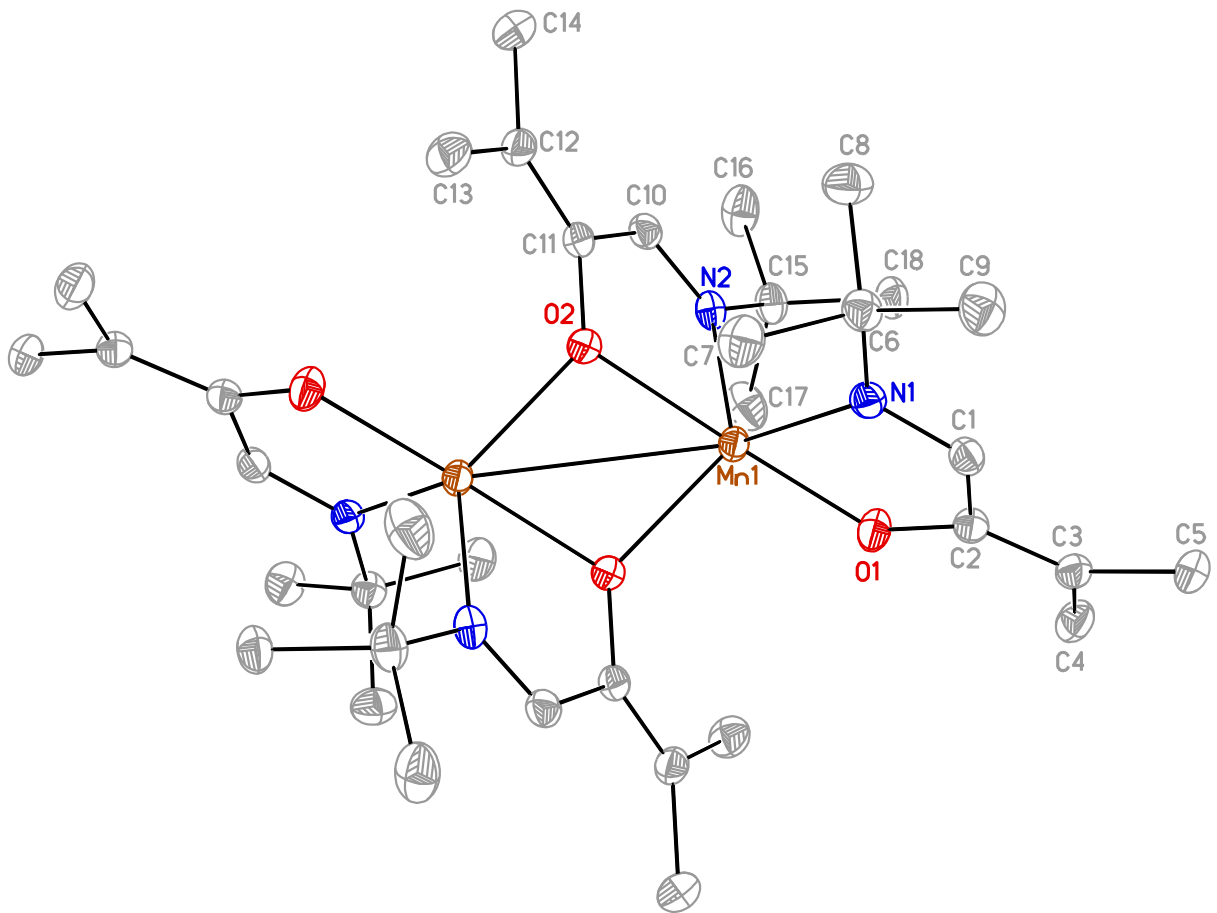


Table 9. Selected bond lengths (Å) and angles (°) for **18**.

Fe1–O1	2.0231(19)	C11–C12	1.505(4)
Fe1–O2	2.0334(17)	C2–N1	1.322(4)
Fe1–O3	2.0693(19)	C32–N4	1.332(4)
Fe2–O4	2.0957(19)	C22–N3	1.299(4)
Fe2–O2	2.0184(17)	C12–N2	1.272(4)
Fe2–O3	2.1943(18)	C2– C1–C3	125.0(2)
Fe1–N1	2.161(2)	C2– C1–O1	117.7(2)
Fe1–N2	2.308(2)	C3– C1–O1	117.3(2)
Fe2–N4	2.048(2)	C32– C31–C33	124.2(2)
Fe2–N3	2.087(2)	C33– C31–O4	117.6(2)
C1–O1	1.290(3)	C32– C31–O4	117.9(2)
C31–O4	1.289(3)	C22– C21–C23	120.6(3)
C11–O2	1.404(3)	C22– C21–O3	114.5(3)
C21–O3	1.329(4)	C23– C21–O3	119.4(3)
C1–C2	1.394(4)	C12– C11–C13	110.9(2)
C31–C32	1.407(4)	C13– C11–O2	111.5(2)
C21–C22	1.453(4)	C12– C11–O2	109.9(2)

Table 10. Selected bond lengths (Å) and angles (°) for **19**.

Mn1–O4	2.075(5)	C2–C3	1.459(9)
Mn 1–O1	2.062(5)	C35–N4	1.397(8)
Mn 1–O2	2.093(4)	C11–N2	1.268(9)
Mn 2–O3	2.130(4)	C22–N3	1.253(8)
Mn 2–O2	2.086(4)	C2–N1	1.286(8)
Mn 2–O1	2.116(4)	C37– C36–C35	123.3(6)
Mn 1–N4	2.143(5)	C37– C36–O4	118.9(6)
Mn 1–N3	2.324(5)	C35– C36–O4	117.8(7)
Mn 2–N2	2.143(5)	C13– C12–C11	122.5(6)
Mn 2–N1	2.256(5)	C13– C12–O3	118.8(6)
C36–O4	1.270(8)	C11– C12–O3	118.6(5)
C12–O3	1.279(7)	C22– C21–C27	109.7(5)
C21–O2	1.366(8)	C22– C21–O2	110.6(5)
C3–O1	1.403(6)	C27– C21–O2	115.1(5)
C35–C36	1.326(10)	C2– C3–C4	111.8(5)
C11–C12	1.446(10)	C2– C3–O1	110.3(5)
C21–C22	1.547(9)	C4– C3–O1	113.2(4)

H Atom Abstraction. As described previously, **18** and **19** demonstrate an H atom abstraction in the bridging ligands. Experimental data other than X-ray crystal structures are not available to understand this H atom abstraction process. However, these complexes can be compared with other literature reported α -imino ketonate complexes. Wieghardt⁷⁴ and others⁷⁵ have reported homoleptic and heteroleptic α -imino ketonate complexes with various transition

metal centers. All of these complexes have been synthesized with ligands containing aromatic substituents and none of the complexes exhibited an H atom abstraction process as observed in this work. H atom abstractions by S and O atoms via radical mechanisms have been studied by computational calculations using kinetic parameters.⁷⁸ In these studies S and O atom containing substrates have been reacted with simple molecules such as H₂, methane, benzene, and methylhydrazine. Induced radicals on S and O atoms abstract H atoms from these simple molecules. These reports suggest that a radical should be localized on an atom and that radical can abstract an H atom from a neighboring molecule. According to the results obtained from this dissertation work an H atom has been abstracted by a C atom that is bonded to the O atom. It is possible that the radical is localized on this C atom leaving the negative charge on the O atom in the intermediate formed during the H abstraction. Then the radical on the C atom may abstract an H atom from a neighboring molecule. Locating the negative charge on the O atom and the presence of a neutral N atom are exemplified by the Fe–O and Fe–N bonds of **18**. In **18**, Fe1–O2 (2.0334(17) Å) and Fe2–O2 (2.0184(17) Å) (H abstracted ligand) bond distances are smaller than those of Fe1–O3 (2.0693(19) Å) and Fe2–O3 (2.1943(18) Å) (Figure 17). Also, the Fe–N bond distances of the H abstracted ligand are longer than those of the regular α -imino ketonate bridging ligand, which suggests a neutral N atom in the H abstracted ligand and a slightly negative N atom in the regular α -imino ketonate bridging ligand. The complexes reported by Wieghardt⁷⁴ and others⁷⁵ do not show this behavior presumably because they used aromatic ligands that can delocalize radicals. The next concern is where the H atom is abstracted from. The possibilities are the radical may have abstracted an H atom from a solvent molecule or ligand molecule.

Evaluation of Thermal Stability, Volatility, and Reactivity Toward Co-Reagents.

The preparative sublimation data, melting points, and solid state decomposition temperatures for **16–25** are summarized in Table 11. Complexes **16–19** sublime on ~0.5 g scales over three hours between 135 and 145 °C/0.05 Torr with $\leq 8\%$ nonvolatile residues and $\geq 93\%$ recovery of analytically pure complexes. On this scale, **20–25** sublime between 115 and 165 °C/0.05 Torr with $\leq 3\%$ nonvolatile residues and $\geq 98\%$ recovery. The dimeric precursors have lower volatility than monomeric precursors in both series as listed in Table 11. High thermal stability is critical for ALD precursors, because decomposition of the precursor is expected to hinder self-limited growth resulting in CVD-like growth. In the α -imino ketonate series, **19** has the highest decomposition temperature (245 °C), while **16** has the lowest (180 °C). In the α -imino enolate series, the highest (295 °C) and lowest (190 °C) decomposition temperatures were observed for **24** and **20**, respectively. When each metal is considered, the α -imino enolate precursors have higher decomposition temperatures than those observed for α -imino ketonate precursors. These decomposition temperatures are remarkably high for each metal precursor. The decomposition temperature of **21** (260 °C) is much higher than that of the widely reported Ni(II) precursor Ni(iPrNCMeNiPr)₂ (180 °C).⁷⁹

Table 11. Volatility and thermal stability data for **16–25**.

Complex	Sublimation temperature (°C/0.05 Torr)	Melting point (°C)	Solid state decomposition temperature (°C)	% Recovery	% Non volatile residue
16	135	180-183	180	90	5
17	135	194–196	235	93	6
18	145	143–145	241	90	8
19	145	175–177	245	91	6
20	110	135–138	190	97	2
21	120	166–168	260	97	2
22	135	166–168	276	98	<1
23	155	172–174	262	97	2
24	165	193–195	295	97	2
25	120	150–152	220	96	3

TGA was carried out on **16–25** to understand their behavior upon heating. Due to the higher air sensitivity of **16–19**, TGA of **16–19** was carried out in a glove box, avoiding air exposure. TGA plots of **16**, **18**, **19**, and **20–25** and DTA plots of **20–22** and **24** are shown in Figures 21 (top), 21 (bottom), and 22, respectively. Complex **16** has a single weight loss due to sublimation between 130 and 200 °C. Complex **18** has a single weight loss due to sublimation between 130 and 240 °C, however it starts decomposing before the sublimation is complete as shown by another weight loss. TGA plots of **20** and **21** displayed similar single step weight losses due to sublimation between 150 and 250 °C. Complexes **22–25** are air sensitive,

consequently, began decomposing during the loading of the TGA balance. Therefore, TGA curves of **22–25** displayed sublimation as well as competitive decomposition that lead to higher non volatile residues. DTA plots of **20–22** and **24** displayed endothermic peaks for melting and sublimation, and exothermic peaks for decomposition. Melting points and decomposition temperatures obtained from DTA curves are similar to the values obtained from the melting point determinations.

Figure 21. TGA of **16, 18, and 19** (top), TGA of **20–25** (bottom).

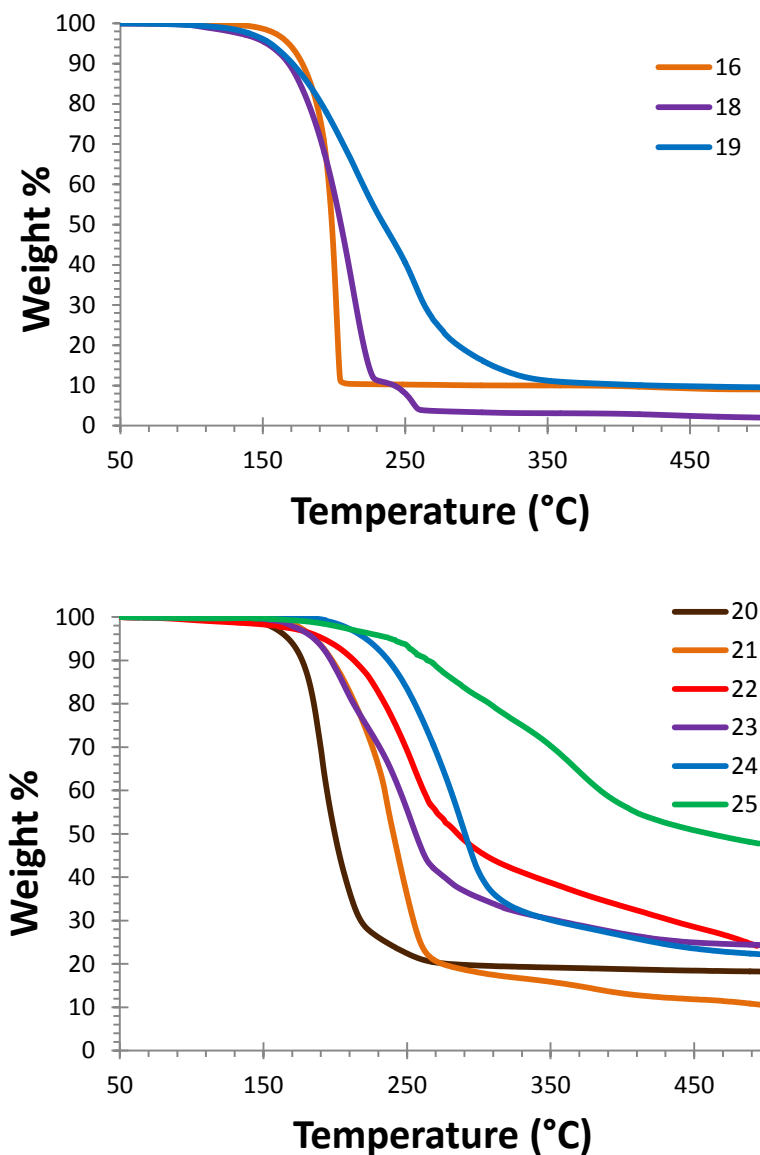
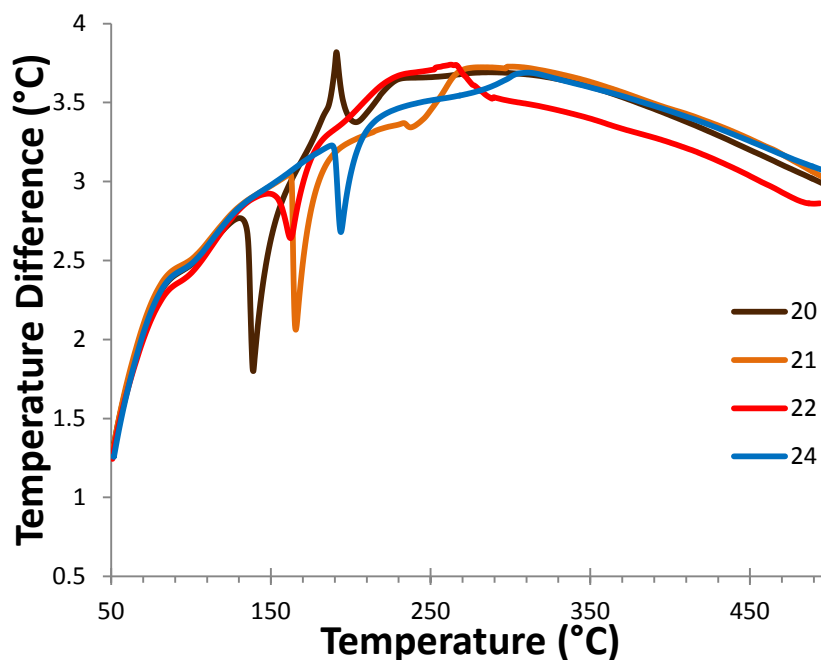


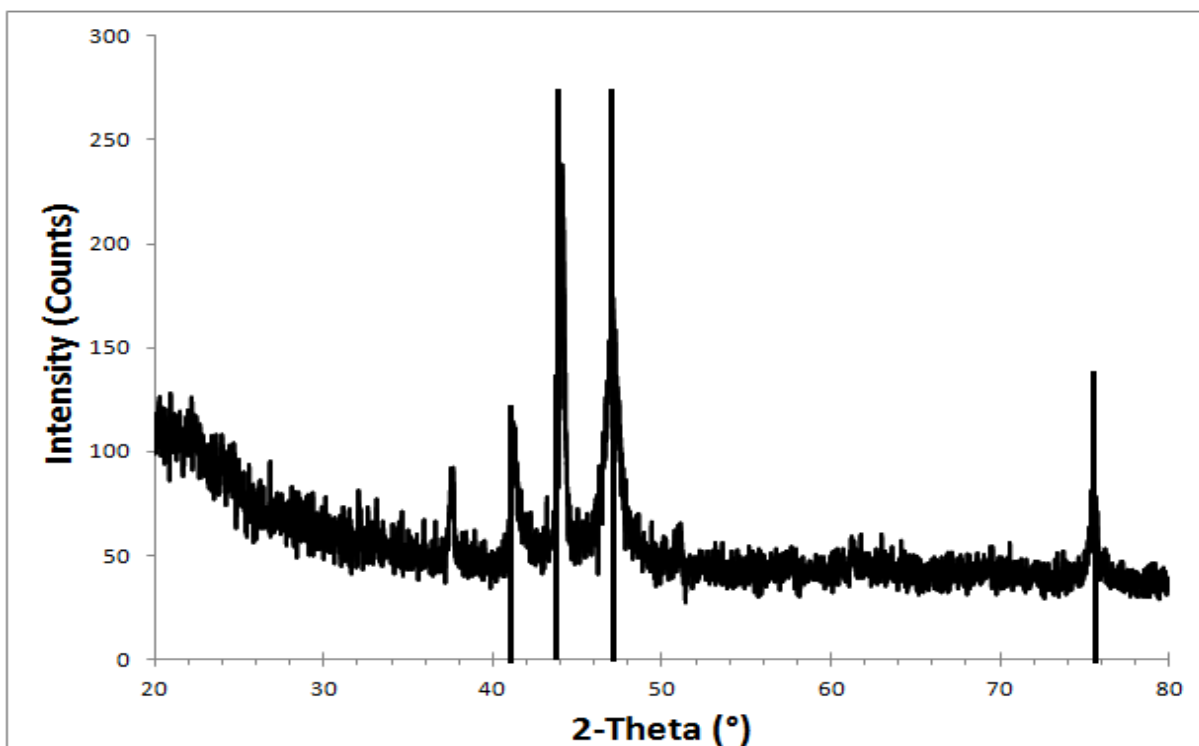
Figure 22. DTA of 20–22 and 24.



To explore the reactivity of these precursors, **16–22** were treated with reducing co-reagents. In these reactions, a solution of **16–22** in tetrahydrofuran was treated with a 5-fold molar excess of anhydrous NH_2NH_2 or $\text{BH}_3(\text{NHMe}_2)$ in separate flasks. Treatment of **16–18** with $\text{BH}_3(\text{NHMe}_2)$ afforded black powders at ambient temperature in < 0.25 h. Black powders produced from **17** and **18** stuck to the stir bar confirming that magnetic Co and Fe metals were formed. The powder obtained from **17** and $\text{BH}_3(\text{NHMe}_2)$ showed reflections for Co metal in the powder XRD spectrum (Figure 23). However, the powder obtained from **18** and $\text{BH}_3(\text{NHMe}_2)$ did not show reflections in the powder XRD spectrum, possibly due to the amorphous nature of the Fe powder. Treatment of **16–19** with NH_2NH_2 and **19** with $\text{BH}_3(\text{NHMe}_2)$ did not afford black powders. Treatment of **20** with NH_2NH_2 and $\text{BH}_3(\text{NHMe}_2)$ afforded a Cu colored powder at ambient temperature in < 0.25 h, and the formation of Cu metal was supported by the reflections corresponding to Cu metal in the XRD pattern. Additionally, **21** reacted with NH_2NH_2 at ambient

temperature in 1 h and with $\text{BH}_3(\text{NHMe}_2)$ in 0.25 h to afford Ni metal, which was confirmed by powder XRD. Similarly, **22** reacted with $\text{BH}_3(\text{NHMe}_2)$ at ambient temperature in < 0.25 h and resulted in a black precipitate which stuck to stir bar, suggesting the formation of Co metal. The formation of crystalline Co metal was also confirmed by powder XRD. However, treatment of **22** with NH_2NH_2 did not afford a black solution or a black precipitate. Treatment of **23** and **24** with the above mentioned reducing agents did not afford a black solution or black powder, even at reflux conditions.

Figure 23. Powder XRD of Co produced upon treatment of **17** with $\text{BH}_3(\text{NHMe}_2)$ in tetrahydrofuran at 23 °C. The reference spectrum for Co metal is overlaid (JCPDS 05-0727).



3.3 Conclusions

Two new classes of ALD precursors containing α -imino ketonate and α -imino enolate ligands have been synthesized, characterized, and evaluation of their volatility, thermal stability, and reactivity was performed. These complexes have useful ALD precursor properties, and some of them react with $\text{BH}_3(\text{NHMe}_2)$ and N_2H_2 reducing co-reagents to afford corresponding metals in solution. These precursor combinations might be converted to viable ALD growth of metal thin films.

Due to the redox active nature of the α -imino ketonate ligand, an H atom abstraction was observed in dimeric complexes containing α -imino ketonate ligands. This type of H atom abstraction process is not present in previously reported α -imino ketonate complexes, due to the delocalization of the radical over aromatic groups. Further experimental studies should be done to understand where the H atom comes from and density functional theory calculations should be carried out to understand the electronic structures of the complexes.

3.4 Experimental Section

General Considerations. All manipulations were carried out under argon using either Schlenk or glove box techniques, except that the ligand was prepared under ambient atmosphere. Tetrahydrofuran was distilled from sodium benzophenone ketyl, hexane was distilled from P_2O_5 . Anhydrous transition metal chlorides (CuCl_2 , NiCl_2 , CoCl_2 , FeCl_2 , MnCl_2 , and CrCl_2) were obtained from Strem Chemicals Inc. and used as received. $\text{NiCl}_2 \cdot \text{CH}_3\text{CN}$ was prepared according to a literature procedure.⁷¹ Potassium hydride (30 wt% dispersion in mineral oil; washed with hexane before use) was purchased from Sigma–Aldrich. 3-Methylbutanal and *tert*-butyl amine were purchased from acros organics. SeO_2 and pinacolone were purchased from Alfa

Aesar. 3-Methyl-2-oxobutanal⁷² and 3,3-dimethyl-2-oxobutanal⁷³ were prepared using published procedures.

¹H and ¹³C{¹H} NMR spectra were obtained at 400 and 100 MHz, respectively, in C₆D₆ and were referenced to the residual proton and the ¹³C resonances of the solvents. Infrared spectra were obtained using Nujol as the medium. Magnetic moments were determined in the solid state using a Johnson Mathey magnetic susceptibility apparatus, and by, ¹H NMR in benzene solution using Evans method.⁸⁰ Melting points were determined on a Thermo Scientific Mel-Temp 3.0 digital melting point apparatus and are uncorrected. TGA and DTA were carried out with a SDT-2960 TGA/DTA instrument at a rate of 10 °C/min.

Preparation of 1-(*tert*-butylimino)-3,3-dimethylbutan-2-one (L⁴). A 100 mL round bottomed flask was charged with a magnetic stir bar, 3,3-dimethyl-2-oxobutanal (1.00 g, 8.77 mmol) and diethyl ether (20 mL). To this stirred solution at ambient temperature was slowly added *tert*-butyl amine (0.90 mL, 8.8 mmol), and the solution was stirred for 6 h. The resultant yellow solution was washed with water (5 mL) and the organic layer was separated. The organic layer was dried over anhydrous Na₂SO₄ and the volatile components were removed under reduced pressure. L⁴ was isolated as a light yellow oil upon vacuum distillation of the crude product at 65 °C/0.05 Torr (1.28 g, 86%): ¹H NMR (C₆D₆, 23 °C, δ) 7.48 (s, 1H, CHN), 1.32 (s, 9H, C(CH₃)₃), 0.95 (s, 9H, C(CH₃)₃); ¹³C{¹H} NMR (C₆D₆, 23 °C, ppm) 205.45 (s, CO), 153.76 (s, CN), 58.16 (s, C(CH₃)₃), 43.88 (s, C(CH₃)₃), 28.64 (s, C(CH₃)₃), 27.13 (s, C(CH₃)₃); ESI-HRMS: calcd for C₁₀H₂₀NO ([M + H]⁺) 170.1545; found 170.1549.

Preparation of 1-(*tert*-butylimino)-3-methylbutan-2-one (L⁵). A 100 mL round bottomed flask was charged with a magnetic stir bar, 3-methyl-2-oxobutanal (1.00 g, 9.99 mmol), and diethyl ether (20 mL). To this stirred solution at ambient temperature was slowly

added *tert*-butyl amine (1.1 mL, 10 mmol), and the solution was stirred for 6 h. The resultant yellow solution was washed with water (5 mL) and the organic layer was separated. The organic layer was dried over anhydrous Na_2SO_4 and the volatile components were removed under reduced pressure. L^5 was isolated as a light yellow oil upon vacuum distillation of the crude product at 60 °C/0.05 Torr (1.15 g, 74%): ^1H NMR (C_6D_6 , 23 °C, δ) 7.45 (s, 1H, CHN), 3.67 (sep, 1H, $J = 8.0$ Hz, $\text{CH}(\text{CH}_3)_2$), 1.08 (d, 6H, $J = 8.0$ Hz, $\text{CH}(\text{CH}_3)_2$), 0.96 (s, 9H, $\text{C}(\text{CH}_3)_3$); $^{13}\text{C}\{^1\text{H}\}$ NMR (C_6D_6 , 23 °C, ppm) 205.00 (s, CO), 153.93 (s, CN), 58.07 (s, $\text{C}(\text{CH}_3)_3$), 34.12 (s, $\text{CH}(\text{CH}_3)_2$), 28.79 (s, $\text{C}(\text{CH}_3)_3$), 18.52 (s, $\text{CH}(\text{CH}_3)_2$).

Preparation of $\text{Ni}(\text{L}^4)_2$ (16**).** A 100 mL Schlenk flask was charged with a magnetic stir bar, 1-(*tert*-butylimino)-3,3-dimethylbutan-2-one (1.00 g, 5.91 mmol) and tetrahydrofuran (30 mL). To this stirred solution at ambient temperature was slowly added lithium metal (0.045 g, 6.49 mmol), and solution was stirred for 6 h. This solution was then slowly added dropwise with a cannula to a stirred suspension of anhydrous $\text{NiCl}_2 \cdot \text{CH}_3\text{CN}$ (0.498 g, 2.95 mmol) in tetrahydrofuran (40 mL) at -78 °C. The resultant dark red solution was stirred for 15 h at ambient temperature. The volatile components were then removed under reduced pressure, and the resultant dark red powder was dissolved in hexane (50 mL). The solution was filtered through a 1 cm pad of Celite on a coarse glass frit, and the volatile components were then removed under reduced pressure. Red crystals of **16** (0.340 g, 30%) were obtained by sublimation at 135 °C/0.05 Torr: mp 180–183 °C; IR (Nujol, cm^{-1}) 1679 (w), 1633 (w), 1484 (m), 1407 (m), 1358 (s), 1264 (m), 1218 (m), 1158 (m), 991 (m), 887 (m), 818 (m), 761 (m), 621 (m); ^1H NMR (C_6D_6 , 23 °C, δ) 9.93 (s, 1H, CHN), 2.27 (s, 9H, $\text{C}(\text{CH}_3)_3$), 0.70 (s, 9H, $\text{C}(\text{CH}_3)_3$); $^{13}\text{C}\{^1\text{H}\}$ NMR (C_6D_6 , 23 °C, ppm) 148.50 (s, CO), 132.07 (s, CN), 73.63 (s, $\text{C}(\text{CH}_3)_3$), 54.56 (s, $\text{C}(\text{CH}_3)_3$), 23.26 (s, $\text{C}(\text{CH}_3)_2$),

15.30 (s, C(CH₃)₃); Anal. Calcd for C₂₀H₃₈NiN₂O₂: C, 60.47; H, 9.64; N, 7.05. Found: C, 59.95; H, 9.38; N, 7.06.

Preparation of Co(L⁴)₂ (17) In a fashion similar to the preparation of **16**, treatment of anhydrous cobalt(II) chloride (0.383 g, 2.95 mmol) in tetrahydrofuran (40 mL) with a solution of the lithium radical anion of 1-(*tert*-butylimino)-3,3-dimethylbutan-2-olate (prepared from 1-(*tert*-butylimino)-3,3-dimethylbutan-2-one (1.000 g, 5.91 mmol) and lithium metal (0.045 g, 6.49 mmol) in tetrahydrofuran (30 mL)) for 15 h at ambient temperature afforded **17** (0.869 g, 79%) as dark red crystals upon sublimation at 135 °C/0.05 Torr: mp 194–196 °C; IR (Nujol, cm⁻¹) 1686 (w), 1667 (w), 1626 (w), 1482 (m), 1407 (m), 1357 (m), 1332 (m), 1265 (w), 1216 (m), 1156 (m), 992 (w), 815 (w); $\mu_{\text{eff}} = 1.79$ and $1.73 \mu_{\text{B}}$ in the solid state and in benzene solution, respectively Anal. Calcd for C₂₀H₃₈CoN₂O₂: C, 60.44; H, 9.64; N, 7.05. Found: C, 60.42; H, 9.48; N, 7.07.

Preparation of Fe₂(L⁴)₄ (18) In a fashion similar to the preparation of **17**, treatment of anhydrous iron(II) chloride (0.381 g, 2.95 mmol) in tetrahydrofuran (40 mL) with a solution of the lithium radical anion of 1-(*tert*-butylimino)-3,3-dimethylbutan-2-olate (prepared from 1-(*tert*-butylimino)-3,3-dimethylbutan-2-one (1.000 g, 5.91 mmol) and lithium metal (0.045 g, 6.49 mmol) in tetrahydrofuran (30 mL)) for 15 h at ambient temperature afforded **18** (0.210 g, 18%) as dark green crystals upon sublimation at 140 °C/0.05 Torr: mp 143–145 °C; IR (Nujol, cm⁻¹) 1687 (w), 1650 (w), 1365 (m), 1263 (w), 1214 (m), 1156 (w), 1125 (w), 1022 (w), 800 (w); $\mu_{\text{eff}} = 4.82$ and $4.74 \mu_{\text{B}}$ in the solid state and in benzene solution, respectively Anal. Calcd for C₄₀H₇₇Fe₂N₄O₄: C, 60.83; H, 9.83; N, 7.09. Found: C, 60.74; H, 9.60; N, 7.22.

Preparation of Mn₂(L⁴)₄ (19) In a fashion similar to the preparation of **17**, treatment of anhydrous manganese(II) chloride (0.365 g, 2.95 mmol) in tetrahydrofuran (40 mL) with a

solution of the lithium radical anion of 1-(*tert*-butylimino)-3,3-dimethylbutan-2-olate (prepared from 1-(*tert*-butylimino)-3,3-dimethylbutan-2-one (1.000 g, 5.91 mmol) and lithium metal (0.045 g, 6.49 mmol) in tetrahydrofuran (30 mL)) for 15 h at ambient temperature afforded **19** (0.407 g, 37%) as dark orange crystals upon sublimation at 145 °C/0.05 Torr: mp 175–177 °C; IR (Nujol, cm^{-1}) 1713 (w), 1686 (w), 1650 (w), 1360 (m), 1344 (m), 1262 (w), 1211 (w), 1153 (w); $\mu_{\text{eff}} = 5.96$ and $5.86 \mu_{\text{B}}$ in the solid state and in benzene solution, respectively Anal. Calcd for $\text{C}_{40}\text{H}_{78}\text{Mn}_2\text{N}_4\text{O}_4$: C, 60.89; H, 9.97; N, 7.10. Found: C, 60.92; H, 10.04; N, 6.84.

Preparation of $\text{Cu}(\text{L}^5)_2$ (20**).** A 100 mL Schlenk flask was charged with a magnetic stir bar, 1-(*tert*-butylimino)-3-methylbutan-2-one (1.00 g, 6.44 mmol), and tetrahydrofuran (30 mL). To this stirred solution at ambient temperature was slowly added KH (0.284 g, 7.08 mmol), and the resulting solution was stirred for 4 h. This solution was then slowly added dropwise with a cannula to a stirred suspension of anhydrous CuCl_2 (0.430 g, 3.22 mmol) in tetrahydrofuran (40 mL) at -78 °C. The resultant brown solution was stirred for 15 h at ambient temperature. The volatile components were then removed under reduced pressure, and the resultant brown powder was dissolved in hexane (50 mL). The resultant solution was filtered through a 1 cm pad of Celite on a coarse glass frit, and hexane was then removed under reduced pressure. Brown crystals of **20** (0.505 g, 43%) were obtained by sublimation at 110 °C/0.05 Torr: mp 135–138 °C; IR (Nujol, cm^{-1}) 1607 (m), 1586 (s), 1365 (m), 1350 (m), 1300 (s), 1239 (m), 1214 (s), 1126 (m), 1035 (m), 971 (m), 675 (m); $\mu_{\text{eff}} = 1.88$ and $1.80 \mu_{\text{B}}$ in the solid state and in benzene solution, respectively. Anal. Calcd for $\text{C}_{18}\text{H}_{32}\text{CuN}_2\text{O}_2$: C, 58.12; H, 8.67; N, 7.53. Found: C, 58.33; H, 8.76; N, 7.58.

Preparation of $\text{Ni}(\text{L}^5)_2$ (21**).** In a fashion similar to the preparation of **20**, treatment of anhydrous $\text{NiCl}_2 \cdot \text{CH}_3\text{CN}$ (0.540 g, 3.22 mmol) in tetrahydrofuran (40 mL) with a solution of

potassium 1-(*tert*-butylimino)-3-methylbutan-2-olate (prepared from 1-(*tert*-butylimino)-3-methylbutan-2-one (1.00 g, 6.44 mmol) and KH (0.284 g, 7.08 mmol) in tetrahydrofuran (30 mL)) for 15 h at ambient temperature afforded **21** (0.767 g, 66%) as pale green crystals upon sublimation at 120 °C/0.05 Torr: mp 166–168 °C; IR (Nujol, cm^{-1}) 1607 (w), 1574 (m), 1366 (m), 1351 (m), 1299 (m), 1213 (m), 978 (w), 799 (w); ^1H NMR (C_6D_6 , 23 °C, δ) 7.94 (s, 1H, CHN), 2.48 (s, 3H, $\text{C}(\text{CH}_3)_2$), 2.31 (s, 3H, $\text{C}(\text{CH}_3)_2$), 1.35 (s, 9H, $\text{C}(\text{CH}_3)_3$); $^{13}\text{C}\{^1\text{H}\}$ NMR (C_6D_6 , 23 °C, ppm) 156.31(s, CO), 150.64 (s, $\text{C}(\text{CH}_3)_2$), 126.95 (s, CN), 61.42 (s, $\text{C}(\text{CH}_3)_3$), 30.29 (s, $\text{C}(\text{CH}_3)_2$), 18.05 (s, $\text{C}(\text{CH}_3)_3$), 17.61 (s, $\text{C}(\text{CH}_3)_2$); Anal. Calcd for $\text{C}_{18}\text{H}_{32}\text{NiN}_2\text{O}_2$: C, 58.88; H, 8.78; N, 7.63. Found: C, 58.97; H, 8.89; N, 7.61.

Preparation of $\text{Co}_2(\text{L}^5)_4$ (22). In a fashion similar to the preparation of **20**, treatment of anhydrous cobalt(II) chloride (0.418 g, 3.22 mmol) in tetrahydrofuran (40 mL) with a solution of potassium 1-(*tert*-butylimino)-3-methylbutan-2-olate (prepared from 1-(*tert*-butylimino)-3-methylbutan-2-one (1.00 g, 6.44 mmol) and KH (0.284 g, 7.08 mmol) in tetrahydrofuran (30 mL)) for 15 h at ambient temperature afforded **22** (0.933 g, 80%) as dark red crystals upon sublimation at 135 °C/0.05 Torr: mp 166–168 °C; IR (Nujol, cm^{-1}) 1601 (m), 1588 (m), 1365 (m), 1348 (m), 1307 (m), 1290 (m), 1203 (m), 964 (m), 799 (m); $\mu_{\text{eff}} = 6.83$ and $7.01 \mu_{\text{B}}$ in the solid state and in benzene solution, respectively. Anal. Calcd for $\text{C}_{18}\text{H}_{32}\text{CoN}_2\text{O}_2$: C, 58.85; H, 8.79; N, 7.62. Found: C, 59.02; H, 8.81; N, 7.67.

Preparation of $\text{Fe}_2(\text{L}^5)_4$ (23). In a fashion similar to the preparation of **20**, treatment of anhydrous iron(II) chloride (0.414 g, 3.22 mmol) in tetrahydrofuran (40 mL) with a solution of potassium 1-(*tert*-butylimino)-3-methylbutan-2-olate (prepared from 1-(*tert*-butylimino)-3-methylbutan-2-one (1.00 g, 6.44 mmol) and KH (0.284 g, 7.08 mmol) in tetrahydrofuran (30 mL)) for 15 h at ambient temperature afforded **23** (0.562 g, 49%) as dark red crystals upon

sublimation at 145 °C/0.05 Torr: mp 172–174 °C; IR (Nujol, cm^{-1}) 1621 (w), 1595 (m), 1365 (m), 1348(m), 1300 (m), 1260 (m), 1090 (m), 1020 (m), 799 (m); $\mu_{\text{eff}} = 7.21$ and $6.72 \mu_{\text{B}}$ in the solid state and in benzene solution, respectively. Anal. Calcd for $\text{C}_{18}\text{H}_{32}\text{FeN}_2\text{O}_2$: C, 59.34; H, 8.85; N, 7.69. Found: C, 59.34; H, 8.76; N, 7.79.

Preparation of $\text{Mn}_2(\text{L}^5)_4$ (24). In a fashion similar to the preparation of **20**, treatment of anhydrous manganese(II) chloride (0.403 g, 3.22 mmol) in tetrahydrofuran (40 mL) with a solution of potassium 1-(*tert*-butylimino)-3-methylbutan-2-olate (prepared from 1-(*tert*-butylimino)-3-methylbutan-2-one (1.00 g, 6.44 mmol) and KH (0.284 g, 7.08 mmol) in tetrahydrofuran (30 mL)) for 15 h at ambient temperature afforded **24** (0.429 g, 37%) as orange crystals upon sublimation at 165 °C/0.05 Torr: mp 193–195 °C; IR (Nujol, cm^{-1}) 1609 (m), 1594 (m), 1365 (m), 1349 (m), 1310 (m), 1291 (m), 1218 (m), 1202 (m), 1031 (w), 956 (m), 798 (w); $\mu_{\text{eff}} = 8.45$ and $7.89 \mu_{\text{B}}$ in the solid state and in benzene solution, respectively. Anal. Calcd for $\text{C}_{18}\text{H}_{32}\text{MnN}_2\text{O}_2$: C, 59.49; H, 8.88; N, 7.71. Found: C, 59.39; H, 8.78; N, 7.64.

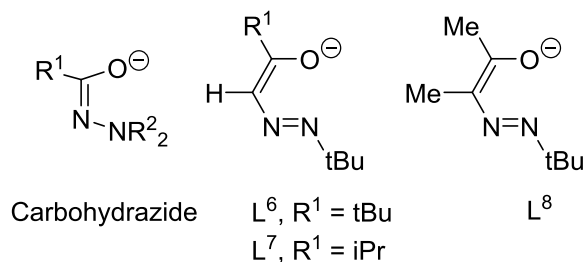
Preparation of $\text{Cr}(\text{L}^5)_2$ (25). In a fashion similar to the preparation of **20**, treatment of anhydrous chromium(II) chloride (0.393 g, 3.22 mmol) in tetrahydrofuran (40 mL) with a solution of potassium 1-(*tert*-butylimino)-3-methylbutan-2-olate (prepared from 1-(*tert*-butylimino)-3-methylbutan-2-one (1.00 g, 6.44 mmol) and KH (0.284 g, 7.08 mmol) in tetrahydrofuran (30 mL)) for 15 h at ambient temperature afforded **25** (0.115 g, 10%) as dark green crystals upon sublimation at 120 °C/0.05 Torr: mp 150–152 °C; IR (Nujol, cm^{-1}) 1601 (m), 1580 (m), 1366 (m), 1352 (m), 1305 (m), 1215 (m), 971 (w), 799 (w); $\mu_{\text{eff}} = 4.80$ and $4.98 \mu_{\text{B}}$ in the solid state and in benzene solution, respectively. Anal. Calcd for $\text{C}_{18}\text{H}_{32}\text{CrN}_2\text{O}_2$: C, 59.98; H, 8.95; N, 7.77. Found: C, 59.81; H, 8.86; N, 7.66.

CHAPTER 4

Synthesis, Structure, and Solution Reduction Reactions of Volatile and Thermally Stable Mid to Late First Row Transition Metal Complexes Containing Hydrazone Ligands

4.1 Introduction

Chapters 2 and 3 described the synthesis, structure, and precursor properties of a series of Cu, Ni, Co, Fe, Mn, and Cr complexes containing α -imino alkoxide, α -imino ketonate, and α -imino enolate ligands. Due to the small size of the ligands, Mn alkoxide, Fe and Mn ketonate, and Co, Fe, and Mn enolate complexes form dimeric complexes, all of which have low volatility. Also, Winter and coworkers recently reported the synthesis, structure, and precursor properties of a series of Cu, Ni, Co, Fe, Mn, and Cr complexes containing carbohydrazide ligands (Chart 9).⁶⁹ Cu(II), Ni(II), Co(II), and Cr(II) complexes containing carbohydrazide ligands formed monomeric species, but only the Cu, Ni, and Co complexes were volatile. Additionally, the Fe(II) and Mn(II) complexes formed nonvolatile, dimeric complexes. The five-membered rings formed upon bidentate coordination of α -imino alkoxide, α -imino ketonate, α -imino enolate, and carbohydrazide ligands to the metal ions are not sufficiently bulky to block dimerization of the larger metal ions and may not protect the metal centers from intermolecular decomposition pathways. As a response to this problem, ligands that form six-membered chelate rings were envisioned. Ligands that form six-membered rings with the metal center might provide additional steric protection of the metal centers, and could thus lead to monomeric, volatile, and thermally stable complexes.

Chart 9. Chemical Structures of carbohydrazone and L⁶–L⁸.

Chapter 4 describes the synthesis, structure, and precursor properties of a series of monomeric Ni, Co, Fe, Mn, and Cr complexes that contain the hydrazonate ligands L⁶–L⁸ (Chart 9). The hydrazonate ligands form six-membered chelate rings with metal centers. These complexes have tunable volatilities, high decomposition temperatures, and thus have useful ALD precursor properties. The coordination chemistry of hydrazonate ligands is poorly developed to date, and is limited to a few Cu(II) and Ni(II) complexes containing aryl groups on the terminal nitrogen atom.⁸¹ There is a small family of crystallographically characterized metal complexes that contain the hydrazonate ligand core within more elaborate chelating ligands.⁸²

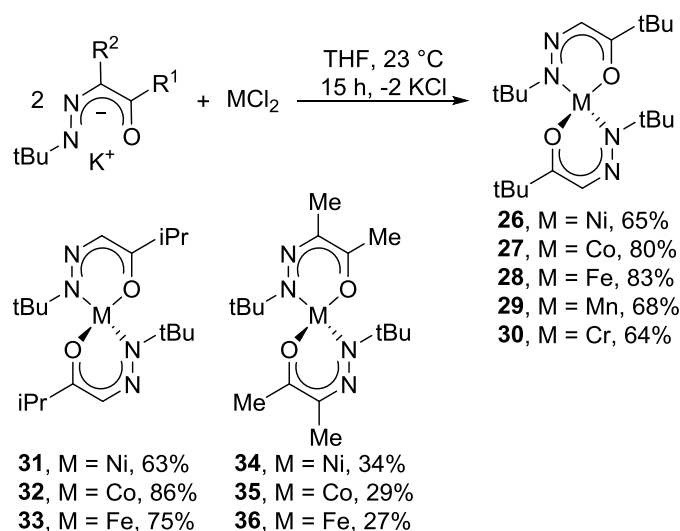
4.2 Results and Discussion

Synthetic Aspects. The hydrazonate ligand precursors L⁶H–L⁸H (Chart 9) were synthesized and characterized as described in the Experimental Section upon treatment of *tert*-butyl glyoxal, isopropyl glyoxal, or 2, 3-butanedione with *tert*-butyl hydrazine hydrochloride and potassium hydroxide. The potassium salts KL⁶–KL⁸ were prepared by treatment of L⁶H–L⁸H with KH in tetrahydrofuran, and these solutions were then treated directly with anhydrous MCl₂ (M = Ni, Co, Fe, Mn, Cr) as depicted in Scheme 5 to afford complexes **26–36** as crystalline solids in the indicated yields upon sublimation between 100 and 135 °C at 0.05 Torr. Similar treatment of MnCl₂ and CrCl₂ with KL⁷ afforded products in very low yields and isolable products were not obtained upon treatment of these chlorides with KL⁸. Treatment of CuCl₂ with

KL⁶–KL⁸ resulted in the precipitation of Cu metal and use of LiL⁶–LiL⁸ did not afford isolable products.

The structures of **26**–**36** were assigned by spectral and analytical data. In addition, X-ray crystal structure of **27**, **31**, **32**, and **34**–**36** were determined, as described below. Complexes **26**–**36** are paramagnetic and show very broad peaks in their ¹H NMR spectra. The magnetic moment values of **26**–**36** are consistent with high spin tetrahedral geometries. Additionally, the solid state and solution state magnetic moment values of **26**–**36** were close to each other, suggesting similar monomeric, tetrahedral structures in the solid state and solution.

Scheme 5. Synthesis of **26**–**36**.



X-Ray Crystal Structures. The X-ray crystal structures of **27**, **31**, **32**, and **34**–**36** were obtained to establish the solid state configurations. Experimental crystallographic data are summarized in Table 12 and selected bond lengths and angles are presented in Table 13. Representative perspective views of **27**, **32**, and **35** are shown in Figures 24–26. The spectral and analytical data of **26**, **28**, **29**, **30**, and **33** are similar to those of **27**, **31**, **32**, and **34**–**36**, which suggest that **26**, **28**, **29**, **30**, and **33** also adopt monomeric, tetrahedral structures.

The molecular structures of **27**, **31**, **32**, and **34–36** are remarkably similar. All display distorted tetrahedral geometry about the metal centers with κ^2 -N,O coordination of L^6-L^8 through the carbonyl oxygen atom and terminal nitrogen atom. The M–O distances fall into the narrow range of 1.903 to 1.921 Å. The M–N distances lie between 1.925 and 1.963 Å for **27**, **31**, **32**, **34**, and **35**, but are 1.982(5) and 2.002(5) Å in **36**. The slightly longer Fe–N bond lengths in **36** are consistent with the larger Fe(II) ion, compared to the slightly smaller Co(II) and Ni(II) ions in **27**, **31**, **32**, **34**, and **35**. The N–N, C–C, and C–O bond lengths within the L^6-L^8 cores are in between the lengths expected for single and double bonds, which suggest monoanionic, delocalized ligands. The intraligand N–M–O angles of **27**, **31**, **32**, and **34–36** fall between 91 and 96°, and the interligand angles range from 113.2 to 120.6°. The corresponding interligand N–M–N and O–M–O angles are between 119.1 and 126.4° and 113.1 and 120.6°, respectively. These angles illustrate the distorted tetrahedral geometry about the metal ions.

There have been three previously reported crystal structures of Cu(II) complexes containing hydrazonate ligands with aryl groups on the terminal nitrogen atom and acyl groups on the central carbon atom of the ligand.⁸¹ As noted above, attempts to prepare Cu(II) complexes containing L^6-L^8 resulted in the precipitation of Cu metal and coordination complexes could not be isolated. The presence of electron-withdrawing phenyl and acyl groups on the ligand cores must render the ligands less basic than L^6-L^8 , thus preventing the reduction of the Cu(II) ion. The complex Ni(PhNNC(COMe)C(Me)O)₂ is the only other first row transition metal hydrazonate complex that has been crystallographically characterized.^{81b} This complex adopts square planar geometry about Ni, apparently due to the lower steric profile of the ligand compared to the larger L^6-L^8 in **27**, **31**, **32**, and **34–36**. The Ni–N and Ni–O distances in Ni(PhNNC(COMe)C(Me)O)₂ are 1.882(2) and 1.816(2) Å, respectively, which are shorter than

those of **31** and **34** due to the differing geometries. Several similar complexes containing κ^2 -N,O- β -ketimate or related N,O-based ligands with tetrahedral geometries about the metal ions have been structurally characterized, including a Ni(II) pyrazolanoto complex (Ni–O 1.924(1) Å, Ni–N 1.951(1) Å),⁸³ a Co(II) pyrazolanoto complex (Co–O 1.932(2), 1.933(2) Å, Co–N 1.969(2), 1.982(2) Å),⁸⁴ and Fe(iPrNC(Me)CHC(Me)O)₂ (Fe–O 1.9407(8), 1.9419(8) Å, Fe–N 2.0373(9), 2.0447(8) Å).⁸⁵ These bond lengths are very similar to those observed in **27**, **31**, **32**, and **34–36**.

Table 12. Experimental crystallographic data for **27**, **31**, **32**, and **34–36**.

	27	31	32	34	35	36
Formula	C ₂₀ H ₃₈ CoN ₄ O ₂	C ₁₈ H ₃₄ NiN ₄ O ₂	C ₁₈ H ₃₄ CoN ₄ O ₂	C ₁₆ H ₃₀ NiN ₄ O ₂	C ₁₆ H ₃₀ CoN ₄ O ₂	C ₁₆ H ₃₀ FeN ₄ O ₂
FW	425.48	397.19	397.43	369.14	369.38	366.38
Space group	P2 ₁ 2 ₁ 2 ₁	Pbca	Pbca	P2 ₁ 2 ₁ 2	P2 ₁ 2 ₁ 2	P12 ₁ 1
a (Å)	11.0676(8)	10.7214(6)	10.799(2)	31.3403(7)	31.287(2)	11.2423(9)
b (Å)	11.0757(7)	11.3118(6)	11.334(2)	8.0896(2)	8.1317(6)	8.1136(7)
c (Å)	18.946(1)	34.753(2)	34.616(5)	11.1323(3)	11.1558(8)	31.476(3)
V (Å ³)	2322.4(3)	4214.7(4)	4237(1)	2822.4(1)	2838.2(4)	2871.1(4)
Z	8	8	8	4	6	2
T (K)	100(2)	100(2)	100(2)	100(2)	100(2)	100(2)
λ (Å)	0.71073	0.71073	0.71073	0.71073	0.71073	0.71073
ρ _{calc} (g cm ⁻³)	1.214	1.271	1.240	1.317	1.297	1.280
μ (mm ⁻¹)	0.759	0.940	0.827	1.046	0.921	0.802
R(F) ^a (%)	3.86	3.27	3.72	2.44	2.98	7.92
Rw(F) ^b (%)	13.35	14.46	13.27	7.04	6.87	27.92

$${}^a R(F) = \frac{\sum | |F_o| - |F_c| |}{\sum |F_o|}, {}^b R_w(F)^2 = \frac{[\sum w(F_o^2 - F_c^2)^2]}{\sum w(F_o^2)^2}^{1/2}$$

Table 13a. Selected bond lengths (Å) for **27**, **31**, **32**, and **34–36**.

	27	31	32	34^a	35^a	36^b
M–O	1.910(1)	1.9067(9)	1.920(1)	1.903(1)	1.921(1)	1.919(5)
	1.911(1)	1.904(1)	1.919(1)	1.904(1)	1.921(1)	1.914(5)
				1.906(1)	1.918(1)	
M–N	1.963(2)	1.943(1)	1.956(2)	1.925(1)	1.945(2)	2.002(5)
	1.962(2)	1.941(1)	1.956(2)	1.931(1)	1.949(2)	1.982(5)
				1.926(1)	1.944(2)	
C–O	1.283(3)	1.280(2)	1.281(2)	1.275(2)	1.279(2)	1.262(8)
	1.282(3)	1.280(2)	1.286(2)	1.278(2)	1.276(2)	1.279(9)
				1.273(2)	1.276(2)	
N–N	1.286(3)	1.280(2)	1.288(2)	1.290(2)	1.296(2)	1.309(7)
	1.287(3)	1.279(1)	1.291(2)	1.289(2)	1.287(2)	1.302(7)
				1.292(2)	1.289(2)	
C–C _{core}	1.399(4)	1.383(2)	1.387(3)	1.402(2)	1.405(3)	1.40(1)
	1.380(4)	1.387(2)	1.383(3)	1.405(2)	1.405(3)	1.39(1)
				1.406(2)	1.403(3)	
C–N _{core}	1.337(3)	1.350(2)	1.352(2)	1.348(2)	1.351(3)	1.354(9)
	1.361(3)	1.352(2)	1.363(3)	1.347(2)	1.358(2)	1.343(9)
				1.345(2)	1.359(3)	

^aAsymmetric unit contains 1.5 independent molecules^bAsymmetric unit contains 3 independent molecules; only data for molecule with Fe1 are listed

Table 13b. Selected bond angles (°) for **27**, **31**, **32**, and **34–36**.

	27	31	32	34^a	35^a	36^b
N–M–O	95.12(7)	93.58(4)	95.23(6)	91.96(5)	93.91(6)	91.0(2)
	95.13(7)	93.23(4)	96.01(6)	91.76(5)	93.83(6)	91.6(2)
	115.62(7)	114.42(4)	116.03(6)	91.64(5)	94.37(6)	120.6(2)
	115.43(7)	118.10(4)	113.64(6)	116.72(5)	113.22(6)	116.8(2)
				119.43(5)	117.81(6)	
				113.54(5)	115.58(6)	
N–M–N	122.12(7)	119.08(4)	121.48(6)	125.07(8)	126.17(7)	120.3(2)
				126.35(5)	124.85(9)	
O–M–O	114.99(6)	120.60(4)	115.99(6)	116.74(8)	113.10(6)	119.2(2)
				116.19(5)	113.43(6)	

^aAsymmetric unit contains 1.5 independent molecules

^bAsymmetric unit contains 3 independent molecules; only data for molecule with Fe1 are listed

Figure 24. Perspective view of **27** with thermal ellipsoids at the 50% probability level.

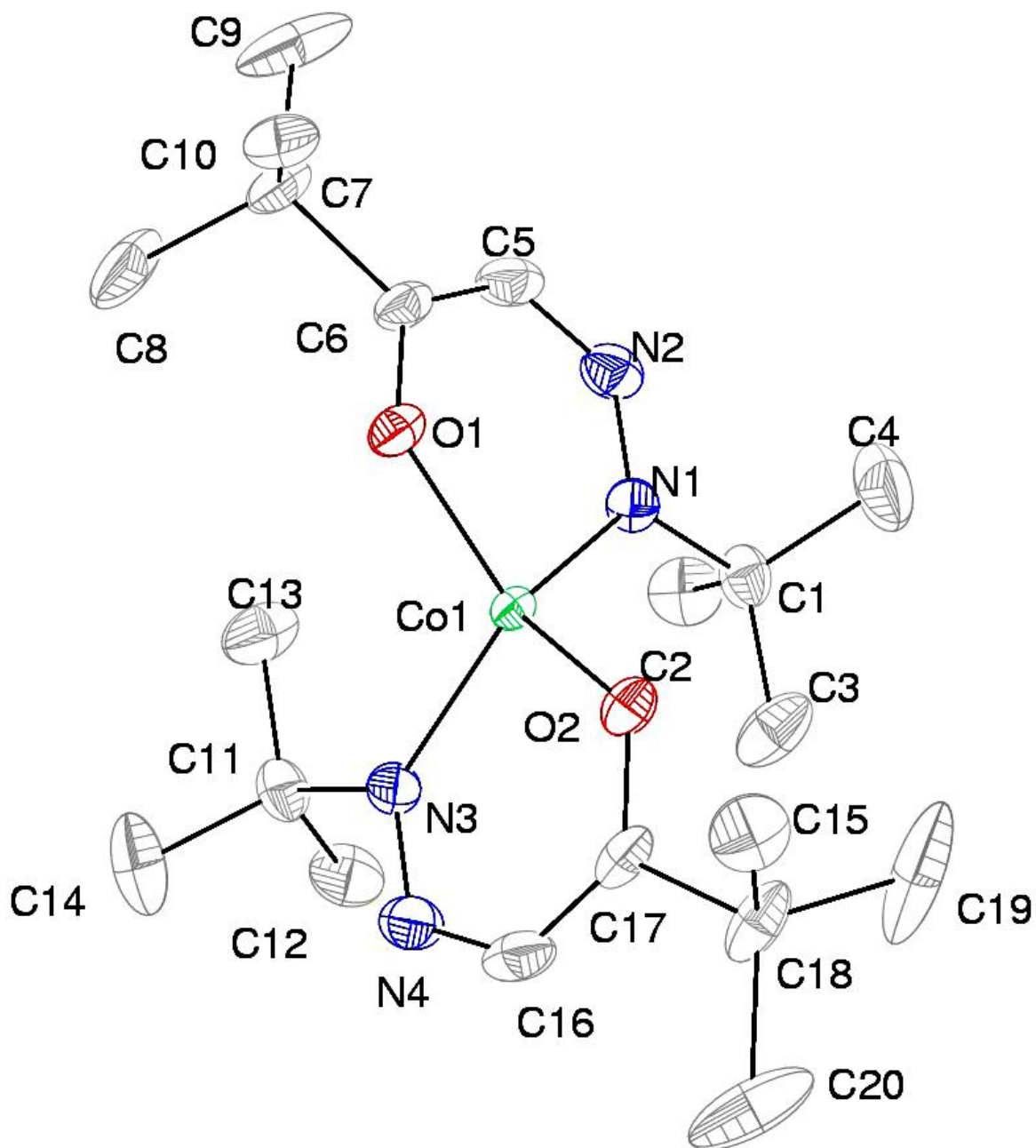


Figure 25. Perspective view of **32** with thermal ellipsoids at the 50% probability level.

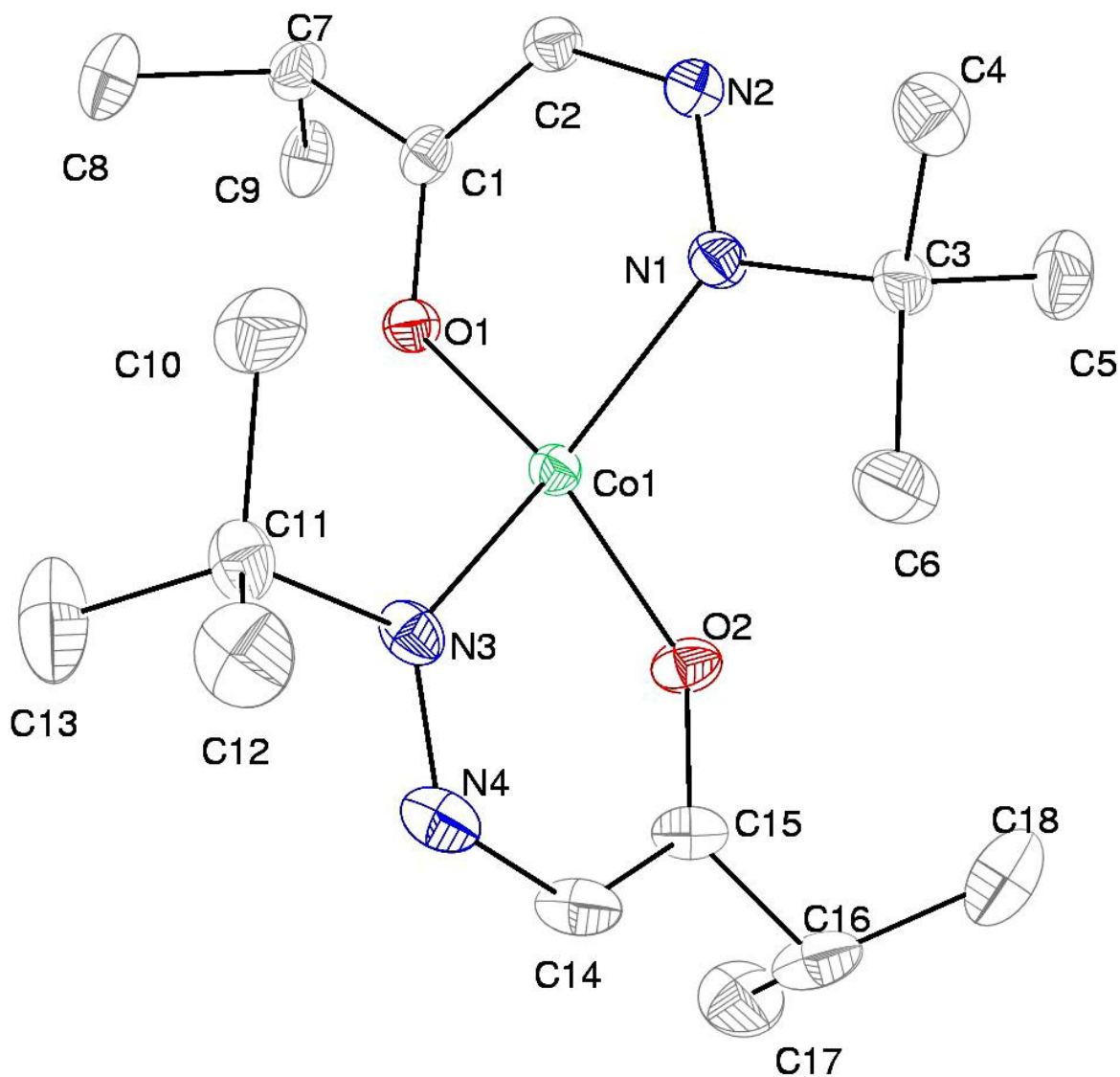
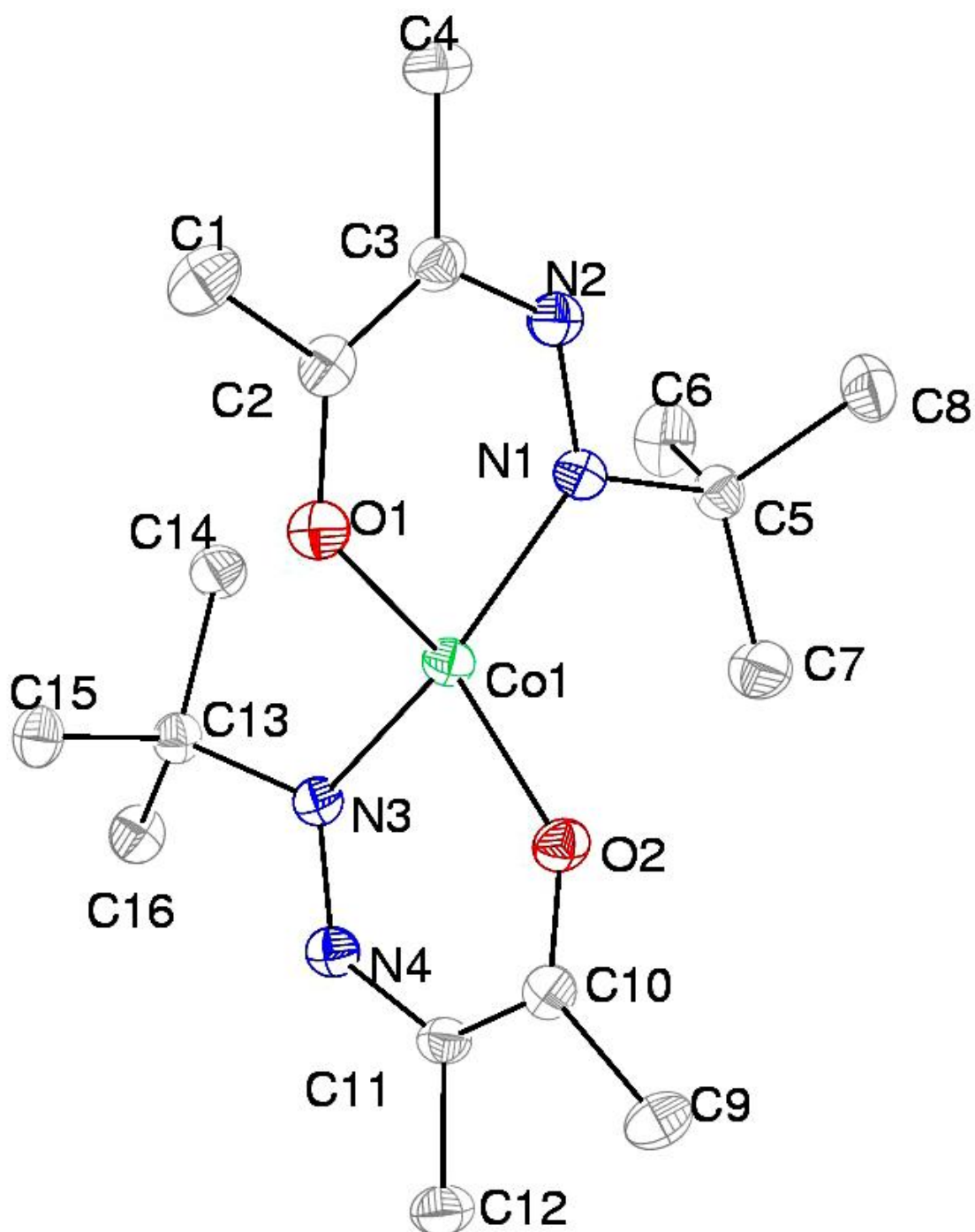


Figure 26. Perspective view of **35** with thermal ellipsoids at the 50% probability level.



Volatility, Thermal Stability, and Screening of Reducing Co-Reagents. The preparative sublimation data, melting points, and solid state decomposition temperatures for **26–36** are summarized in Table 14. Complexes **26–36** sublime on ~ 0.5 g scales over 3 hours between 120–135 °C (**26–30**) and 100–105 °C (**31–36**) at 0.05 Torr. In all cases, $\geq 96\%$ of the complexes were recovered upon sublimation of analytically pure **26–36**, and $\leq 3\%$ of nonvolatile residues were obtained. The lower sublimation temperatures of **31–36**, compared to **26–30**, are consistent with their lower molecular weights. The decomposition temperatures were highest for **31–32** (273–308 °C), intermediate for **26–30** (241–278 °C), and lowest for **34–36** (235–250 °C). The ligands in **34–36** may not be bulky enough to protect the metal centers from intermolecular decomposition reactions, and the very bulky ligands in **26–30** may lead to decomposition reactions that alleviate steric interactions in the coordination spheres. The thermal decomposition temperature of **31** (273 °C) is much higher than that of the widely promoted Ni(II) film growth precursor Ni(iPrNCMeNiPr) (180 °C).⁷⁹ High thermal stability is very important for ALD precursors, since the precursor thermal decomposition temperature is usually close to the temperature at which loss of self-limited ALD growth occurs and CVD-like growth ensues.^{12,15} Interestingly, **31** melts below its sublimation temperature, and thus vapor transport occurs from the liquid state. Liquid ALD precursors are desirable because they provide more reproducible dosing and may reduce particle levels during film growth.^{12d}

Table 14. Volatility and thermal stability data for **26–36**.

Complex	Sublimation temperature (°C/0.05 Torr)	Melting point (°C)	Solid state decomposition temperature (°C)	% Recovery	% Nonvolatile residues
26	120	157–159	245	97	2
27	130	162–164	260	99	< 1
28	120	177–179	241	99	< 1
29	135	169–171	257	95	2
30	130	274–276	278	96	3
31	100	92–94	273	96	< 1
32	100	109–111	308	97	< 1
33	105	114–116	307	97	< 1
34	100	133–135	235	98	1
35	100	143–145	250	98	2
36	100	120–122	250	97	2

TGA and DTA were carried out on **26–36** to understand their thermal stabilities. TGA plots for **26–28** and **30** are shown in Figure 27, and plots for **31–36** are shown in Figure 28. Complexes **26–28** and **31–36** show similar single step weight losses due to sublimation between 150 and 250 °C in the TGA curves. Complex **29** is very air sensitive and decomposed during the several seconds of ambient atmosphere exposure required to load the TGA balance. Due to its lower volatility, **30** has a single step weight loss between 175 and 290 °C due to sublimation, but also undergoes competitive solid state decomposition at 250–290 °C, leading to a higher

nonvolatile residue than the others. Each DTA plot of **26–36** shows two endothermic peaks that are consistent with melting and sublimation (Representative DTA plots for **26–28** and **30** are shown in Figure 29). Melting points obtained from DTA curves are similar to the values obtained with a melting point apparatus.

Figure 27. TGA plots of **26–28** and **30**.

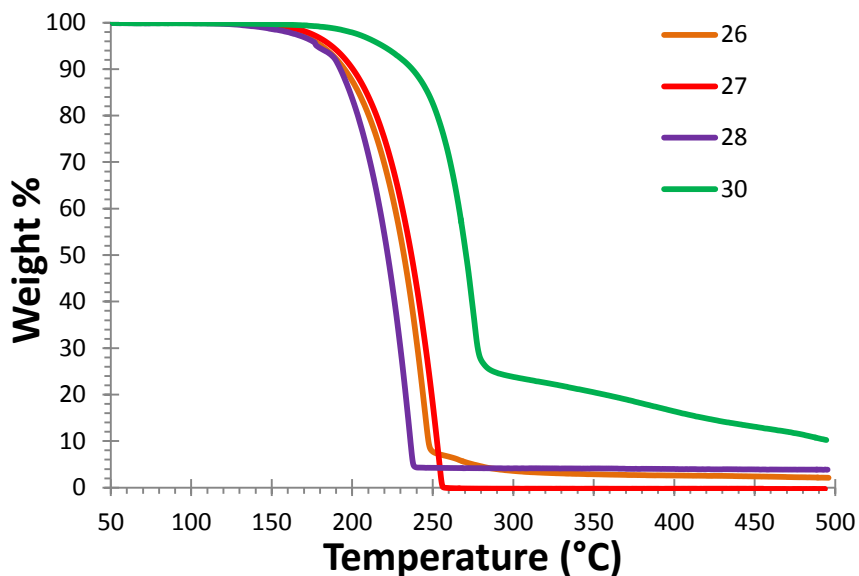


Figure 28. TGA plots of **31–36**.

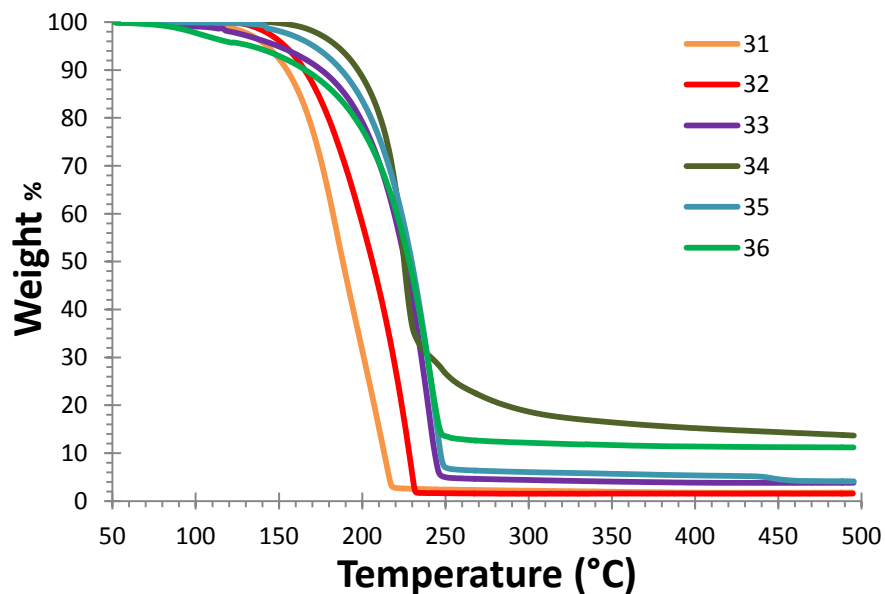
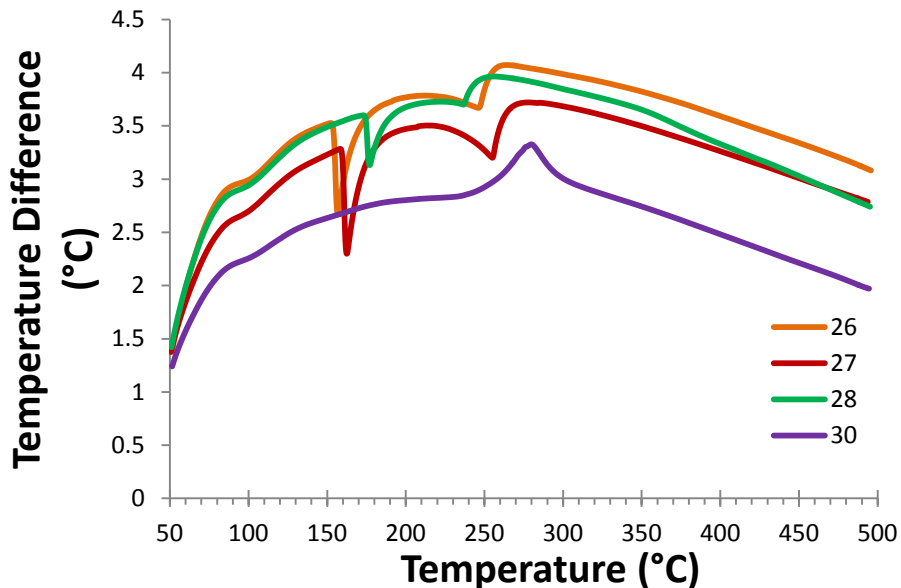


Figure 29. DTA plots of **26–28** and **30**.

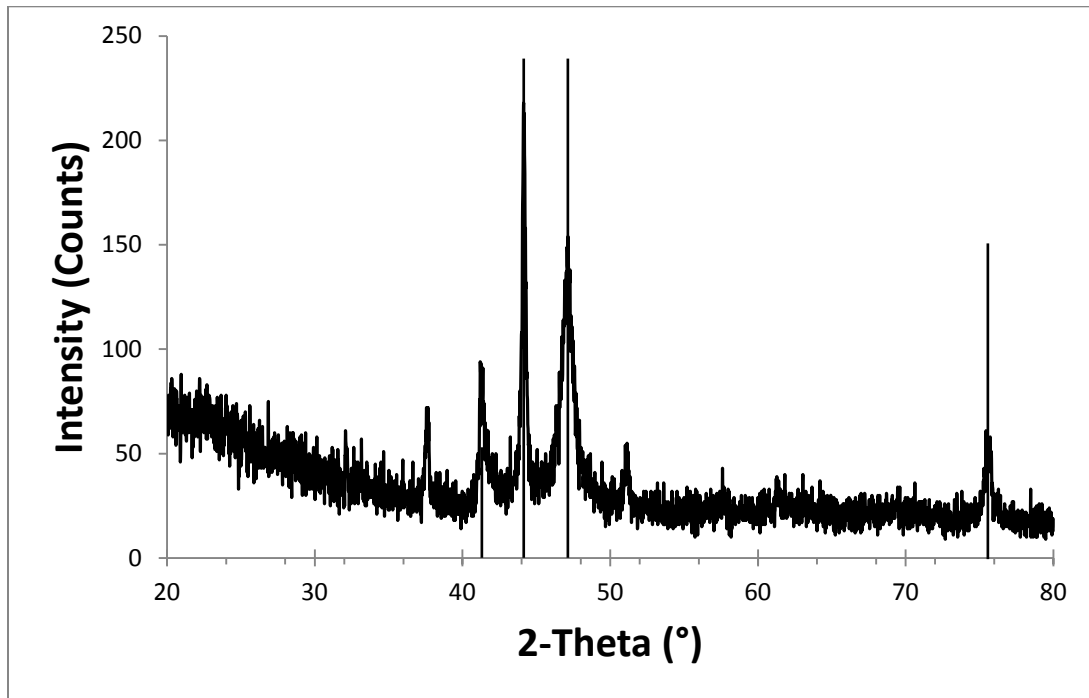
Complexes **27** and **29** were chosen for solution reduction studies, since their electrochemical potentials bracket those of the metal(II) ions in this study (E° (V): Ni, -0.257; Co, -0.280; Fe, -0.447; Mn, -1.185; Cr, -0.913).^{20a} In these reactions, a solution of **27** or **29** in tetrahydrofuran was treated with a five-fold molar excess of each potential reducing co-reagent listed in Table 15. Reactions that did not afford a black precipitate or black solution after one hour at ambient temperature were then refluxed for one hour. Treatment of **27** with anhydrous hydrazine at ambient temperature afforded a black precipitate in < 0.25 hour that stuck to the stir bar, suggesting the formation of magnetic Co metal. Indeed, the powder XRD spectrum of this powder confirmed crystalline Co metal (Figure 30 (a)). Additionally, treatment of **27** with LiAlH_4 , $\text{BH}_3(\text{NHMe}_2)$, pinacol borane, $\text{BH}_3(\text{SMe}_2)$, or $\text{BH}_3(\text{THF})$ either at room temperature (entries 2, 6) or upon reflux (entries 3–5) afforded black powders or black solutions. These black powders did not stick to the magnetic stir bar and showed no reflections in the powder XRD spectra. Annealing of the powder obtained with **27** and $\text{BH}_3(\text{SMe}_2)$ at 600 °C for four hours afforded crystalline Co metal (Figure 30 (b)). The products of these latter reactions are likely

very small Co metal nanoparticles. Analogous treatment of **29** with LiAlH₄, pinacol borane, or BH₃(THF) at room temperature (entry 2) or upon reflux (entries 4, 6) afforded black solutions. X-ray diffraction patterns of the reaction products did not show any reflections, even after annealing at 800 °C for four hours. Mn metal nanoparticles have been reported from several different synthetic routes, and are oxidized rapidly upon exposure to air.⁸⁶ While the powders derived from **29** were handled under argon until after annealing at 800 °C, the argon was not of high purity and it is possible that there was enough oxygen or water present in the reaction flasks to promote oxidation of small Mn nanoparticles. Treatment of **27** or **29** under the conditions noted above did not yield black precipitates or black solutions with the following reagents: 1,1-dimethylhydrazine, trimethylaluminum, triethylaluminum, triethylsilane, lithium triethylborohydride, BH₃(2-picoline), BH₃(morpholine), B₁₀H₁₄, or 9-borabicyclononane.

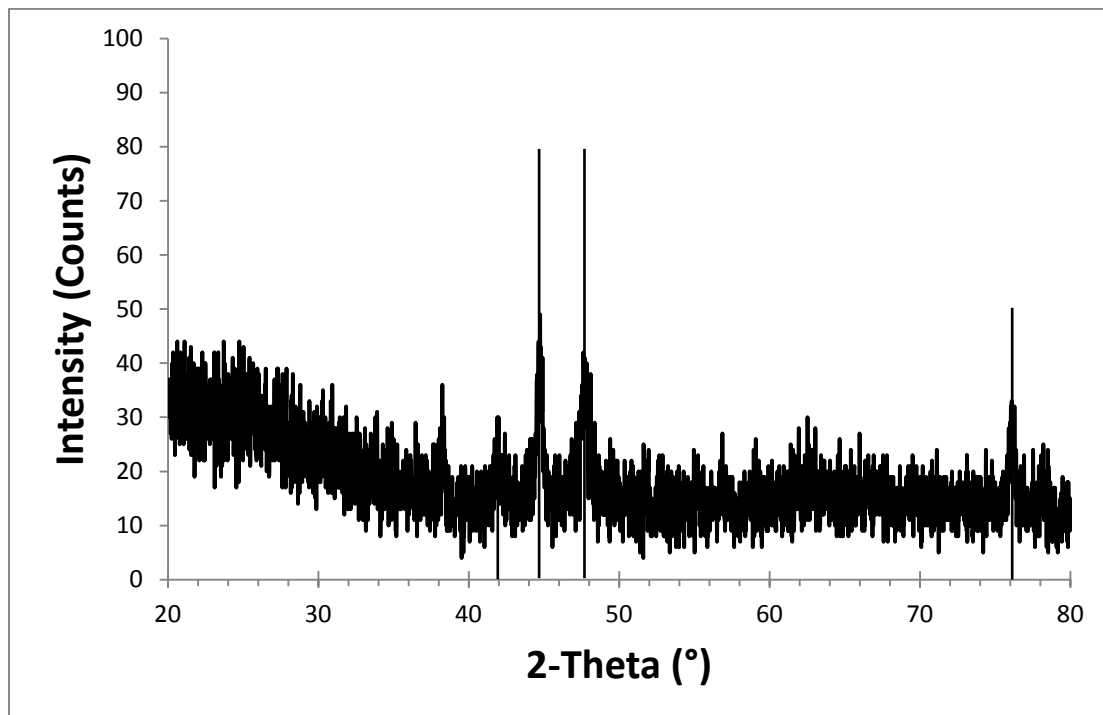
Table 15. Reactivity of **27** and **29** toward reducing agents in tetrahydrofuran: a, ambient temperature; b, upon reflux.

Entry	Reducing agent	CoL ₂ (27)	MnL ₂ (29)
1	NH ₂ NH ₂	Black powder; ^a sticks to stir bar	No change
2	LiAlH ₄	Bubbling, black solution ^a	Bubbling, black solution ^a
3	BH ₃ (NHMe ₂)	Black solution ^b	No change
4	pinacol borane	Black solution ^b	Black solution ^b
5	BH ₃ (SMe ₂)	Black powder; ^b does not stick to stir bar	Became colorless
6	BH ₃ (THF)	Black powder; ^a does not stick to stir bar	Black solution ^b

Figure 30. (a) Powder XRD spectrum of the Co powder obtained from the reaction between **27** and N_2H_4 . The reference spectrum for Co metal is overlaid (JCPDS 05-0727).



(b) Powder XRD spectrum of the Co powder obtained from the reaction between **27** and $\text{BH}_3(\text{SMe}_2)$ after annealing at 600 °C for 4 hours under argon. The reference spectrum for Co metal is overlaid (JCPDS 05-0727).



Precursor Properties of 26–36. The handful of crystallographically characterized Cu and Ni hydrazonate complexes⁸¹ contain N-aryl groups and are thus unlikely to be volatile due to π - π stacking interactions in the solid state. Complexes **26–36** combine good volatilities and high thermal stabilities, and **27** and **29** react readily with several hydride co-reagents to provide metal powders. These properties suggest that **26–36** may be excellent precursors for use in ALD metal film growth.^{12,15} Importantly, **26–30** contain the same ligand, are all monomeric in the solid state, and **27** and **29** are both reduced by hydride co-reagents to the metals. Such similar chemistry should make **26–30** promising precursors for the ALD growth of metal alloy films, such as Cu/Mn alloys for self-forming barrier layers,^{7,87} since ALD growth of metal alloys requires overlap of the self-limited growth temperature ranges for the separate metals.^{12,15} The properties of **26–36** can be compared with several classes of previously reported ALD precursors. The carbohydrazide complexes $M(\text{Me}_2\text{NNC}(\text{tBu})\text{O})_2$ ($M = \text{Cu}, \text{Ni}, \text{Co}$) sublime between 70 and 80 °C at 0.05 Torr, and have solid state decomposition temperatures of 255 (Cu), 245 (Co), and 325 °C (Ni).⁶⁹ These complexes are more volatile than **26–36** and have similar to slightly higher thermal stabilities than **26–36**. However, $\text{Cr}(\text{Me}_2\text{NNCHC}(\text{tBu})\text{O})_2$ is not volatile and the Fe(II) and Mn(II) analogs are dimeric and non-volatile.⁶⁹ Few related complexes have been evaluated for their potential to serve as ALD precursors. The β -ketoiminate complexes $M(\text{iPrNCMeCHCMeO})_2$ ($M = \text{Cu},$ ^{67a} Fe ⁸⁸) have been reported. $\text{Cu}(\text{iPrNCMeCHCMeO})_2$ sublimates at 80 °C/0.01 Torr, is reduced to Cu metal in solution by diethyl zinc, but appears to decompose thermally at about 200 °C as inferred from the TGA trace.^{67a} The β -diketimate complex $\text{Cu}(\text{MeNCMeCHCMeNMe})_2$ sublimates at 80 °C/0.01 Torr with concurrent decomposition.^{67a}

4.3 Conclusions

The hydrazone complexes **26–36** were prepared by treatment of anhydrous metal(II) chlorides with K(tBuNNCHCtBuO), K(tBuNNCHCiPrO), or K(tBuNNCMeCMeO). Crystal structure determinations of **27**, **31**, **32**, and **34–36** revealed monomeric complexes with tetrahedral geometries about the metal centers, and the similar magnetic moment data in solution and the solid state for **26**, **28**, **29**, **30**, and **33** suggest monomeric, tetrahedral structures. The six-membered rings formed upon bidentate coordination of hydrazone ligand to the metal ions are sufficiently bulky to block dimerization of the larger metal ions and protect the metal centers from intermolecular decomposition pathways. A combination of preparative sublimations, thermogravimetric analyses, solid state decomposition studies, and solution reactions with reducing co-reagents suggest that **26–36** are promising precursor for the growth of the respective metals in ALD film growth processes.

4.4 Experimental Section

General Considerations. All manipulations were carried out under argon using either Schlenk or glove box techniques, except that the ligands were prepared in ambient atmosphere. Tetrahydrofuran was distilled from sodium benzophenone ketyl, and hexane was distilled from P₂O₅. Anhydrous transition metal chlorides (CrCl₂, MnCl₂, FeCl₂, CoCl₂, and NiCl₂) were obtained from Strem Chemicals Inc. and were used as received. NiCl₂•CH₃CN was prepared according to a literature procedure.⁷¹ Potassium hydride (30 wt% dispersion in mineral oil; washed with hexane before use) was purchased from Sigma-Aldrich. *tert*-Butyl hydrazine hydrochloride and 3-methylbutanal were purchased from Acros Organics. Pinacolone, SeO₂, and 2,3-butanedione were purchased from Alfa Aesar. 3,3-Dimethyl-2-oxobutanal⁷³ and 3-methyl-2-

oxobutanal⁷² were prepared using published procedures. The reducing co-reagents were obtained from Sigma-Aldrich, Alfa Aesar, or Strem Chemicals Inc. and were used as received.

¹H and ¹³C{¹H} NMR spectra were obtained at 400 and 100 MHz, respectively, in C₆D₆ or CDCl₃ as indicated and were referenced to the residual proton and carbon resonances of the solvents. Infrared spectra were obtained using Nujol as the medium. Magnetic moments were determined in the solid state using a Johnson Mathey magnetic susceptibility apparatus, and by ¹H NMR in benzene solution using the Evans method.⁷¹ Melting points were determined on a Thermo Scientific Mel-Temp 3.0 digital melting point apparatus and are uncorrected. TGA and DTA were carried out with a SDT-2960 TGA/DTA instrument at a rate of 10 °C/min.

Preparation of 1-(2-*tert*-Butyl)hydrazono-3,3-dimethylbutan-2-one (L⁶H). A 100 mL round-bottomed flask was charged with a magnetic stir bar, 3,3-dimethyl-2-oxobutanal (1.00 g, 8.76 mmol), and methanol (15 mL). To this stirred solution at ambient temperature was slowly added a mixture of *tert*-butyl hydrazine hydrochloride (1.11 g, 8.76 mmol) and potassium hydroxide (0.578 g, 8.76 mmol) in methanol (20 mL). This solution was stirred for 6 h. The volatile components were removed under reduced pressure. Light yellow crystals of L⁶H were obtained upon sublimation of the crude solid at 60 °C/0.05 Torr (1.08 g, 67%): mp 70 °C; ¹H NMR (C₆D₆, 23 °C, δ) 13.01 (s, broad 1H, NH), 7.12 (s, 1H, CHN), 1.11 (s, 9H, C(CH₃)₃), 1.05 (s, 9H, C(CH₃)₃); ¹³C{¹H} NMR (C₆D₆, 23 °C, ppm) 201.22 (s, CO), 119.37 (s, CHN), 54.76 (s, C(CH₃)₃), 41.68 (s, C(CH₃)₃), 28.52 (s, C(CH₃)₃), 27.04 (s, C(CH₃)₃); ESI-HRMS calcd for C₁₀H₂₁N₂O ([M+H]⁺) 185.1656, found 185.1654.

Preparation of 1-(2-*tert*-Butyl)hydrazono-3-methylbutan-2-one. (L⁷H). A 100 mL round-bottomed flask was charged with a magnetic stir bar, 3-methyl-2-oxobutanal (1.00 g, 9.99 mmol), and methanol (15 mL). To this stirred solution at ambient temperature was slowly added

a mixture of *tert*-butyl hydrazine hydrochloride (1.24 g, 9.99 mmol) and potassium hydroxide (0.659 g, 9.99 mmol) in methanol (20 mL). This solution was stirred for 6 h. The volatile components were removed under reduced pressure, and the resultant yellow oily solid was dissolved in diethyl ether (15 mL). This solution was dried over anhydrous Na₂SO₄ and filtered. The volatile components were then removed under reduced pressure and the resultant yellow oil was vacuum distilled. L⁷H was obtained as a yellow liquid that distilled at 48 °C/0.05 Torr (0.935 g, 55%): ¹H NMR (CDCl₃, 23 °C, δ) 6.86 (s, 1H, CHN), 6.63 (s, broad 1H, NH), 3.49 (septet, J = 7.0 Hz, 1H, CH(CH₃)₂), 1.25 (s, 9H, C(CH₃)₃), 1.08 (d, 6H, J = 7.0 Hz, CH(CH₃)₂); ¹³C{¹H} NMR (CDCl₃, 23 °C, ppm) 203.69 (s, CO), 131.86 (s, CHN), 54.91 (s, C(CH₃)₃), 33.98 (s, CH(CH₃)₂), 28.68 (s, C(CH₃)₃), 19.00 (s, CH(CH₃)₂); ESI-HRMS calcd for C₉H₁₉N₂O ([M+H]⁺) 171.1497, found 171.1497.

Preparation of 3-(2-*tert*-Butylhydrazono)butan-2-one (L⁸H). A 100 mL round-bottomed flask was charged with a magnetic stir bar, 2,3-butanedione (1.000 g, 11.62 mmol), and water (15 mL). To this stirred solution at ambient temperature was slowly added a mixture of *tert*-butyl hydrazine hydrochloride (1.448 g, 11.62 mmol) and potassium hydroxide (0.767 g, 11.62 mmol) in water (20 mL). This solution was allowed to stand for 2 h, during which time the initially formed oil turned to a solid. This solution was filtered and the solid was dissolved in diethyl ether (10 mL) and allowed to crystallize at -23 °C over 24 h. Colorless crystals were obtained by bulb-to-bulb distillation of the crystals obtained from diethyl ether at 60 °C/0.05 Torr (0.926 g, 51%): mp 58 °C; ¹H NMR (CDCl₃, 23 °C, δ) 5.69 (s, broad 1H, NH), 2.28 (s, 3H, C(CH₃)), 1.73 (s, 3H, C(CH₃)), 1.25 (s, 9H, C(CH₃)₃); ¹³C{¹H} NMR (CDCl₃, 23 °C, ppm) 197.16 (s, CO), 139.35 (s, CHN), 54.73 (s, C(CH₃)₃), 28.82 (s, C(CH₃)₃), 23.73 (s, C(CH₃)), 6.77 (s, C(CH₃)); ESI-HRMS calcd for C₈H₁₇N₂O ([M+H]⁺) 157.1342, found 157.1341.

Preparation of Ni(L⁶)₂ (26). A 100 mL Schlenk flask was charged with a magnetic stir bar, L⁶H (1.00 g, 5.43 mmol), and tetrahydrofuran (30 mL). To this stirred solution at ambient temperature was slowly added KH (0.239 g, 5.97 mmol), and solution was stirred for 4 h. This solution was then slowly added dropwise with a cannula to a stirred suspension of anhydrous NiCl₂•CH₃CN (0.456 g, 2.71 mmol) in tetrahydrofuran (40 mL) at -78 °C. The resultant dark orange solution was stirred for 15 h at ambient temperature. The volatile components were then removed under reduced pressure, and the resultant dark orange powder was dissolved in hexane (60 mL). The solution was filtered through a 1 cm pad of Celite on a coarse glass frit, and the volatile components were then removed under reduced pressure. Dark orange crystals of **26** (0.749 g, 65%) were obtained by sublimation at 120 °C/0.05 Torr: mp 157 °C; IR (Nujol, cm⁻¹) 1485 (m), 1362 (m), 1332 (s), 1264 (m), 1246 (m), 1221 (m), 1187 (m), 1116 (m), 1034 (w), 1019 (w), 996 (w), 892 (w), 803 (w); ¹H NMR (C₆D₆, 23 °C, δ) 15.35 (s, broad, 2H, C(H)N), 5.99 (s, 18H, broad, C(CH₃)₃), -1.24 (s, broad, 18H, C(CH₃)₃); μ_{eff} = 2.88 and 2.93 μ_B in the solid state and in benzene solution, respectively. Anal. Calcd for C₂₀H₃₈NiN₄O₂: C, 56.49; H, 9.01; N, 13.18. Found: C, 56.49; H, 8.88; N, 13.07.

Preparation of Co(L⁶)₂ (27). In a fashion similar to the preparation of **26**, treatment of anhydrous CoCl₂ (0.350 g, 2.71 mmol) in tetrahydrofuran (40 mL) with a solution of KL⁶ (prepared from L⁶H (1.00 g, 5.43 mmol) and KH (0.239 g, 5.97 mmol) in tetrahydrofuran (30 mL)) for 15 h at ambient temperature afforded **27** (0.904 g, 80%) as red crystals upon sublimation at 130 °C/0.05 Torr: mp 162–164 °C; IR (Nujol, cm⁻¹) 1483 (m), 1462 (s), 1362 (m), 1334 (s), 1264 (m), 1248 (m), 1221 (m), 1189 (m), 1109 (m), 1033 (w), 1018 (w), 995 (w), 894 (w), 805 (m); μ_{eff} = 4.02 and 3.94 μ_B in the solid state and in benzene solution, respectively. Anal. Calcd for C₂₀H₃₈CoN₄O₂: C, 56.46; H, 9.00; N, 13.17. Found: C, 56.49; H, 8.86; N, 13.14.

Preparation of Fe(L⁶)₂ (28). In a fashion similar to the preparation of **26**, treatment of anhydrous FeCl₂ (0.349 g, 2.71 mmol) in tetrahydrofuran (40 mL) with a solution of KL⁶ (prepared from L⁶H (1.00 g, 5.43 mmol) and KH (0.239 g, 5.97 mmol) in tetrahydrofuran (30 mL)) for 15 h at ambient temperature afforded **28** (0.913 g, 83%) as red crystals upon sublimation at 120 °C/0.05 Torr: mp 177–179 °C; IR (Nujol, cm⁻¹) 1492 (m), 1361 (m), 1331 (s), 1264 (m), 1248 (w), 1221 (w), 1187 (m), 1109 (m), 1033 (w), 1019 (w), 991 (w), 892 (w), 822 (w), 808 (w); $\mu_{\text{eff}} = 4.82$ and $4.86 \mu_{\text{B}}$ in the solid state and in benzene solution, respectively. Anal. Calcd for C₂₀H₃₈FeN₄O₂: C, 56.87; H, 9.07; N, 13.26. Found: C, 56.78; H, 8.98; N, 13.16.

Preparation of Mn(L⁶)₂ (29). In a fashion similar to the preparation of **26**, treatment of anhydrous MnCl₂ (0.340 g, 2.71 mmol) in tetrahydrofuran (40 mL) with a solution of KL⁶ (prepared from L⁶H (1.00 g, 5.43 mmol) and KH (0.239 g, 5.97 mmol) in tetrahydrofuran (30 mL)) for 15 h at ambient temperature afforded **29** (0.774 g, 68%) as dark orange crystals upon sublimation at 135 °C/0.05 Torr: mp 169–171 °C; IR (Nujol, cm⁻¹) 1498 (m), 1484 (m), 1363 (m), 1333 (s), 1261 (m), 1220 (w), 1187 (m), 1106 (m), 1090 (w), 1031 (w), 1017 (w), 987 (w), 889 (w), 800 (w); $\mu_{\text{eff}} = 5.73$ and $5.71 \mu_{\text{B}}$ in the solid state and in benzene solution, respectively. Anal. Calcd for C₂₀H₃₈MnN₄O₂: C, 56.99; H, 9.09; N, 13.29. Found: C, 57.23; H, 9.06; N, 13.36.

Preparation of Cr(L⁶)₂ (30). In a fashion similar to the preparation of **26**, treatment of anhydrous CrCl₂ (0.334 g, 2.71 mmol) in tetrahydrofuran (40 mL) with a solution of KL⁶ (prepared from L⁶H (1.00 g, 5.43 mmol) and KH (0.239 g, 5.97 mmol) in tetrahydrofuran (30 mL)) for 15 h at ambient temperature afforded **30** (0.726 g, 64%) as dark orange crystals upon sublimation at 130 °C/0.05 Torr: mp 274–276 °C; IR (Nujol, cm⁻¹) 1507 (m), 1495 (m), 1418 (m), 1364 (s), 1347 (s), 1261 (w), 1219 (w), 1183 (m), 1164 (m), 1115 (m), 1021 (w), 987 (w), 947 (w), 885 (w), 793 (w); $\mu_{\text{eff}} = 2.73$ and $2.91 \mu_{\text{B}}$ in the solid state and in benzene solution,

respectively. Anal. Calcd for $C_{20}H_{38}CrN_4O_2$: C, 57.39; H, 9.15; N, 13.39. Found: C, 57.54; H, 9.23; N, 13.41.

Preparation of $Ni(L^7)_2$ (31). In a fashion similar to the preparation of **26**, treatment of anhydrous $NiCl_2 \cdot CH_3CN$ (0.495 g, 2.93 mmol) in tetrahydrofuran (40 mL) with a solution of KL^7 (prepared from L^7H (1.00 g, 5.87 mmol) and KH (0.259 g, 6.46 mmol) in tetrahydrofuran (30 mL)) for 15 h at ambient temperature afforded **31** (0.724 g, 63%) as dark orange crystals upon sublimation at 100 °C/0.05 Torr: mp 92–94 °C; IR (Nujol, cm^{-1}) 1504 (m), 1481 (m), 1363 (s), 1338 (m), 1307 (s), 1262 (m), 1221 (w), 1190 (m), 1120 (m), 1092 (m), 1049 (w), 1022 (w), 999 (w), 802 (m); 1H NMR (C_6D_6 , 23 °C, δ) 16.22 (s, broad), 4.74 (s, broad); $\mu_{eff} = 3.00$ and $3.01 \mu_B$ in the solid state and in benzene solution, respectively. Anal. Calcd for $C_{18}H_{34}NiN_4O_2$: C, 54.43; H, 8.63; N, 14.11. Found: C, 54.63; H, 8.55; N, 14.12.

Preparation of $Co(L^7)_2$ (32). In a fashion similar to the preparation of **26**, treatment of anhydrous $CoCl_2$ (0.380 g, 2.93 mmol) in tetrahydrofuran (40 mL) with a solution of KL^7 (prepared from L^7H (1.00 g, 5.87 mmol) and KH (0.259 g, 6.46 mmol) in tetrahydrofuran (30 mL)) for 15 h at ambient temperature afforded **32** (0.989 g, 86%) as red crystals upon sublimation at 100 °C /0.05 Torr: mp 109–111 °C; IR (Nujol, cm^{-1}) 1493 (m), 1478 (m), 1364 (m), 1337 (m), 1305 (s), 1264 (w), 1219 (w), 1190 (m), 1113 (m), 1092 (m), 1048 (w), 1021 (w), 998 (w), 913 (w), 865 (w), 807 (m); $\mu_{eff} = 3.97$ and $3.78 \mu_B$ in the solid state and in benzene solution, respectively. Anal. Calcd for $C_{18}H_{34}CoN_4O_2$: C, 54.40; H, 8.62; N, 14.10. Found: C, 54.60; H, 8.74; N, 14.13.

Preparation of $Fe(L^7)_2$ (33). In a fashion similar to the preparation of **26**, treatment of anhydrous $FeCl_2$ (0.371 g, 2.93 mmol) in tetrahydrofuran (40 mL) with a solution of KL^7 (prepared from L^7H (1.00 g, 5.87 mmol) and KH (0.259 g, 6.46 mmol) in tetrahydrofuran (30

mL)) for 15 h at ambient temperature afforded **33** (0.862 g, 75%) as red crystals upon sublimation at 105 °C /0.05 Torr: mp 114–116 °C; IR (Nujol, cm^{-1}) 1488 (m), 1359 (s), 1334 (m), 1302 (s), 1262 (m), 1209 (m), 1189 (m), 1114 (m), 1091 (m), 994 (w), 910 (w), 807 (m); $\mu_{\text{eff}} = 5.14$ and $4.73 \mu_{\text{B}}$ in the solid state and in benzene solution, respectively. Anal. Calcd for $\text{C}_{18}\text{H}_{34}\text{FeN}_4\text{O}_2$: C, 54.82; H, 8.69; N, 14.21. Found: C, 54.92; H, 8.58; N, 14.22.

Preparation of $\text{Ni}(\text{L}^8)_2$ (34**).** In a fashion similar to the preparation of **26**, treatment of anhydrous $\text{NiCl}_2 \cdot \text{CH}_3\text{CN}$ (0.543 g, 3.22 mmol) in tetrahydrofuran (40 mL) with a solution of KL^8 (prepared from L^8H (1.00 g, 6.44 mmol) and KH (0.284 g, 7.08 mmol) in tetrahydrofuran (30 mL)) for 15 h at ambient temperature afforded **34** (0.394 g, 34 %) as dark orange crystals upon sublimation at 100 °C /0.05 Torr: mp 120–122 °C; IR (Nujol, cm^{-1}) 1500 (m), 1405 (s), 1357 (s), 1302 (s), 1263 (s), 1237 (m), 1222 (m), 1185 (s), 1148 (s), 1043 (w), 980 (m), 931 (w), 805 (w), 752 (w); ^1H NMR (C_6D_6 , 23 °C, δ) 68.51 (s, 6H, $\text{C}(\text{CH}_3)\text{O}$), 14.70 (s, 18H, $\text{C}(\text{CH}_3)_3$), -34.24 (s, 6H, $\text{C}(\text{CH}_3)\text{N}$); $\mu_{\text{eff}} = 2.75$ and $2.67 \mu_{\text{B}}$ in the solid state and in benzene solution, respectively. Anal. Calcd for $\text{C}_{16}\text{H}_{30}\text{NiN}_4\text{O}_2$: C, 52.06; H, 8.19; N, 15.18. Found: C, 52.20; H, 8.21; N, 15.06.

Preparation of $\text{Co}(\text{L}^8)_2$ (35**).** In a fashion similar to the preparation of **26**, treatment of anhydrous CoCl_2 (0.418 g, 3.22 mmol) in tetrahydrofuran (40 mL) with a solution of KL^8 (prepared from L^8H (1.00 g, 6.44 mmol) and KH (0.284 g, 7.08 mmol) in tetrahydrofuran (30 mL)) for 15 h at ambient temperature afforded **35** (0.336 g, 29%) as red crystals upon sublimation at 100 °C/0.05 Torr: mp 142–145 °C; IR (Nujol, cm^{-1}) 1494 (m), 1401 (m), 1359 (m), 1303 (s), 1262 (m), 1231 (w), 1187 (w), 1148 (m), 981 (m), 801 (w), 751 (w); $\mu_{\text{eff}} = 3.95$ and $3.69 \mu_{\text{B}}$ in the solid state and in benzene solution, respectively. Anal. Calcd for $\text{C}_{16}\text{H}_{30}\text{CoN}_4\text{O}_2$: C, 52.03; H, 8.19; N, 15.17. Found: C, 52.14; H, 8.17; N, 15.18.

Preparation of $\text{Fe}(\text{L}^8)_2$ (36**).** In a fashion similar to the preparation of **26**, treatment of anhydrous FeCl_2 (0.408 g, 3.22 mmol) in tetrahydrofuran (40 mL) with a solution of KL^8 (prepared from L^8H (1.00 g, 6.44 mmol) and KH (0.284 g, 7.08 mmol) in tetrahydrofuran (30 mL)) for 15 h at ambient temperature afforded **36** (0.313 g, 27%) as red crystals upon sublimation at 100 °C /0.05 Torr: mp 120–122 °C; IR (Nujol, cm^{-1}) 1401 (m), 1361 (m), 1299 (m), 1261 (w), 1227 (w), 1188 (m), 1147 (w), 983 (w), 800 (w), 750 (w); $\mu_{\text{eff}} = 4.80$ and $4.65 \mu_{\text{B}}$ in the solid state and in benzene solution, respectively. Anal. Calcd for $\text{C}_{16}\text{H}_{30}\text{FeN}_4\text{O}_2$: C, 52.47; H, 8.26; N, 15.30. Found: C, 52.39; H, 7.99; N, 15.32.

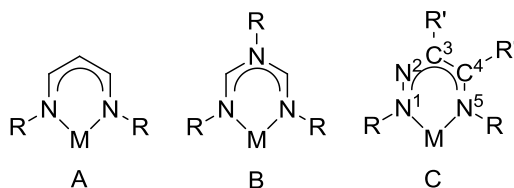
CHAPTER 5

**Volatility and High Thermal Stability in Mid to Late First Row Transition Metal
Complexes Containing 1,2,5-Triazapentadienyl Ligands**

5.1 Introduction

Metal complexes containing β -diketiminate ligands have been widely explored.⁸⁹ The κ^2 -coordination mode through the nitrogen atoms is most common (Chart 10, A), and the steric and electronic nature of the ligand can be tuned through variation of the nitrogen and carbon atom substituents. Recently, there have been many reports of late transition metal complexes containing related 1,3,5-triazapentadienyl ligands.^{90,91} In addition to the terminal κ^2 -coordination mode to the 1- and 5-nitrogen atoms (Chart 10, B), coordination of 1,3,5-triazapentadienyl ligands can also occur at the 3-nitrogen atom, leading to new terminal and bridging coordination modes.^{90,91} Complexes containing the isomeric 1,2,5-triazapentadienyl ligands are rare (Chart 10, C), and are limited to a few Ni(II) and Cu(II) complexes containing 1-phenyl, 3-acyl or 3-benzoyl, and 5-alkyl substituents,⁹² although the 1,2,5-triazapentadienyl ligand core is also found within more complex chelating ligands.⁹³

Chart 10. β -Diketiminato (A), 1,3,5-triazapentadienyl (B), and 1,2,5-triazapentadienyl (C) ligands.

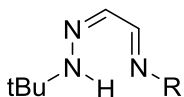


Winter has reported the synthesis and properties of some main group metal complexes that contain β -diketiminate ligands,⁹⁴ and others have examined the use of β -diketiminate

complexes for the CVD and ALD growth of Cu metal films.^{54,67} However, group 2 and Cu complexes containing β -diketiminato ligands have generally low thermal stabilities and may not be appropriate for widespread use as ALD precursors.^{54,67}

In this chapter, the synthesis, structure, volatility, and thermal stability of a series of Ni(II), Co(II), Fe(II), Mn(II), and Cr(II) complexes that contain 1,2,5-triazapentadienyl ligands (Chart 11) are described. These complexes adopt tetrahedral, monomeric structures, exhibit good volatilities and very high thermal stabilities, and thus have excellent properties for use as ALD precursors. Additionally, 1,2,5-triazapentadienyl ligands are easily prepared with a variety of nitrogen and carbon atom substituents, and should uniquely complement the rapidly expanding chemistry of metal complexes with β -diketiminato and 1,3,5-triazapentadienyl ligands.⁸⁹⁻⁹¹

Chart 11. Chemical Structures of L⁹H and L¹⁰H.

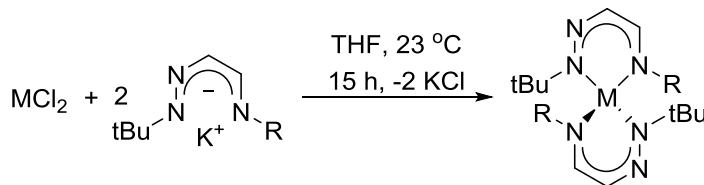


L⁹H, R = tBu

L¹⁰H, R = NMe₂

4.2 Results and Discussion

Synthetic Aspects. The protonated ligand precursors were prepared as described in the Experimental Section through stepwise treatment of glyoxal with tBuNHNH₂/tBuNH₂ or Me₂NNH₂/tBuNHNH₂. Treatment of the protonated ligands with KH in tetrahydrofuran, followed by addition of anhydrous MCl₂, afforded complexes **37–45** upon sublimation (Scheme 6). These complexes were characterized by spectral and analytical methods, and by X-ray crystallography as described below. All of the new complexes are paramagnetic in solution and exhibited very broad resonances in the ¹H NMR spectra. Magnetic moments for **37–45** in the solid state and in solution were consistent with high spin, tetrahedral geometries.

Scheme 6. Synthesis of **37–45**.

37 , M = Ni, R = tBu, 35%	42 , M = Ni, R = NMe ₂ , 23%
38 , M = Co, R = tBu, 57%	43 , M = Co, R = NMe ₂ , 27%
39 , M = Fe, R = tBu, 73%	44 , M = Fe, R = NMe ₂ , 18%
40 , M = Mn, R = tBu, 54%	45 , M = Mn, R = NMe ₂ , 32%
41 , M = Cr, R = tBu, 55%	

X-Ray Crystal Structures. The X-ray crystal structures of **37–43** were obtained to establish the solid state configurations. Experimental crystallographic data are summarized in Table 16 and selected bond lengths and angles are presented in Table 17. Complexes **37–41** exhibit merohedral twinning, which leads to inherent 50/50 occupancy of the core N²/C⁴ atoms. Such disorder is not present in **42** and **43** due to the asymmetric ligand substitution, and the structures of **42** and **43** are presented in Figures 31 and 32. The structure of **42** is described here and it presents the typical structural features for **37–43**. Complex **42** is monomeric and four-coordinate, contains κ²-1,2,5-triazapentadienyl ligands bound through the 1- and 5-nitrogen atoms, and has distorted tetrahedral geometry about the Ni ion as exemplified by the 84.0° angle between the best planes of the NiN₃C₂ groups. The Ni–N bond lengths range between 1.932(3) and 1.969(3) Å, which are similar to other tetrahedral, high spin Ni(II) complexes containing κ²-β-diketimate ligands.⁹⁵ The intraligand N–Ni–N angles are 92.7(1) and 92.8(1)°, while the corresponding interligand angles range between 112.3(1) and 122.0(1)°. Within the NiN₃C₂ ligand cores, the N–N bond lengths are 1.314(4) and 1.307(4) Å, the N–C distances are between 1.304(5) and 1.322(5), and the C–C bond lengths are 1.414(2) and 1.415(2) Å. These values are in between N–N, C–N, and C–C single and double bonds, and suggest delocalized, monoanionic 1,2,5-triazapentadienyl ligands.

Table 16. Experimental crystallographic data for **42** and **43**.

	42	43
Formula	C ₁₆ H ₃₄ NiN ₈	C ₁₆ H ₃₄ CoN ₈
FW	397.22	397.44
Space group	P1	P1
a (Å)	8.8652(8)	8.8829(12)
b (Å)	8.9505(7)	8.9541(12)
c (Å)	14.3752(13)	14.462(2)
V (Å ³)	1011.59(16)	1022.0(2)
Z	2	2
T (K)	100(2)	100(2)
λ (Å)	0.71073	0.71073
ρ _{calc} (g cm ⁻³)	1.304	1.291
μ (mm ⁻¹)	0.975	0.856
R(F) ^a (%)	7.19	2.61
Rw(F) ^b (%)	20.21	6.84

$$^a R(F) = \frac{\sum ||F_o| - |F_c||}{\sum |F_o|}$$

$$^b R_w(F)^2 = \left[\frac{\sum w(F_o^2 - F_c^2)^2}{\sum w(F_o^2)^2} \right]^{1/2}$$

Table 17. Selected bond lengths (Å) and angles (°) for **42** and **43**.

	42	43
M–N	1.932(3)	1.9514(10)
	1.949(3)	1.9600(10)
	1.952(3)	1.9658(10)
	1.969(3)	1.9892(11)
C–N _{core}	1.304(4)	1.3123(15)
	1.309(5)	1.3140(15)
	1.319(5)	1.3264(17)
	1.322(5)	1.3332(16)
C–C _{core}	1.415(5)	1.3112(14)
	1.414(5)	1.4082(17)
N _{core} –N _{core}	1.307(4)	1.3112(14)
	1.314(4)	1.3143(14)
N–M–N	92.83(12)	95.38(4)
	92.68(12)	96.22(4)
	117.70(13)	111.58(4)
	112.26(12)	116.15(4)
	121.77(13)	119.37(4)
	122.03(12)	119.76(4)

Figure 31. Perspective view of **42** with thermal ellipsoids at the 50% probability level.

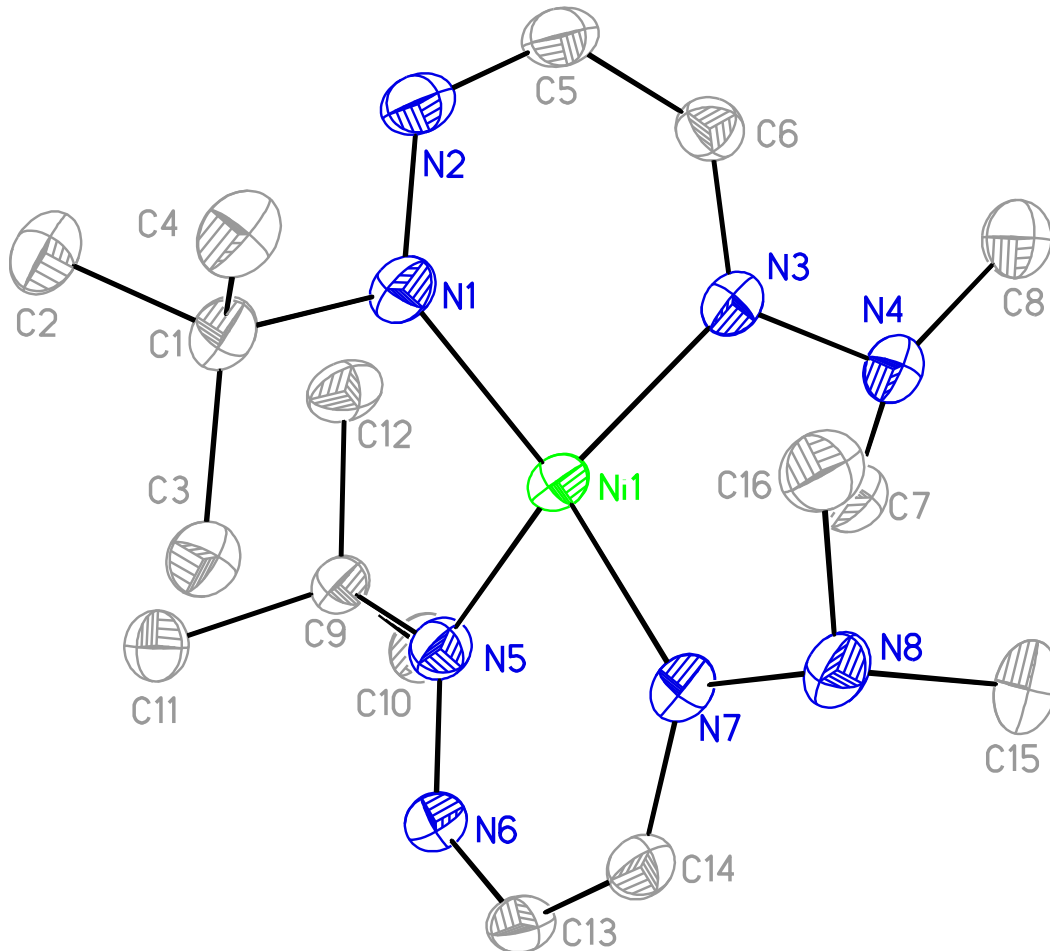
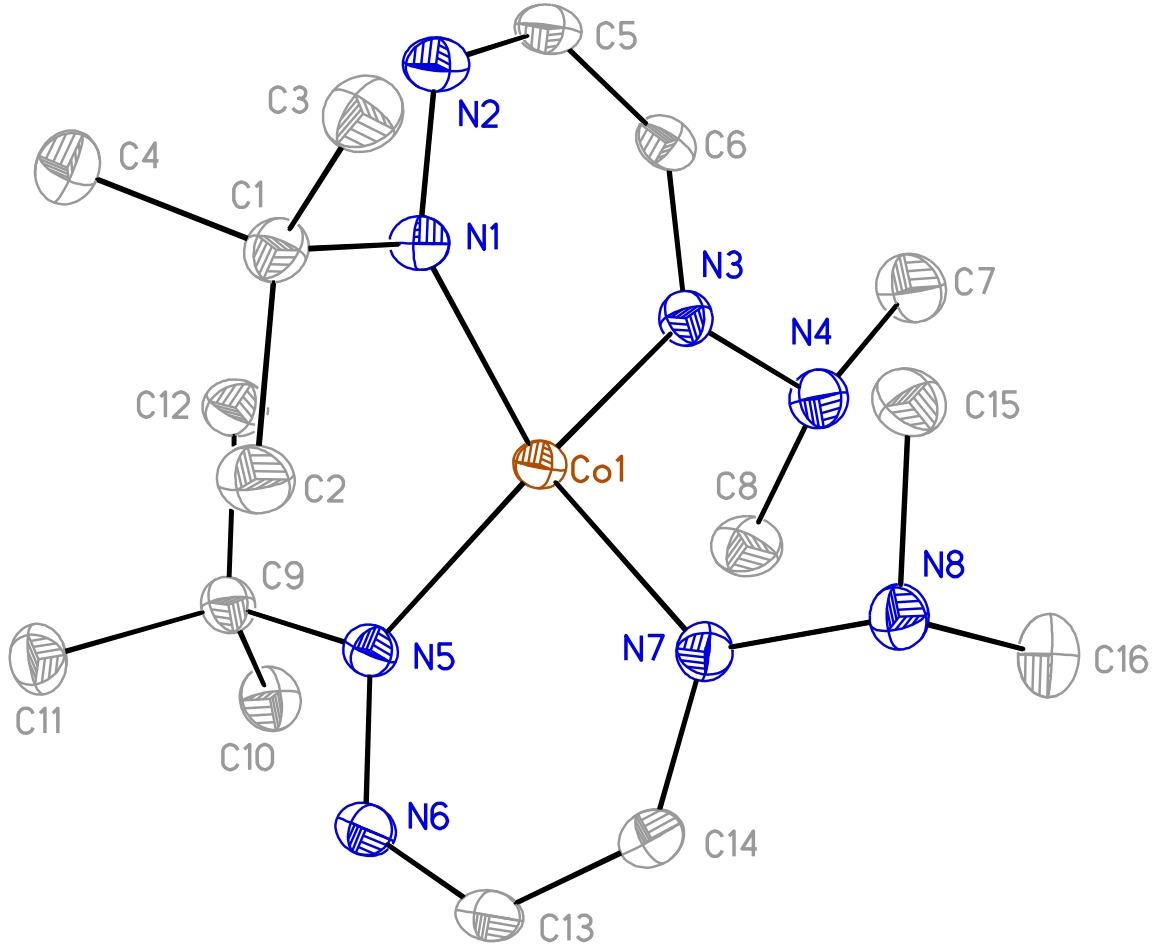


Figure 32. Perspective view of **43** with thermal ellipsoids at the 50% probability level.



Volatility, Thermal Stability, and Screening of Reducing Co-Reagents. To assess the suitability of **37–45** for use as ALD precursors, their volatilities and thermal stabilities were determined by preparative sublimation experiments, solid state decomposition point measurements, and TGA. Complexes **37–41** sublime on ~0.5 g scales over 2–3 hours with <2% nonvolatile residues between 155 and 175 °C at 0.05 Torr, whereas the N-dimethylamino complexes **42–45** sublime at 105 °C under similar conditions (Table 18). Winter has previously demonstrated that Mg and Ca β -diketimate complexes containing N-dimethylamino groups sublime at considerably lower temperatures than analogous complexes containing *tert*-butyl or isopropyl substituents.^{94a,b} The lower sublimation temperatures in the former complexes were attributed to intermolecular lone pair-lone pair repulsions between the non-bonded dimethylamino groups, which lowers the lattice energies and thereby increases the volatilities. Complexes **42–45** have melting points that are close to the sublimation temperatures, hence, these complexes evaporate from the liquid state. Liquid precursors are highly desirable in ALD to promote steady vapor phase delivery and to avoid particle incorporation into the growing films.¹² The solid state decomposition temperatures of **37–41** range between 280 and 310 °C, which are extraordinarily high for complexes containing these elements. High thermal stability is desirable for ALD precursors, since thermal decomposition of the precursor usually signals loss of the self-limited growth mechanism and onset of CVD-like growth.¹² Complexes **42–45** have decomposition temperatures that range between 181 and 225 °C, which are much lower than those of **37–41**. However, **42–45** have much lower sublimation temperatures than **37–41** and their decomposition points are still high enough to be useful in the ALD growth of transition metal thin films.¹² The TGA data for **37–40** (Figure 33) showed single step weight losses and residues of < 10% upon reaching 300 °C, **41** gave poor behavior likely due to its extreme air

sensitivity, and **42–45** (Figure 34) showed single-step weight losses up to about the decomposition temperatures that are shown in Table 18. As a comparison, the Ni(II) amidinate complex Ni(iPrNCMeNiPr)₂ undergoes solid state decomposition at about 180 °C,⁷⁹ whereas the Ni complex **37** decomposes at 290 °C. Additionally, **37–45** do not contain oxygen and have only M–N bonds, which tend to be more reactive than M–O bonds in ALD film growth processes.^{12,79}

Table 18. Volatility and thermal stability data for **37–45**.

Compound	Sublimation Temp. (°C)	Melting Point (°C)	Decomposition Point (°C)
37	155	262	290
38	160	260	296
39	175	275	310
40	165	284	310
41	165	257	280
42	105	99	188
43	105	105	225
44	105	106	181
45	105	108	200

Figure 33. TGA plots of 37–40.

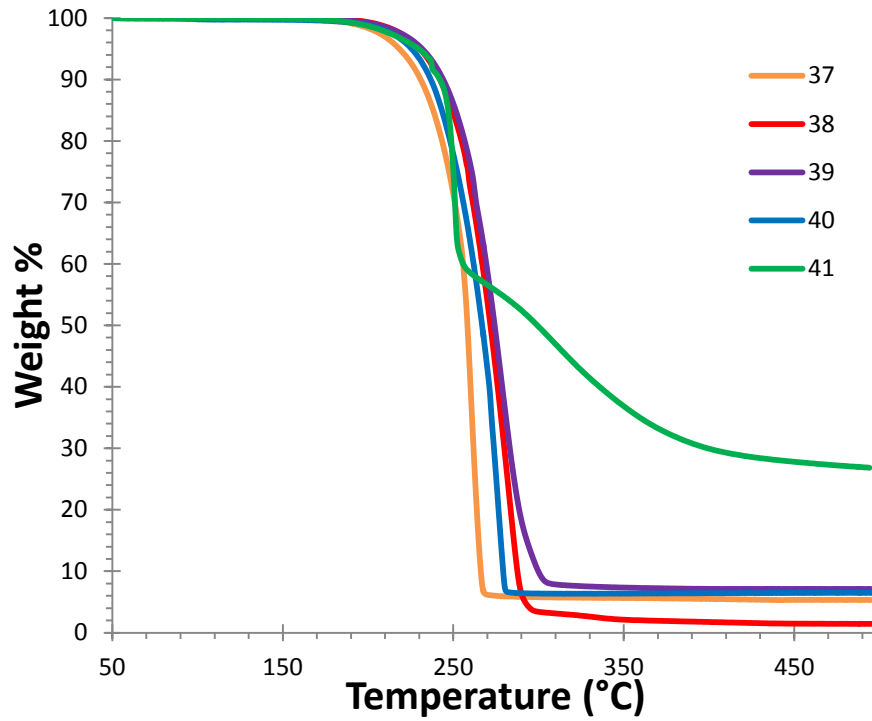
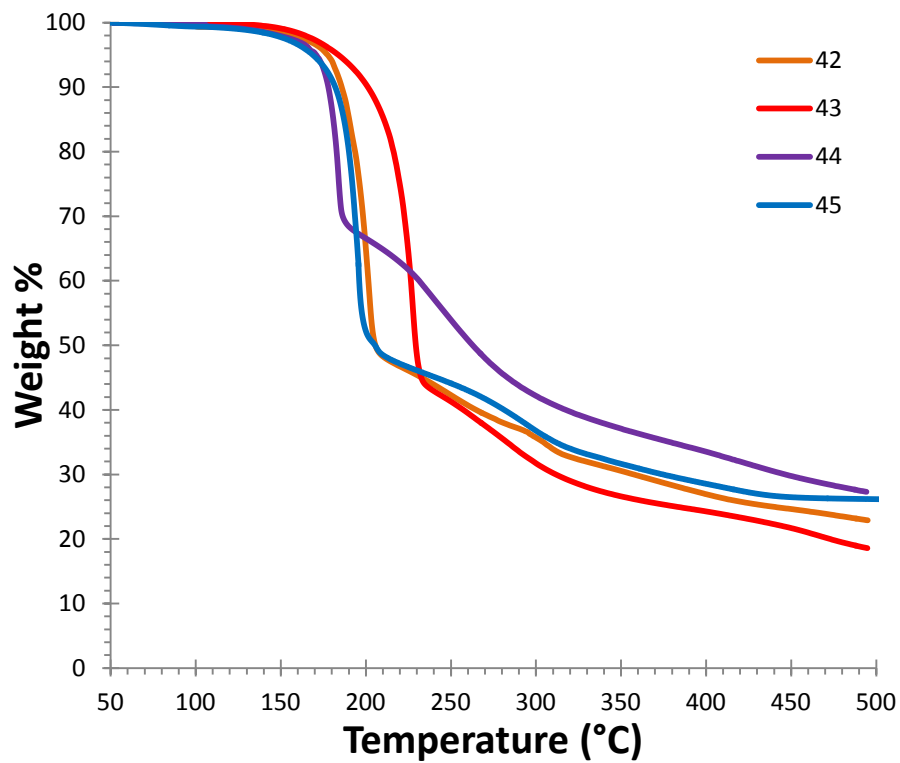
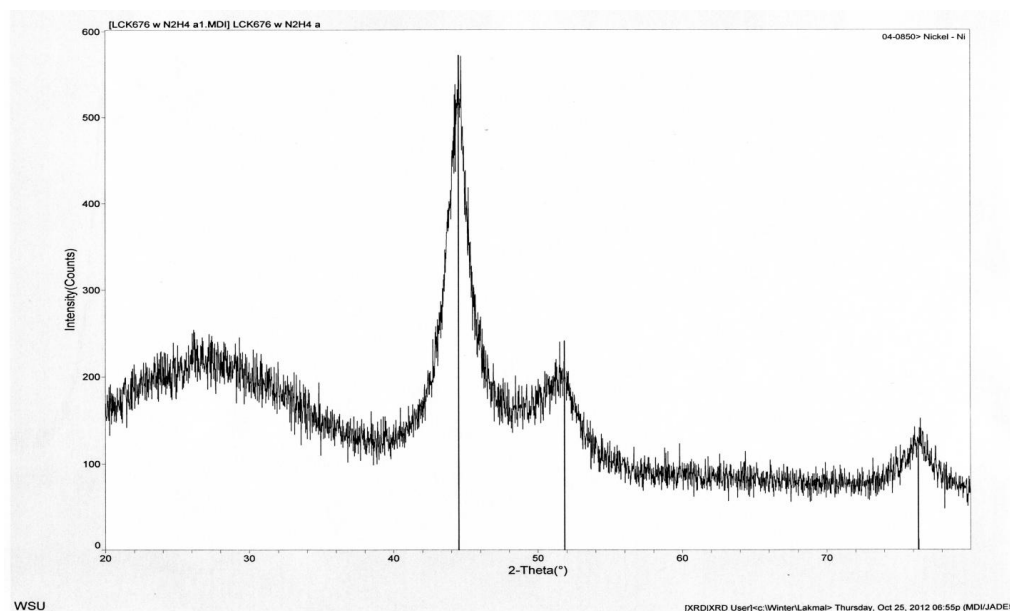


Figure 34. TGA plots of 42–45.



To assess initial viability for use in ALD film growth, **42** was treated with anhydrous hydrazine in tetrahydrofuran at 23 °C. A metallic black precipitate was observed within 0.25 h. The precipitate stuck to the magnetic stir bar and a powder X-ray diffraction spectrum indicated the formation of Ni metal. Hence, **42** is reduced rapidly by hydrazine, and this chemistry may lead to a Ni ALD process. Previous reports have shown that solution reactions are useful in screening precursor pairs for transition metal ALD processes.⁶⁷

Figure 35. Powder XRD spectrum of Ni metal produced upon treatment of **42** with hydrazine. The reference spectrum for Ni metal is overlaid (JCPDS 04-0850).



5.3 Conclusions

This chapter demonstrates that metal complexes containing 1,2,5-triazapentadienyl ligands are easily prepared. The synthetic approach to the ligand precursors is inherently flexible and should allow incorporation of a broad range of ligand core nitrogen and carbon atom substituents. Complexes containing 1,2,5-triazapentadienyl ligands should be electronically distinct from those with β -diketiminato and 1,3,5-triazapentadienyl ligands, since the 1-nitrogen atom is bonded to an electronegative nitrogen atom in the former. In addition to the unique

characteristics of 1,2,5-triazapentadienyl ligands, they afford monomeric, volatile complexes, and have very high thermal decomposition temperatures. As seen in hydrazone precursors, the six-membered rings formed upon ligand coordination to the metal ions are sufficiently bulky to block dimerization of the larger metal ions and protect the metal centers from intermolecular decomposition pathways.

5.4 Experimental Section

General Considerations. All manipulations were carried out under argon using either Schlenk or glove box techniques, except that the ligands were prepared in ambient atmosphere. Tetrahydrofuran was distilled from sodium benzophenone ketyl, and hexane was distilled from P_2O_5 . Anhydrous transition metal chlorides ($CrCl_2$, $MnCl_2$, $FeCl_2$, $CoCl_2$, and $NiCl_2$) were obtained from Strem Chemicals Inc. and used as received. $NiCl_2 \cdot CH_3CN$ was prepared according to a literature procedure.⁷¹ Potassium hydride (30 wt% dispersion in mineral oil; washed with hexane before use), *tert*-butyl amine, and 1,1-dimethylhydrazine were purchased from Sigma-Aldrich. *tert*-Butyl hydrazine hydrochloride was purchased from Acros Organics. Glyoxal was purchased from Alfa Aesar.

1H and $^{13}C\{^1H\}$ NMR spectra were obtained at 400 and 100 MHz in C_6D_6 or $CDCl_3$ and were referenced to the residual proton and the ^{13}C resonances of the solvents. Infrared spectra were obtained using Nujol as the medium. Melting points were obtained on a Thermo Scientific Mel-Temp 3.0 digital melting point apparatus and are uncorrected. TGA were carried out with a SDT-2960 TGA/DTA instrument at a rate of 10 °C/min. Magnetic moments were determined in the solid state using a Johnson Mathey magnetic susceptibility apparatus, and by 1H NMR in benzene solution using the Evans method.⁸⁰

Preparation of 1,5-di-*tert*-butyl-1,2,5-triazapentadiene (L⁹H). 2-(2-(*tert*-Butyl)hydrazono)acetaldehyde was prepared according to a published procedure.⁹⁶ A 100 mL round bottom flask was charged with a magnetic stir bar, 2-(2-(*tert*-butyl)hydrazono)acetaldehyde (1.00 g, 7.80 mmol), and diethyl ether (15 mL). To this stirred solution at ambient temperature was slowly added *tert*-butyl amine (0.83 mL, 7.80 mmol) and the solution was stirred for 4 h. The resultant yellow solution was washed with water (20 mL) and the organic layer was separated. The organic layer was dried over anhydrous Na₂SO₄ and the volatile components were removed under reduced pressure. Light yellow crystals were obtained by sublimation of the crude solid at 80 °C/0.05 Torr (0.786 g, 55%): mp 200 °C; IR (Nujol, cm⁻¹) 3144 (m), 1620 (m), 1547 (m), 1365 (m), 1346 (m), 1304 (w), 1260 (w), 1222 (m) 1166 (m), 1096 (w), 1026 (w), 970 (w), 883 (w), 799 (w); ¹H NMR (CDCl₃, 23 °C, δ) 7.84 (s, 1H, CHN), 7.30 (s, 1H, CHN), 5.28 (s, broad 1H, NH), 1.22 (s, 9H, C(CH₃)₃), 1.21 (s, 9H, C(CH₃)₃); ¹³C{¹H} NMR (CDCl₃, 23 °C, ppm) 155.22 (s, CHN), 137.35 (s, CHN), 56.91 (s, C(CH₃)₃), 54.50 (s, C(CH₃)₃), 29.65 (s, C(CH₃)₃), 28.57 (s, C(CH₃)₃); ESI-HRMS: calcd for C₁₀H₂₂N₃ ([M+H]⁺) 184.1814, found 184.1814.

Preparation of 1-*tert*-butyl-5-dimethylamino-1,2,5-triazapentadiene (L¹⁰H). 2-(2,2-Dimethylhydrazono)acetaldehyde was prepared according to a published procedure.⁹⁷ A 100 mL round bottom flask was charged with a magnetic stir bar, 2-(2,2-dimethylhydrazono)acetaldehyde (1.00 g, 9.98 mmol), and water (20 mL). To this stirred solution at ambient temperature was slowly added a mixture of *tert*-butyl hydrazine hydrochloride (1.37 g, 11.00 mmol) and potassium hydroxide (0.726 g, 11.0 mmol) in water (30 mL). This solution was stirred for 15 min and was set aside for 18 hours. An oil formed initially, which converted to a yellow solid over this time. The solution was filtered and the solid was

dried using a desiccator filled with P₂O₅. Light yellow crystals were obtained by sublimation at 60 °C/0.05 Torr (1.12 g, 66%): mp 56 °C; IR (Nujol, cm⁻¹) 3214 (m), 1559 (w), 1365 (m), 1300 (w), 1261 (w), 1229 (w) 1132 (w), 1038 (m), 1022 (m); ¹H NMR (C₆D₆, 23 °C, δ) 7.49 (d, 1H, (J = 8.0 Hz), CH), 7.17 (d, 1H, (J = 8.0 Hz), CH), 4.65 (s, broad 1H, NH), 2.47 (s, 6H, N(CH₃)₂), 1.14 (s, 9H, C(CH₃)₃); ¹³C{¹H} NMR (100 MHz, C₆D₆, 23 °C, ppm) 139.26 (s, CHN), 133.22 (s, CHN), 53.44 (s, C(CH₃)₃), 42.26 (s, N(CH₃)₂), 28.66 (s, C(CH₃)₃); ESI-HRMS: calcd for C₈H₁₉N₄ ([M+H]⁺) 171.1610, found 171.1607.

Preparation of Ni(L⁹)₂ (37). A 100 mL Schlenk flask was charged with a magnetic stir bar, 1,5-di-*tert*-butyl-1,2,5-triazapentadiene (1.00 g, 5.45 mmol), and tetrahydrofuran (30 mL). To this stirred solution at ambient temperature was slowly added potassium hydride (0.241 g, 6.00 mmol), and the solution was stirred for 4 h. This solution was then slowly added dropwise by cannula to a stirred suspension of anhydrous NiCl₂•CH₃CN (0.456 g, 2.70 mmol) in tetrahydrofuran (40 mL) at -78 °C. The resultant dark brown solution was stirred for 15 h at ambient temperature. The volatile components were then removed under reduced pressure, and the resultant dark red powder was dissolved in hexane (60 mL). The solution was filtered through a 1 cm pad of Celite on a coarse glass frit, and the hexane was then removed under reduced pressure. Dark red crystals of **37** were obtained by sublimation at 155 °C/0.05 Torr (0.397 g, 35%): mp 262 °C; IR (Nujol, cm⁻¹) 1548 (m), 1365 (s), 1339 (m), 1253 (w), 1213 (m), 1174 (m), 1060 (w), 791 (w); ¹H NMR (C₆D₆, 23 °C, δ) 16.64 (s, broad 18H, C(CH₃)₃), 15.20 (s, broad 18H, C(CH₃)₃); μ_{eff} = 2.84 and 2.86 μ_B in the solid state and in benzene solution, respectively. Anal. Calcd for C₂₀H₄₀NiN₆: C, 56.75; H, 9.53; N, 19.86. Found: C, 56.66; H, 9.49; N, 19.84.

Preparation of $\text{Co}(\text{L}^9)_2$ (38). In a fashion similar to the preparation of **37**, treatment of anhydrous cobalt(II) chloride (0.350 g, 2.70 mmol) in tetrahydrofuran (40 mL) with a solution of potassium 1,5-di-*tert*-butyl-1,2,5-triazapentadienate (prepared from 1,5-di-*tert*-butyl-1,2,5-triazapentadiene (1.00 g, 5.45 mmol) and potassium hydride (0.241 g, 6.00 mmol) in tetrahydrofuran (30 mL)) for 15 h at ambient temperature afforded **38** (0.623 g, 57%) as dark green crystals upon sublimation at 160 °C/0.05 Torr: mp 260 °C; IR (Nujol, cm^{-1}) 1542 (s), 1364 (s), 1354 (s), 1340 (s), 1255 (m), 1214 (m), 1178 (s), 1054 (m), 996 (w), 790 (m); $\mu_{\text{eff}} = 3.78$ and $3.95 \mu_{\text{B}}$ in the solid state and in benzene solution, respectively. Anal. Calcd for $\text{C}_{20}\text{H}_{40}\text{CoN}_6$: C, 56.72; H, 9.52; N, 19.84. Found: C, 56.59; H, 9.46; N, 19.79.

Preparation of $\text{Fe}(\text{L}^9)_2$ (39). In a fashion similar to the preparation of **37**, treatment of anhydrous iron(II) chloride (0.342 g, 2.70 mmol) in tetrahydrofuran (40 mL) with a solution of potassium 1,5-di-*tert*-butyl-1,2,5-triazapentadienate (prepared from 1,5-di-*tert*-butyl-1,2,5-triazapentadiene (1.00 g, 5.45 mmol) and potassium hydride (0.241 g, 6.00 mmol) in tetrahydrofuran (30 mL)) for 15 h at ambient temperature afforded **39** (0.805 g, 73%) as dark red crystals upon sublimation at 175 °C/0.05 Torr: mp 275 °C; IR (Nujol, cm^{-1}) 1529 (s), 1362 (m), 1350 (m), 1336 (s), 1254 (m), 1242 (m), 1215 (m), 1176 (s), 1055 (m), 994 (m), 926 (m), 918 (m), 791 (m); $\mu_{\text{eff}} = 5.00$ and $4.92 \mu_{\text{B}}$ in the solid state and in benzene solution, respectively. Anal. Calcd for $\text{C}_{20}\text{H}_{40}\text{FeN}_6$: C, 57.14; H, 9.59; N, 19.99. Found: C, 57.76; H, 9.29; N, 20.14.

Preparation of $\text{Mn}(\text{L}^9)_2$ (40). In a fashion similar to the preparation of **37**, treatment of anhydrous manganese(II) chloride (0.340 g, 2.70 mmol) in tetrahydrofuran (40 mL) with a solution of potassium 1,5-di-*tert*-butyl-1,2,5-triazapentadienate (prepared from 1,5-di-*tert*-butyl-1,2,5-triazapentadiene (1.00 g, 5.45 mmol) and potassium hydride (0.241 g, 6.00 mmol) in tetrahydrofuran (30 mL)) for 15 h at ambient temperature afforded **40** (0.597 g, 54%) as dark

yellow crystals upon sublimation at 165 °C/0.05 Torr: mp 284 °C; IR (Nujol, cm^{-1}) 1552 (m), 1366 (m), 1346 (m), 1257 (m), 1176 (m), 1052 (w), 786 (w); $\mu_{\text{eff}} = 5.89$ and $5.85 \mu_{\text{B}}$ in the solid state and in benzene solution, respectively. Anal. Calcd for $\text{C}_{20}\text{H}_{40}\text{MnN}_6$: C, 57.26; H, 9.61; N, 20.03. Found: C, 57.55; H, 9.50; N, 20.12.

Preparation of $\text{Cr}(\text{L}^9)_2$ (41). In a fashion similar to the preparation of **37**, treatment of anhydrous chromium(II) chloride (0.332 g, 2.70 mmol) in tetrahydrofuran (40 mL) with a solution of potassium 1,5-di-*tert*-butyl-1,2,5-triazapentadienate (prepared from 1,5-di-*tert*-butyl-1,2,5-triazapentadiene (1.00 g, 5.45 mmol) and potassium hydride (0.241 g, 6.00 mmol) in tetrahydrofuran (30 mL)) for 15 h at ambient temperature afforded **41** (0.602 g, 55%) as brown crystals upon sublimation at 165 °C/0.05 Torr: mp 257 °C; IR (Nujol, cm^{-1}) 1500 (w), 1366 (m), 1351 (m), 1334 (m), 1313 (w), 1266 (s), 1231 (w), 1211 (w), 1179 (s), 1143 (m), 1135 (m), 1046 (m), 967 (s), 792 (m); $\mu_{\text{eff}} = 4.85$ and $4.96 \mu_{\text{B}}$ in the solid state and in benzene solution, respectively. Anal. Calcd for $\text{C}_{20}\text{H}_{40}\text{CrN}_6$: C, 57.67; H, 9.68; N, 20.17. Found: C, 57.98; H, 9.48; N, 20.19.

Preparation of $\text{Ni}(\text{L}^{10})_2$ (42). In a fashion similar to the preparation of **37**, treatment of anhydrous $\text{NiCl}_2 \cdot \text{CH}_3\text{CN}$ (0.490 g, 2.95 mmol) in tetrahydrofuran (40 mL) with a solution of potassium 1-*tert*-butyl-5-dimethylamino-1,2,5-triazapentadienate (prepared from 1-*tert*-butyl-5-dimethylamino-1,2,5-triazapentadiene (1.00 g, 5.90 mmol) and potassium hydride (0.259 g, 6.50 mmol) in tetrahydrofuran (30 mL)) for 15 h at ambient temperature afforded **42** (0.267 g, 23%) as dark red crystals upon sublimation at 105 °C/0.05 Torr: mp 99 °C; IR (Nujol, cm^{-1}) 1535 (w), 1366 (m), 1351 (m), 1317 (m), 1255 (m), 1195 (m), 1174 (m), 1055 (m), 1037 (m), 961 (m), 792 (m); ^1H NMR (C_6D_6 , 23 °C, δ) 32.57 (s, broad 12H, $\text{N}(\text{CH}_3)_2$), 16.53 (s, broad 18H, $\text{C}(\text{CH}_3)_3$);

$\mu_{\text{eff}} = 2.86$ and $2.85 \mu_{\text{B}}$ in the solid state and in benzene solution, respectively. Anal. Calcd for $\text{C}_{16}\text{H}_{34}\text{NiN}_8$: C, 48.38; H, 8.63; N, 28.21. Found: C, 48.27; H, 8.53; N, 28.23.

Preparation of $\text{Co}(\text{L}^{10})_2$ (43). In a fashion similar to the preparation of **37**, treatment of anhydrous cobalt(II) chloride (0.376 g, 2.95 mmol) in tetrahydrofuran (40 mL) with a solution of potassium 1-*tert*-butyl-5-dimethylamino-1,2,5-triazapentadienate (prepared from 1-*tert*-butyl-5-dimethylamino-1,2,5-triazapentadiene (1.00 g, 5.90 mmol) and potassium hydride (0.259 g, 6.50 mmol) in tetrahydrofuran (30 mL)) for 15 h at ambient temperature afforded **43** (0.301 g, 27%) as dark green crystals upon sublimation at 105 °C/0.05 Torr: mp 105 °C; IR (Nujol, cm^{-1}) 1529 (m), 1366 (m), 1352 (s), 1316 (m), 1256 (m), 1235 (m), 1216 (m), 1198 (m), 1178 (m), 1051 (m), 1029 (m), 963 (m), 789 (m), 779 (m); $\mu_{\text{eff}} = 3.92$ and $3.95 \mu_{\text{B}}$ in the solid state and in benzene solution, respectively. Anal. Calcd for $\text{C}_{16}\text{H}_{34}\text{CoN}_8$: C, 48.35; H, 8.62; N, 28.19. Found: C, 48.24; H, 8.66; N, 28.14.

Preparation of $\text{Fe}(\text{L}^{10})_2$ (44). In a fashion similar to the preparation of **37**, treatment of anhydrous iron(II) chloride (0.374 g, 2.95 mmol) in tetrahydrofuran (40 mL) with a solution of potassium 1-*tert*-butyl-5-dimethylamino-1,2,5-triazapentadienate (prepared from 1-*tert*-butyl-5-dimethylamino-1,2,5-triazapentadiene (1.00 g, 5.90 mmol) and potassium hydride (0.259 g, 6.50 mmol) in tetrahydrofuran (30 mL)) for 15 h at ambient temperature afforded **44** (0.190 g, 18%) as dark green crystals upon sublimation at 105 °C/0.05 Torr: mp 106 °C; IR (Nujol, cm^{-1}) 1515 (w), 1368 (m), 1351 (m), 1312 (w), 1258 (w), 1196 (w), 1176 (w), 1026 (w), 794 (w); $\mu_{\text{eff}} = 4.78$ and $4.82 \mu_{\text{B}}$ in the solid state and in benzene solution, respectively. Anal. Calcd for $\text{C}_{16}\text{H}_{34}\text{FeN}_8$: C, 48.73; H, 8.69; N, 28.42. Found: C, 49.05; H, 8.72; N, 28.10.

Preparation of $\text{Mn}(\text{L}^{10})_2$ (45). In a fashion similar to the preparation of **37**, treatment of anhydrous manganese(II) chloride (0.371 g, 2.95 mmol) in tetrahydrofuran (40 mL) with a

solution of potassium 1-*tert*-butyl-5-dimethylamino-1,2,5-triazapentadienate (prepared from 1-*tert*-butyl-5-dimethylamino-1,2,5-triazapentadiene (1.00 g, 5.90 mmol) and potassium hydride (0.259 g, 6.50 mmol) in tetrahydrofuran (30 mL)) for 15 h at ambient temperature afforded **45** (0.350 g, 32%) as dark orange crystals upon sublimation at 105 °C /0.05 Torr: mp 108 °C; IR (Nujol, cm^{-1}) 1539 (m), 1357 (m), 1323 (m), 1256 (m), 1196 (m), 1186 (m), 1152(w), 1048 (m), 957(w), 1021 (m), 786 (w), 730 (w); $\mu_{\text{eff}} = 5.80$ and $5.82 \mu_{\text{B}}$ in the solid state and in benzene solution, respectively. Anal. Calcd for $\text{C}_{16}\text{H}_{34}\text{MnN}_8$: C, 48.84; H, 8.71; N, 28.48. Found: C, 48.86; H, 8.78; N, 28.32.

CHAPTER 6

Low Temperature Atomic Layer Deposition of Copper Films Using Borane Dimethylamine as the Reducing Co-Reagent

6.1 Introduction

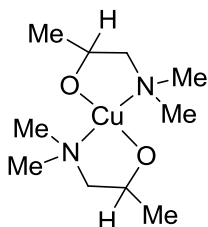
Cu is the primary interconnect material in microelectronic devices, because of its low resistivity and high resistance to electromigration.³ Cu is currently deposited in trenches and vias by a two-step process that employs the formation of a thin, conformal Cu seed layer by physical vapor deposition, followed by Cu fill using electrodeposition.⁴ Cu metal needs to be deposited by ALD to meet future conformality and film thickness uniformity requirements in microelectronic devices. In addition, the Cu metal should be deposited ideally at ≤ 160 °C to afford the lowest surface roughness, promote facile nucleation, and give continuous films even at thicknesses of a few nanometers.⁹⁸

Recent reports demonstrated that annealing of a 150 nm thick 90/10 Cu/Mn alloy film on SiO₂ substrates at temperatures between 250 and 450 °C led to the migration of the Mn atoms to the SiO₂ interface to form a segregated 2–8 nm MnSi_xO_y layer between the SiO₂ and Cu layers.^{7,48} Most significantly, this Mn-containing layer served as a Cu diffusion barrier for up to 100 h at 450 °C.^{7c} This work is very important, since it suggests that ultrathin Mn-based films can replace current nitride-based barriers (TaN, WN_x) in future microelectronic devices. However, growth of the Cu/Mn alloy films relied upon a physical deposition method (sputtering),^{7,48} which affords poor conformal coverage in the narrow and deep features of future microelectronic devices. A plasma-based ALD process for Cu/Mn metal alloy films with up to

10% Mn was reported, using $\text{Cu}(\text{OCMe}_2\text{CH}_2\text{NMe}_2)_2$, $\text{Mn}(\text{tmhd})_3$, and H_2 plasma with substrate temperatures between 100 and 180 °C,⁵² however a thermal Cu/Mn alloy ALD process has not been disclosed to date. A key breakthrough to enable a thermal, low temperature Cu/Mn ALD process would be identification of a highly reactive reducing co-reagent that can reduce the Cu(II) ion ($E^\circ = 0.3419 \text{ V}^{20a}$) and Mn(II) ion ($E^\circ = -1.185 \text{ V}^{20a}$) equally well.

Within the above considerations, new Cu ALD processes that employ the highly reactive reducing co-reagent borane dimethylamine ($\text{BH}_3(\text{NHMe}_2)$) are discussed in this chapter. A two-step ALD process employing **46** (Chart 12) and $\text{BH}_3(\text{NHMe}_2)$ affords Cu films within an ALD window of 130–160 °C on Ru substrates, but the films have rough surfaces due to the agglomeration of the Cu atoms during the initial stages of growth. However, three-step processes using **46**, formic acid, and $\text{BH}_3(\text{NHMe}_2)$ gives high purity, low resistivity Cu films within ALD windows of 135–160 °C on Pd and Pt substrates. Importantly, these three-step processes afford dispersed, smooth Cu films at film thicknesses as low as 2 nm.

Chart 12. Structure of **46**.



6.2 Results and Discussion

Precursor Selection and Properties. The complex **46** was chosen as the Cu precursor, since it has been widely used as a CVD and ALD precursor for Cu-containing films.^{23,24,34} The Winter group has previously reported that **46** sublimes on a preparative scale (~1 g) at 90 °C/0.05 Torr within ~4 h with 89% sublimed recovery and 3% nonvolatile residue, and undergoes solid state decomposition between 185 and 188 °C.²⁴ Winter and coworkers described

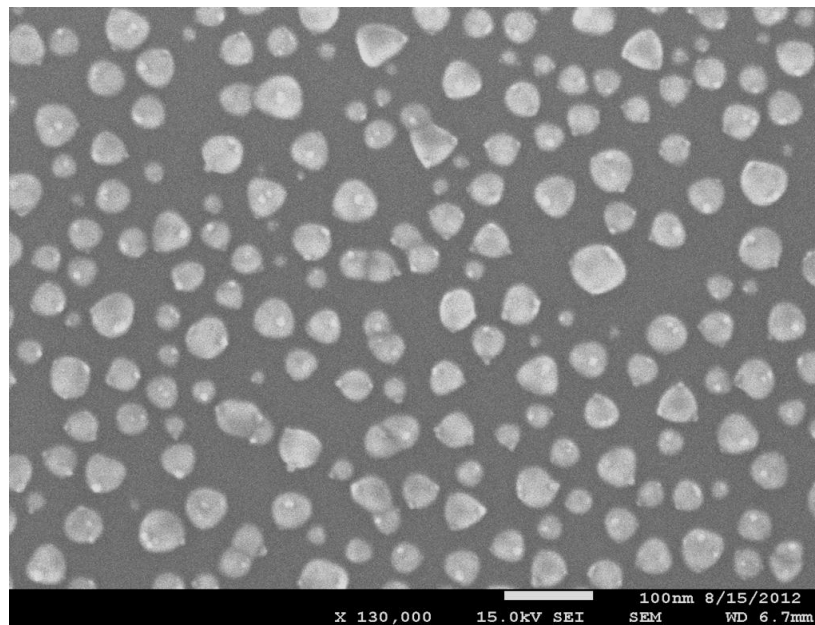
the ALD growth of Cu films from **46**, formic acid, and hydrazine within an ALD window of 100-170 °C.²⁴

In order to find a suitable reducing co-reagent that can reduce **46** to Cu(0), solution screening reactions were carried out with various commercially available reducing agents.^{24,67} This screening was restricted to Lewis base adducts of boranes, since many of these compounds are available commercially, most are volatile, and first row transition metal hydrides MH_2 are known to undergo rapid reductive elimination of H_2 to afford the metals.⁹⁹ Treatment of **46** with 5 equivalents of $BH_3(NHMe_2)$, $BH_3(NEt_3)$, or $BH_3(NiPr_2Et)$ at ambient temperature in tetrahydrofuran afforded immediate precipitation of Cu metal powders which were confirmed by XRD. Among these borane adducts, $BH_3(NHMe_2)$ had the highest volatility (sublimes 70 °C/0.05 Torr) and could be delivered reproducibly in the ALD reactor. $BH_3(NHMe_2)$ is reported to decompose at 130 °C to afford H_2 and $[BH_2NMe_2]_2$.¹⁰⁰

Binary Process Growth Studies. Initial deposition studies were carried out using **46** as the Cu source and $BH_3(NHMe_2)$ as the reducing agent. A range of substrates was employed in initial growth trials, including Si with native oxide, SiO_2 (100 nm)/Si, Si-H/Si, Ru (5 nm)/ SiO_2 (100 nm)/Si, Pd (15 nm)/Ti (2 nm)/ SiO_2 (100 nm)/Si, Pt (15 nm)/Ti (2 nm)/ SiO_2 (100 nm)/Si, Cu (10 nm)/Ta (3 nm)/Si, and TiN (20 nm)/Si. Initial deposition studies resulted in thin (2–3 nm), discontinuous Cu films on Ru (5 nm)/ SiO_2 (100 nm)/Si, TiN (20 nm)/Si, SiO_2 , Si with native oxide, and Si-H/Si. These results clearly indicated poor nucleation. To enhance nucleation, 50 cycles comprising a 20 second pulse of **46**, a 5 second nitrogen purge, a 1 second pulse of $BH_3(NHMe_2)$, and a 10 second purge were carried out. Figure 36 shows a scanning electron microscopy (SEM) top view of a Ru (5 nm)/ SiO_2 (100 nm)/Si substrate after the 50 cycle nucleation sequence at a growth temperature of 150 °C. The nucleation sequence leads to

separated nanoparticles, with diameters ranging from about 10 to 90 nm. The height of the nanoparticles is about 13 nm, as determined by side view SEM. The 50 cycle sequence led to improved nucleation on Ru (5 nm)/SiO₂ (100 nm)/Si, TiN/Si, SiO₂, Si with native oxide, and Si-H/Si substrates, but the deposits on Ru (5 nm)/SiO₂ (100 nm)/Si were the densest. Accordingly, the deposition study described below was carried out on the Ru-coated substrates.

Figure 36. Surface SEM views of ALD Cu after nucleation step.



Cu film growth studies were carried out on Ru (5 nm)/SiO₂ (100 nm)/Si substrates that were subjected to the 50 nucleation cycles described above prior to regular ALD growth. The growth behavior was investigated by changing the precursor pulse lengths, substrate temperatures, and number of deposition cycles. A plot of growth rate versus pulse length of **46** at 150 °C is shown in Figure 37. In these experiments, the number of deposition cycles, length of BH₃(NHMe₂) pulse, and lengths of the purge cycles after the pulses of **46** and BH₃(NHMe₂) were kept constant at 1000 cycles, 1.0 s, 5.0 s, and 10 s, respectively. In ALD, a constant growth rate is observed once sufficient precursor has been passed over the substrate to use up the surface

reactive sites. According to Figure 37, saturation with **46** occurs at ≥ 3.0 s pulse lengths. A saturative growth rate of 0.26 \AA per cycle was obtained, although this value includes the ca. 13 nm of Cu nanoparticles documented in the nucleation step. Pulse lengths below 3.0 s afforded sub-saturative growth. A similar plot of growth rate versus $\text{BH}_3(\text{NHMe}_2)$ pulse length showed saturative growth with ≥ 1.0 s pulse lengths, and also afforded an apparent growth rate of 0.26 \AA per cycle (Figure 38). Pulse lengths of 3.0 and 1.0 s for **46** and $\text{BH}_3(\text{NHMe}_2)$, respectively, were used in the growth studies described below. The purge lengths were 5.0 and 10.0 s after the pulses of **46** and $\text{BH}_3(\text{NHMe}_2)$, respectively. The long purge time after the $\text{BH}_3(\text{NHMe}_2)$ pulse was used to minimize B incorporation in the films.

Figure 39 shows the dependence of growth rate on substrate temperature. A constant growth rate of about 0.26 \AA per cycle was observed over the temperature range of 130 to 160 °C. This temperature range is known as “ALD Window”, where the growth rate does not vary with the substrate temperature. Lower growth rates were observed below 130 °C, most likely due to low precursor reactivity. Higher growth rates were observed above 160 °C, presumably due to increasingly rapid gas phase thermal decomposition of **46**.

Figure 37. Growth rate as a function of the pulse length of **46** at a substrate temperature of 150 °C on Ru.

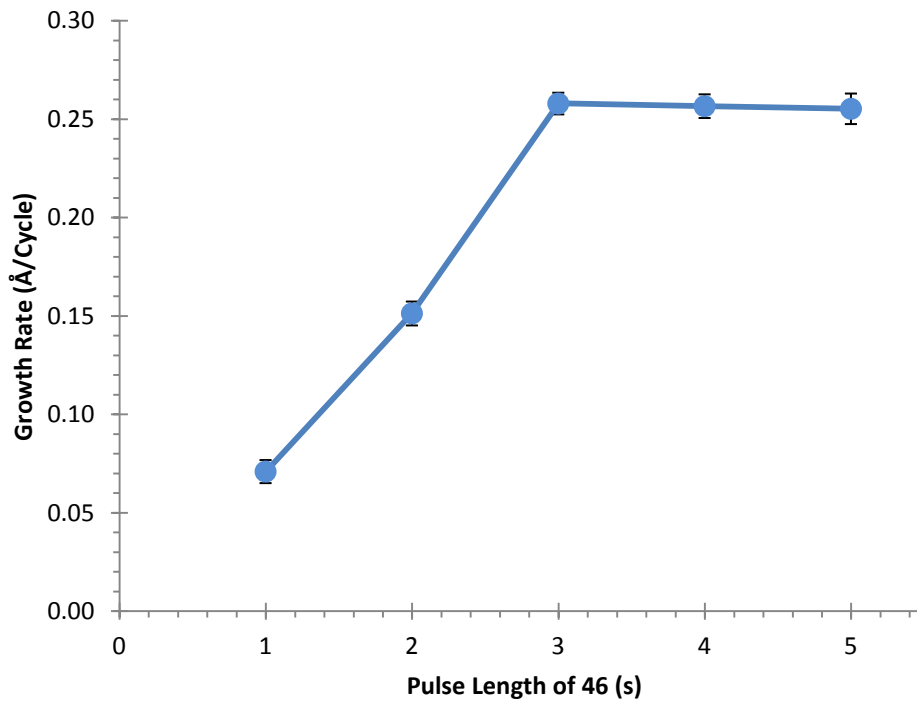


Figure 38. Growth rate as a function of the pulse length of $\text{BH}_3(\text{NHMe}_2)$ at a substrate temperature of 150 °C on Ru.

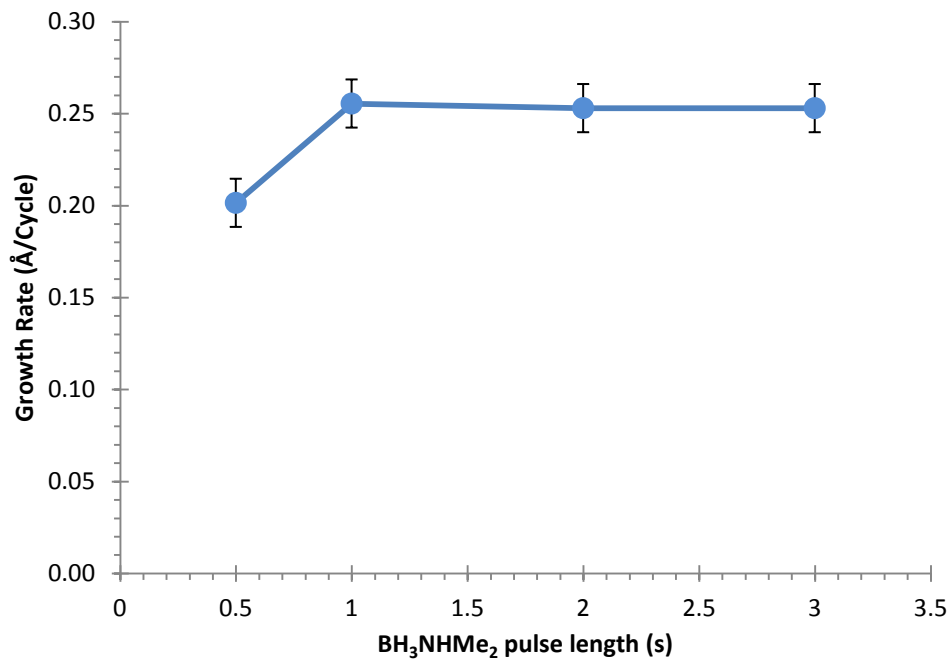
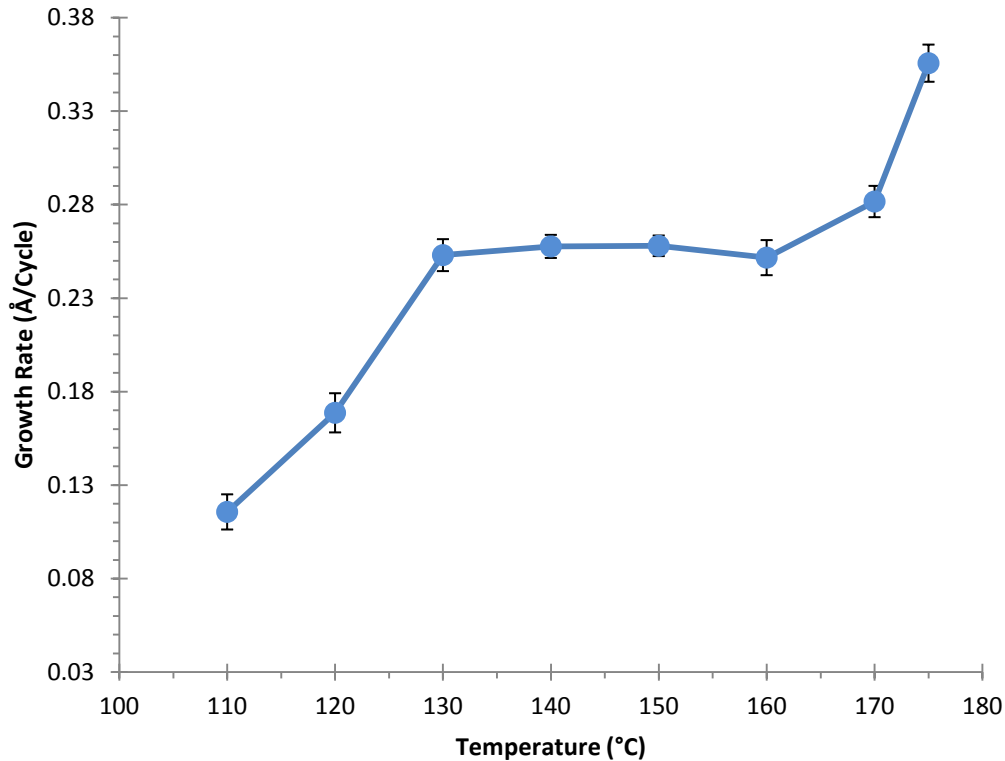
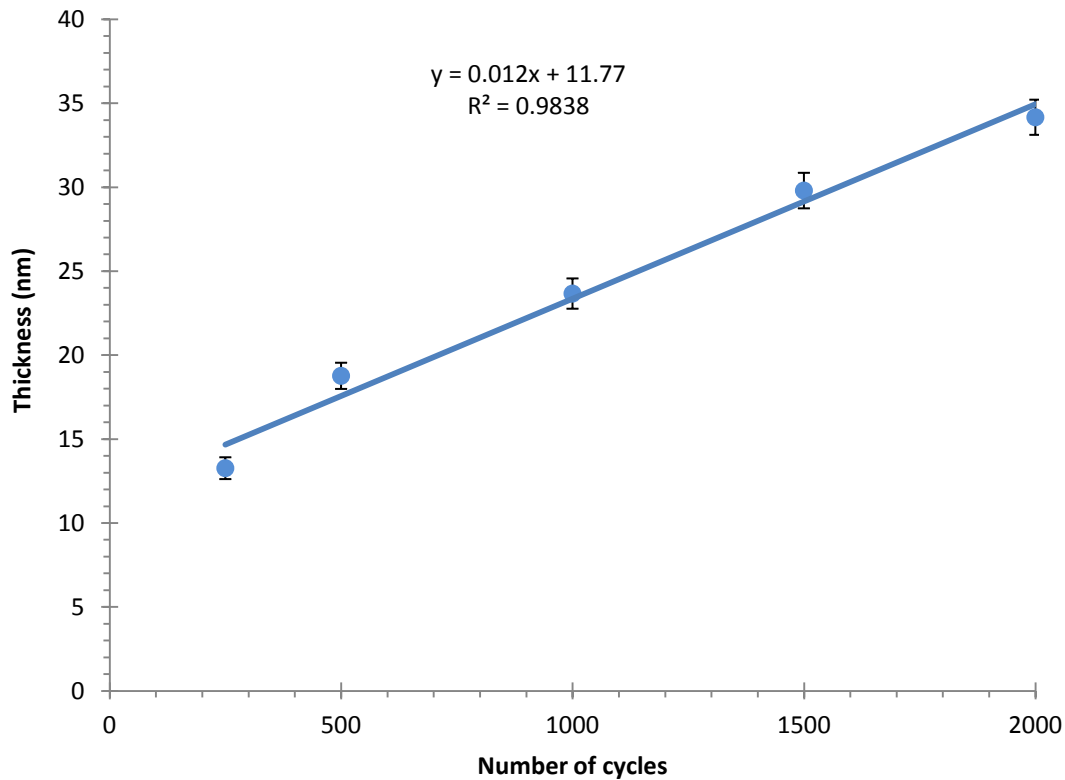


Figure 39. Growth rate as a function of deposition temperature in the binary process on Ru.



A plot of thickness versus number of cycles is shown in Figure 40. The substrate temperature for these depositions was 150 °C. There is a linear relationship between the film thickness and number of cycles. The slope of the line indicates a growth rate of about 0.12 Å/cycle, which fits the growth rate described in Figure 37 when the film thickness from the nucleation step is subtracted. The y-intercept in Figure 40 is about 12 nm, which is close to the 13 nm film thickness that was measured for the nucleation step by SEM.

Figure 40. Film thickness as a function of the number of deposition cycles at a growth temperature of 150 °C on Ru.



Characterization of Cu Films from the Binary Process. The compositions of films deposited at 120, 140, and 160 °C were assessed by XPS (Figure 41a). Similar compositions were obtained at all temperatures, and are summarized in Table 19 (Entries 1–3). Oxygen contents of 2.5–7.9% were observed, even after sputtering. Low B contents of 1.2–3.1% were obtained after sputtering. High resolution scans of the Cu 2p region revealed ionizations at 952.0 and 932.2 eV, which are very similar to the reference ionization values for Cu metal of 952.2 and 932.4 eV (Figure 41b).¹⁰¹ However, Cu₂O also shows Cu 2p ionizations that are very similar to those of Cu metal. Therefore, further analysis is required. A recent report showed that Cu metal shows an LMM Auger ionization at 567.7–567.9 eV, whereas the corresponding ionization for Cu₂O appears at 570.0 eV.^{21c} The Cu LMM Auger ionization for all films in from the binary process appears at 568.0 eV, which confirms Cu metal.

Figure 41a. XPS spectra of 25 nm Cu films deposited at 150 °C on Ru.

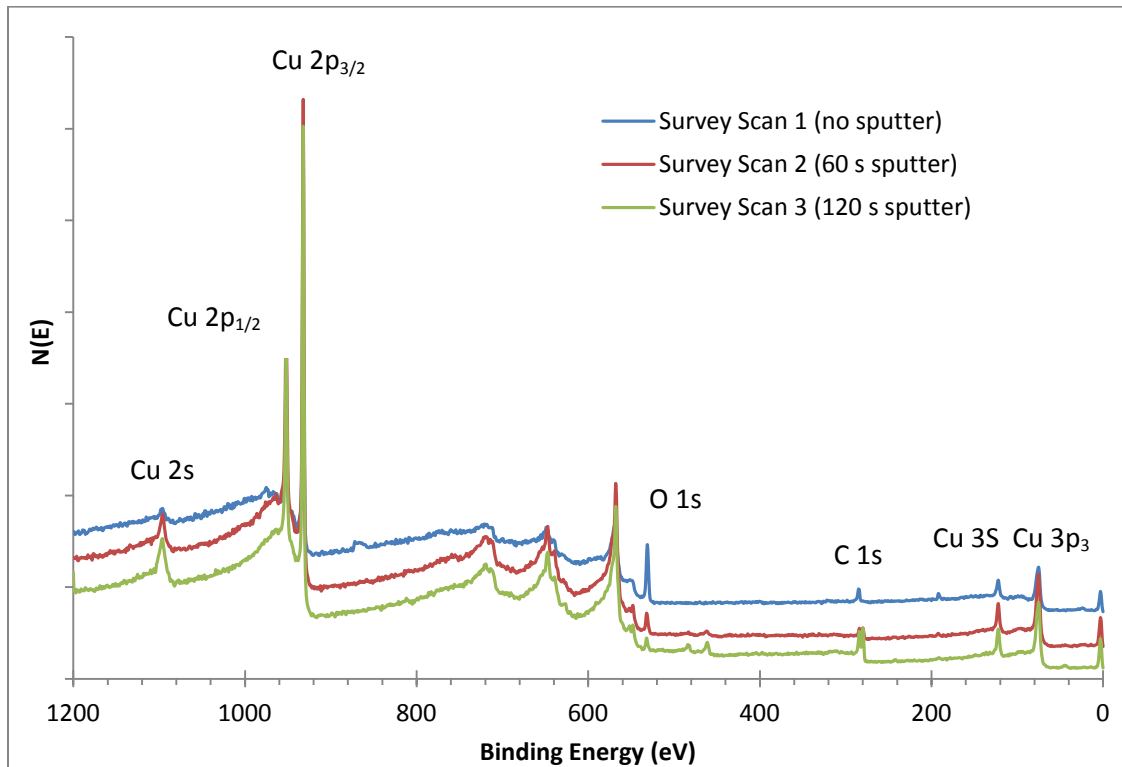


Figure 41b. High-resolution XPS multiplex of Cu 2p region.

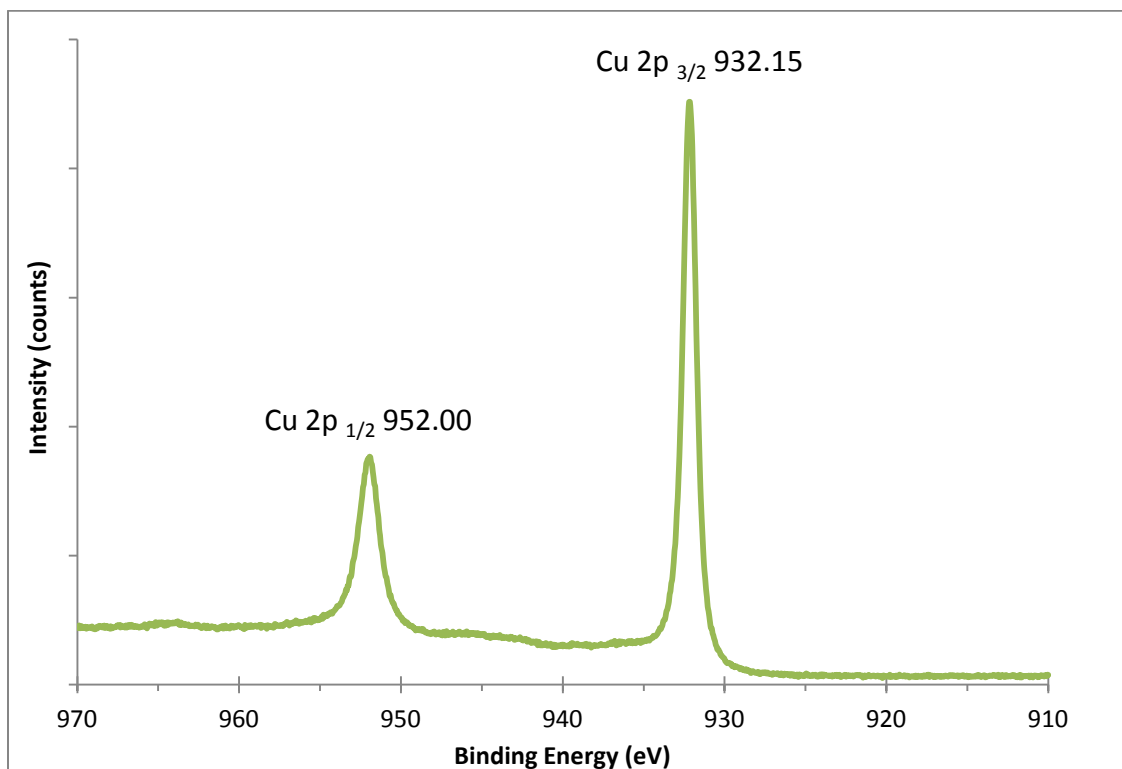
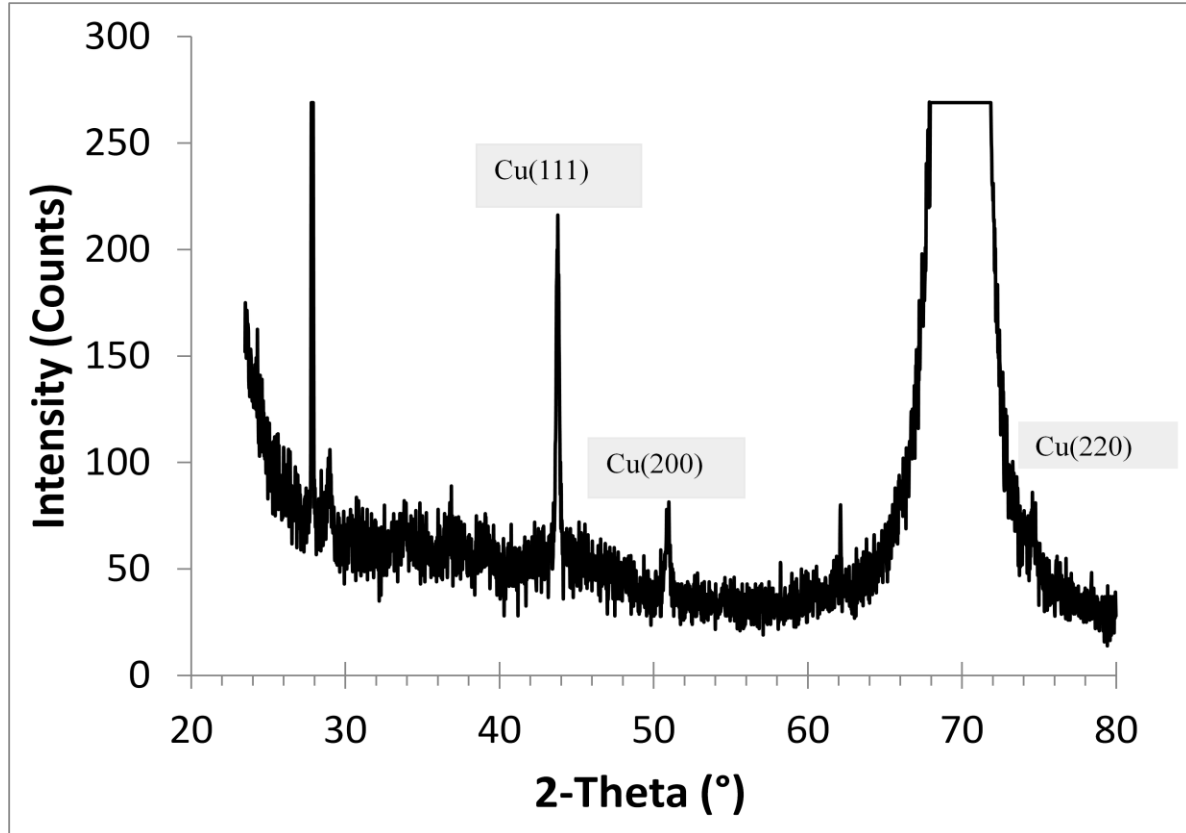


Table 19. Atomic concentrations of Cu, C, N, O, and B obtained by XPS after 120 s of Ar ion sputtering on the indicated substrates.

Entry	T (°C)	% Cu	% C	% N	% O	% B
1	120 (Ru)	85.0	6.8	2.7	2.5	2.4
2	140 (Ru)	87.1	0.2	2.4	7.9	1.2
3	160 (Ru)	89.2	0.4	0.4	6.6	3.1
4	140 (Pd)	96.1	0.0	1.7	1.8	0.4
5	150 (Pd)	91.3	2.5	1.4	4.7	0.1
6	160 (Pd)	93.5	0.1	0.1	6.3	0.0
7	140 (Pt)	97.5	0.1	0.1	1.3	0.9
8	150 (Pt)	95.9	1.5	1.9	0.5	0.2
9	160 (Pt)	95.4	0.9	0.4	3.3	0.0

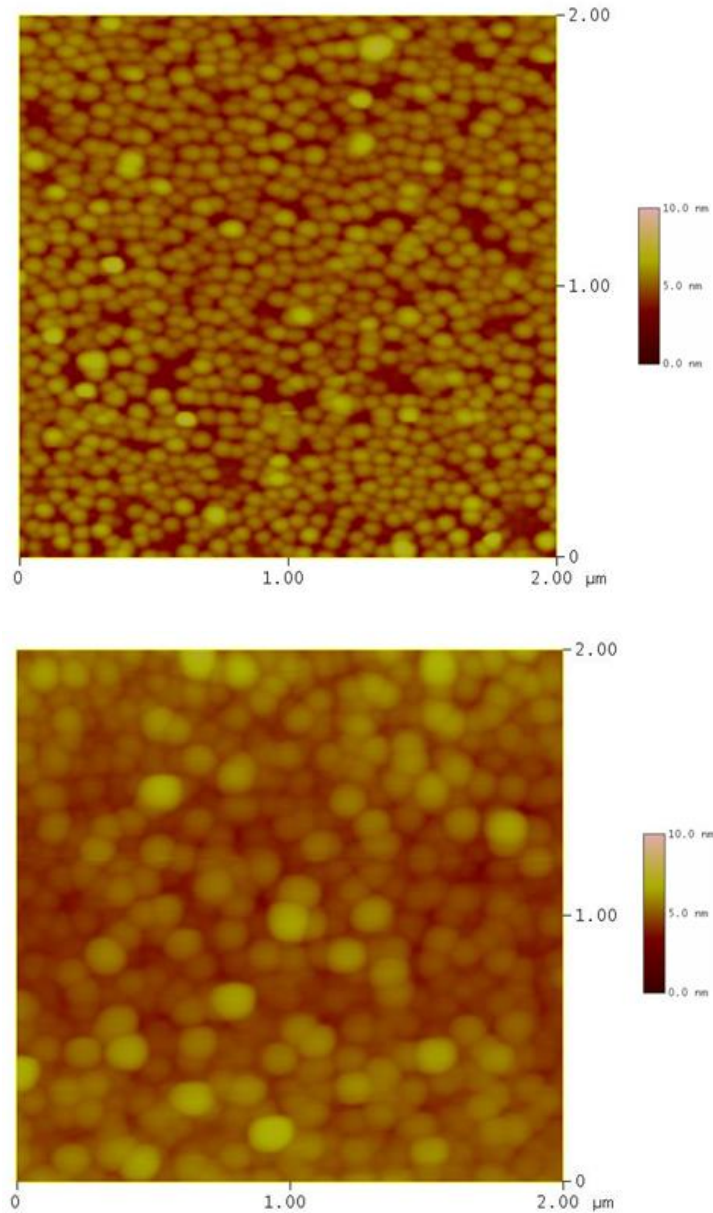
XRD experiments of the as-deposited films revealed that they are amorphous at all temperatures. A film deposited at 150 °C was annealed for three hours at 300 °C under Ar. The annealed film revealed reflections for the (111), (200), and (220) planes of Cu metal (JCPDS file no. 04-0836) (Figure 42). The surface morphologies of the deposited films were examined by AFM and SEM. AFM images of 2 μm \times 2 μm area of the films deposited at 120 and 160 °C are shown in Figure 43. The rms surface roughnesses of 25 nm thick films deposited at 120 and 160 °C were 5.8 and 4.2 nm, respectively. SEM micrographs of the films deposited at these conditions also show rough surfaces. The SEM micrographs of the films after the nucleation step (Figure 36) showed the formation of separated nanoparticles, which results in rough surfaces after the regular ALD cycles.

Figure 42. Powder XRD spectrum of a Cu film after annealing for 3 h at 300 °C.



The sheet resistivities of the films deposited between 120 and 160 °C ranged from 400 to 500 Ω /sq. These sheet resistivity values are close to those obtained upon annealing the Ru substrates at 120–160 °C under vacuum, and suggest poorly conductive Cu films. Additionally, the sheet resistivities of these films increased with time upon storage in air, suggesting slow oxidation of the films by ambient atmosphere. Cu nanoparticles are well known to oxidize to Cu_2O and CuO upon exposure to air.^{68c} As outlined above, AFM and SEM images revealed that the films consist of densely packed nanoparticles, and XPS showed higher than expected levels of oxygen, even in sputtered samples. Accordingly, it is likely that the Cu particles on Ru substrates oxidize upon exposure to air to form Cu_2O or CuO coatings on the surfaces of the constituent nanoparticles, leading to poorly conductive films.

Figure 43. AFM images of Cu film surfaces deposited at 120 (top, rms roughness = 5.8 nm) and 160 °C (bottom, rms roughness = 4.2 nm) on Ru.



Formic Acid as a Nucleating Agent on Pd and Pt Substrates. As documented above, a successful nucleation sequence was developed that allowed ALD growth of Cu films on Ru substrates, but the films were rough due to the isolated nanoparticles in the seed layer. Winter and coworkers recently reported the growth of Cu films from **46**, formic acid, and hydrazine, and

were able to grow films on substrates such as thermal SiO₂ and Si with native oxide without the need for any nucleation steps.²⁴ Based upon this precedent, formic acid may serve as a nucleation agent. Accordingly, the growth of Cu films by a three-step process comprising **46**, formic acid, and BH₃(NHMe₂) was investigated to determine if higher quality films would result. Initial depositions were carried out at 150 °C on the same range of substrates listed above for the two-step process. Specular Cu-colored films were obtained on the Pd (15 nm)/Ti (2 nm)/SiO₂ (100 nm)/Si and Pt (15 nm)/Ti (2 nm)/SiO₂ (100 nm)/ Si substrates, whereas the other substrates did not show improved film growth. Complete deposition studies were carried out on the Pd and Pt substrates. Unlike the two-step process described above, films grown on Pd and Pt substrates by the three-step process did not require a separate nucleation step. Initial studies demonstrated saturative growth at 150 °C on the Pd and Pt substrates with pulse lengths of ≥ 3.0 s for **46** (Figures 44a and 44b), ≥ 0.3 s for formic acid (Figures 45a and 45b), and ≥ 1.0 s for BH₃(NHMe₂) (Figures 46a and 46b). The saturative pulse lengths for **46** and BH₃(NHMe₂) are identical to those of the two-step process on the Ru substrates. Purge lengths of 5.0 s (after **46** and formic acid pulses) and 10.0 s (after BH₃(NHMe₂) pulse) were used. With 1000 cycles, films grown at 150 °C showed a saturative growth rate of 0.20 Å/cycle on both Pd and Pt substrates.

Figure 44a. Growth rate as a function of the pulse length of **46** at a substrate temperature of 150 °C on Pd.

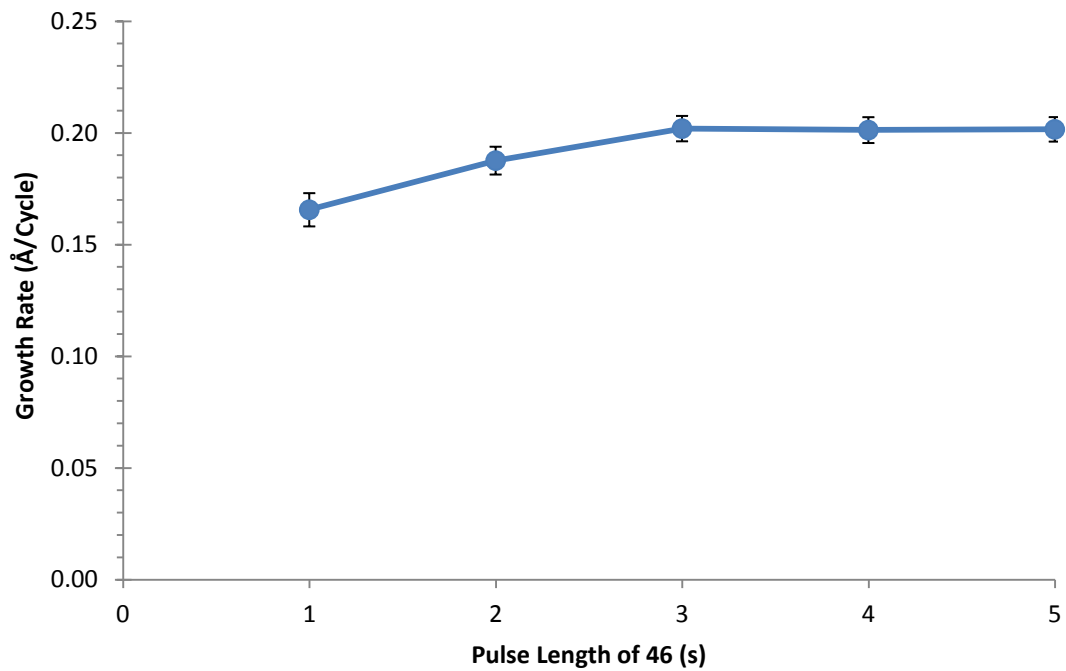


Figure 44b. Growth rate as a function of the pulse length of **46** at a substrate temperature of 150 °C on Pt.

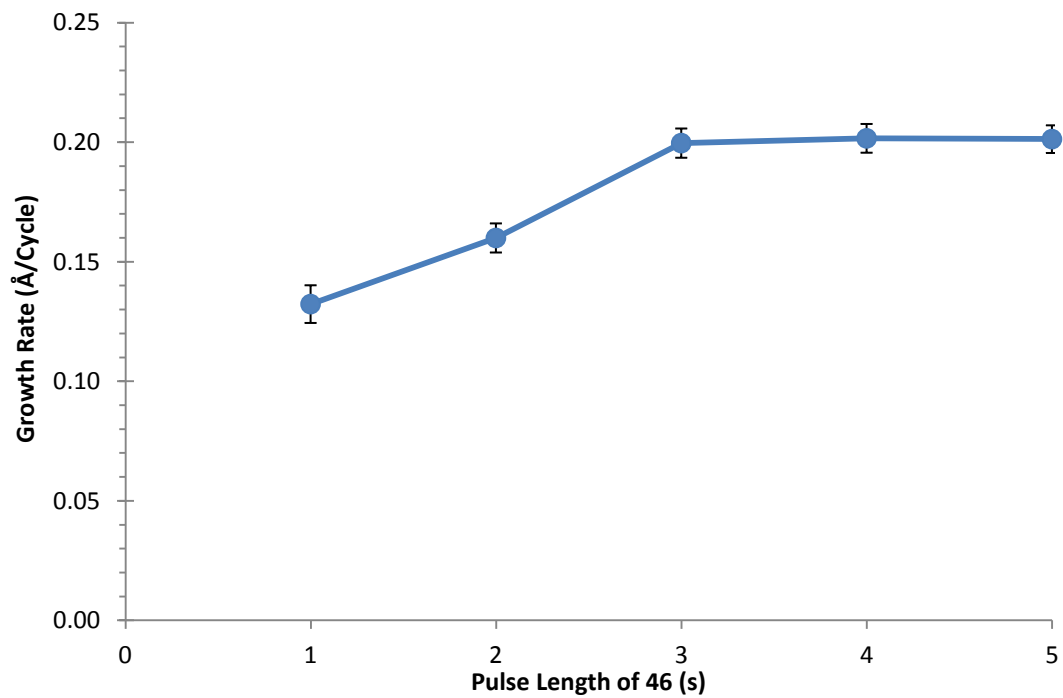


Figure 45a. Growth rate as a function of the pulse length of formic acid at a substrate temperature of 150 °C on Pd.

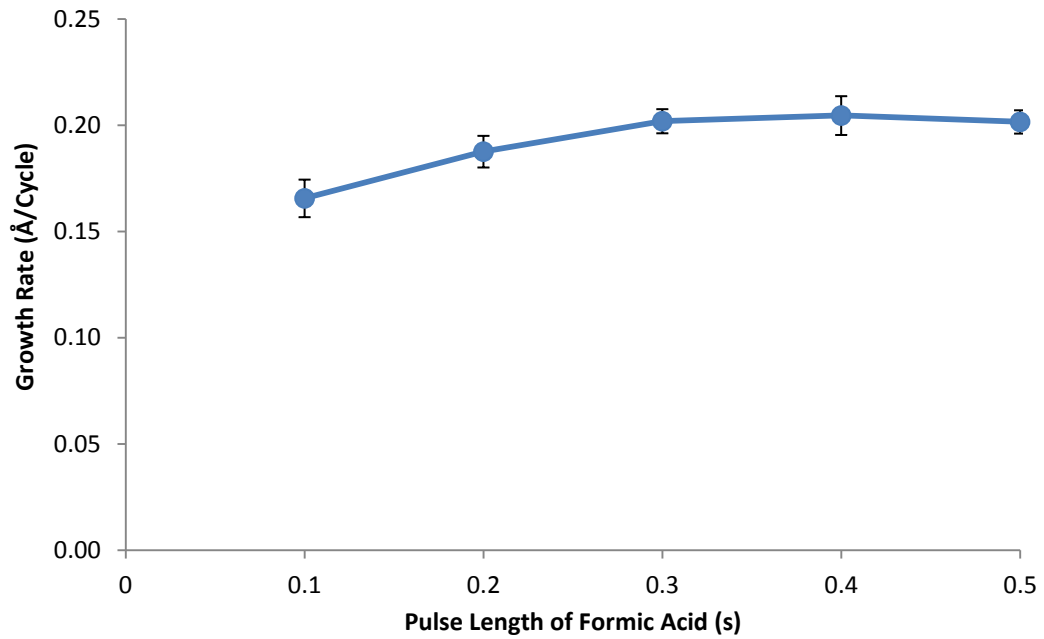


Figure 45b. Growth rate as a function of the pulse length of formic acid at a substrate temperature of 150 °C on Pt.

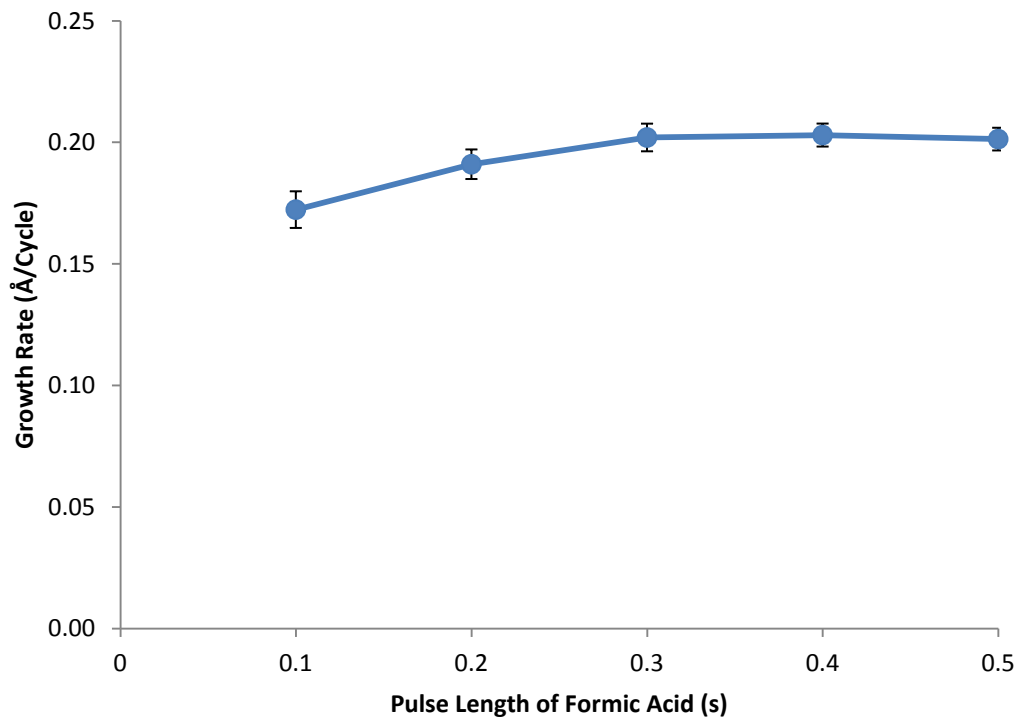


Figure 46a. Growth rate as a function of the pulse length of $\text{BH}_3(\text{NHMe}_2)$ at a substrate temperature of 150 °C on Pd.

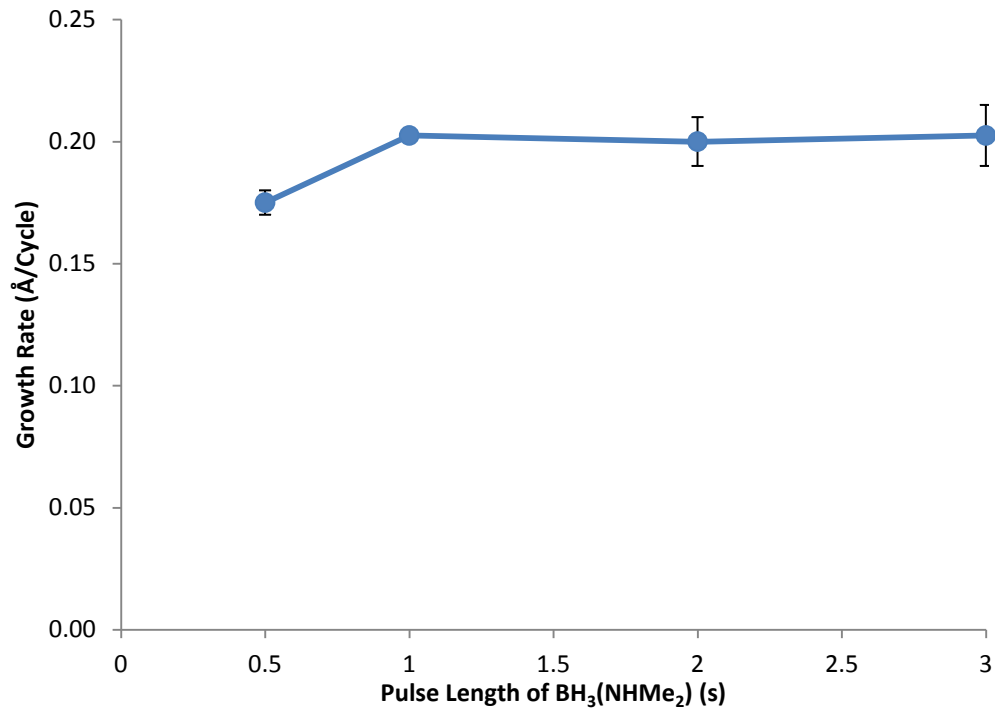


Figure 46b. Growth rate as a function of the pulse length of $\text{BH}_3(\text{NHMe}_2)$ at a substrate temperature of 150 °C on Pt.

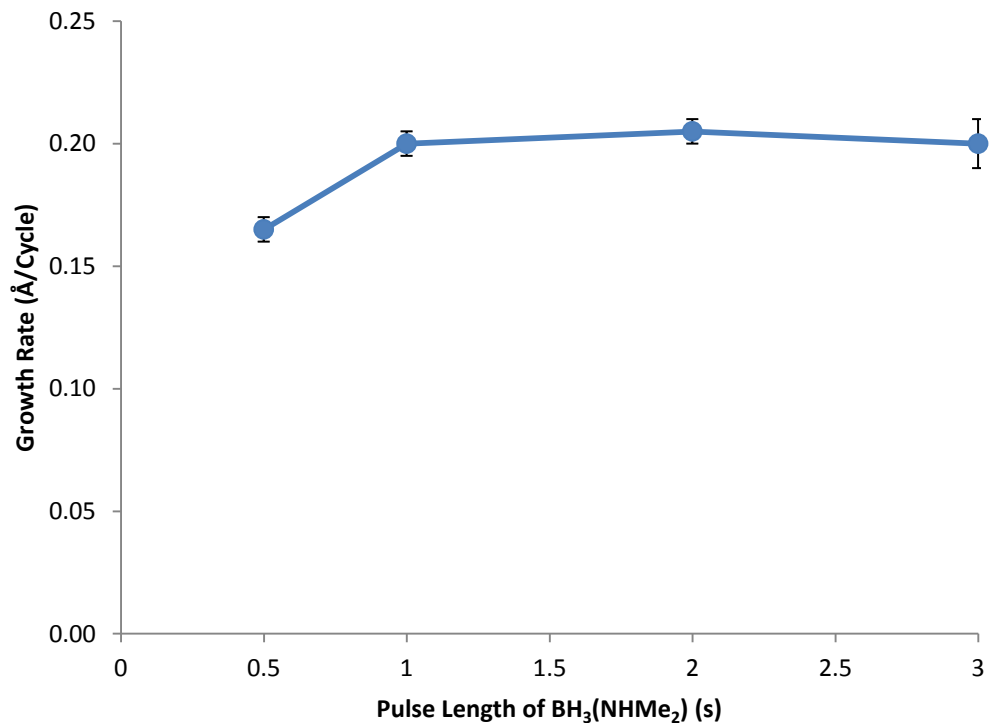


Figure 47a shows the dependence of growth rate on temperature with a Pd substrate, 1000 cycles, and the optimized pulse and purge lengths outline above. An ALD window was observed between 135 to 165 °C, with a constant growth rate of 0.20 Å/cycle in this range. A similar plot on a Pt substrate was identical (Figure 47b). The ALD window range observed with the three-step process on Pd and Pt substrates is identical to that of the two step process. However, the growth rate decreased at > 170 °C in the three step process, but increased at > 170 °C in the two step process.

Figure 47a. Growth rate as a function of deposition temperature on Pd in the ternary process.

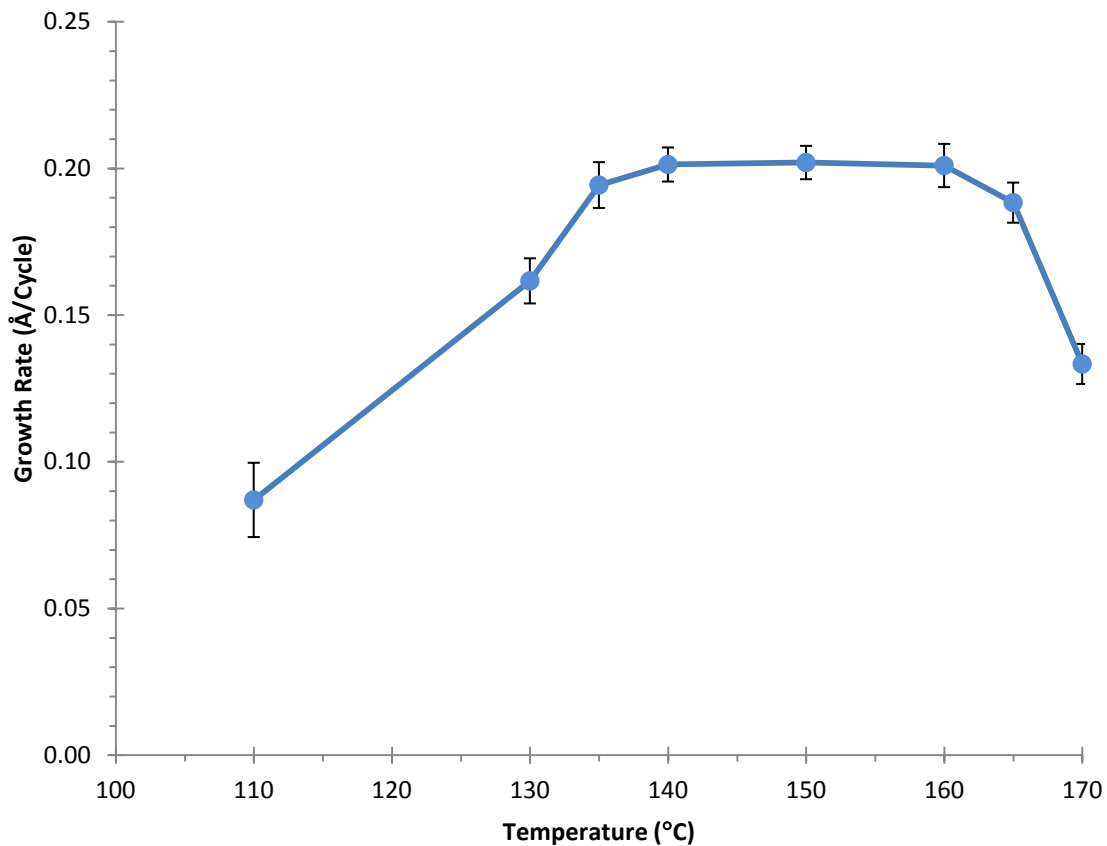
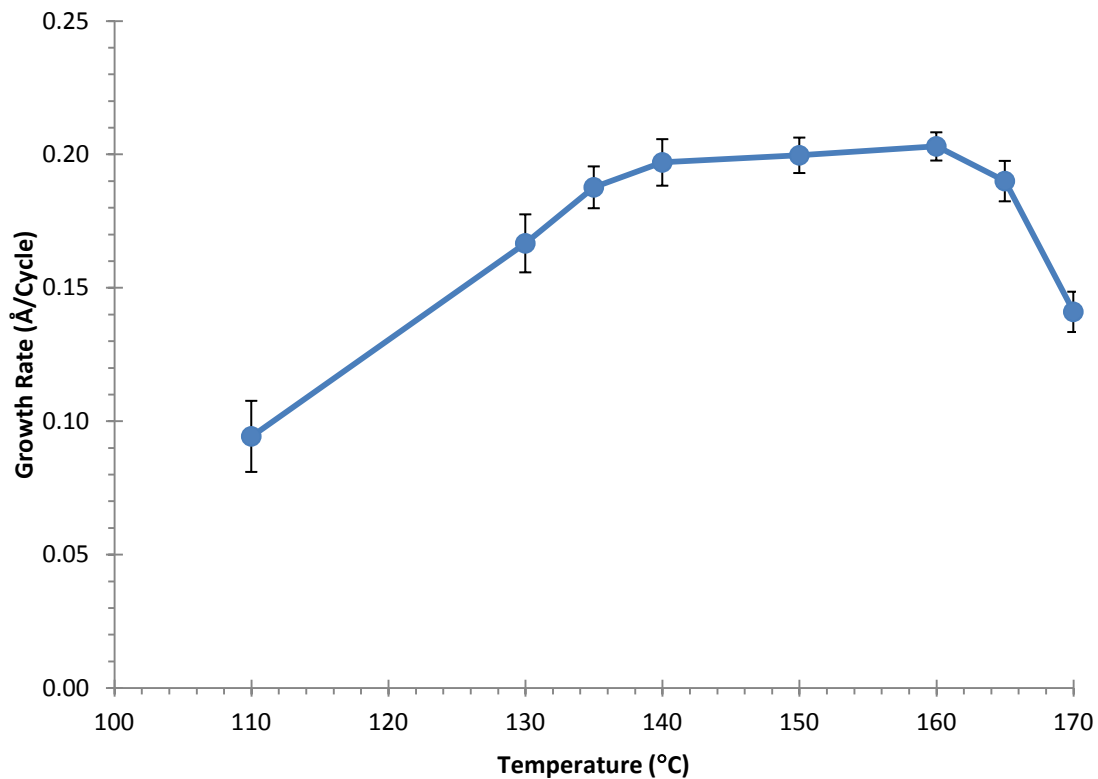


Figure 47b. Growth rate as a function of deposition temperature on Pt in the ternary process.



Plots of film thickness versus number of cycles for growth on Pd and Pt substrates are shown in Figures 48a and 48b, respectively. These films were grown at 150 °C using the optimized pulse and purge lengths outlined above. The plot for growth on Pd (Figure 48a) varies linearly with the number of cycles, with a slope of 0.20 Å/cycle. The y-intercept was 3.4, which is within experimental error of zero and suggests good nucleation at early stages of the deposition. By contrast, a similar plot for growth on a Pt substrate revealed nonlinear growth behavior (Figure 48b). Between 250 and 500 cycles, a growth rate of 0.4 Å/cycle was observed, but the growth rate decreased to about 0.03 Å/cycle between 500 and 2000 cycles.

Figure 48a. Film thickness as a function of the number of deposition cycles at a growth temperature of 150 °C on Pd.

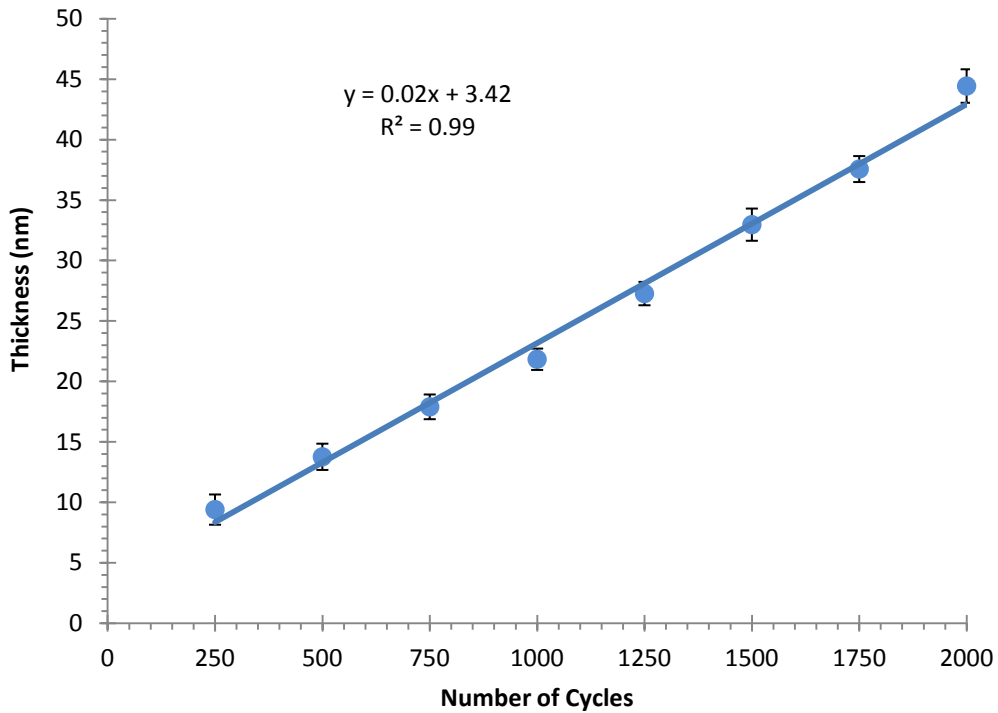
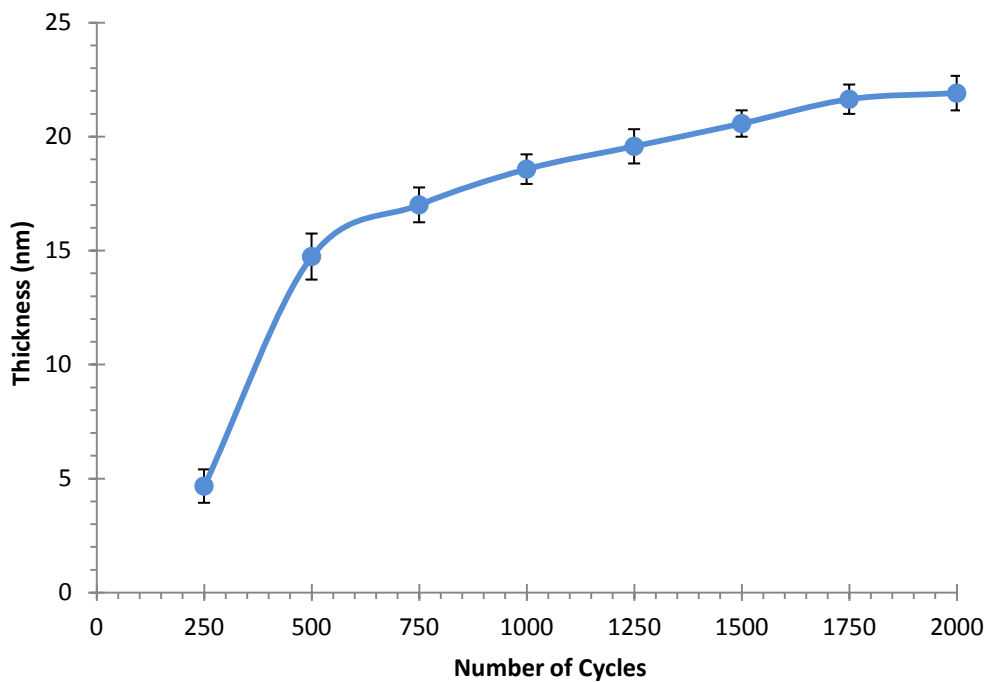


Figure 48b. Film thickness as a function of the number of deposition cycles at a growth temperature of 150 °C on Pt.



Characterization of Cu Films from the Ternary Process. Cu films deposited by the three-step processes were characterized in detail. XPS analyses of 20 nm thick films grown at 140, 150, and 160 °C after Ar ion sputtering revealed metallic Cu. Compositions are listed in Table 19 (Entries 4–9), and XPS survey scans and high resolution multiplex in Cu 2p region are shown in Figures 49a and 49b. High resolution scans of the Cu 2p region revealed ionizations at 952.0 and 932.2 eV, which are very close to the reference ionization values for Cu metal of 952.2 and 932.4 eV.¹⁰¹ The Cu LMM Auger ionization for all films in from the ternary process appears at 568.0 eV, which confirms Cu metal. The Cu films grown on Pd and Pt substrates were of higher purity than those grown on Ru by the two step process. The Cu atomic concentrations ranged from 91.3 to 97.5%, and the highest values were obtained at 140 °C on both Pd and Pt substrates. Atomic concentrations of C (0.0–2.5%), N (0.1–1.9%), and B (0.0–0.9%) were low and showed no clear trend with deposition temperature or substrate. The uncertainties in these concentrations are probably 0.5 to 1.0%, which suggests that there is little difference among these values. Atomic concentrations of oxygen ranged from 0.5 to 6.3%. The oxygen concentrations were slightly higher on Pd substrates, and the levels increased with deposition temperature. On Pt substrates, the oxygen concentrations were lower, and there was not a clear trend with deposition temperature. Overall, Cu films grown by the three step process on Pd and Pt substrates are high purity, and have similar compositions to the previously reported Cu films grown from **46**, formic acid, and anhydrous hydrazine.²⁴ The slightly high oxygen concentrations may arise from surface oxidation of the films upon exposure to ambient atmosphere during XPS sample preparation.

Figure 49a. XPS spectra of 20 nm Cu films deposited at 150 °C.

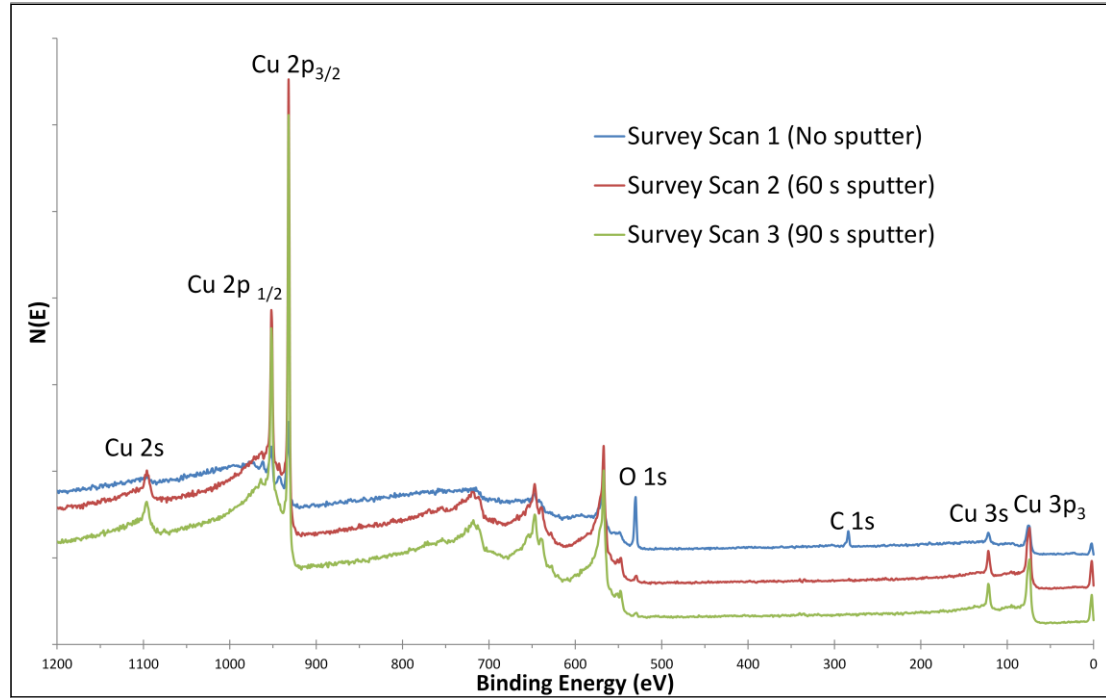
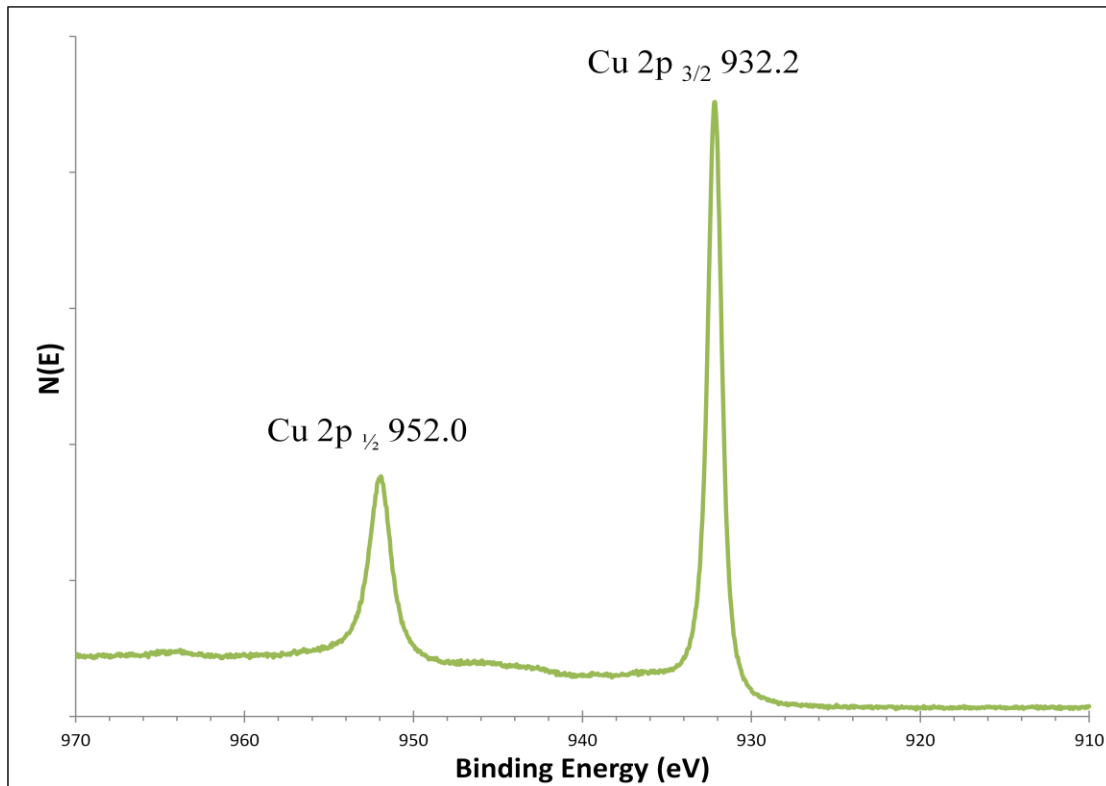


Figure 49b. High-resolution XPS multiplex of Cu 2p region.



Powder X-ray diffraction spectra of the as-deposited films on Pd and Pt substrates showed polycrystalline Cu at all deposition temperatures. The surface morphologies of the films were examined by AFM and SEM. The AFM rms surface roughnesses of 20 nm thick films deposited at 140 and 160 °C on Pd were 1.9 and 2.0 nm, respectively (Figure 50). The rms surface roughnesses of 20 nm thick films deposited on Pt were 1.8 nm at 140 and 160 °C (Figure 51). Top-down SEM views of 20 nm thick Cu films on Pd and Pt were featureless. Sheet resistivities of 20 nm thick Cu films grown on Pd substrates ranged from 3.2 to 4.6 Ω/sq , which translates to bulk resistivity values of 6.4 to 9.2 $\mu\Omega \text{ cm}$. Sheet and bulk resistivity values for 20 nm thick films grown on Pt substrates were 7.8 to 10.7 Ω/sq and 15.6 to 21.4 $\mu\Omega \text{ cm}$, respectively. For comparison, the bulk resistivity of Cu metal is 1.72 $\mu\Omega \text{ cm}$ at 20 °C,¹⁰² the bulk resistivities of 20 nm thick sputtered Cu films is 3–6 $\mu\Omega \text{ cm}$,¹⁰² and the resistivities of the Pd and Pt substrates were 15 and 39 Ω/sq , respectively. Accordingly, the resistivity values of the Cu films grown on Pd and Pt substrates are similar to those of high purity sputtered Cu films. Additionally, the sheet resistivities of Cu films on Pd were measured with respect to the number of cycles (Figures 52). This plot demonstrates a steep sheet resistivity drop in the early stage of the growth process, which suggests the growth of continuous Cu films.

Figure 50. AFM images of Cu films surfaces deposited at 140 (top, rms roughness = 1.9 nm) and 160 °C (bottom, rms roughness = 2.0 nm) on Pd.

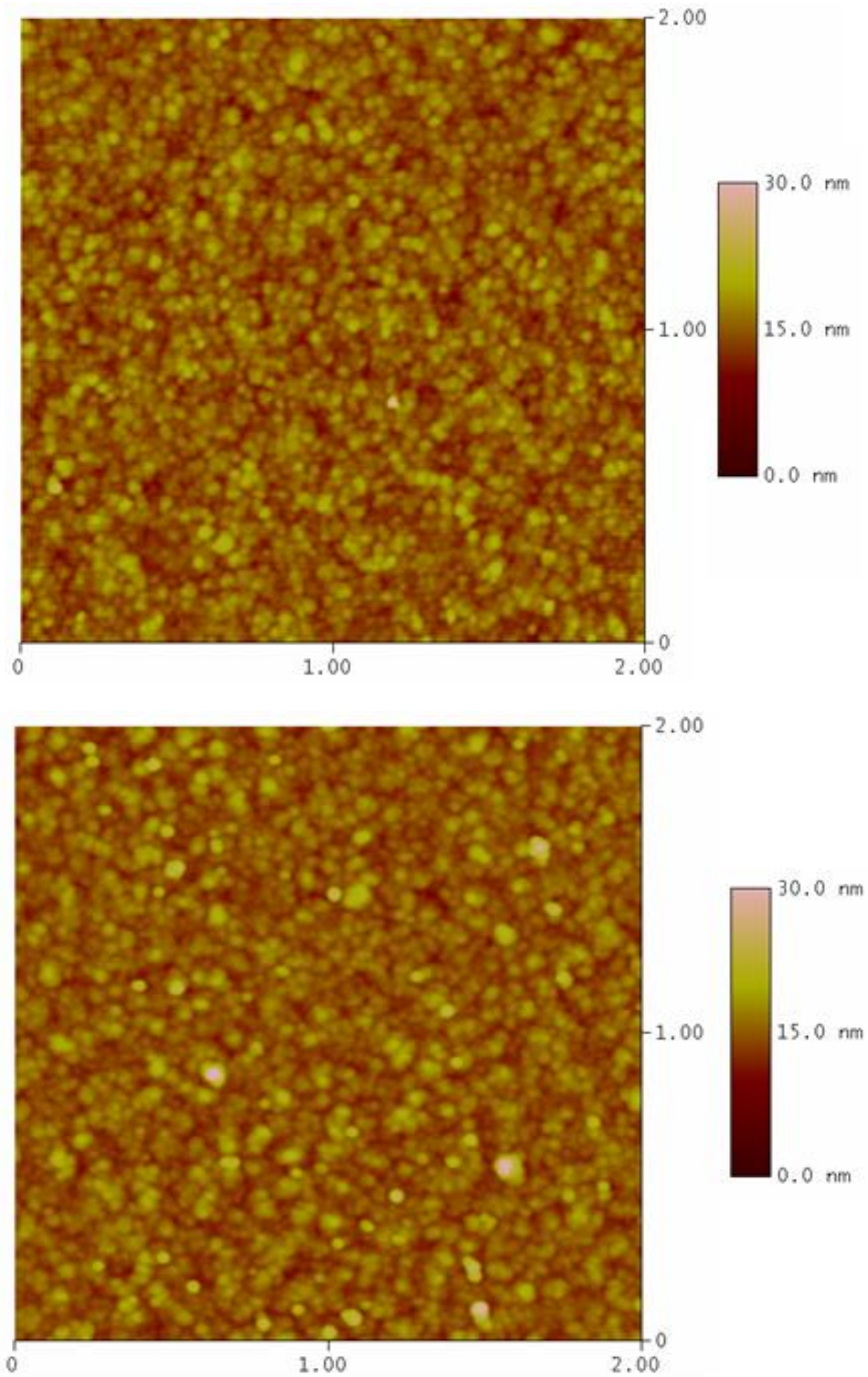


Figure 51. AFM images of Cu films surfaces deposited at 140 (top, rms roughness = 1.8 nm) and 160 °C (bottom, rms roughness = 1.8 nm) on Pt.

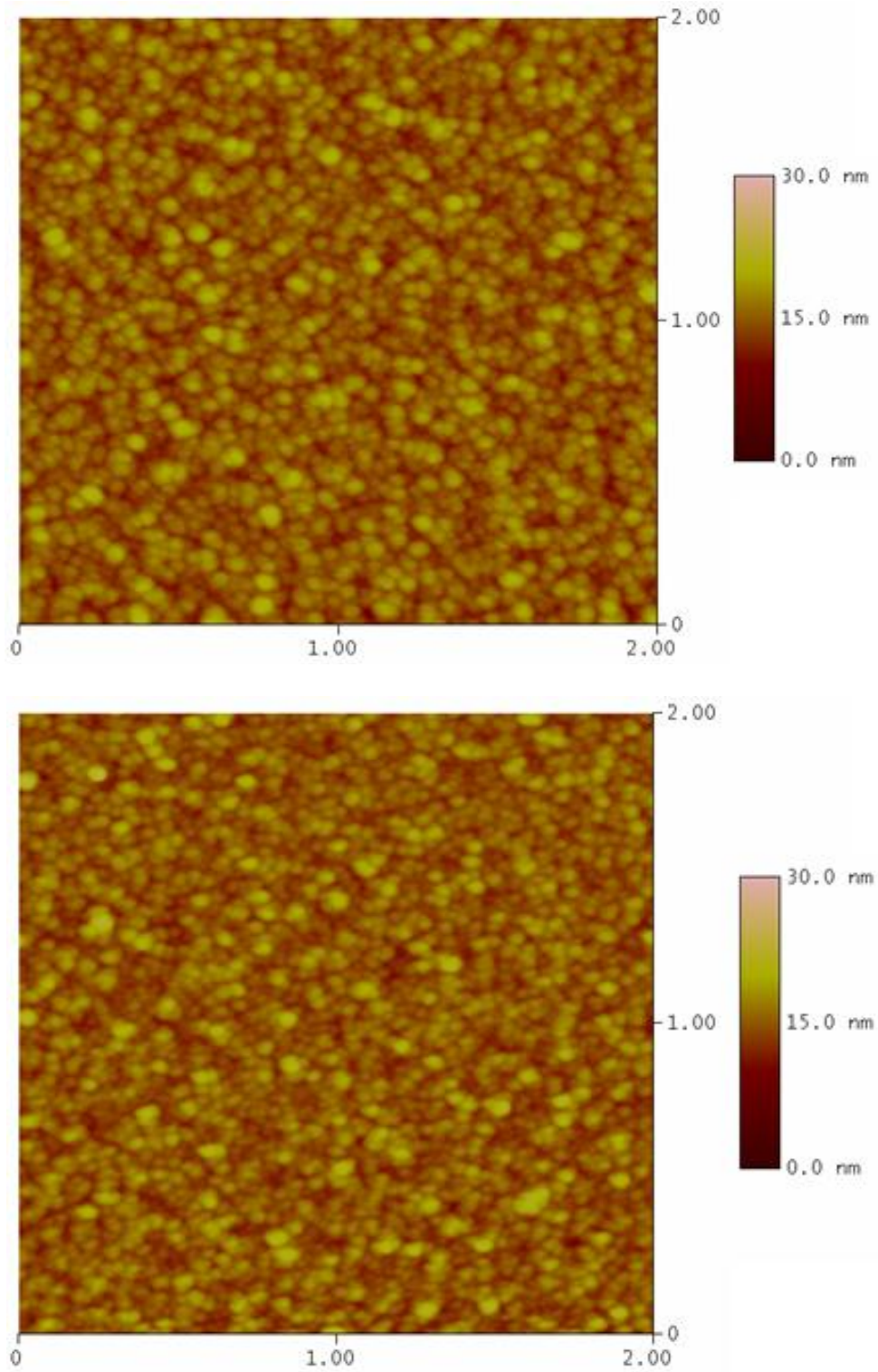
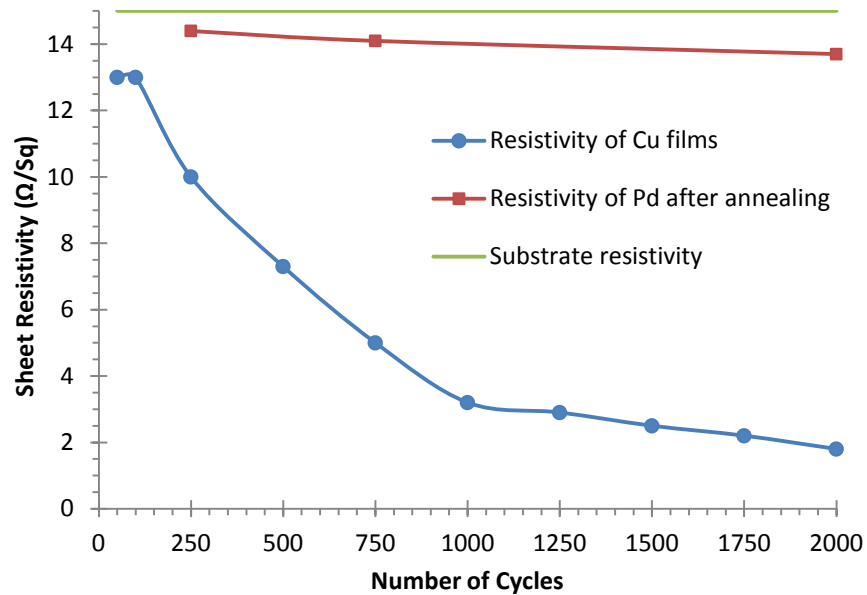
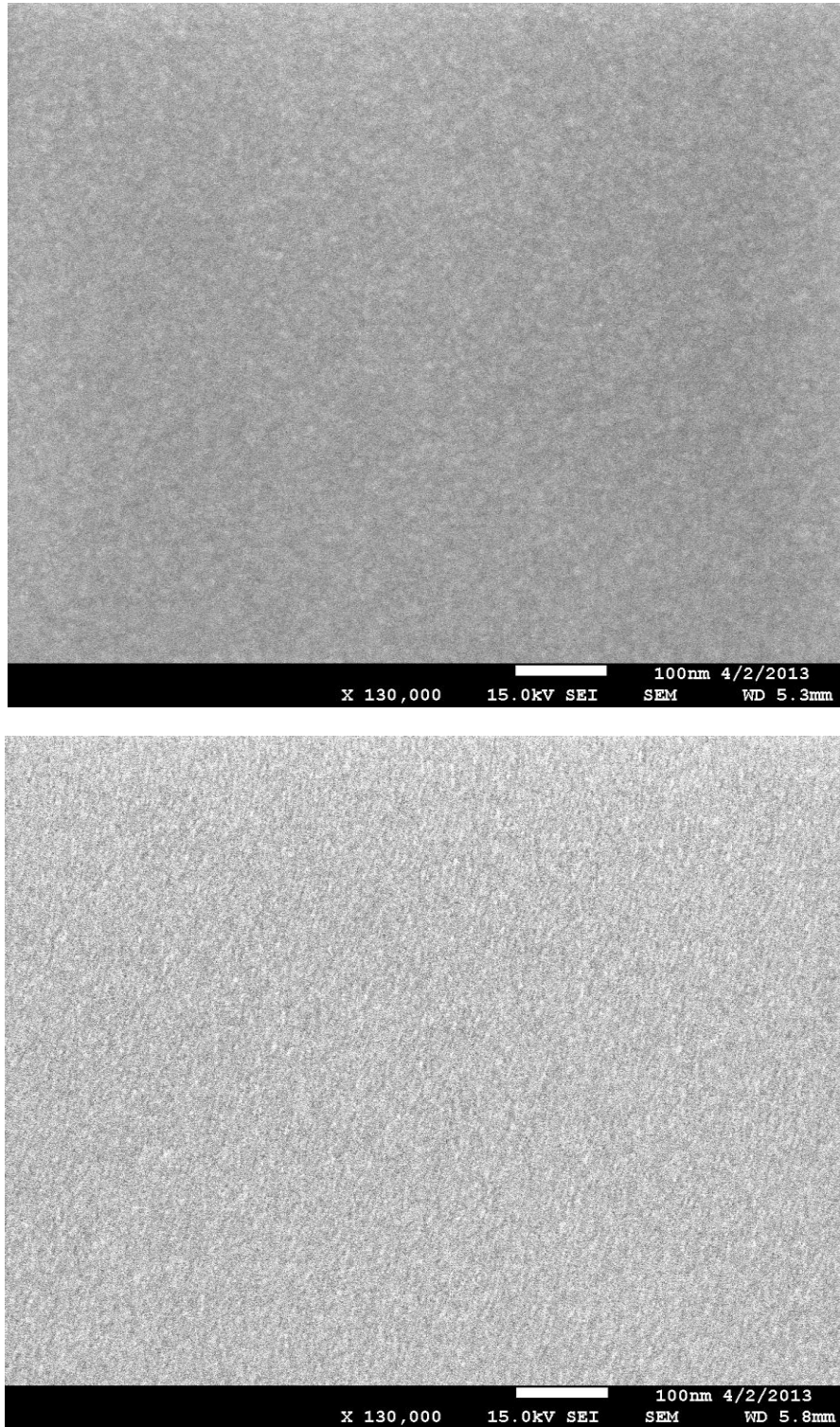


Figure 52. Sheet resistivity as a function of the number of deposition cycles at a growth temperature of 150 °C on Pd.



The initial stages of Cu film growth on the Pd and Pt substrates were investigated by examining top-down SEM micrographs after 50 and 100 cycles, at a growth temperature of 150 °C. On both substrates, no islanding and no surface structure was observed (Figure 53). In addition, Figure 52 shows a sheet resistivity drop even after 50 cycles, which suggests a continuous Cu layer (Figure 52, blue line) is formed after 50 cycles. Annealing studies of the substrates also suggest that this drop is not due to the annealed substrate and XPS of these films confirms the presence of metallic Cu. These findings suggest that this process offers efficient Cu nucleation and smooth films even at early stages of growth. The low temperatures used in these depositions reduce the metal atom surface mobility and thereby increase the nucleation at the early stage leading to smooth films. Also, Willis and coworkers have reported that Cu deposited on Pd substrates makes Cu/Pd alloys at 350 °C due to the metal atom migration.^{22a} The formation of Cu/Pd alloy in the present deposition study may have enhanced the nucleation affording smooth films at the early stages of the film growth.

Figure 53. SEM views of Cu films deposited at 150 °C on Pd substrate (top) and Pt substrate (bottom) after 50 cycles.



6.3 Conclusions

Low temperature ALD growth of high purity, low resistivity Cu metal films was demonstrated using binary and ternary processes. The films grown by the ternary process are of higher quality than the films obtained from the binary process, due to the good nucleation of the former. The deposition of smooth and continuous ~2 nm thick Cu films was demonstrated, suggesting a good nucleation at the early stage of the film growth. The deposition of continuous, smooth Cu layer at this thickness (~2 nm) is not natural, because Cu tends to agglomerate and/or high deposition temperatures increase the surface atom mobility to afford discontinuous rough films. Gordon also has reported the deposition of conformal continuous Cu metal films (~1 nm) on Co and Ru substrates at the temperatures between 150 and 190 °C.¹⁰³

Recently, low temperature Cu ALD processes have been reported. Examples of low temperature thermal Cu ALD processes include **46**/ZnEt₂ at 100-150 °C,²³ CuL₂/ZnEt₂ at 120-150 °C (L = β-ketiminate, β-diketiminate),⁶⁷ and **46**/formic acid/hydrazine at 100-170 °C.²⁴ However, the processes using ZnEt₂ lead to Cu/Zn alloys through competitive thermal decomposition of ZnEt₂, perhaps even at the lowest growth temperatures.⁶⁷ The **46**/formic acid/hydrazine process affords high purity Cu films,²⁴ however hydrazine may present handling issues due to its toxicity. This work demonstrates the use of BH₃(NHMe₂) as the reducing co-reagent and BH₃(NHMe₂) is easy to handle which increases the viability of this Cu process. Also, this Cu ALD process does not incorporate unwanted impurities as Zn in the film.

6.3 Experimental Section

General Considerations. Precursor **46** was synthesized according to a literature procedure,^{64d} and was purified by sublimation. The borane adducts were purchased from Alfa Aesar and used as received. Prime grade Si(100) substrates with native oxide were obtained from

Silicon Quest International. The other substrates were obtained from Intel Corporation. The lines in the saturation and ALD window plots were drawn by connecting the data points. The lines in the thickness versus number of cycles plots represent the best fit curves of the data points.

Film Depositions. An R-75BE ALD reactor manufactured by Picosun Oy was used for thin film deposition experiments. The pressure of the reactor was kept at 8–12 mbar under a flow of nitrogen (99.9995%), which was supplied by a Texol GeniSys nitro Generator. Nitrogen obtained from this generator was used as both the carrier and purge gas. The deposition of Cu metal thin films was studied with **46** as the copper source and $\text{BH}_3(\text{NHMe}_2)$ as the reducing agent. Formic acid was used in the deposition experiments carried out on Pd and Pt substrates. The sublimation temperature of **46** and $\text{BH}_3(\text{NHMe}_2)$ were 100 and 80 °C, respectively, at the reactor pressure. The substrate temperatures were varied from 110 to 175 °C. The pulse lengths of **46** and $\text{BH}_3(\text{NHMe}_2)$ and nitrogen purge lengths were varied to determine the extent of surface saturation, as described in the text. Films from binary process were grown on 5 nm of sputtered Ru 100 nm thermal SiO_2 . The surface ruthenium oxide layer was not removed prior to deposition. Films from the three step process were grown on Pd (15 nm)/Ti (2 nm)/ SiO_2 (100 nm) or Pt (20 nm)/Ti (2 nm)/ SiO_2 (100 nm).

Film Characterization Methods. Film thicknesses were measured using cross-sectional SEM micrographs collected on a JEOL-6510LV electron microscope. Growth rates were calculated by dividing the measured film thickness by the number of deposition cycles. Film thicknesses were measured at three positions of the film to evaluate the uniformity. The measured film thicknesses varied < 5% across the substrates. Powder X-ray diffraction experiments were performed on a Rigaku R200B 12 kW rotating anode diffractometer, using Cu α radiation (1.54056 Å) at 40 kV and 150 mA. AFM micrographs were obtained using a

MultiMode nanoscope IIIa (Digital Instruments, VEECO). The samples were measured using the tapping mode in air with an E scanner with a maximum scanning size of 12 μm at a frequency of a 1 or 2 Hz. Tap150AI-G tip was used with a resonance frequency of 150 kHz and a force constant of 5 N m^{-1} . Surface roughness was calculated as root-mean-square (rms) values. XPS analyses were performed with a Perkin-Elmer 5500 XPS system using monochromatized Al $K\alpha$ radiation. The surface was sputtered using 0.5 kV Ar ions.

CHAPTER 7

Low Temperature Thermal Atomic Layer Deposition of Ni, Co, Fe, Mn, and Cr Metal Thin Films Using Borane Dimethylamine as the Reducing Co-Reagent

7.1 Introduction

The ALD growth of noble metals and Cu films has been well developed due to their positive reduction potentials. However, as described in Chapter 1, ALD growth of other first row transition metal containing films is poorly documented due to the high negative reduction potentials of their M(II) ions. Thermal ALD growth of Ni, Co, and Fe films has been reported using the amidinate precursors $M(\text{RNCMeNR})_2$ ($R = i\text{Pr}$ or $t\text{Bu}$) and H_2 at $250\text{ }^\circ\text{C}$.^{22b} Another process comprising (2-*tert*-butylallyl)Co(CO)₃ and 1,1-dimethylhydrazine claimed the growth of Co metal films at a substrate temperature of $140\text{ }^\circ\text{C}$.³⁹ Moreover, PEALD processes for the deposition of Ni, Co, Fe, and Mn have been reported.¹⁸ PEALD has its limitations because films deposited in high aspect ratio features tend to be rough and non-conformal. Therefore, thermal ALD is preferred over PEALD. The deposition of Cr thin films has never been reported by any ALD method.¹⁸

The major reason for the scarcity of thermal ALD for these metals is lack of a powerful reducing agent. The screenings of the reducing power of commercially available reducing co-reagents were described throughout this dissertation. Chapter 2 demonstrates that α -imino alkoxide precursors react with $\text{BH}_3(\text{NHMe}_2)$ to afford the corresponding metals in tetrahydrofuran. Moreover, Chapter 6 describes Cu ALD growth using $\text{BH}_3(\text{NHMe}_2)$ as the reducing co-reagent. Therefore, $\text{BH}_3(\text{NHMe}_2)$ is a viable reducing co-reagent to use in metal

ALD processes. Most importantly, a reducing co-reagent that can reduce more than one M(II) might enable the deposition of alloy thin films.

In this chapter, thermal ALD studies of Ni, Co, Fe, Mn, and Cr are discussed. α -Imino alkoxide precursors described in Chapter 2 and $\text{BH}_3(\text{NHMe}_2)$ were used as metal precursors and reducing co-reagent, respectively. The precursors used in this study include, **2**, **3**, and **7–9**, and the precursors were chosen by assessment of the volatility and thermal stability of **1–15**.

7.2 Results and Discussion

Film depositions were investigated on various substrates that included Ru/SiO₂/Si, Pd/Ti/SiO₂/Si, Pt/Ti/SiO₂/Si, thermal SiO₂, Si with native oxide, and H-terminated Si. Initial studies did not afford metal films on any of these substrates under any deposition conditions. To enhance film growth, a nucleation process was applied prior to the regular ALD cycles. This nucleation process was developed by trial and error. The final nucleation process entailed 50 cycles comprising 20 s pulses of **2**, **3**, **7**, **8**, or **9** and 1 s pulses of $\text{BH}_3(\text{NHMe}_2)$. Nitrogen purge times were 5 s after the metal pulses and 10 s after the $\text{BH}_3(\text{NHMe}_2)$ pulses. The nucleation step was followed by regular ALD cycles to afford metal films only on the Ru substrates. SEM investigations of the Ru substrates after the nucleation processes did not show metal films within the measurement uncertainties (± 1 nm). However, these modified Ru substrates led to metal film growth.

Deposition of Cr Metal Films. A complete ALD study was carried out on Cr films, using **9** and $\text{BH}_3(\text{NHMe}_2)$. Saturative growth occurred at 180 °C with pulse lengths of ≥ 4.0 s for **9** (Figure 54) and ≥ 1.0 s for $\text{BH}_3(\text{NHMe}_2)$ (Figure 55). As shown in Figure 56, an ALD window was observed between 170 and 185 °C, with a growth rate of 0.08 Å/cycle in this range. A plot of thickness versus number of cycles revealed linear growth up to 1000 cycles, however the film

thickness plateaued at > 1000 cycles (Figure 57). Ni, Co, and Mn films grown with > 1000 cycles were also the same thicknesses as those grown with 1000 cycles. The origins of this effect are not clear, however it is possible that the Ru substrate plays a catalytic role in activating the $\text{BH}_3(\text{NHMe}_2)$ until the growing metal layer blocks all of the active Ru sites. It is known that $\text{BH}_3(\text{NHMe}_2)$ decomposes thermally at 130 °C and by the catalyst $\text{RuMe}_2(\text{PMe}_3)_4$ to $[\text{BH}_2(\text{NMe}_2)_2]_2$ and H_2 (Chart 13).¹⁰⁵ Since the depositions were carried out > 130 °C, $\text{BH}_3(\text{NHMe}_2)$ may have been decomposed to $[\text{BH}_2(\text{NMe}_2)_2]_2$ and H_2 . Also, the Ru substrate may have catalyzed the decomposition of $\text{BH}_3(\text{NHMe}_2)$. Assuming that either one of these byproducts is the active reducing agent, deposition studies were carried out using $[\text{BH}_2(\text{NMe}_2)_2]_2$ as the reducing agent. This dimer was synthesized according to the reported procedure.¹⁰⁵ However, these depositions did not afford Cr or other metal films on Ru or on other substrates. Moreover, H_2 is known to have low reactivity toward first row transition metal complexes.¹⁸ Therefore, it is likely that the decomposition of $\text{BH}_3(\text{NHMe}_2)$ forms Ru-H on the Ru substrate and Ru-H is the active reducing agent that is responsible for the film growth. Once all the Ru-H sites are consumed growth process ceases as seen in Figure 57. XPS spectra of an as-deposited Cr film grown at 170 °C showed Cr 2p binding energies consistent with Cr_2O_3 , but Ar ion sputtering for 60–90 seconds led to Cr 2p binding energies that match Cr metal (Figures 58 and 59). Hence, the surfaces of the Cr films are oxidized upon exposure to air, consistent with the easily oxidized nature of Cr metal and other first row transition metals, particularly in nanoscale form.⁶⁸ AFM images of films grown at 170 and 180 °C had rms surface roughnesses of 0.37–0.59 nm, indicating smooth surfaces (Figure 60).

Figure 54. Growth rate as a function of the pulse length of **9** at a substrate temperature of 180 °C.

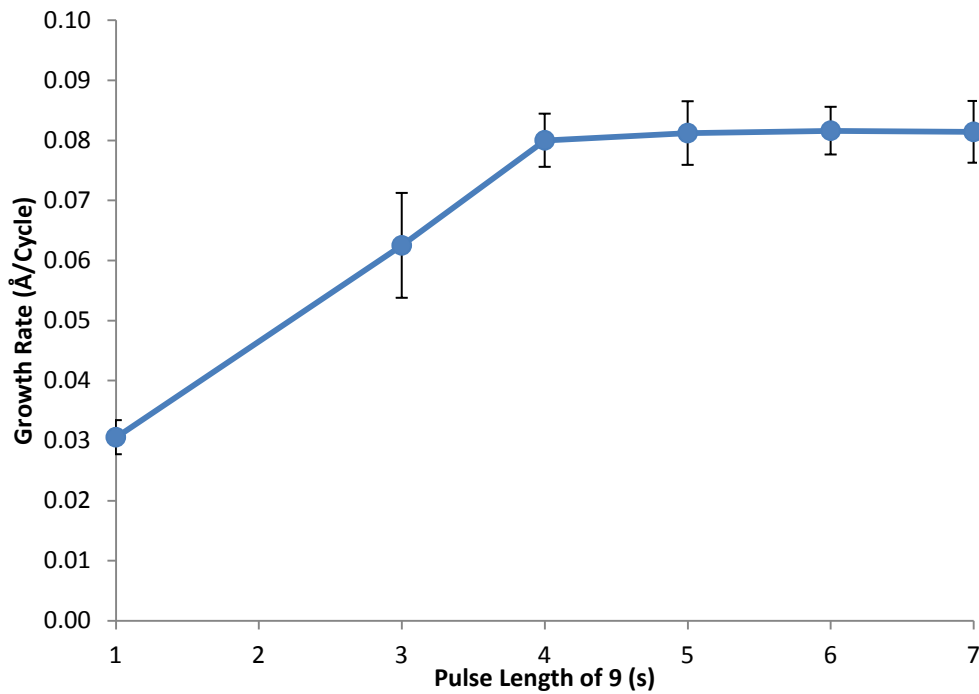


Figure 55. Growth rate as a function of the pulse length of $\text{BH}_3(\text{NHMe}_2)$ at a substrate temperature of 180 °C

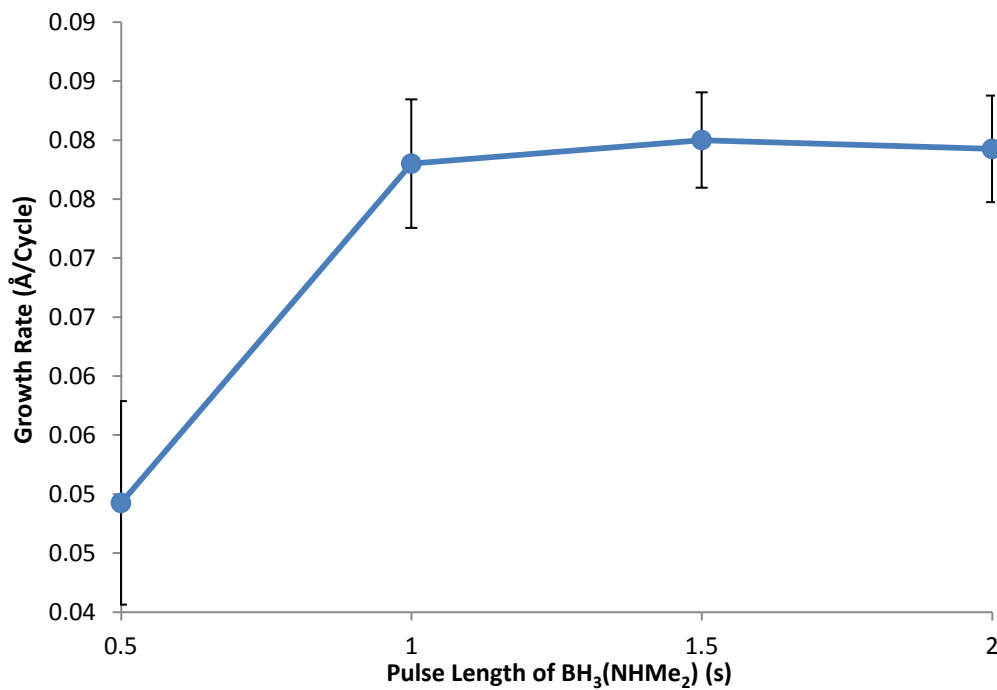


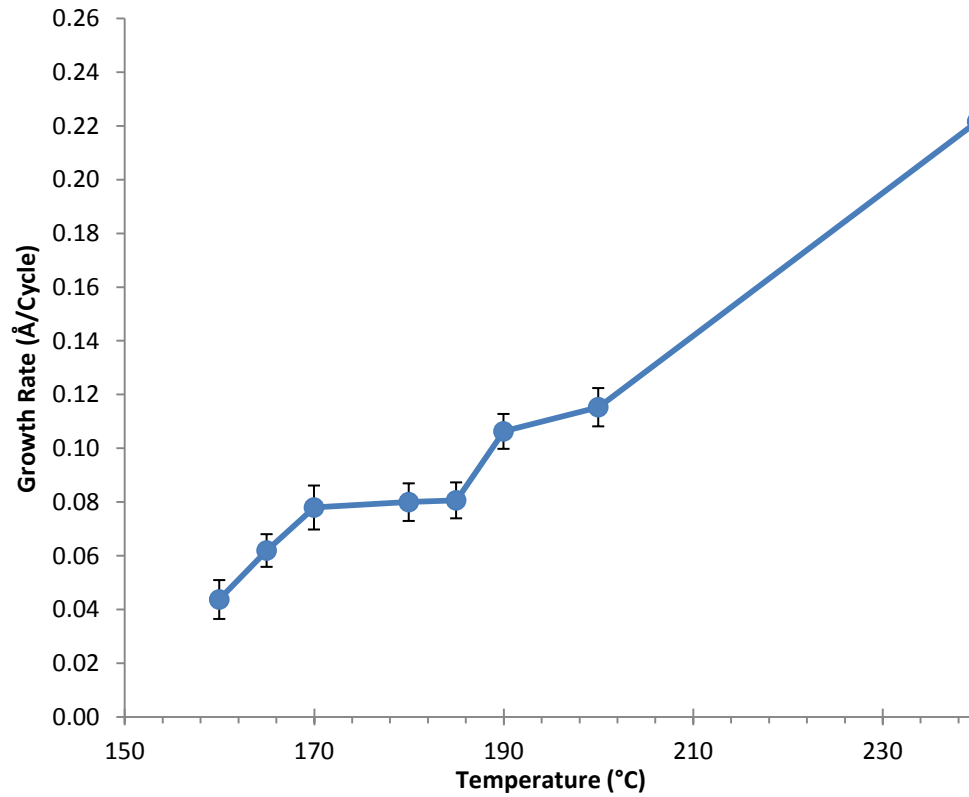
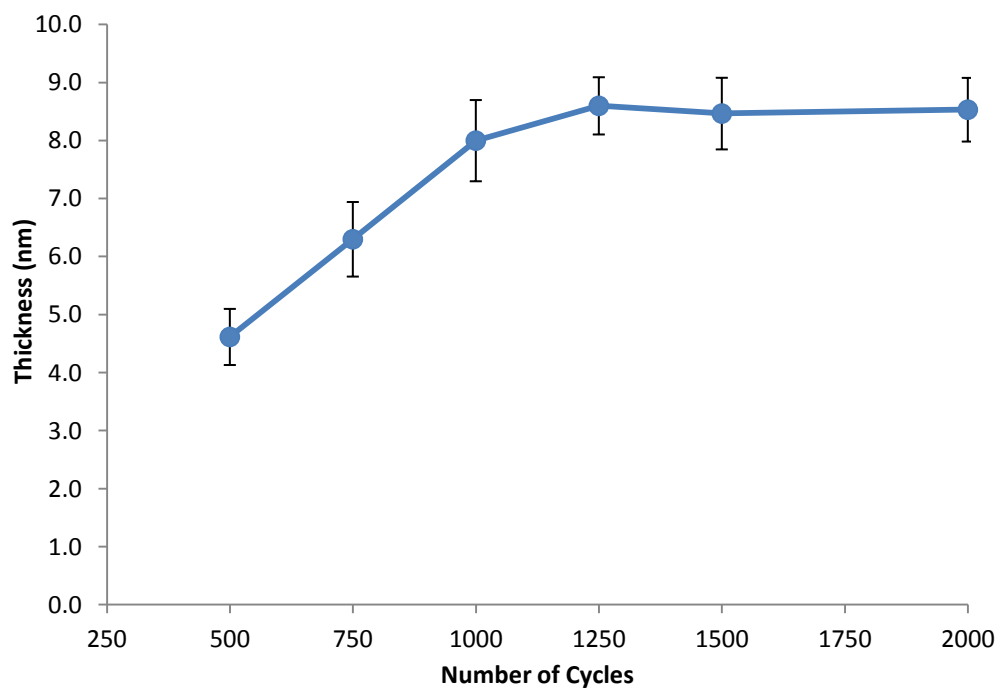
Figure 56. Growth rate of Cr as a function of deposition temperature.**Figure 57.** Cr film thickness as a function of the number of deposition cycles at a deposition temperature of 180 °C.

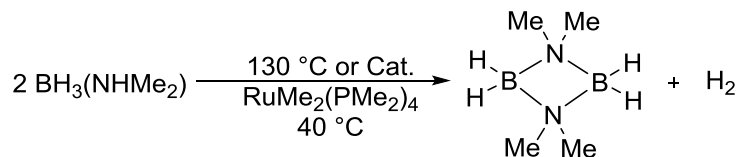
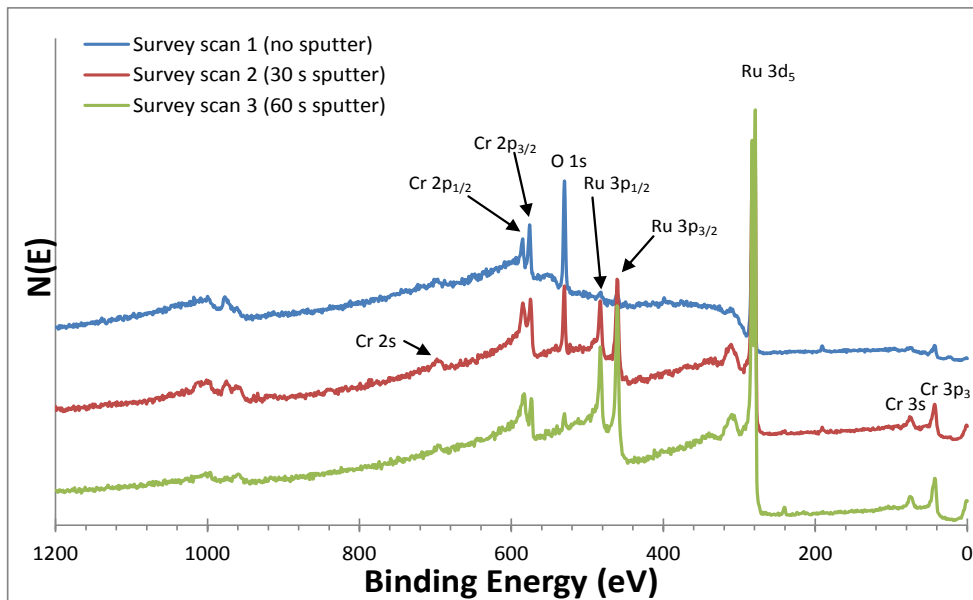
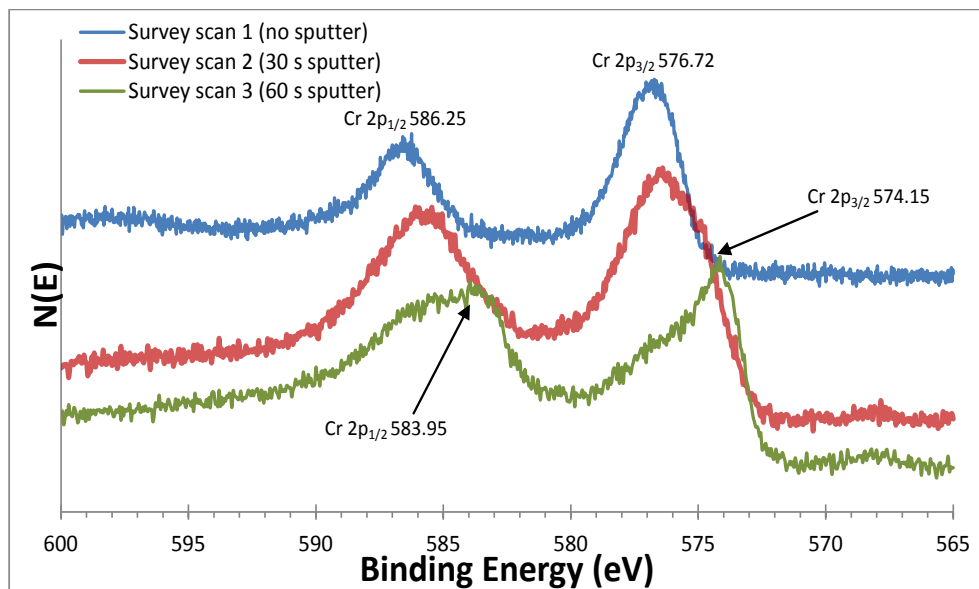
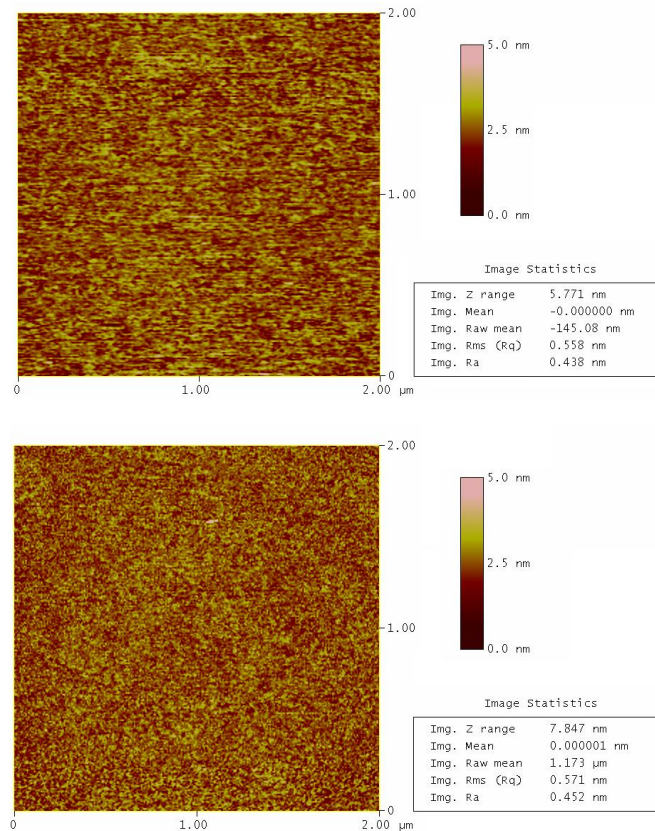
Chart 13. The decomposition of $\text{BH}_3(\text{NHMe}_2)$.**Figure 58.** XPS survey scan of an 8 nm thick Cr film deposited at 170 °C.**Figure 59.** High resolution XPS scan of the Cr 2p region of an 8 nm thick Cr film deposited at 170 °C. Reference 2p binding energies for Cr metal: 583.4 and 574.1 eV; Cr_2O_3 : 586.3 and 576.6 eV.¹⁰¹

Figure 60. AFM images of an 8 nm thick Cr film deposited at 170 °C (top) and 180 °C (bottom).



Deposition of Ni and Co metal films. Complete ALD studies for Ni and Co were carried out using **2** and **3** as metal precursors, respectively, and $\text{BH}_3(\text{NHMe}_2)$ as the reducing co-reagent. Saturative growth was observed at 180 °C with pulse lengths of ≥ 3.0 s for **2** (Figure 61) and ≥ 4.0 s for **3** (Figure 62), and ≥ 1.0 s for $\text{BH}_3(\text{NHMe}_2)$ (Figures 63 and 64). ALD windows are observed between 170 and 190 for the growth of Ni, and between 160 and 200 for Co, with growth rates of 0.08 and 0.07 Å/cycle, respectively (Figures 65 and 66). The thickness versus number of cycles plots revealed the same behavior as observed in the Cr deposition, which is thicknesses plateauing at > 1000 cycles (Figures 67 for Ni and 68 for Co). As observed in the Cr deposition, the XPS spectra of as-deposited Ni and Co films grown at 180 °C showed M 2p binding energies consistent with MO (Figures 69 and 70 for Ni, 71 and 72 for Co). However, Ar ion sputtering for 60–90 seconds led to M 2p binding energies that match Ni and Co metal,

consistent with oxidized thin films upon exposure to air. AFM images of Ni and Co films grown at 170 and 190 °C had rms surface roughnesses of 0.16–0.20 nm and 0.15–0.22 nm, respectively, indicating the smooth surfaces (Figures 73 for Ni, 74 for Co).

Figure 61. Growth rate as a function of the pulse length of **2** at a substrate temperature of 180 °C.

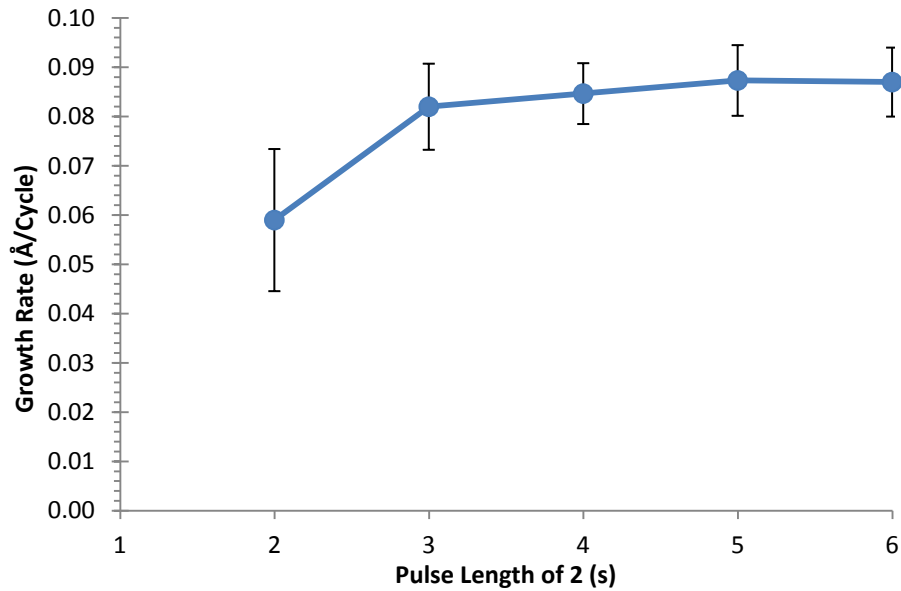


Figure 62. Growth rate as a function of the pulse length of **3** at a substrate temperature of 180 °C.

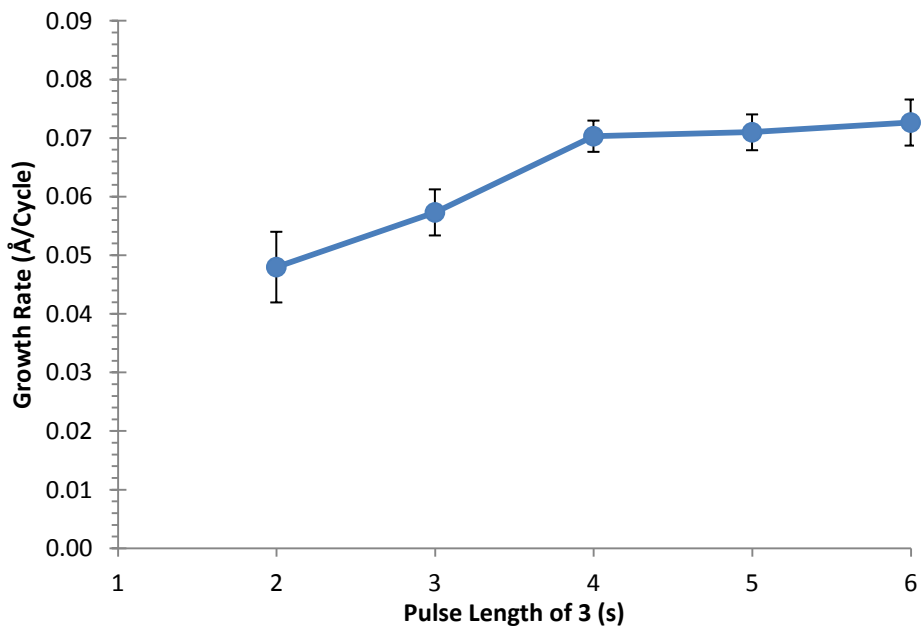


Figure 63. Growth rate as a function of the pulse length of $\text{BH}_3(\text{NHMe}_2)$ at a substrate temperature of $180\text{ }^\circ\text{C}$ for the Ni deposition.

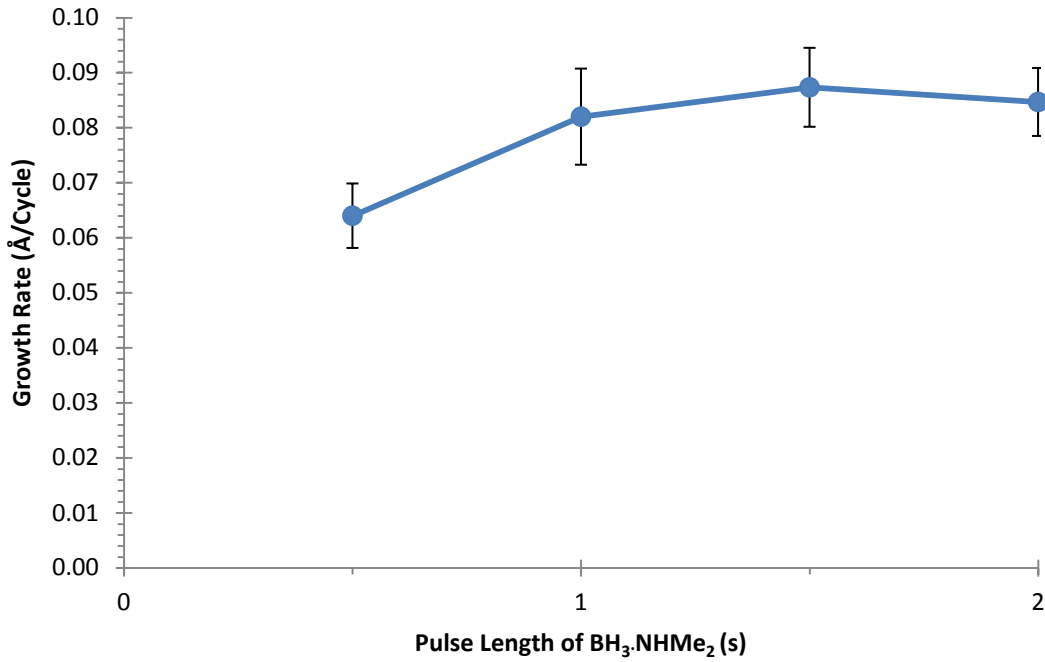


Figure 64. Growth rate as a function of the pulse length of $\text{BH}_3(\text{NHMe}_2)$ at a substrate temperature of $180\text{ }^\circ\text{C}$ for the Co deposition.

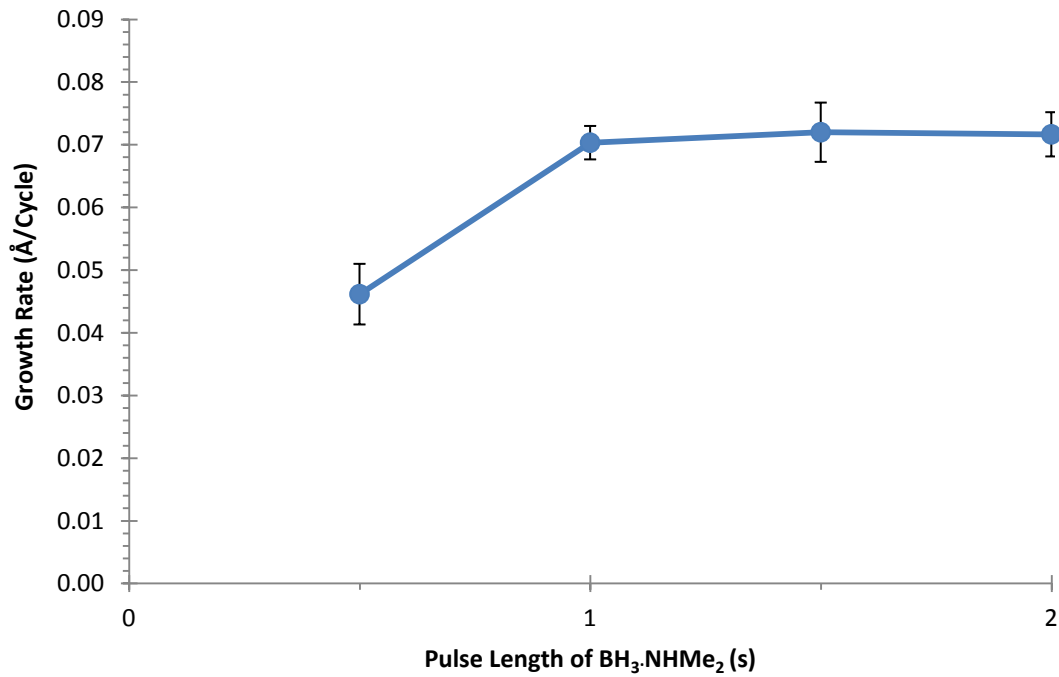


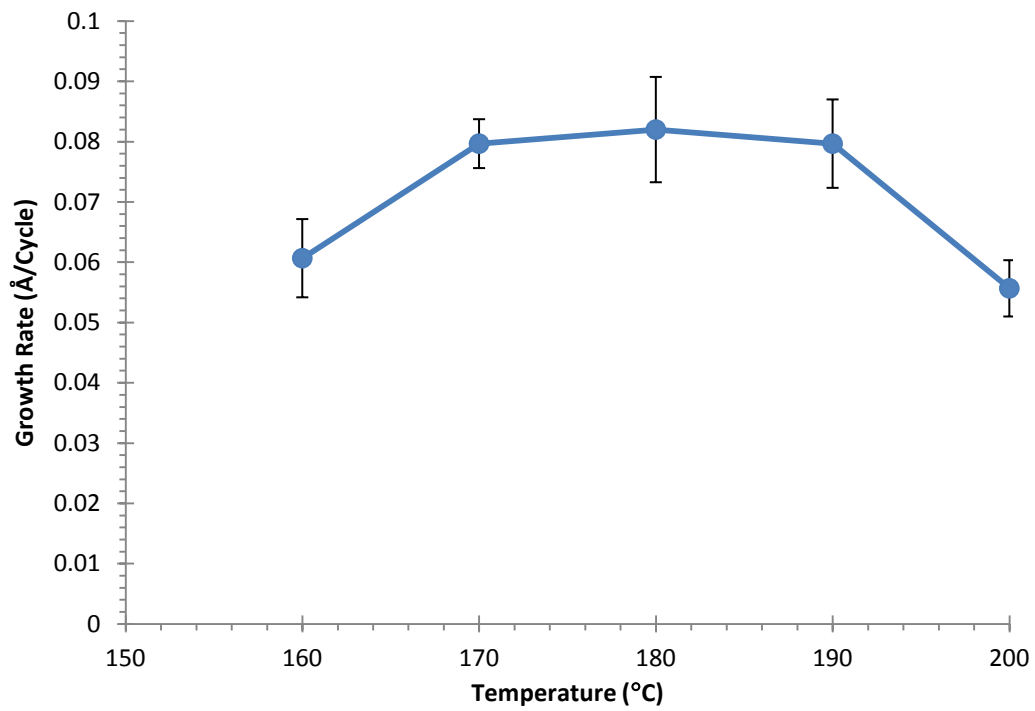
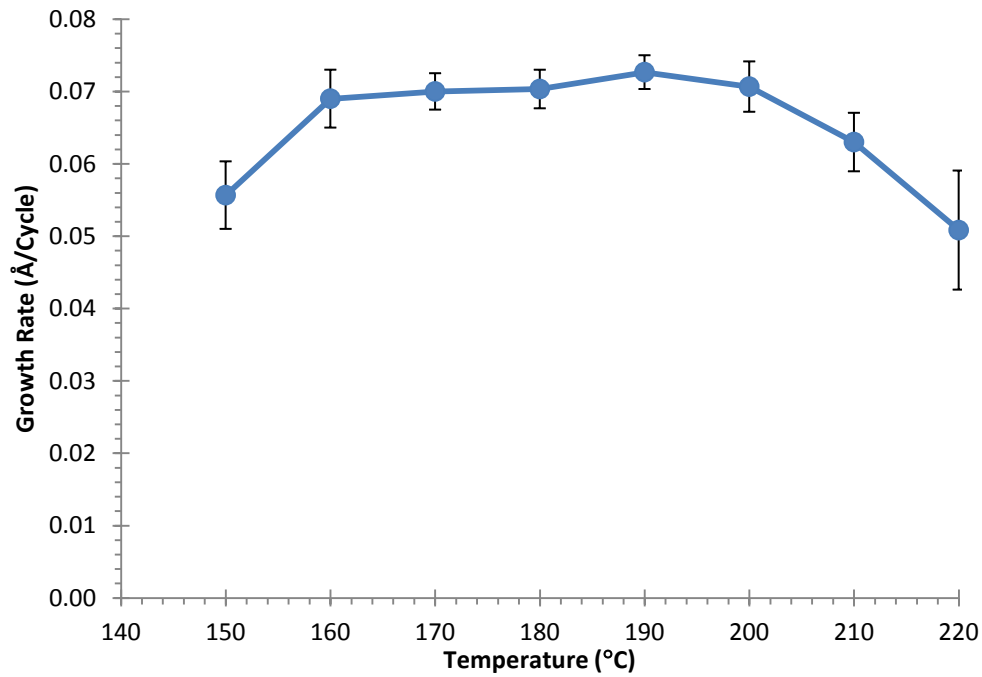
Figure 65. Growth rate of Ni as a function of deposition temperature.**Figure 66.** Growth rate of Co as a function of deposition temperature.

Figure 67. Ni film thickness as a function of the number of deposition cycles at a deposition temperature of 180 °C.

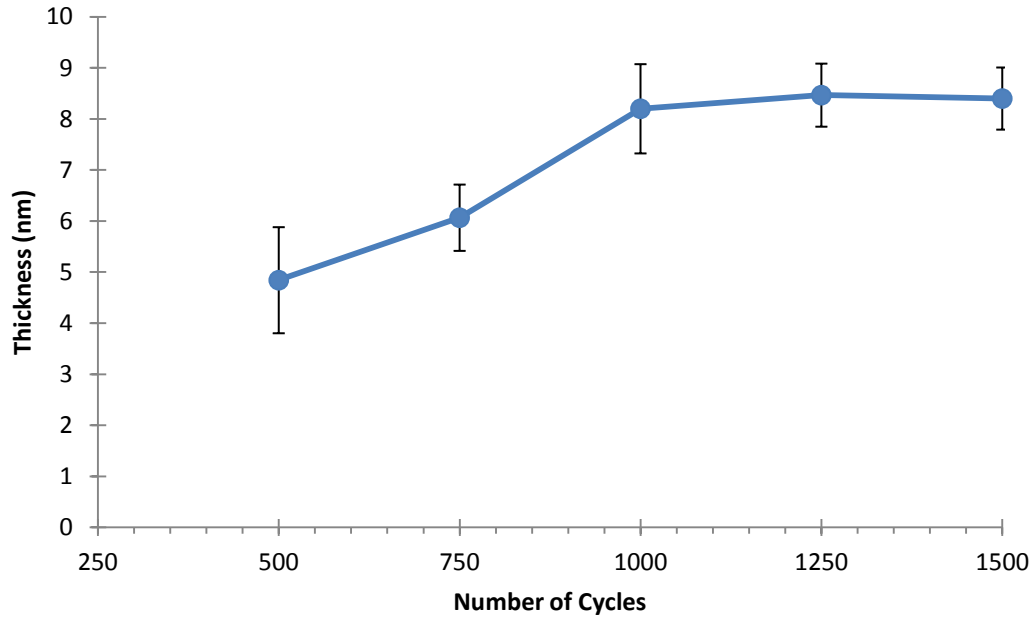


Figure 68. Co film thickness as a function of the number of deposition cycles at a deposition temperature of 180 °C.

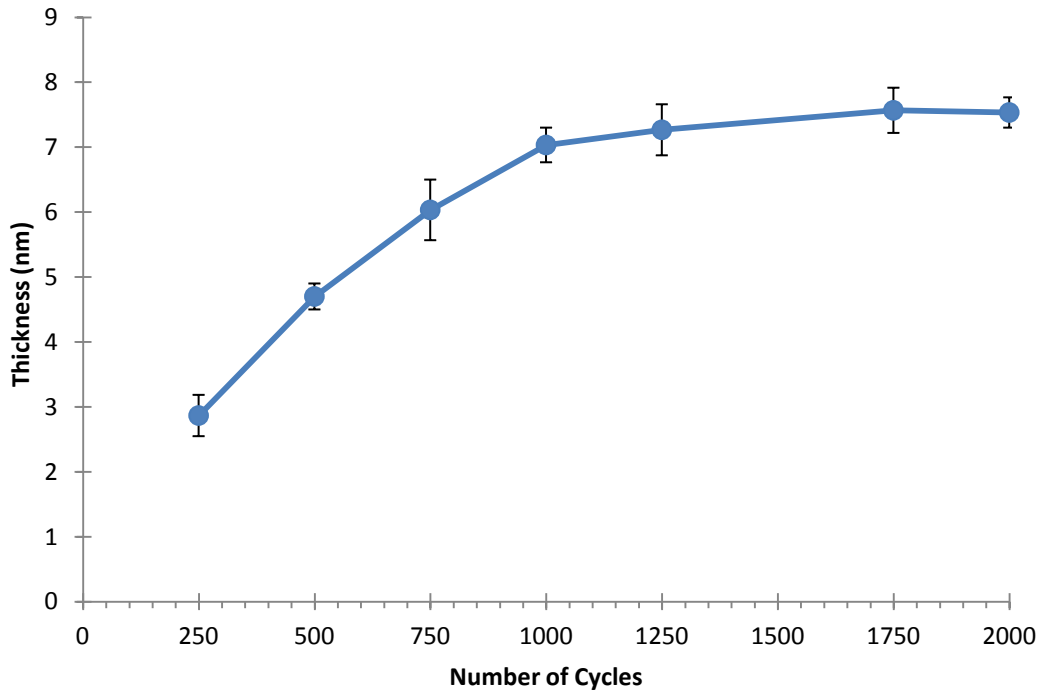


Figure 69. XPS survey scans of an 8 nm thick Ni film deposited at 180 °C.

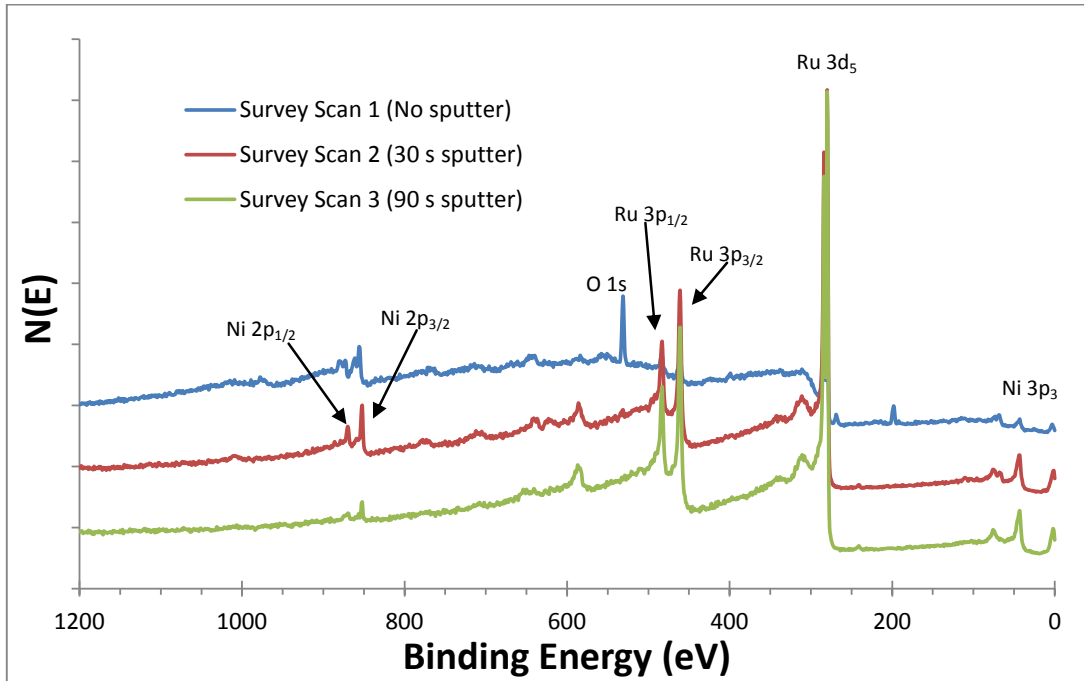


Figure 70. High resolution XPS scan of Ni 2p region of an 8 nm thick Ni film deposited at 180 °C. Reference 2p binding energies for Ni metal: 869.7 and 852.3 eV; NiO: 871.7 and 853.3 eV.¹⁰¹

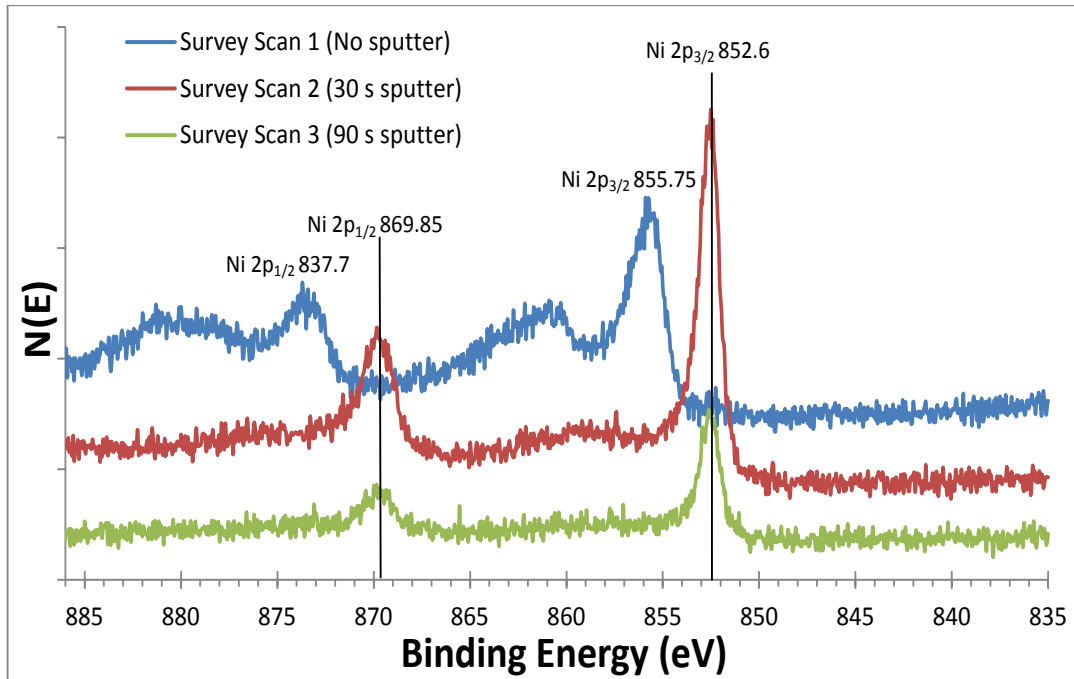


Figure 71. XPS survey scan of a 7 nm thick Co film deposited at 180 °C.

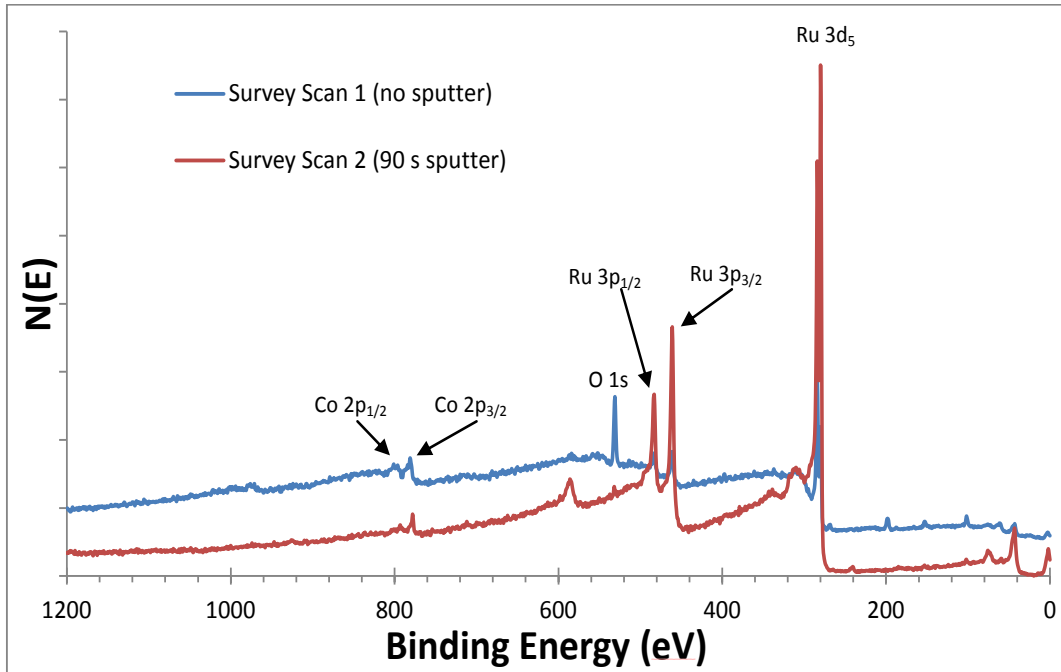


Figure 72. High resolution XPS scan of the Co 2p region of a 7 nm thick Co film deposited at 180 °C. Reference 2p binding energies for Co metal: 792.95 and 777.9 eV; CoO: 795.5 and 780.0 eV.¹⁰¹

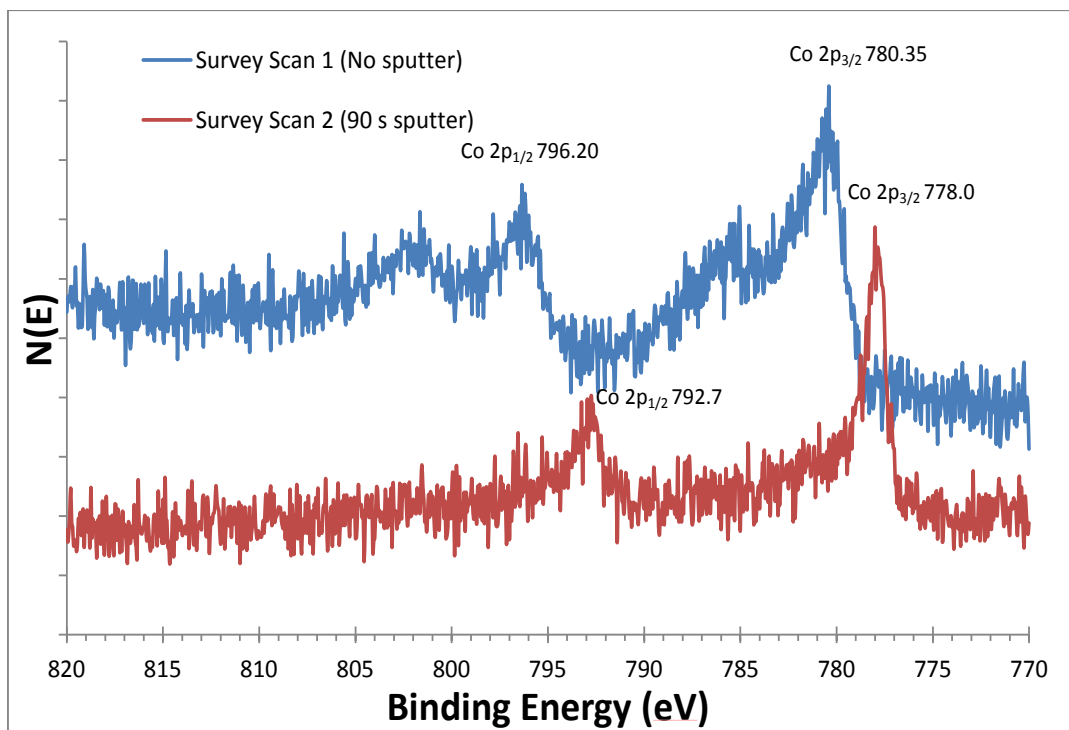


Figure 73. AFM images of an 8 nm thick Ni film deposited at 170 (top) and 190 °C (bottom).

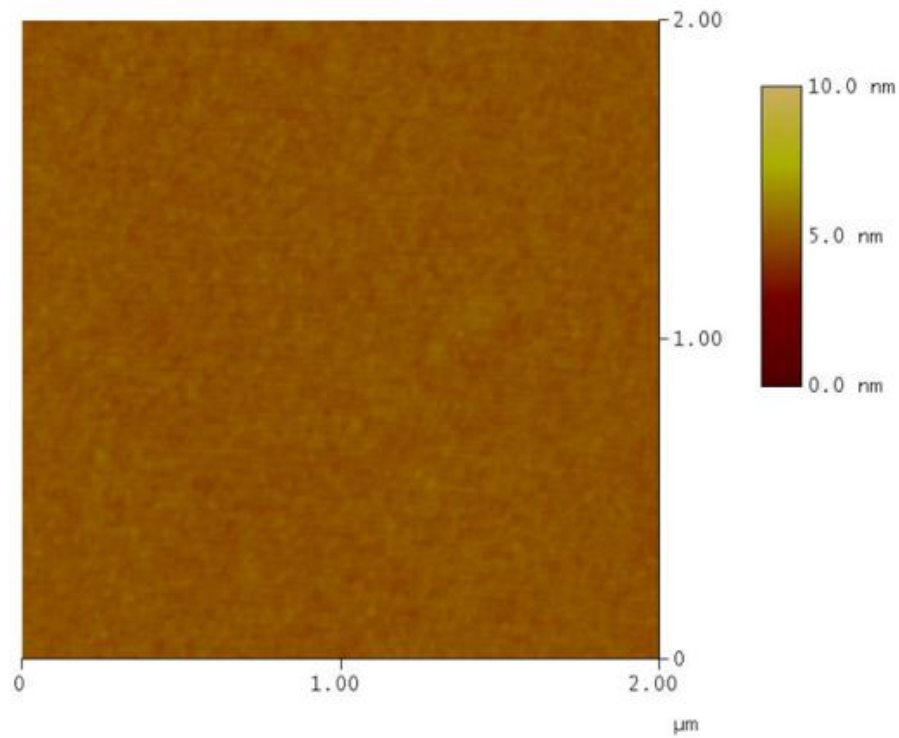
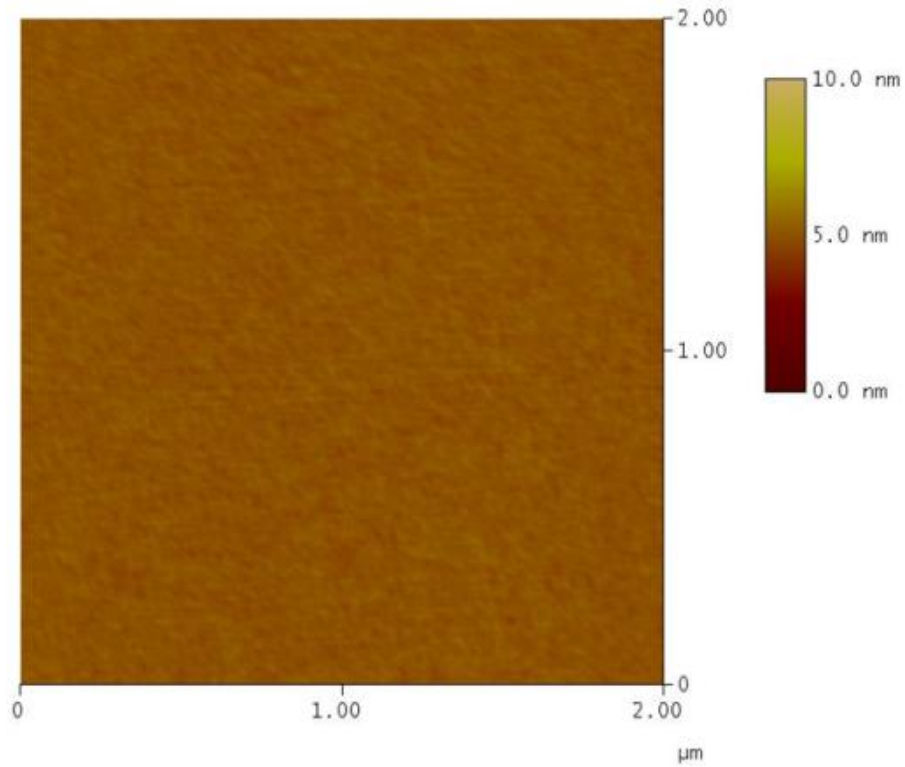
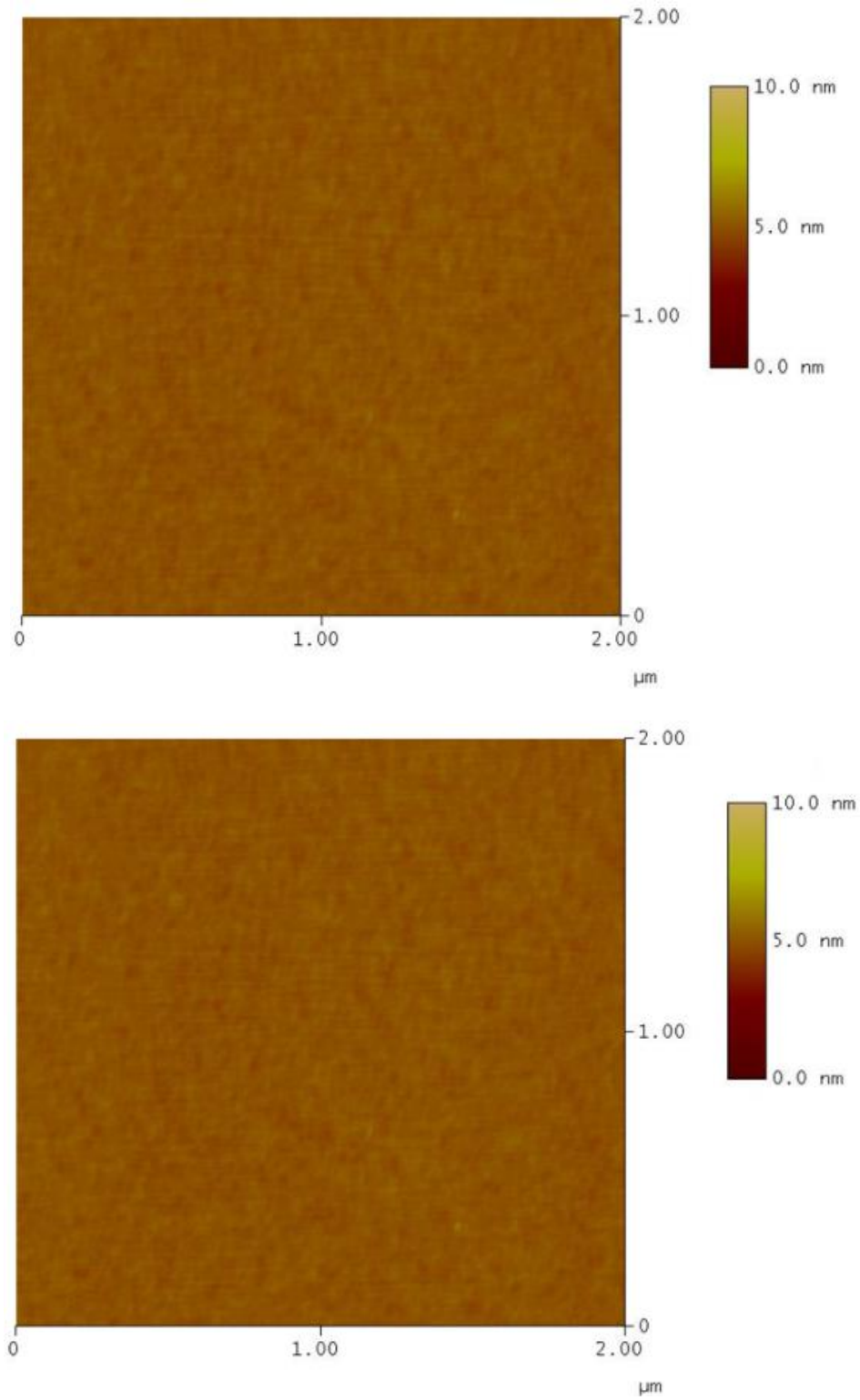


Figure 74. AFM images of a 7 nm thick Co film deposited at 170 (top) and 190 °C (bottom).



Deposition of Fe and Mn metal films. Partial studies were done for the deposition of Fe and Mn metal films. The ALD behavior was established by plotting the saturation curves. Saturative growth was observed with pulse lengths of ≥ 4.0 s at 180 °C for **7** (Figure 75) and at 225 °C for **8** (Figure 76). The XPS spectra of as-deposited Fe films grown at 180 °C showed Fe 2p binding energies consistent with Fe₂O₃. However, Ar ion sputtering for 60–90 seconds led to Fe 2p binding energies that match Fe metal (Figures 77 and 78), consistent with oxidized thin films upon exposure to air. The XPS spectra of Mn films always yielded MnO₂, even after sputtering (Figures 79 and 80), suggesting that Mn films are oxidized completely.

Figure 75. Growth rate as a function of the pulse length of **7** at a substrate temperature of 180 °C.

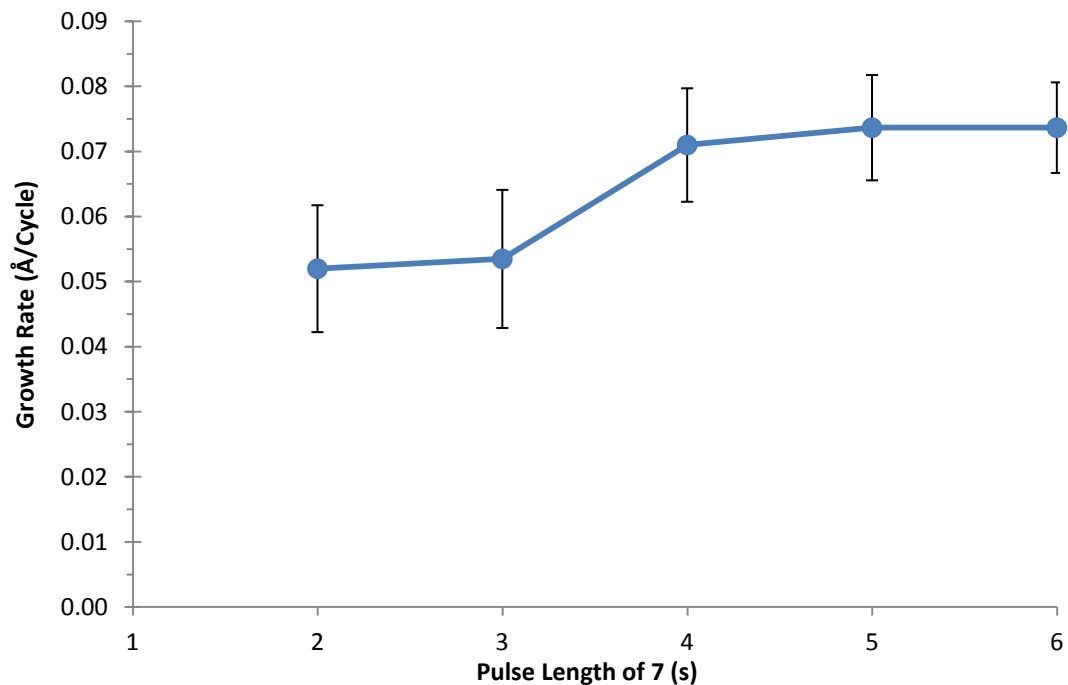


Figure 76. Growth rate as a function of the pulse length of **8** at a substrate temperature of 225 °C.

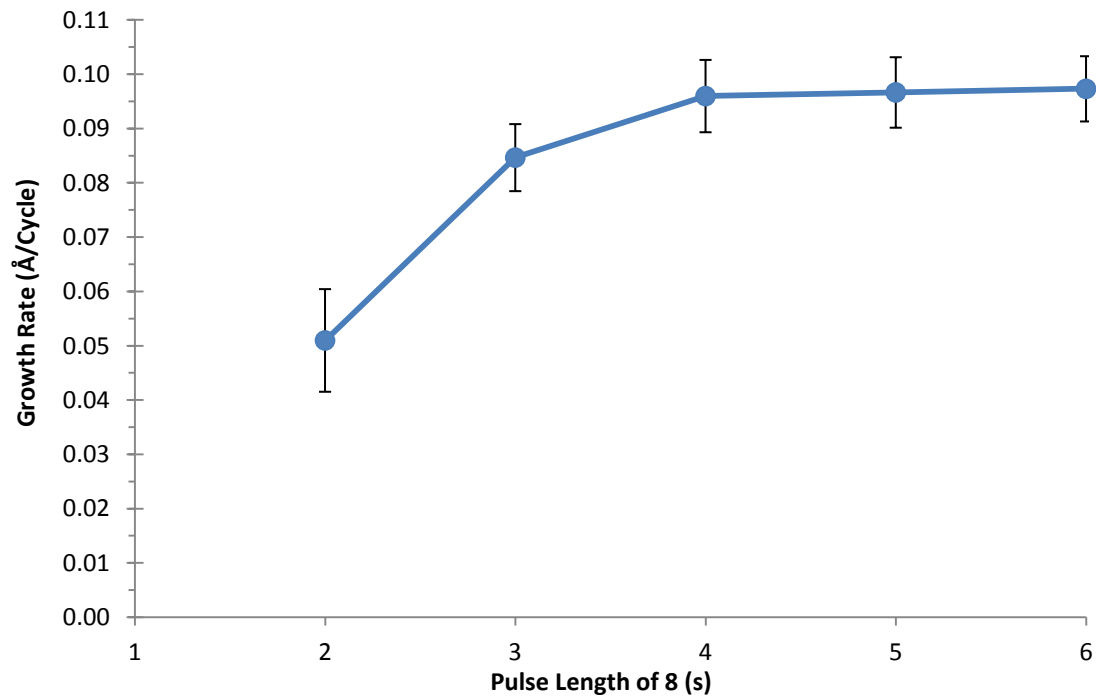


Figure 77. XPS survey scan of a 4 nm thick Fe film deposited at 180 °C.

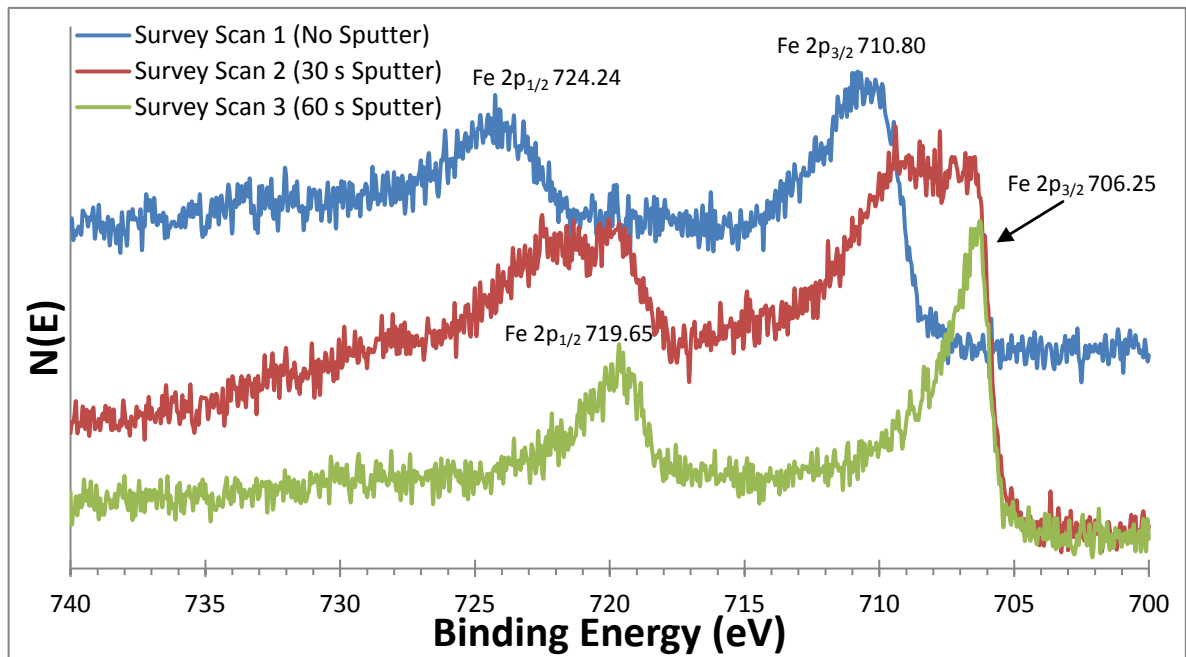


Figure 78. High resolution XPS scan of the Fe 2p region of a 4 nm thick Fe film deposited at 180 °C. Reference 2p binding energies for Fe metal: 719.95 and 706.75 eV; Fe₂O₃: 724.3 and 710.7 eV.¹⁰¹

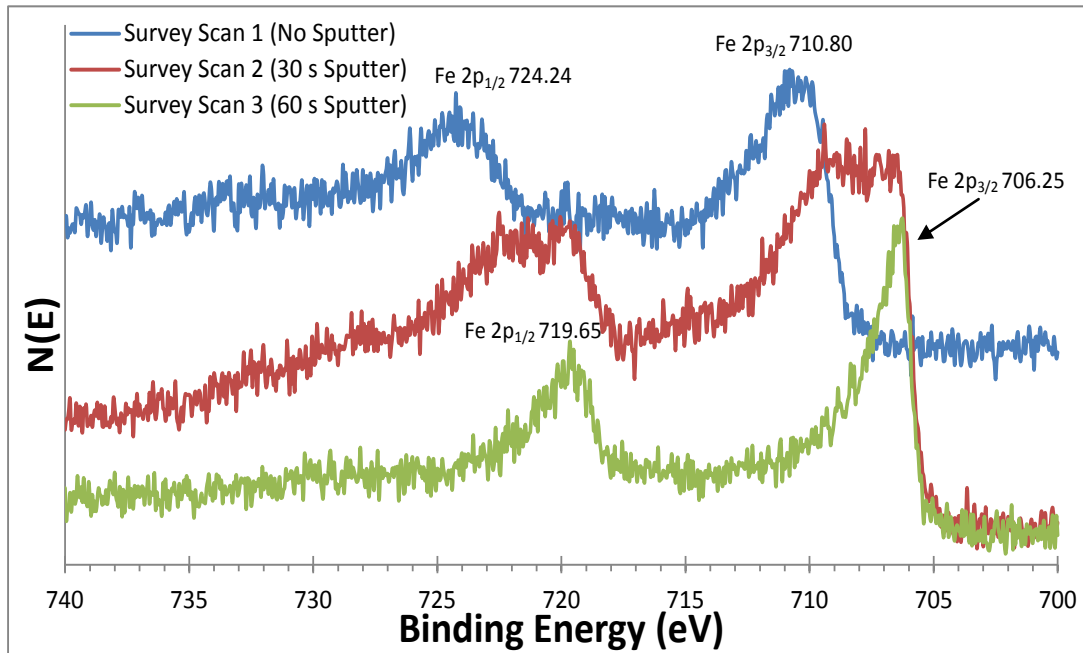


Figure 79. XPS survey scan of a 10 nm thick Mn film deposited at 225 °C.

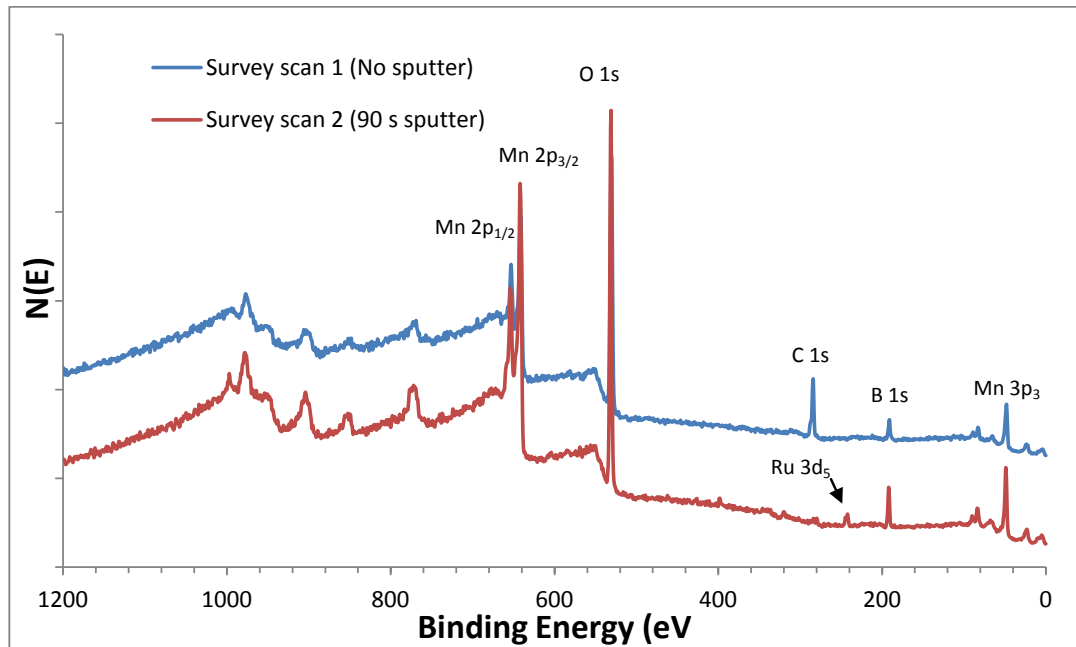
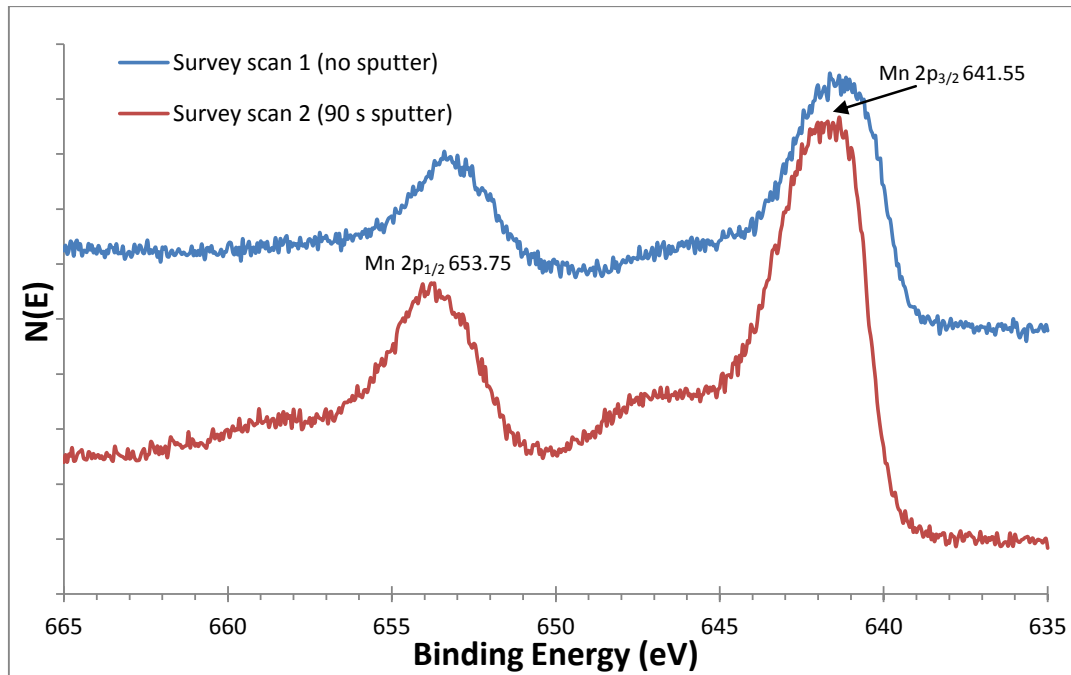


Figure 80. High resolution XPS scan of the Mn 2p region of a 10 nm thick Mn film deposited at 225 °C. Reference 2p binding energies for Mn metal: 650.05 and 638.8 eV; MnO₂: 653.9 and 642.2 eV.¹⁰¹



7.3 Conclusions

This chapter has demonstrated the thermal ALD growth of Ni, Co, Fe, and Cr films using $\text{BH}_3(\text{NHMe}_2)$ as the co-reagent. Cr films have not been previously grown by ALD and this is the first report of the deposition of Cr metal films by any chemical vapor method (ALD or CVD). In a previous report, thermal ALD growth of Ni, Co, and Fe films was claimed using the amidinate precursors $\text{M}(\text{RNCMeNR})_2$ ($\text{R} = \text{iPr}$ or tBu) and H_2 at 250 °C.^{22b} While the growth rates in these processes (0.04-0.12 Å/cycle) were similar to those reported herein, the 250 °C deposition temperature is well above the decomposition point of $\text{Ni}(\text{iPrNCMeNiPr})_2$ (180 °C¹⁰⁴) and the Co and Fe precursors.¹⁸ Hence, these processes are almost certainly strongly enhanced by precursor decomposition (CVD-like growth). A process comprising (2-*tert*-butylallyl)Co(CO)₃ and 1,1-dimethylhydrazine claimed the growth of Co metal films at a substrate temperature of 140 °C,³⁹ although the basic ALD growth parameters of this process were not reported. In the present

study, the high reactivity of $\text{BH}_3(\text{NHMe}_2)$ toward **2**, **3**, **7**, and **9** permits self-limited film growth at < 200 °C. These attributes should enable many new applications of ALD-grown first row transition metal films.

Due to the easily oxidized nature of the first row transition metals, as-deposited films are oxidized upon exposure to air, surfaces of the Ni, Co, Fe, and Cr films are oxidized and Mn films are fully oxidized. As described in Chapter 6, similar metal precursors and one reducing agent that reduce one or more metal ions are needed to deposit metal alloy films. This chapter describes the deposition of metal films using similar metal precursors and $\text{BH}_3(\text{NHMe}_2)$ which may lead to viable ALD alloy growth processes.

7.4 Experimental Section

A Picosun Oy R-75BE ALD reactor was used for thin film deposition experiments. The pressure of the reactor was kept at 8–12 mbar under a flow of nitrogen (99.9995%), which was supplied by Texol GeniSys nitrogen generator. Nitrogen obtained from this generator was used as both the carrier and purge gas. The deposition of metal thin films was studied with **2**, **3**, and **7-9** as the as the metal precursors and $\text{BH}_3(\text{NHMe}_2)$ as the reducing agent. The delivery temperature of $\text{BH}_3(\text{NHMe}_2)$ was 80 °C at the reactor pressure. The following delivery temperatures were employed for the metal precursors: **2**, 120 °C; **3**, 130 °C; **7**, 120 °C; **8**, 180 °C; **9**, 140 °C. Substrate temperatures were 180 °C for growth with **2** and **3**, 200 °C with **7**, 225 °C with **8**, and ranged from 160 to 240 °C with **9**. Pulse lengths of **2**, **3**, **7-9** and $\text{BH}_3(\text{NHMe}_2)$ and the nitrogen purge lengths were changed to determine the extent of surface saturation. Films were deposited on substrates consisting of 5 nm of sputtered Ru grown on 100 nm of thermal SiO_2 . The surface RuO_2 layer was not removed prior to deposition. The lines in the saturation

and ALD window plots were drawn by connecting the data points. The lines in the thickness versus number of cycles plots represent the best fit curves of the data points.

Film thicknesses were measured using cross-sectional SEM micrographs collected on a JEOL-6510LV electron microscope. Growth rates were calculated by dividing the measured film thicknesses by the number of deposition cycles. Film thicknesses were measured at three positions on the films to evaluate the uniformity. In all cases, the measured film thicknesses varied $< 5\%$ across the substrate. AFM micrographs were obtained with a MultiMode Nanoscope IIIa (Digital Instruments, VEECO). The samples were measured using the tapping mode in air with an E scanner with a maximum scanning size of $12\ \mu\text{m}$ at a frequency of 1 or 2 Hz. A Tap150AI-G tip was used, with a resonance frequency of 150 kHz and a force constant of $5\ \text{N m}^{-1}$. Surface roughnesses were calculated as root-mean-square (rms) values. XPS analyses were performed with a Perkin-Elmer 5500 XPS system using monochromatized Al $K\alpha$ radiation. Surfaces were sputtered using 0.5 kV Ar ions.

CHAPTER 8

Synthesis and Structure of Volatile and Thermally Stable Molybdenum(II) and Tungsten(II) Complexes Containing N, O Donor Ligands

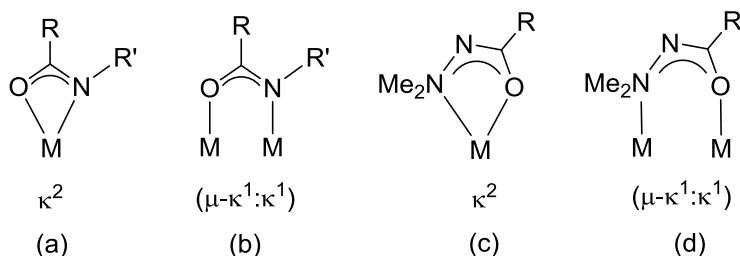
8.1 Introduction

Chelating ligands containing N and O donor atoms are widely used in Mo and W chemistry.¹⁰⁶ Among these ligand types, carboxylates (RCOO), amidinates (RNC(R)NR), amidates (RCONR), and some other complex chelating ligands are widely used.¹⁰⁶ These chelating ligands promote dimeric structures with Mo and W centers. Most reported Mo and W complexes have bulky ligands which reduce the volatility of the complexes. Designing volatile ligands of these types should lead to volatile complexes that can be used in ALD. This chapter describes attempts that were made to synthesize Mo(II) and W(II) complexes as potential ALD precursors for the deposition of MoO and WO films. As described in the introduction chapter, reactive Mo(II) and W(II) complexes may afford oxide films that are in the same oxidation state as the metal precursor.

Amidate ligands, $[\text{RCONR}']^-$, also known as carboxamidates, are bidentate ligands which can chelate in a κ^2 -fashion (Chart 14(a)) or by bridging two metal centers through (μ - $\kappa^1:\kappa^1$) σ donation (Chart 14(b)).¹⁰⁷ The protonated form of amidates are secondary amides. Amides form the backbones of proteins (polypeptides) and synthetic polyamide (nylon) polymers due to their chemical stability.¹⁰⁸ Amides show resonance stabilization by conjugation through C–N and C–O bonds, which makes the C–N bond stronger than a normal C–N single bond.¹⁰⁸ Therefore, amidate ligands may form thermally stable metal complexes. These ligands

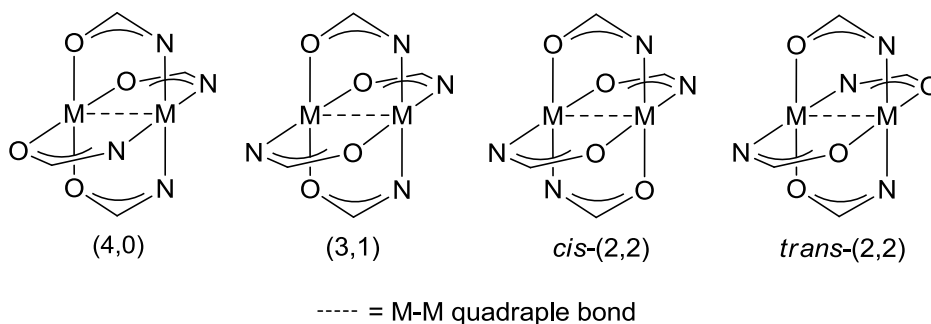
can easily be modified both sterically and electronically by changing the R groups, thereby changing the stability and volatility of the coordinated complex.¹⁰⁹ Therefore, amidates should be suitable for synthesizing thermally stable and volatile Mo_2^{4+} and W_2^{4+} ALD precursors. The carbohydrazide ligands also have two types of potential coordination modes, which can chelate in a κ^2 -fashion (Chart 14(c)) or by bridging two metal centers through $(\mu-\kappa^1:\kappa^1)$ σ donation (Chart 14(d)). Due to the chelating nature of carbohydrazides they also should form stable complexes

Chart 14. Coordination modes of amidate and carbohydrazide ligands.



Homoleptic dinuclear paddlewheel (lantern) compounds for Cr and Mo have been synthesized using amidate ligands.¹⁰⁶ There are several types of regioisomers that may occur in paddlewheel compounds, as illustrated in Chart 15, where the notations are stated below the structure. Since the axial positions are sterically open in paddlewheel compounds, there is a high possibility of having one or two axial donor molecules coordinated to the metal centers.¹⁰⁶

Chart 15. Possible regioisomers of paddlewheel compounds which contain amidates.¹⁰⁶



Mo(II) amidate complexes have been previously synthesized by the reaction of $\text{Mo}_2(\text{OAc})_4$ with the potassium or lithium salt of the amide ligands.¹⁰⁶ Because $\text{Mo}_2(\text{OAc})_4$ is commercially available and can easily be synthesized from $\text{Mo}(\text{CO})_6$, it has been widely used as starting materials for the synthesis of Mo amidate complexes and some other Mo complexes.¹⁰⁶ Cotton has reported the homoleptic Mo amidate complexes including $\text{Mo}_2[\text{PhNCOtBu}]_4$ ¹¹⁰ and $\text{Mo}_2[\text{tBuNCOCH}_3]_4$.¹¹¹ Also, Cotton has reported dimolybdenum complexes that contain neutral ligands in the axial positions including $\text{Mo}_2[\text{PhNCOCH}_3]_4 \cdot 2\text{THF}$,¹¹² $\text{Mo}_2[(2,6\text{-xylyl})\text{NCOCH}_3]_4 \cdot 2\text{CH}_2\text{Cl}_2$,¹¹¹ $\text{Mo}_2[(2,6\text{-xylyl})\text{NCOCH}_3]_4 \cdot 2\text{CH}_2\text{Br}_2$,¹¹³ $\text{Mo}_2[(2,6\text{-xylyl})\text{NCOH}]_4 \cdot 2\text{THF}$,¹¹⁴ $\text{Mo}_2[(2,6\text{-xylyl})\text{NCOCH}_3]_4 \cdot 2\text{THF}$,¹¹⁵ $\text{Mo}_2[(2,6\text{-xylyl})\text{NCOH}]_4 \cdot \text{py} \cdot \text{C}_6\text{H}_6$,¹⁵¹ and $\text{Mo}_2[(2,6\text{-xylyl})\text{NCOH}]_4 \cdot 4\text{-pic}$.¹¹⁶

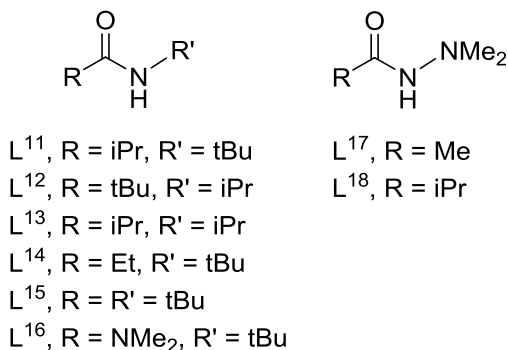
Although Mo amidate complexes are widely explored, Mo complexes containing carbohydrazide ligands (Chart 15) are rare. The carbohydrazide structure can be found in Mo(IV) and Mo(VI) complexes that contain complex chelating ligand structures¹¹⁷ while W complexes containing carbohydrazide ligands are unknown. Moreover, homoleptic W complexes containing amidate ligands are unknown although heteroleptic complexes are reported with complex chelating ligands.¹¹⁸

Although Mo(II) compounds can be synthesized using $\text{Mo}_2(\text{OAc})_4$ as the precursor, the $\text{W}_2(\text{OAc})_4$ precursor is neither commercially available nor can it be conveniently synthesized. This is due to the difficulty of forming W–W quadruple bonds in an acidic medium.¹¹⁹ Mo carboxylate have been synthesized by the reaction of $\text{Mo}(\text{CO})_6$ with various carboxylic acids in diglyme.¹¹⁹ However, researchers have spent almost twenty years trying to synthesize W carboxylate compounds and in all attempts, no indication of W(II) carboxylate has been observed and only a trinuclear W(IV) species $\{[\text{W}_3\text{O}_2(\text{O}_2\text{CR})_6(\text{H}_2\text{O})_3]^{2+}\}$ was obtained.^{120,121} The first

successful synthesis of a W carboxylate was the synthesis of $W_2(O_2CCF_3)_4$ using non acidic medium in 1981.^{115,122} In this synthesis, WCl_4 is reduced by two equivalents of Na/Hg in the presence of sodium trifluoroacetate. The difficulty in synthesizing W carboxylate compounds is due to the weak δ component of the W–W bond, which makes this bond easily undergo oxidative addition in an acidic medium.¹²² This fact has been confirmed experimentally.^{123,124} After synthesizing the first W carboxylate, W benzoate¹²⁰ and benzoate derivatives such as $W_2(O_2CC_6H_4-p-OMe)_4$,¹²⁵ $W_2(O_2CC_6H_2-2,4,6-Me_3)_4$ ¹²⁰ have been prepared avoiding acidic media. $W_2(C_6H_5CO_2)_4$ was the first and most accessible intermediate for the synthesis of other W(II) compounds.

The suitability of Mo(II) and W(II) complexes containing amidate and carbohydrazide ligands have not been evaluated as ALD precursors. In this chapter, the synthesis and characterization of Mo and W complexes containing ligands with N, O donor atoms, including amidates and carbohydrazides are described, and their volatility and thermal stability are evaluated. Mo complexes were synthesized from ligands L^{11} – L^{18} and W complexes were synthesized from ligands L^{11} – L^{13} (Chart 16).

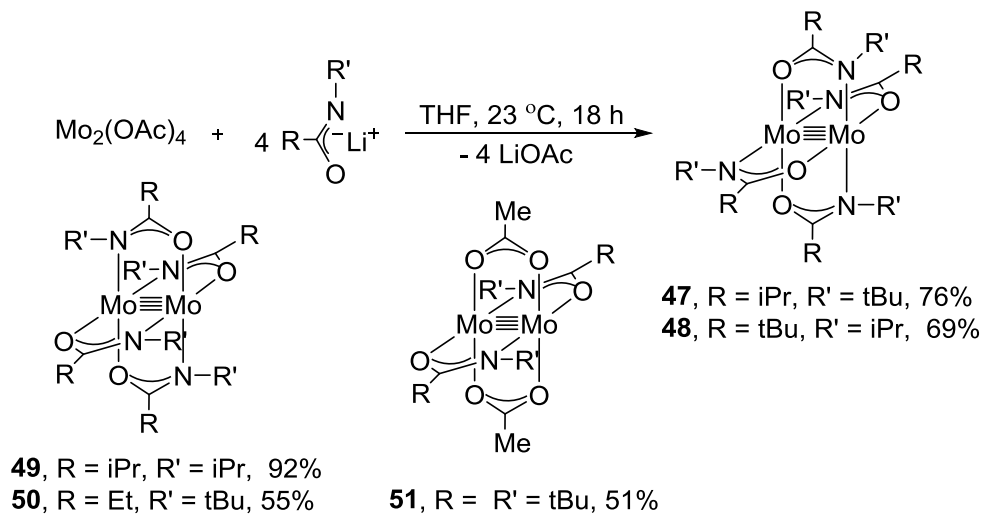
Chart 16. Chemical structures of amidate (L^{11} – L^{16}) and carbohydrazide (L^{17} and L^{18}) ligands.



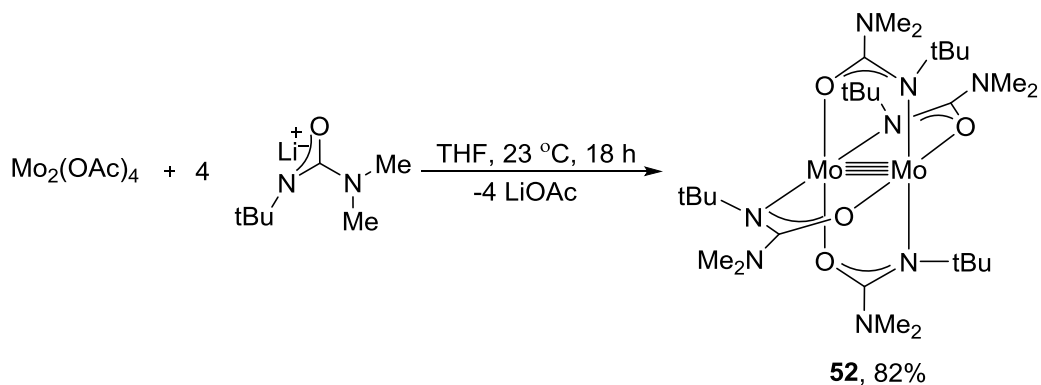
8.2 Results and Discussion

Synthetic Aspects. The ligand precursors $L^{11}H-L^{18}H$ (Chart 16) were synthesized and characterized as described in the literature.¹²⁶ The lithium salts $LiL^{11}-LiL^{18}$ were prepared by treatment of $L^{11}H-L^{18}H$ with *n*-butyl lithium in tetrahydrofuran. The Mo complexes were synthesized by treating the solutions of $LiL^{11}-LiL^{16}$ directly with anhydrous $Mo_2(OAc)_4$ to afford complexes **47–52** as yellow crystalline solids upon sublimation (Scheme 7 and 8). In a similar fashion, treatments of LiL^{17} and LiL^{18} with $Mo_2(OAc)_4$ afforded **56–59** as two isomeric compounds with each ligand, as shown in Scheme 9. Extensive trials to separate these isomers were unsuccessful and they were separated physically by hand after purifying both isomers together by crystallization. Complexes **56** and **58** are yellow in color and **57** and **59** are red in color. These isomers were later identified as paddle wheel compounds (yellow) and compounds with two bridging ligands and two terminal ligands (red) as depicted in Scheme 9. The synthesis of W complexes involves the reduction of W(IV) to W(II) using Na/Hg amalgam. Tungsten tetrachloride in tetrahydrofuran was treated with 0.05% Na/Hg amalgam and this solution was then treated with the solutions of $LiL^{11}-LiL^{13}$ to afford complexes **53–55** as crystalline solids upon sublimation (Scheme 10). Similar treatments of $LiL^{14}-LiL^{18}$ or $KL^{14}-KL^{18}$ with the W(II) solutions did not afford isolable products.

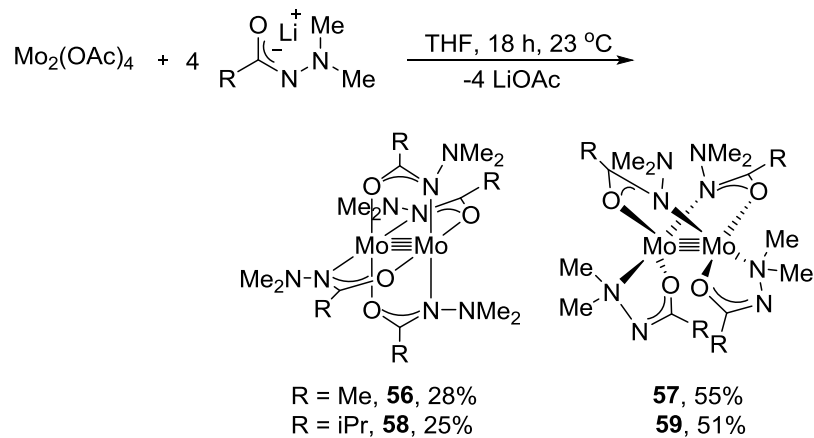
Scheme 7. Synthesis of 47–51.



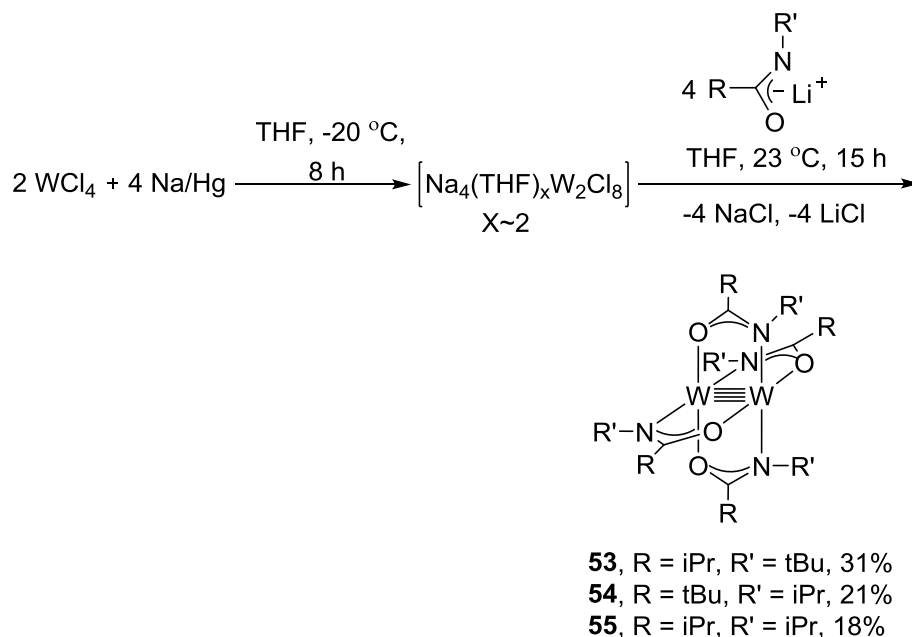
Scheme 8. Synthesis of 52.



Scheme 9. Synthesis of 56–59.



Scheme 10. Synthesis of 53–55.



The structures of **47–59** were assigned by spectral and analytical data. In addition, X-ray crystal structures of **47**, **49**, **50**, **52**, **53**, **56**, **57**, and **59** were determined, as described below. Complexes **47–59** are diamagnetic and show ^1H and ^{13}C NMR resonances for the corresponding substituents of the ligands. Complexes **47–50**, **52–56**, and **58** demonstrate one set of peaks in their ^1H and ^{13}C NMR, confirming that all ligands are in a chemically equivalent environment in each complex. Complex **51** shows NMR resonances for L^{15} and acetate in 1:1 ratio. Complexes **57** and **59** give one set of peaks for bridging ligands and another set of peaks for terminal ligands in 1:1 ratio. The carbonyl stretching frequency of amidate ligands in **47–50** and **52** was observed between 1485 and 1516 cm^{-1} . Similarly, the carbonyl stretching frequency of amidate ligands in **53–55** was observed between 1490 and 1500 cm^{-1} . Although a single carbonyl stretching was observed in amidate complexes, carbonyl complexes with bridging and terminal ligands (**57** and **59**) demonstrated two carbonyl stretching bands. Complexes **57** and **59** have one set of carbonyl stretching bands at 1582 and 1570 cm^{-1} and another set of carbonyl stretching bands at

1508 and 1506 cm^{-1} . Moreover, **56** and **58** have one carbonyl stretching bands at 1512 and 1506 cm^{-1} , respectively.

Structural Aspects. The crystal structures of **47**, **49**, **50**, **52**, **53**, **56**, **57**, and **59** were obtained to establish the solid state structures and to assess the bonding modes of the amidate and carbohydrazide ligands. All complexes demonstrated dimeric structures with four ligands around the metal centers. Experimental crystallographic data are summarized in Table 20 and selected bond lengths and angles are listed in Tables 21 and 22. Representative perspective views of **47**, **53**, **56**, and **57** are given in Figures **81–84**, respectively. A low precision X-ray crystal structure determination of **48** showed similar structure to **47**. Also, a low precision X-ray crystal structure of **51** revealed that this complex has two acetate and two amidate L^{15} ligands. Since L^{15} is a sterically encumbered ligand, four ligand molecules do not fit in the coordination spheres of two Mo centers, instead, two of the acetate ligands that were in Mo acetate are intact and two L^{15} ligands are coordinated to metal centers. The use of other solvents, reflux conditions, or solutions of KL^{15} did not afford a homoleptic amidate complex with L^{15} . The spectral data of **54** and **55** are similar to those of the structurally characterized complex **53**. Similarly, the spectral data of **58** are similar to those of **56**, which suggest similar dimeric paddle wheel complexes.

The complexes **47**, **49**, **50**, **52**, and **53** display dimeric paddle wheel structures with four amidate ligands coordinated to metal centers in a $\mu\text{-}\kappa^1:\kappa^1\text{-N,O}$ fashion and they have similar bond lengths and angles. The amidate ligand core C–O bond lengths range between 1.276(3) and 1.302(4) Å, which are in between the lengths expected for C–O single (1.43 Å) and C=O double bonds (1.22 Å)^{20b}. Similarly, the amidate ligand core C–N bond lengths range between 1.303(4) and 1.328(5) Å, which are in between the lengths expected for C–N single (1.46 Å) and C=N double bonds (1.21 Å).^{20b} These C–N and C–O bond lengths suggest that the negative charge is

delocalized through the ligand core bonds. The Mo–N (2.1643(11) to 2.2031(14) Å) and Mo–O (2.0716(18) to 2.097(2) Å) bond lengths in amidate complexes are greater than those of observed in W complex (W–N, 2.150(3) to 2.161(3) Å; W–O, 2.053(3) to 2.058(3) Å). The oxygen and nitrogen donor atoms in the four ligands of **47**, **48**, **52**, and **53** are mutually trans (*trans*-(2,2)), with N–M–N' and O–M–O' angle ranges of 177.58(9) to 179.40(13)°, and 170.30(8) to 173.75(7)°, respectively. The N–M–N' angles are larger than O–M–O' angles because of the presence of tBu substituent on N atoms. However, oxygen and nitrogen donor atoms in **49** and **50** are not mutually trans (*cis*-(2,2)) and have a inversion center along the Mo–Mo bond.

The Mo–Mo bond lengths of Mo amidate complexes (**47**, 2.0595(3); **49**, 2.0736(2); **50**, 2.0692(3) Å); **52**, 2.0709(3) are in the range of previously reported homoleptic Mo amidate complexes (Mo₂(tBuNCOCH₃)₄, 2.063(1)¹¹¹; Mo₂(PhNCOtBu)₄, 2.070(1) Å¹¹⁰). Mo amidate complexes with axial ligands have slightly longer Mo–Mo bond lengths ((Mo₂(PhNCOCH₃)₄·2THF, 2.086(2)¹¹²; Mo₂((2,6-xylyl)NCOCH₃)₄·2CH₂Cl₂, 2.083(2)¹¹¹; Mo₂((2,6-xylyl)NCOCH₃)₄·2CH₂Br₂, 2.085(2)¹¹³; Mo₂((2,6-xylyl)NCOH)₄·2THF, 2.113(1)¹¹⁴; Mo₂((2,6-xylyl)NCOH)₄·NC₅H₅·C₆H₆, 2.101(1)¹¹⁵; Mo₂((2,6-xylyl)NCOH)₄·NC₅H₅CH₃, 2.102(1)¹¹⁶ Å). Complex **53** has W–W bond length of 2.15430(17) Å, which is similar to the shortest W–W bond length (2.155(2) Å) of W₂(4-hydroxy-2,6-dimethylpyrimidine)₄·0.5(diglyme).¹¹⁸

Carbohydrazide ligands have two coordination modes; κ^2 and $\mu\text{-}\kappa^1\text{:}\kappa^1$. Complex **56** demonstrates a paddle wheel structure with four bridging ligands as seen in Mo amidates. However, **57** and **59** have two bridging ligands coordinated in $\mu\text{-}\kappa^1\text{:}\kappa^1\text{-N,O}$ fashion and two terminal ligands coordinated in $\kappa^2\text{-N,O}$ fashion. The ligand core C–N and C–O bond lengths of **56** and the bridging ligands of **57** and **59** are similar to those of amidate paddle wheel complexes.

In the terminal ligands of **57** and **59**, the C–O bond lengths fall in the range of 1.313(2) to 1.3191(15) Å, and are longer than those of the bridging ligands which fall in the range between 1.291(2) and 1.297(2) Å. Nevertheless, the C–N bond lengths of the terminal ligands (1.289(2) to 1.298(2) Å) are shorter than those of the bridging ligands (1.316(2) to 1.3178(17) Å). The ligand core C–N (1.289(2) to 1.298(2)) Å, C–O (1.313(2) to 1.3191(15) Å), and N–N (1.4753(14) to 1.477(2) Å) bond lengths of terminal ligands, and C–N (1.316(2) to 1.3178(17) Å) and C–O (1.291(2) to 1.297(2)) bond lengths of bridging ligands are in between the lengths for single and double bond, which suggest that the negative charge is delocalized through the ligand core bonds in both terminal and bridging ligands. The Mo–N (2.2247(14) to 2.2290(11) Å) and Mo–O (2.0976(9) to 2.1051(12) Å) bond lengths of the terminal ligands are longer than those of the bridging ligands (Mo–N, 2.1329(14) to 2.1419(11) Å; Mo–O, 2.0688(9) to 2.0770(11) Å). This difference may have arisen because terminal ligands make six membered rings, which are more flexible than five membered rings made by the bridging ligands. The Mo–Mo bond length of **56** (2.0719(2) Å) falls in the range of Mo–Mo lengths of Mo amidate dimers (2.0595(3) to 2.0736(2) Å). On the other hand the Mo–Mo bond lengths of **57** (2.1186(2) Å) and **59** (2.1195 (3) Å) are longer than that of paddle wheel dimers. This elongation occurs because the terminal ligands do not involve keeping two Mo atoms together, whereas four bridging ligands tend to bring the Mo atoms close together. From the structurally characterized Mo complexes in this chapter, the Mo–Mo bond length of **47** (2.0595(3)) is the shortest and it falls near the length of the reported shortest Mo–Mo length, 2.037(3) Å in $\text{Mo}_2((\text{NC}_5\text{H}_4)\text{NCOCH}_3)_4$, which represent $\mu\text{-}\kappa^1\text{:}\kappa^1\text{-N,N}$ coordination mode.¹²⁷

Table 20a. Experimental crystallographic data for **47**, **49**, **50**, and **52**.

	47	49	50	52
Formula	C ₃₂ H ₆₄ Mo ₂ N ₄ O ₄	C ₂₈ H ₅₆ Mo ₂ N ₄ O ₄	C ₂₈ H ₅₆ Mo ₂ N ₄ O ₄	C ₂₈ H ₆₀ Mo ₂ N ₈ O ₄
FW	760.75	704.65	704.65	764.72
Space group	P2 ₁	P2 ₁ /n	p1bar	P2 ₁
a (Å)	11.3531(5)	8.2568(3)	8.1021(3)	11.4055(9)
b (Å)	15.7826(6)	17.4379(7)	10.7540(4)	15.5055(11)
c (Å)	11.5541(5)	11.9084(5)	10.9511(4)	11.5023(8)
V (Å ³)	1916.70(14)	1651.13(11)	820.46(5)	1874.6(2)
Z	2	2	1	2
T (K)	100(2)	100(2)	100(2)	100(2)
λ (Å)	0.71073	0.71073	0.71073	0.71073
ρ _{calc} (g cm ⁻³)	1.318	1.417	1.426	1.355
μ ((mm ⁻¹))	0.690	0.795	0.800	0.709
R(F) ^a ((%)	2.52	2.51	3.28	2.80
Rw(F) ^b (%)	6.31	5.86	7.82	8.02

$$^a R(F) = \frac{\sum ||F_o| - |F_c||}{\sum |F_o|}$$

$$^b R_w(F) = [\sum w(F_o^2 - F_c^2)^2 / \sum w(F_o^2)^2]^{1/2}$$

Table 20b. Experimental crystallographic data for **53**, **56**, **57**, and **59**.

	53	56	57	59
Formula	C ₃₂ H ₆₄ W ₂ N ₄ O ₄	C ₁₆ H ₃₆ Mo ₂ N ₈ O ₄	C ₁₆ H ₃₆ Mo ₂ N ₈ O ₄	C ₂₄ H ₅₂ Mo ₂ N ₈ O ₄
FW	936.57	596.41	596.41	708.62
Space group	P2 ₁	P2 ₁ /n	Pbca	Pbcn
a (Å)	11.3475(3)	9.9205(8)	11.9575(8)	8.5654(6)
b (Å)	15.7961(4)	15.8392(13)	14.6407(9)	24.2501(17)
c (Å)	11.5431(3)	15.3705(13)	27.9370(18)	15.7931(12)
V (Å ³)	1915.60(9)	2402.8(3)	4890.8(5)	3280.4(4)
Z	2	4	8	4
T (K)	100(2)	100(2)	100(2)	100(2)
λ (Å)	0.71073	0.71073	0.71073	0.71073
ρ _{calc} (g cm ⁻³)	1.624	1.649	1.620	1.435
μ ((mm ⁻¹))	6.036	1.081	1.062	0.804
R(F) ^a ((%))	2.47	2.07	2.10	2.10
Rw(F) ^b (%)	5.42	5.05	5.00	5.43

$$^a R(F) = \frac{\sum ||F_o| - |F_c||}{\sum |F_o|}$$

$$^b R_w(F) = [\sum w(F_o^2 - F_c^2)^2 / \sum w(F_o^2)^2]^{1/2}$$

Table 21. Selected bond lengths (Å) and angles (°) for **47**, **49**, **50**, **52**, and **53**.

	47	49	50	52	53
M–M	2.0595(3)	2.0736(2)	2.0692(3)	2.0709(3)	2.15430(17)
M–N	2.187(2)	2.1643(11)	2.1910(15)	2.165(3)	2.155(3)
	2.186(2)	2.1855(10)	2.2031(14)	2.174(3)	2.161(3)
	2.171(2)			2.181(3)	2.150(3)
	2.184(2)			2.184(3)	2.156(3)
	2.0733(15)	2.0926(9)	2.0852(13)	2.091(2)	2.058(3)
M–O	2.0751(18)	2.0945(9)	2.0775(11)	2.086(2)	2.059(2)
	2.0716(18)			2.083(2)	2.053(3)
	2.0720(18)			2.097(2)	2.054(3)
	1.324(4)	1.3229(15)	1.323(2)	1.315(4)	1.328(5)
C–N _{core}	1.311(3)	1.3268(16)	1.316(2)	1.314(4)	1.325(5)
	1.318(3)			1.303(4)	1.313(5)
	1.305(3)			1.305(5)	1.324(5)
	1.287(3)	1.2953(14)	1.301(2)	1.287(4)	1.295(4)
C–O	1.276(3)	1.2951(15)	1.297(2)	1.284(4)	1.287(4)
	1.291(3)			1.290(4)	1.302(4)
					1.295(5)
	119.1(2)	119.58(11)	119.18(16)	120.8(3)	119.4(3)
N–C–O	120.4(2)	119.76(12)	119.66(14)	121.7(3)	119.7(3)
	119.7(2)			122.0(3)	119.9(3)
	119.8(2)			121.3(3)	120.0(3)

Table 22a. Selected bond lengths (Å) for **56**, **57**, and **59**.

	56		57		59	
		Terminal	Bridging	Terminal	Bridging	
M–M	2.0719(2)		2.1186(2)			2.1195(3)
M–N	2.1616(14)	2.2248(14)	2.1329(14)	2.2290(11)	2.1419(11)	
	2.1680(14)	2.2247(14)	2.1367(14)			
	2.1615(14)					
	2.1711(14)					
M–O	2.0952(12)	2.1051(12)	2.0809(12)	2.0976(9)	2.0688(9)	
	2.0972(12)	2.1002(12)	2.0770(11)			
	2.0893(11)					
	2.0915(11)					
C _{core} –N _{core}	1.321(2)	1.298(2)	1.316(2)	1.2918(17)	1.3178(17)	
	1.319(2)	1.289(2)	1.317(2)			
	1.323(2)					
	1.317(2)					
C–O	1.291(2)	1.313(2)	1.291(2)	1.3191(15)	1.2948(16)	
	1.295(2)	1.318(2)	1.297(2)			
	1.292(2)					
	1.290(3)					
N–N	-	1.477(2)	1.4506(18)	1.4753(14)	1.4479(15)	
		1.476(2)	1.4475(18)			

Table 22b. Selected bond angles (°) for **56**, **57**, and **59**.

	56		57		59	
		Terminal	Bridging	Terminal	Bridging	
N-M-O	-	73.28(5)	-	73.95(4)	-	-
		73.79(5)				
N-C-O	118.26(15)	125.95(16)	117.46(15)	126.09(12)	117.18(12)	
	118.15(15)	126.64(16)	117.05(15)			
	118.55(15)					

Figure 81. Perspective view of **47** with thermal ellipsoids at the 50% probability level.

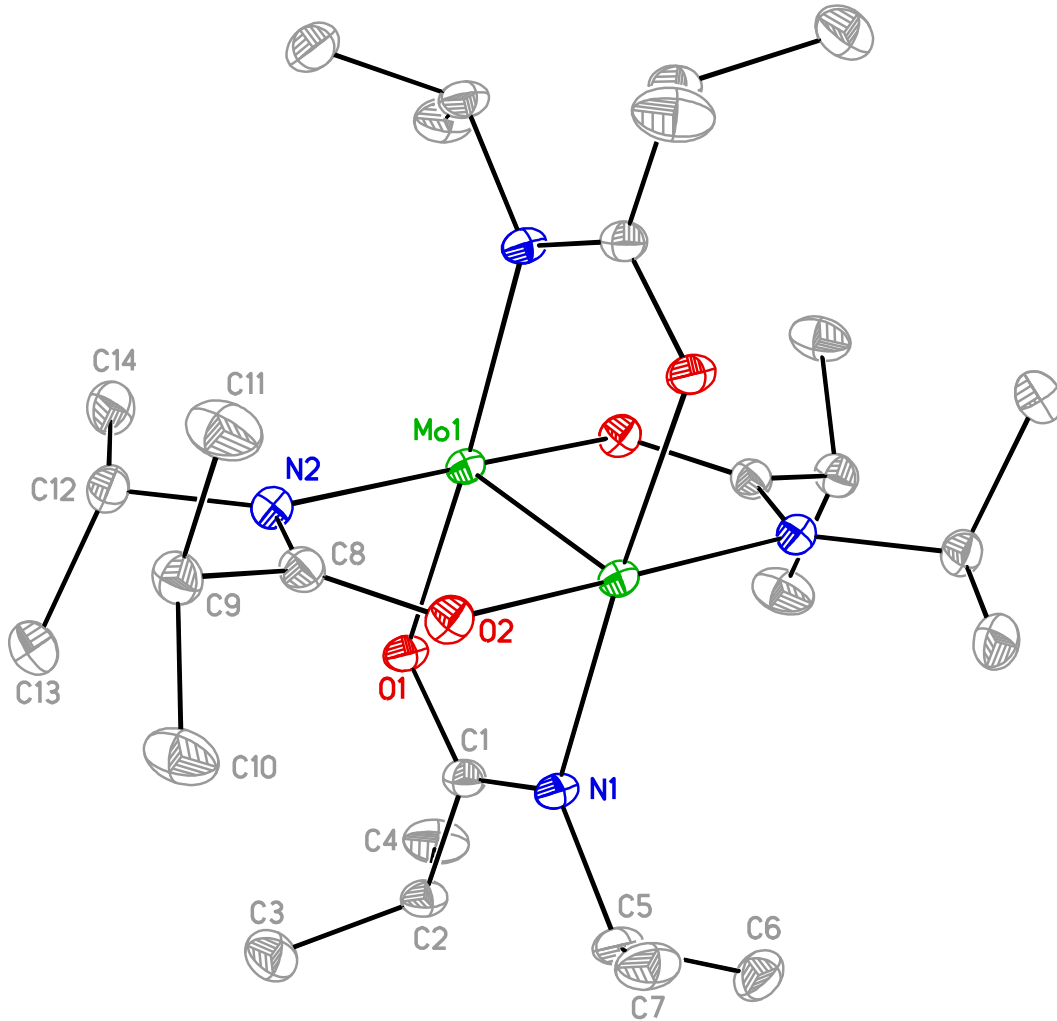


Figure 82. Perspective view of **53** with thermal ellipsoids at the 50% probability level.

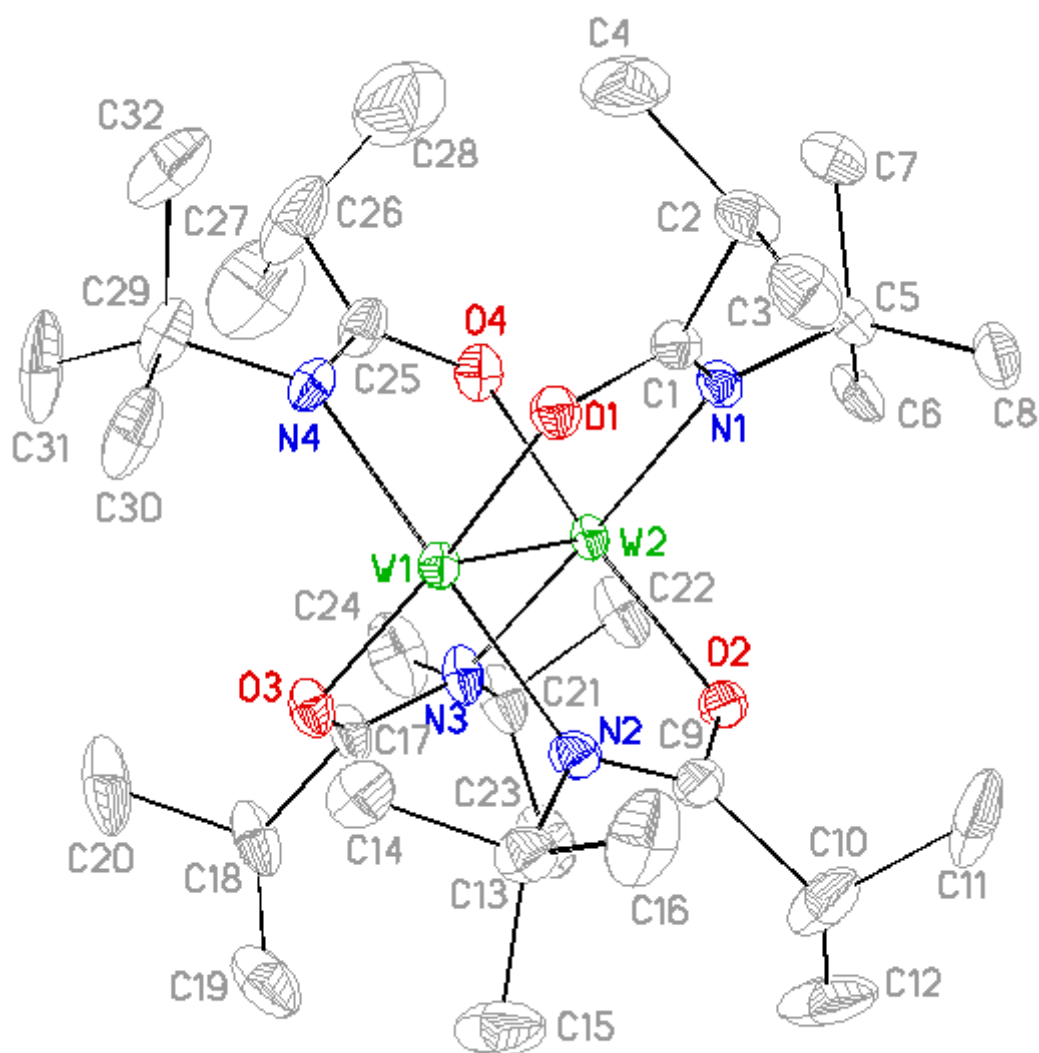


Figure 83. Perspective view of **56** with thermal ellipsoids at the 50% probability level.

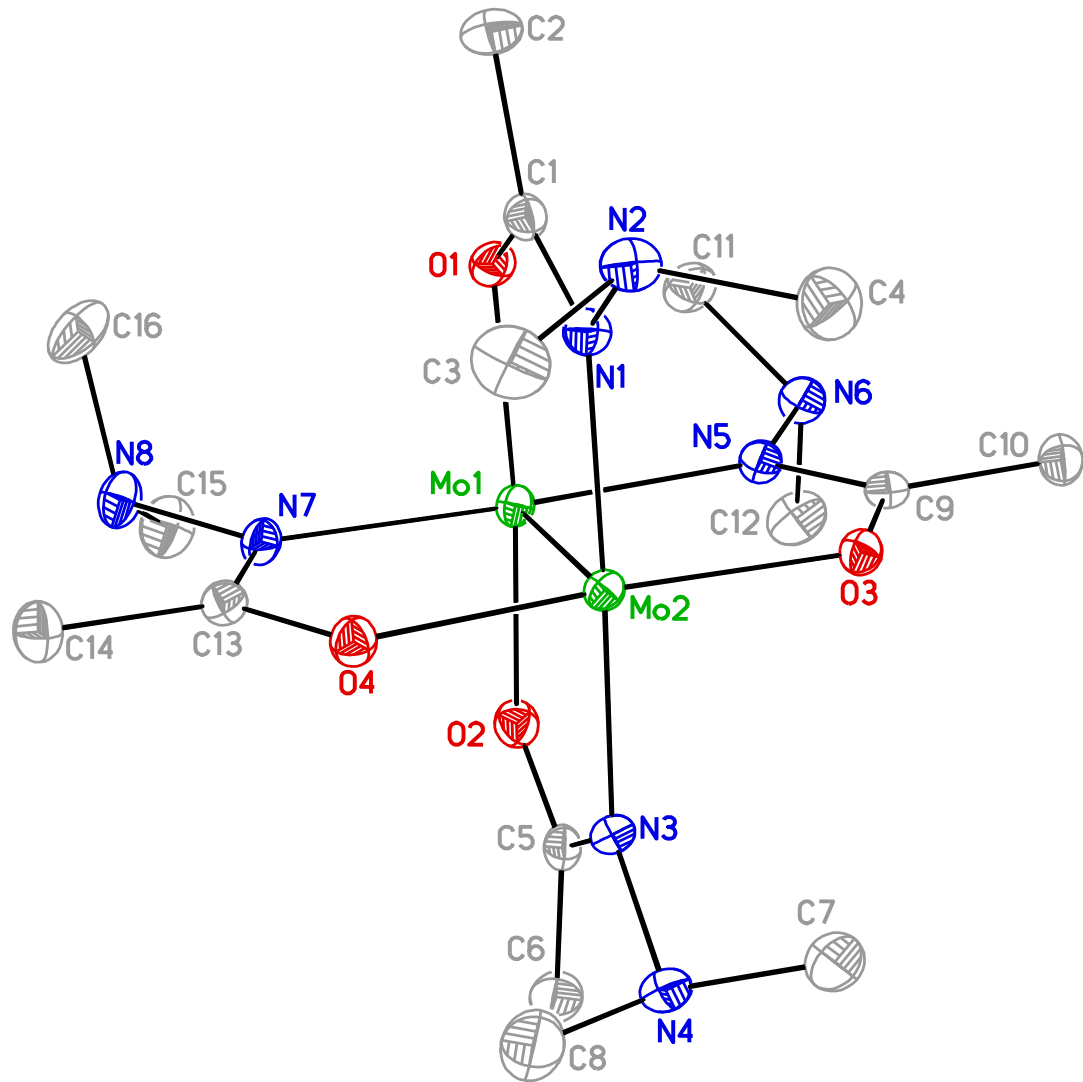
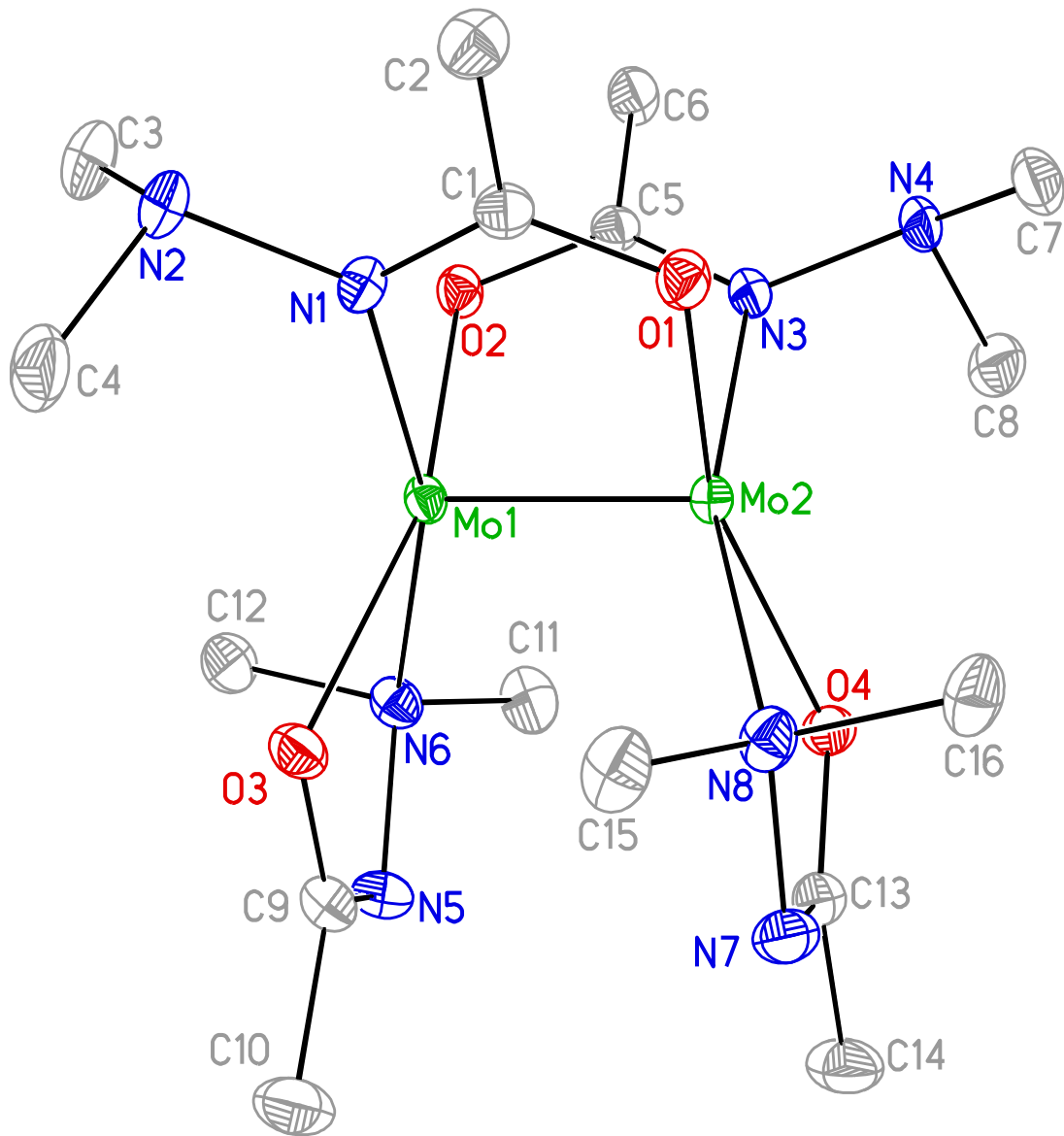


Figure 84. Perspective view of **57** with thermal ellipsoids at the 50% probability level.



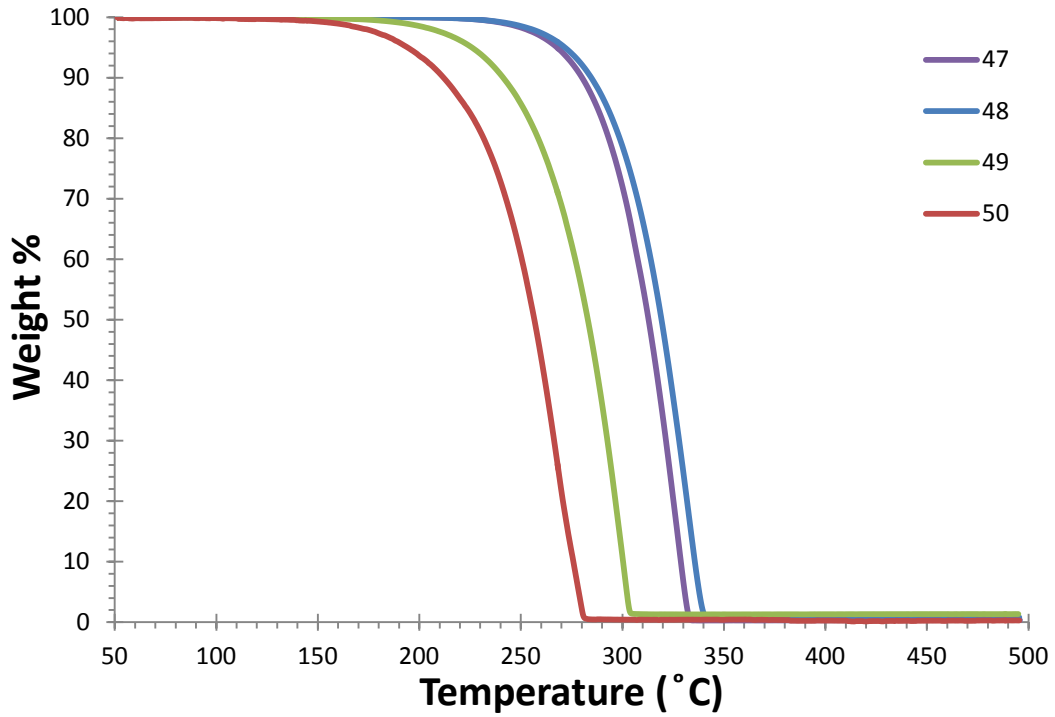
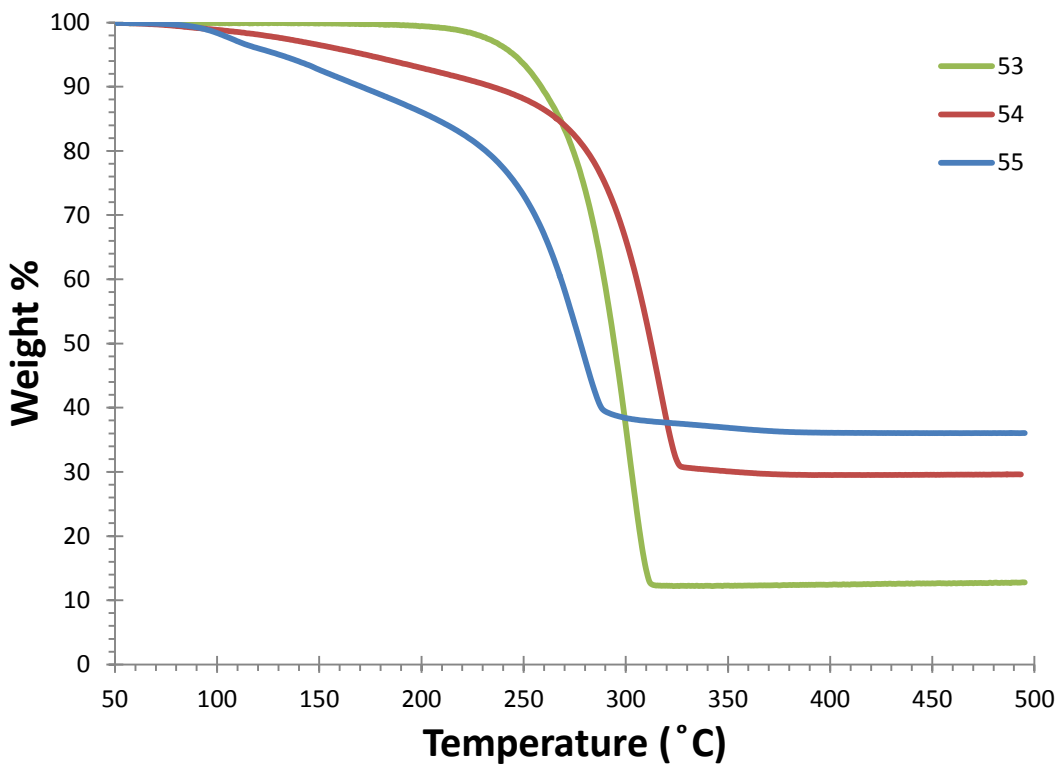
Evaluation of Thermal Stability and Volatility. The preparative sublimation data, melting points, and solid state decomposition temperatures for **47–59** are summarized in Table 23. Complexes **47–59** sublime on ~0.5 g scales over three hours between 120 and 170 °C/0.05 Torr with < 6% nonvolatile residues and > 88% recovery. The lower sublimation temperatures of **56–59**, compared to the other complexes are due to the presence of dimethyl amino groups in the ligands of the former. The intermolecular lone pair-lone pair repulsion in dimethyl amino groups decreases the lattice energy, which increases the volatility of **56–59**. High thermal stability is very important for ALD precursors, because decomposition of precursor will stop self-limited growth and CVD-like growth will occur. The Mo (**47–52**) and W (**53–55**) amidate complexes demonstrate rigid structures and have very high thermal stabilities. The paddle wheel Mo carbohydrazide complexes have much higher thermal decomposition temperatures (**56**, 250 and **58**, 280 °C) than those of non-paddle wheel Mo carbohydrazide complexes (**57**, 193 and **59**, 220 °C). The decomposition temperatures of **47–50** and **55** (269–355 °C) are much higher than those of the reported Mo precursors $\text{Mo}(\text{NtBu})_2(\text{NMe}_2)_2$ (190 °C)¹²⁸ and $\text{Mo}(\text{NtBu})_2(\text{NiPr}_2)_2$ (114 °C).¹²⁸ Similarly, **53–55** decompose from 250 to 335 °C, which are higher than the reported decomposition temperatures of $\text{W}(\text{NtBu})_2(\text{NMe}_2)(\text{iPrNC}(\text{NMe}_2)\text{NiPr})$ (205 °C),¹²⁰ $\text{W}(\text{NtBu})_2(\text{H})(\text{iPrNC}(\text{NMe}_2)\text{NiPr})$ (175 °C),¹²⁹ and $\text{W}_2(\text{NMe}_2)_6$ (230 °C).¹³⁰

TGA and DTA were carried out on **47–50** and **53–55** to understand their behavior upon heating. TGA plots of **47–50** and **53–55** are shown in Figure 75 and 76, respectively. Complexes **47–50** show similar single step weight losses due to sublimation between 160 and 340 °C in the TGA plots. These TGA traces clearly show that the volatility increases in the order of **50** > **49** > **47** > **48** which was also observed in sublimation experiments and can be attributed to the molecular weight of the complexes. The W complexes are very air sensitive and start

decomposing during the sample loading to the TGA balance. Therefore, TGA curves of **53–55** show sublimation and competitive decomposition that lead to higher percentage of non volatile residues. Due to the high air sensitivity of **51** a TGA trace could not be obtained. Simultaneous DTA plots of **47–50** and **53–55** show endothermic peaks for melting and sublimation, and exothermic peaks for decomposition. These transition points are similar to the values obtained from the melting point apparatus for melting points and decomposition temperatures.

Table 23. Volatility and thermal stability data for **47–59**.

Complex	Sublimation temperature (°C/0.05 Torr)	Melting point (°C)	Solid state decomposition temperature (°C)	% Recovery	% Non volatile residue
47	160	331–333	333	97	<1
48	165	353–355	355	98	1
49	155	290–292	292	95	<1
50	145	267–269	269	92	<1
51	140	225–227	227	88	5
52	170	294–297	297	96	2
53	160	313–315	315	94	1
54	170	333–335	335	93	3
55	140	304–306	306	93	2
56	120	205–207	250	91	5
57	120	190–193	193		
58	130	231–233	280	90	6
59	130	121–123	220		

Figure 85. TGA plots of 47–50.**Figure 86.** TGA plots of 53–55.

8.3 Conclusions

The Mo and W complexes containing amidate and carbohydrazide ligands were prepared and their properties were evaluated. Although the Mo complexes can be synthesized directly by $\text{Mo}_2(\text{OAc})_4$, a different synthetic route was employed to synthesize the W complexes due to the lack of starting materials. The Mo and W amidates are dinuclear paddlewheel complexes that have four bridging ligands. However, carbohydrazide complexes form two dinuclear isomers: one isomer is a paddlewheel structure and the other one has two bridging ligands and two terminal ligands because of the presence of additional NMe_2 group. All of the complexes described in this chapter are volatile and thermally stable. The volatility and thermal stability can be tuned by changing the ligand core substituents. The deposition trials with these precursors have not performed to date. Due to the air sensitivity of the precursors they may afford MO films with retention of the oxidation state.

8.4 Experimental Section

General Considerations. All manipulations were carried out under argon using either Schlenk or glove box techniques, except that the ligands were prepared under ambient atmosphere. Tetrahydrofuran was distilled from sodium benzophenone ketyl, hexane was distilled from P_2O_5 . $\text{Mo}_2(\text{OAc})_4$ and WCl_4 were obtained from Strem Chemicals Inc. and used as received. L^{11} – L^{18} were prepared according to the previously published procedures.¹¹⁸ 5% Na/Hg was purchased from Sigma-Aldrich and diluted with Hg to prepare 0.5% Na/Hg.

^1H and $^{13}\text{C}\{^1\text{H}\}$ NMR spectra were obtained at 400 and 100 MHz, respectively, in C_6D_6 or CDCl_3 as indicated and were referenced to the residual proton and the ^{13}C resonances of the solvents. Infrared spectra were obtained using Nujol as the medium. Melting points were determined on a Thermo Scientific Mel-Temp 3.0 digital melting point apparatus and are

uncorrected. TGA and DTA were carried out with a SDT-2960 TGA/DTA instrument at a rate of 10 °C/min.

Preparation of Mo₂(L¹¹)₄ (47). A 100 mL Schlenk flask was charged with a magnetic stir bar, N-(*tert*-butyl)isobutyramide (0.670 g, 4.68 mmol) and tetrahydrofuran (30 mL). To this stirred solution at 0 °C was slowly added n-butyl lithium (3.2 ml, 5.1 mmol), and the solution was stirred for 4 h. This solution was then slowly added dropwise with a cannula to a stirred suspension of anhydrous Mo₂(OAc)₄ (0.500 g, 1.17 mmol) in tetrahydrofuran (40 mL). The resultant green solution was stirred for 15 h at ambient temperature. The volatile components were then removed under reduced pressure, and the resultant green powder was dissolved in hexane (50 mL). The solution was filtered through a 1 cm pad of Celite on a coarse glass frit, and the volatile components were then removed under reduced pressure. Yellow crystals of **47** (0.676 g, 76%) were obtained by sublimation at 160 °C/0.05 Torr: mp 331–333 °C; IR (Nujol, cm⁻¹) 1500 (m), 1397 (m), 1362 (m), 1298 (m), 1201 (m), 1083 (m), 1000 (w), 734 (w); ¹H NMR (C₆D₆, 23 °C, δ) 3.23 (sep, 1H, J = 6.4 Hz, CH(CH₃)₂), 1.45 (d, 6H, J = 6.4 Hz, C(CH₃)₂), 1.08 (s, 9H, C(CH₃)₃); ¹³C{¹H} NMR (C₆D₆, 23 °C, ppm) 175.71 (s, CO), 50.52 (s, C(CH₃)₃), 36.23 (s, C(CH₃)₂), 28.78 (s, C(CH₃)₃), 19.91 (s, C(CH₃)₂); Anal. Calcd for C₃₂H₆₈Mo₂N₄O₄: C, 50.52; H, 8.48; N, 7.36. Found: C, 50.65; H, 8.21; N, 7.53.

Preparation of Mo₂(L¹²)₄ (48). In a fashion similar to the preparation of **47**, treatment of Mo₂(OAc)₄ (0.500 g, 1.17 mmol) in tetrahydrofuran (40 mL) with a solution of lithium isopropyl(pivaloyl)amide (prepared from N-isopropylpivalamide (0.670 g, 4.68 mmol) and n-butyl lithium (3.2 ml, 5.1 mmol) in tetrahydrofuran (30 mL)) for 15 h at ambient temperature afforded **48** (0.614 g, 69%) as yellow crystals upon sublimation at 165 °C/0.05 Torr: mp 353–355 °C; IR (Nujol, cm⁻¹) 1485 (m), 1405 (m), 1318 (m), 1214 (m), 1154 (m), 997 (m), 800

(w); ^1H NMR (C_6D_6 , 23 °C, δ) 4.63 (sep, 1H, $J = 6.4$ Hz, $\text{CH}(\text{CH}_3)_2$), 1.49 (s, 9H, $\text{C}(\text{CH}_3)_3$), 0.95 (d, 6H, $J = 6.4$ Hz, $\text{C}(\text{CH}_3)_2$); $^{13}\text{C}\{^1\text{H}\}$ NMR (C_6D_6 , 23 °C, ppm) 175.83 (s, CO), 48.83 (s, $\text{C}(\text{CH}_3)_2$), 40.24 (s, $\text{C}(\text{CH}_3)_3$), 30.35 (s, $\text{C}(\text{CH}_3)_3$), 27.08 (s, $\text{C}(\text{CH}_3)_2$); Anal. Calcd for $\text{C}_{32}\text{H}_{64}\text{Mo}_2\text{N}_4\text{O}_4$: C, 50.52; H, 8.48; N, 7.36. Found: C, 50.66; H, 8.09; N, 7.36.

Preparation of $\text{Mo}_2(\text{L}^{13})_4$ (49). In a fashion similar to the preparation of **47**, treatment of $\text{Mo}_2(\text{OAc})_4$ (0.500 g, 1.17 mmol) in tetrahydrofuran (40 mL) with a solution of lithium isopropyl(pivaloyl)amide (prepared from N-isopropylisobutyramide (0.605 g, 4.68 mmol) and n-butyl lithium (3.2 ml, 5.1 mmol) in tetrahydrofuran (30 mL)) for 15 h at ambient temperature afforded **49** (0.758 g, 92%) as yellow crystals upon sublimation at 155 °C/0.05 Torr: mp 290–292 °C; (Nujol, cm^{-1}) 1516 (s), 1407 (m), 1345 (m), 1312 (m), 1260 (m), 1167 (m), 1084 (m), 1009 (m), 798 (m); ^1H NMR (C_6D_6 , 23 °C, δ) 4.11 (sep, 1H, $J = 6.4$ Hz, $\text{CH}(\text{CH}_3)_2$), 3.02 (sep, 1H, $J = 6.4$ Hz, $\text{CH}(\text{CH}_3)_2$), 1.36 (d, 6H, $J = 6.4$ Hz, $\text{C}(\text{CH}_3)_2$), 0.94 (d, 6H, $J = 6.4$ Hz, $\text{C}(\text{CH}_3)_2$); $^{13}\text{C}\{^1\text{H}\}$ NMR (C_6D_6 , 23 °C, ppm) 177.07 (s, CO), 50.00 (s, $\text{C}(\text{CH}_3)_2$), 30.39 (s, $\text{C}(\text{CH}_3)_2$), 25.85 (s, $\text{C}(\text{CH}_3)_2$), 22.00 (s, $\text{C}(\text{CH}_3)_2$); Anal. Calcd for $\text{C}_{28}\text{H}_{56}\text{Mo}_2\text{N}_4\text{O}_4$: C, 47.73; H, 8.01; N, 7.95. Found: C, 47.64; H, 8.18; N, 7.81.

Preparation of $\text{Mo}_2(\text{L}^{14})_4$ (50). In a fashion similar to the preparation of **47**, treatment of $\text{Mo}_2(\text{OAc})_4$ (0.500 g, 1.17 mmol) in tetrahydrofuran (40 mL) with a solution of lithium *tert*-butyl(propionyl)amide (prepared from N-(*tert*-butyl)propionamide (0.605 g, 4.68 mmol) and n-butyl lithium (3.2 ml, 5.1 mmol) in tetrahydrofuran (30 mL)) for 15 h at ambient temperature afforded **50** (0.453 g, 55%) as yellow crystals upon sublimation at 145 °C/0.05 Torr: mp 267–269 °C; (Nujol, cm^{-1}) 1504 (m), 1468 (w), 1451 (w), 1392 (m), 1362 (m), 1041 (s), 1024 (m), 797 (w); ^1H NMR (CDCl_3 , 23 °C, δ) 2.92 (q, 1H, $J = 6.8$ Hz, CH_2CH_3), 2.75 (q, 1H, $J = 6.8$ Hz, CH_2CH_3), 1.36 (t, 3H, $J = 6.8$ Hz, CH_2CH_3), 1.17 (s, 9H, $\text{C}(\text{CH}_3)_3$); $^{13}\text{C}\{^1\text{H}\}$ NMR (C_6D_6 , 23

°C, ppm) 176.88 (s, CO), 54.58 (s, C(CH₃)₃), 32.39 (s, CH₂CH₃), 29.91 (s, C(CH₃)₃), 13.52 (s, CH₂CH₃); Anal. Calcd for C₂₈H₅₆Mo₂N₄O₄: C, 47.72; H, 8.01; N, 7.95. Found: C, 47.87; H, 7.98; N, 8.09.

Preparation of Mo₂(L¹⁵)₄ (51). In a fashion similar to the preparation of **47**, treatment of Mo₂(OAc)₄ (0.500 g, 1.17 mmol) in tetrahydrofuran (40 mL) with a solution of lithium *tert*-butyl(pivaloyl)amide (prepared from *N*-(*tert*-butyl)pivalamide (0.736 g, 4.68 mmol) and *n*-butyl lithium (3.2 ml, 5.1 mmol) in tetrahydrofuran (30 mL)) for 15 h at ambient temperature afforded **51** (0.453 g, 51%) as yellow crystals upon sublimation at 140 °C/0.05 Torr: mp 225–227 °C; ¹H NMR (C₆D₆, 23 °C, δ) 2.45 (s, 3H, CH₃CO₂), 1.63 (s, 9H, C(CH₃)₃), 1.02 (s, 9H, C(CH₃)₂); ¹³C{¹H} NMR (C₆D₆, 23 °C, ppm) 181.21 (s, CO), 178.52 (s, CO), 55.96 (s, C(CH₃)₃), 43.49 (s, C(CH₃)₃), 32.65 (s, C(CH₃)₃), 32.10 (s, C(CH₃)₃), 23.32 (s, CH₃CO₂).

Preparation of Mo₂(L¹⁶)₄ (52). In a fashion similar to the preparation of **47**, treatment of Mo₂(OAc)₄ (0.500 g, 1.17 mmol) in tetrahydrofuran (40 mL) with a solution of lithium *tert*-butyl(dimethylcarbamoyl)amide (prepared from 3-(*tert*-butyl)-1,1-dimethylurea (0.675 g, 4.68 mmol) and *n*-butyl lithium (3.2 ml, 5.1 mmol) in tetrahydrofuran (30 mL)) for 15 h at ambient temperature afforded **52** (0.722 g, 82%) as yellow crystals upon sublimation at 170 °C/0.05 Torr: mp 294–297 °C; IR (Nujol, cm⁻¹) 1516 (m), 1360 (m), 1225 (w), 1201 (m), 1173 (m), 1089 (w), 1043 (w), 1016 (m), 948 (w), 798 (w); ¹H NMR (C₆D₆, 23 °C, δ) 2.67 (s, 6H, N(CH₃)₂), 1.23 (s, 9H, C(CH₃)₃); ¹³C{¹H} NMR (C₆D₆, 23 °C, ppm) 167.01 (s, CO), 55.96 (s, C(CH₃)₃), 44.30 (s, N(CH₃)₂), 30.83 (s, C(CH₃)₃); Anal. Calcd for C₂₈H₆₀Mo₂N₈O₄: C, 43.98; H, 7.91; N, 14.65. Found: C, 43.86; H, 7.87; N, 14.56.

Preparation of W₂(L¹¹)₄ (53). A 100 mL Schlenk flask was charged with a magnetic stir bar, Na/Hg (14.070 g, Na/3.06 mmol) and tetrahydrofuran (5 mL). To this stirred solution at -20

°C was slowly added a suspension of WCl_4 (0.500 g, 1.53 mmol) in tetrahydrofuran (30 ml). This solution became deep blue while stirring for 8 h at -20 °C. A separate 100 mL Schlenk flask was charged with a magnetic stir bar, *N*-(*tert*-butyl)isobutyramide (0.440 g, 3.07 mmol) and tetrahydrofuran (30 mL). To this stirred solution at 0 °C was slowly added *n*-butyl lithium (2.1 ml, 3.4 mmol), and solution was stirred for 4 h. This solution was then slowly added dropwise with a cannula to the stirred deep blue solution at -20 °C. The resultant brown solution was stirred for 15 h at ambient temperature. The volatile components were then removed under reduced pressure, and the resultant brown sludge was dissolved in hexane (50 mL). The solution was filtered through a 1 cm pad of Celite on a coarse glass frit, and the volatile components were then removed under reduced pressure. Yellow crystals of **53** (0.222 g, 31%) were obtained by sublimation at 160 °C/0.05 Torr: mp 313 – 315 °C; (Nujol, cm^{-1}) 1470 (m), 1365 (m), 1347 (m), 1295 (m), 1199 (m), 1081 (m), 997 (w), 799 (w); 1H NMR (C_6D_6 , 23 °C, δ) 3.17 (sep, 1H, $J = 6.4$ Hz, $CH(CH_3)_2$), 1.44 (d, 6H, $J = 6.4$ Hz, $C(CH_3)_2$), 1.16 (s, 9H, $C(CH_3)_3$); $^{13}C\{^1H\}$ NMR (C_6D_6 , 23 °C, ppm) 175.16 (s, CO), 54.87 (s, $C(CH_3)_3$), 33.20 (s, $C(CH_3)_2$), 30.46 (s, $C(CH_3)_3$), 22.70 (s, $C(CH_3)_2$); Anal. Calcd for $C_{32}H_{64}W_2N_4O_4$: C, 41.04; H, 6.89; N, 5.98. Found: C, 41.19; H, 6.79; N, 5.76.

Preparation of $W_2(L^{12})_4$ (54). In a fashion similar to the preparation of **53**, treatment of W(II) solution (prepared from WCl_4 (0.500 g, 1.53 mmol) and Na/Hg (14.070 g, Na/3.06 mmol) in tetrahydrofuran (35 mL)) with a solution of lithium isopropyl(pivaloyl)amide (prepared from *N*-isopropylpivalamide (0.440 g, 3.07 mmol) and *n*-butyl lithium (2.1 ml, 3.4 mmol) in tetrahydrofuran (30 mL)) for 15 h at ambient temperature afforded **54** (0.150 g, 21%) as red crystals upon sublimation at 170 °C/0.05 Torr: decomposed without melting at 335 °C; IR (Nujol, cm^{-1}) 1475 (m), 1400 (m), 1360 (m), 1315 (m), 1210 (m), 1148 (m), 997 (w), 799 (w); 1H

NMR (C_6D_6 , 23 °C, δ) 5.02 (sep, 1H, $J = 6.4$ Hz, $CH(CH_3)_2$), 1.49 (s, 9H, $C(CH_3)_3$), 1.10 (d, 6H, $J = 6.4$ Hz, $C(CH_3)_2$); $^{13}C\{^1H\}$ NMR (C_6D_6 , 23 °C, ppm) 174.09 (s, CO), 49.47 (s, $C(CH_3)_2$), 40.01 (s, $C(CH_3)_3$), 31.52 (s, $C(CH_3)_3$), 27.40 (s, $C(CH_3)_2$); Anal. Calcd for $C_{28}H_{56}W_2N_4O_4$: C, 41.04; H, 6.89; N, 5.98. Found: C, 41.23; H, 6.85; N, 5.95.

Preparation of $W_2(L^{13})_4$ (55). In a fashion similar to the preparation of **53**, treatment of W(II) solution (prepared from WCl_4 (0.500 g, 1.53 mmol) and Na/Hg (14.070 g, Na/3.06 mmol) in tetrahydrofuran (35 mL)) with a solution of lithium isopropyl(pivaloyl)amide (prepared from N-isopropylisobutyramide (0.396 g, 3.07 mmol) and n-butyl lithium (2.1 ml, 3.4 mmol) in tetrahydrofuran (30 mL)) for 15 h at ambient temperature afforded **55** (0.150 g, 21%) as red crystals upon sublimation at 140 °C/0.05 Torr: mp 304–306 °C; IR (Nujol, cm^{-1}) 1492 (m), 1397 (m), 1361 (m), 1312 (m), 1166 (w), 1083 (m), 1008 (m); 1H NMR (C_6D_6 , 23 °C, δ) 4.44 (sep, 1H, $J = 6.4$ Hz, $CH(CH_3)_2$), 3.01 (sep, 1H, $J = 6.4$ Hz, $CH(CH_3)_2$), 1.36 (d, 6H, $J = 6.4$ Hz, $C(CH_3)_2$), 1.08 (d, 6H, $J = 6.4$ Hz, $C(CH_3)_2$); $^{13}C\{^1H\}$ NMR (C_6D_6 , 23 °C, ppm) 174.90 (s, CO), 51.07 (s, $C(CH_3)_2$), 30.40 (s, $C(CH_3)_2$), 25.68 (s, $C(CH_3)_2$), 23.57 (s, $C(CH_3)_2$); Anal. Calcd for $C_{28}H_{56}W_2N_4O_4$: C, 38.20; H, 6.41; N, 6.36. Found: C, 38.27; H, 6.43; N, 6.30.

Preparation of $Mo_2(\mu-\kappa^1:\kappa^1-L^{17})_4$ (56) and $Mo_2[(\mu-\kappa^1:\kappa^1-L^{17})(\kappa^2-L^{17})]_2$ (57). In a fashion similar to the preparation of **47**, treatment of $Mo_2(OAc)_4$ (0.500 g, 1.17 mmol) in tetrahydrofuran (40 mL) with a solution of lithium 1-acetyl-2,2-dimethylhydrazin-1-ide (prepared from N',N'-dimethylacetohydrazide (0.478 g, 4.68 mmol) and n-butyl lithium (3.2 ml, 5.1 mmol) in tetrahydrofuran (30 mL)) for 15 h at ambient temperature afforded **56** (0.195 g, 28%) and **57** (0.384 g, 55%) as yellow and red crystals, respectively, upon sublimation at 120 °C/0.05 Torr: mp 205–207 °C and 190–193 °C, respectively; **56**-IR (Nujol, cm^{-1}) 1512 (m), 1415 (m), 1341 (m), 1226 (w), 1156 (m), 1053 (m), 1015 (w), 924 (w); 1H NMR (C_6D_6 , 23 °C, δ) 2.69

(s, 3H, CH_3CO), 2.39 (s, 6H, $\text{N}(\text{CH}_3)_2$); $^{13}\text{C}\{^1\text{H}\}$ NMR (C_6D_6 , 23 °C, ppm) 175.87 (s, CO), 49.65 (s, $\text{N}(\text{CH}_3)_2$), 19.78 (s, CH_3CO); **57-IR** (Nujol, cm^{-1}) 1582 (m), 1508 (m), 1401 (m), 1319 (m), 1308 (m), 1224 (m), 1156 (w), 1015 (w), 1008 (m), 972 (w); ^1H NMR (C_6D_6 , 23 °C, δ) 3.41 (s, 3H, CH_3CO), 2.76 (s, 3H, $\text{N}(\text{CH}_3)_2$), 2.40 (s, 3H, $\text{N}(\text{CH}_3)_2$), 2.09 (s, 6H, $\text{N}(\text{CH}_3)_2$), 1.68 (s, 3H, CH_3CO); $^{13}\text{C}\{^1\text{H}\}$ NMR (C_6D_6 , 23 °C, ppm) 178.18 (s, CO), 174.28 (s, CO), 48.80 (s, $\text{N}(\text{CH}_3)_2$), 47.01 (s, $\text{N}(\text{CH}_3)_2$), 20.06 (s, CH_3CO).

Preparation of $\text{Mo}_2(\mu\text{-}\kappa^1\text{:}\kappa^1\text{-L}^{18})_4$ (58) and $\text{Mo}_2[(\mu\text{-}\kappa^1\text{:}\kappa^1\text{-L}^{17})(\kappa^2\text{-L}^{17})]_2$ (59). In a fashion similar to the preparation of **47**, treatment of $\text{Mo}_2(\text{OAc})_4$ (0.500 g, 1.17 mmol) in tetrahydrofuran (40 mL) with a solution of lithium 1-isobutyryl-2,2-dimethylhydrazin-1-ide (prepared from $\text{N}'\text{,N}'$ -dimethylisobutyrohydrazide (0.609 g, 4.68 mmol) and n-butyl lithium (3.2 ml, 5.1 mmol) in tetrahydrofuran (30 mL)) for 15 h at ambient temperature afforded **58** (0.208 g, 25%) and **59** (0.425 g, 51%) as yellow and red crystals, respectively, upon sublimation at 130 °C/0.05 Torr: mp 231–233 °C and 121–123 °C, respectively; **58-IR** (Nujol, cm^{-1}) 1506 (m), 1419 (m), 1356 (m), 1292 (w), 1226 (w), 1211 (w), 1156 (m), 1084 (m), 1038 (m), 1018 (m), 799 (w); ^1H NMR (C_6D_6 , 23 °C, δ) 4.05 (sep, 1H, $J = 6.8$, $\text{CH}(\text{CH}_3)_2$), 2.38 (s, 6H, $\text{N}(\text{CH}_3)_2$), 1.41 (d, 6H, $J = 6.8$, $\text{CH}(\text{CH}_3)_2$); $^{13}\text{C}\{^1\text{H}\}$ NMR (C_6D_6 , 23 °C, ppm) 183.20 (s, CO), 50.39 (s, $\text{N}(\text{CH}_3)_2$), 30.07 (s, $\text{CH}(\text{CH}_3)_2$), 21.54 (s, $\text{CH}(\text{CH}_3)_2$); **59-IR** (Nujol, cm^{-1}) 1570 (m), 1506 (m), 1419 (m), 1356 (m), 1295 (w), 1268 (m), 1225 (w), 1157 (w), 1087 (m), 1035 (m), 1017 (w), 968 (w), 799 (w); ^1H NMR (C_6D_6 , 23 °C, δ) 4.07 (sep, 1H, $J = 6.8$, $\text{CH}(\text{CH}_3)_2$), 3.43 (s, 3H, $\text{N}(\text{CH}_3)_2$), 3.00 (sep, 1H, $J = 6.8$, $\text{CH}(\text{CH}_3)_2$), 2.34 (s, 3H, $\text{N}(\text{CH}_3)_2$), 2.07 (s, 3H, $\text{N}(\text{CH}_3)_2$), 1.65 (s, 3H, $\text{N}(\text{CH}_3)_2$), 1.50 (d, 3H, $J = 6.8$, $\text{CH}(\text{CH}_3)_2$), 1.45 (d, 3H, $J = 6.8$, $\text{CH}(\text{CH}_3)_2$), 1.40 (d, 3H, $J = 6.8$, $\text{CH}(\text{CH}_3)_2$), 1.33 (d, 3H, $J = 6.8$, $\text{CH}(\text{CH}_3)_2$); $^{13}\text{C}\{^1\text{H}\}$ NMR (C_6D_6 , 23 °C, ppm) 186.28 (s, CO), 179.12 (s, CO), 50.39 (s, $\text{N}(\text{CH}_3)_2$), 49.93 (s, $\text{N}(\text{CH}_3)_2$), 49.67 (s, $\text{N}(\text{CH}_3)_2$), 47.96 (s,

$N(CH_3)_2$, 33.38 (s, $CH(CH_3)_2$), 30.48 (s, $CH(CH_3)_2$), 21.90 (s, $CH(CH_3)_2$), 21.17 (s, $CH(CH_3)_2$),
21.07 (s, $CH(CH_3)_2$), 20.76 (s, $CH(CH_3)_2$).

CHAPTER 9

Conclusions and Future Directions

Continuous miniaturization of microelectronics devices forces scientists to innovate new deposition processes and materials. Consequently, new processes and materials are being continually introduced into the semiconductor industry. ALD is the method of choice for the deposition of ultra thin layers in future microelectronics devices, as recognized by the semiconductor industry. New precursors and ALD processes for the deposition of first row transition metal films are required because current precursors and processes do not satisfy the requirements of the semiconductor industry. The precursors should have the highest possible volatility and high thermal stability to afford self-limited growth at the deposition temperatures, along with high reactivity toward the co-reagents. The deposition of metal thin films should be carried out at the lowest possible temperatures ($> 200\text{ }^{\circ}\text{C}$) to afford continuous, conformal films. This dissertation has focused on addressing these concerns by developing new transition metal precursors, screening new reducing co-reagents, and creating new ALD processes for the growth of first row transition metal thin films.

Five series of late first row transition metal complexes have been synthesized and their ALD precursor properties were evaluated. A combination of preparative sublimations, TGA, solid state decomposition studies, and solution reactions with reducing co-reagents suggest that these precursors are promising for the growth of the respective metal films by ALD. α -Imino alkoxide precursors were successfully used in the ALD growth of Ni, Co, Fe, and Cr metal films. The previously reported $\text{Cu}(\text{dmap})_2$ precursor was used to deposit Cu metal films, due to its

higher volatility relative to that of the synthesized new precursors in this dissertation. $\text{BH}_3(\text{NHMe}_2)$ was identified and used as a powerful reducing co-reagent in the ALD growth of first row transition metals. Additionally, Mo(II) and W(II) complexes were synthesized and their ALD precursor properties were evaluated. Their volatilities and thermal stabilities suggest that they can be used in viable ALD processes for the deposition of Mo and W oxide thin films.

During the development of precursors, it was found that the size of the ligand plays a crucial role in determining the volatility and the thermal stability of the metal precursor. In order to form a stable volatile complex, the ligands should saturate the coordination sphere of the metal center. Larger metal centers need bulkier ligands to saturate the coordination spheres. If the ligands do not saturate the coordination sphere, the metal center tends to form a dimeric complex or oligomers, leading to low volatility. The α -imino alkoxide ligand with Me and tBu substituents (L^2 , Chapter 2, Chart 6) affords a dimeric complex with Mn(II). Furthermore, the ligand with Me and iPr substituents (L^1) does not afford volatile complexes with Fe(II), Mn(II), and Cr(II). The sizes of L^2 and L^1 ligands are not large enough to saturate the coordination spheres of Mn(II), Fe(II), and Cr(II) ions, leading to dimeric or non volatile complexes. However, the ligand L^3 (with two tBu groups) affords monomeric complexes with Fe(II), Mn(II), and Cr(II) ions, because the larger size of the ligand saturates the coordination spheres of these metal centers. A similar trend also can be observed in α -imino ketonate and α -imino enolate ligand systems. The α -imino ketonate ligand forms dimeric complexes with Fe(II) and Mn(II) ions, whereas the α -imino enolate ligand forms dimeric complexes with Co(II), Fe(II), and Mn(II) ions.

In ALD, monomeric precursors are preferred over dimeric precursors because monomeric precursors offer higher volatility, due to lower molecular weight. Therefore, in this dissertation

work, attempts were made to synthesize monomeric precursors for all of the desired metal ions. The first three ligands discussed in this dissertation, α -imino alkoxide, α -imino ketonate, and α -imino enolate, form five-membered rings with the metal center upon coordination to the metal center and form dimers due to the small size of the ligand systems. Chelating ligands capable of forming six-membered rings upon coordination would occupy more space of the coordination sphere of the metal center, which is likely to promote the formation of monomeric complexes with larger metal ions, thereby increasing the volatility. Consequently, hydrazonate and 1,2,5-triazapentadienyl complexes were synthesized and they afforded tetrahedral monomeric complexes with all of the desired metal centers. The volatility and thermal stability of these complexes can be tuned by changing the substituents. In the hydrazonate series, L^7 and L^8 did not afford stable volatile complexes with Mn(II) and Cr(II) due to their smaller sizes. However, L^6 afforded monomeric complexes with all of the desired metal centers. Ni, Co, and Fe complexes of L^7 and L^8 have higher volatility than those of the L^6 complexes, due to the lower molecular weight of the L^7 and L^8 ligands. Furthermore, 1,2,5-triazapentadienyl complexes with NMe₂ groups have significantly higher volatility than their tBu analogs, due to the lone pair-lone pair repulsion of the NMe₂ groups which reduces the lattice energy thereby increasing the volatility.

The deposition of Cu, Ni, Co, Fe, and Cr metal films was carried out using alkoxide-based precursors. Cu films were deposited using two step (comprising Cu(dmap)₂ and BH₃(NHMe₂)) and three step (comprising Cu(dmap)₂, formic acid, and BH₃(NHMe₂)) processes. The three step process afforded higher quality Cu films due to the good nucleation offered by formic acid. Also, the three step process afforded continuous, smooth films even at ~2 nm thickness, which is not widely observed in the deposition of Cu films. The ALD growth of Ni,

Co, Fe, and Cr metal films was performed using α -imino alkoxide precursors and $\text{BH}_3(\text{NHMe}_2)$ below 200 °C. This work is of great importance, because this work led to the first ALD growth of Cr metal films and the ALD growth of Ni, Co, and Fe films at temperatures below the decomposition temperatures of the metal precursors. Also, these films were deposited by thermal ALD, which is preferred over PEALD by the semiconductor industry. These films were grown on Ru substrates selectively, due to the catalytic activation of the Ru surface. However, growing films only on Ru may be disadvantageous, because Ru substrates are required for the deposition of these films. Nevertheless, in the integration process of the microelectronics devices, some materials have to be deposited only on one substrate (material) although the deposition surface has more than one substrate. Therefore, the selective ALD growth of first row transition metal films on Ru may be important in the integration process.

Although this dissertation work focused only on using α -imino alkoxide precursors and $\text{BH}_3(\text{NHMe}_2)$ in the ALD growth of first row transition metal films, other precursor combinations may also give afford metallic films. The other precursors reported here were also evaluated in solution screening reactions and most of the precursors reacted with reducing agents, to afford metal powders, suggesting that they may offer viable ALD growth of metal films. Therefore, more ALD studies with best precursor combinations for each metal need be performed. Although this dissertation focused on the deposition of late first row transition metal films, the precursors reported herein can be used to deposit late first row transition metal oxide films as well. Based on the precursor properties (volatility and thermal stability), ALD reactions with oxidizing agents such as H_2O , H_2O_2 , or O_3 should allow the deposition of corresponding MO_y films. Furthermore, the ligands reported herein may be used to synthesize complexes with other metal ions. This dissertation discussed how the size of the ligand affects volatility and

thermal stability of the precursors. Also, this work offers various kinds of ligands (anions, radical anions, N/O donor ligands, N/N donor ligands). The work discussed in this dissertation would allow easy synthesis of complexes with other transition metal ions with similar or different radii and the new precursors are likely to be viable ALD precursors.

When considering each class of precursors reported herein, each class contains the same ligand, and some of them are reduced by commercially available reducing co-reagents to the corresponding metals. Such similar chemistry is crucial for the ALD growth of metal alloy films, such as Cu/Mn alloys for self-forming barrier layers and Ni/Co/Fe magnetic alloys, because ALD growth of metal alloys requires overlap of the self-limited growth temperature ranges for the separate metals. Therefore metal precursors and reducing co-reagents reported herein may be used in viable ALD growth of alloy films.

REFERENCES

1. Moore, G. E. *Electronics* **1965**, 38, 33–35.
2. *International Technology Roadmap for Semiconductors*, 2013 edition; Semiconductor Industry Association, <http://www.itrs.net/reports.html>.
3. Kim, H. *Surf. Coat. Technol.* **2006**, 200, 3104–3111.
4. (a) Merchant, S. M.; Kang, S. H.; Sanganeria, M.; Schravendijk, B.; Mountsier, T. *JOM-J. Min. Met. Mater. Soc.* **2001**, 52, 43–48. (b) Wang, S.-Q. *MRS Bull.* **1994**, 19, 30–40.
5. (a) Winter, C.H. *Aldrichimica Acta* **2000**, 33, 3–8. (b) Won, Y. S.; Kim, Y. S.; Anderson, T. J.; Reitfort, L. L.; Ghiviriga, I.; McElwee-White, L. *J. Am. Chem. Soc.* **2006**, 128, 13781–13788. (c) McElwee-White, L. *Dalton Trans.* **2006**, 5327–5333.
6. Roule, A.; Amuntencei, M.; Deronzier, E.; Haumesser, P.H.; Da Silva, S.; Avale, X.; Pollet, O.; Baskaran, R.; Passemard, G. *Microelectron. Eng.* **2007**, 84, 2610–2614.
7. (a) Haneda, M.; Iijima, J.; Koike, J. *Appl. Phys. Lett.* **2007**, 90, 252107. (b) Usui, T.; Nasu, H.; Takahashi, S.; Shimizu, N.; Nishikawa, T.; Yoshimaru, M.; Shibata, H.; Wada, M.; Koike, J. *IEEE Trans. Electron. Dev.* **2006**, 52, 2492–2499. (c) Koike, J.; Wada, M. *Appl. Phys. Lett.* **2005**, 87, 041911.
8. Chu, J. P.; Lin, C. H.; John, V. S. *Appl. Phys. Lett.* **2007**, 91, 132109.
9. (a) Li, Z.; Gordon, R. G.; Pallen, V.; Li, H.; Shenai, D. V. *Chem. Mater.* **2010**, 22, 3060–3066. (b) Lindsay, R.; Lauwers, A.; De Potter, M.; Roelandts, N.; Vrancken, C.; Maex, K. *Microelectron. Eng.* **2001**, 55, 157–162. (c) Hsia, S. L.; Tan, T. Y.; Smith, P.; McGuire, G. E.; *J. Appl. Phys.* **1992**, 72, 1864–1873.

10. (a) Kang, S. H. *JOM* **2008**, *60*, 28–33. (b) Vaz, C. A. F.; Bland, J. A. C.; Lauhoff, G. *Rep. Prog. Phys.* **2008**, *71*, 056501. (c) Shiratsuchi, Y.; Yamamoto, M.; Bader, S. D. *Progr. Surf. Sci.* **2007**, *82*, 121.
11. Chen, C.-S.; Lin, J.-H.; Lai, T.-W. *Chem. Commun.* **2008**, 4983–4985.
12. (a) Leskelä, M.; Ritala, M. *Angew. Chem. Int. Ed.* **2003**, *42*, 5548–5554. (b) Niinistö, L.; Päiväsaari, J.; Niinistö, J.; Putkonen, M.; Nieminen, M. *Phys. Stat. Sol. A.* **2004**, *201*, 1443–1452. (c) George, S. M. *Chem. Rev.* **2010**, *110*, 111–131. (d) Putkonen, M.; Niinistö, L. *Top. Organomet. Chem.* **2005**, *9*, 125–145. (e) Puurunen, R. L. *J. Appl. Phys.* **2005**, *97*, 121301.
13. Rossnagel, S. M. *J. Vac. Sci. Technol., A* **2003**, *21*, S74–S87.
14. (a) Pierson, H. O. *Handbook of Chemical Vapor Deposition (CVD)*; Noyes Publications/William Andrew Publishing: Norwich, New York, 1999. (b) Gladfelter, W. L. *Chem. Mater.* **1993**, *5*, 1372–1388. (c) Gates, S. M. *Chem. Rev.* **1996**, *96*, 1519–1532. (d) Doppelt, P. *Coord. Chem. Rev.* **1998**, *180*, 1785–1809.
15. (a) Leskelä, M.; Ritala, M. *Angew. Chem. Int. Ed.* **2003**, *42*, 5548–5554. (b) Niinistö, L.; Päiväsaari, J.; Niinistö, J.; Putkonen, M.; Nieminen, M. *Physica Status Solidi A* **2004**, *201*, 1443–1452. (c) Puurunen, R. L. *J. Appl. Phys.* **2005**, *97*, 121301. (d) George, S. M. *Chem. Rev.* **2010**, *110*, 111–131. (e) Knez, M.; Nielsch, K.; Niinistö, L. *Adv. Mater.* **2007**, *19*, 3425–3438.
16. (a) Profijt, H. B.; Potts, S. E.; Van de Sanden, M. C. M.; Kessels, W. M. M. *J. Vac. Sci. Technol., A* **2011**, *29*, 050801. (b) Knoops, H. C. M.; Langereis, E.; Van De Sanden, M. C. M.; Kessels, W. M. M. *J. Electrochem. Soc.* **2010**, *12*, G241–G249.

17. (a) Leskelä, M.; Ritala, M. *Thin Solid Films* **2002**, *409*, 138–146. (b) T. Suntola, *Thin Solid Films* **1992**, *216*, 84–89.
18. Knisley, T. J.; Kalutarage, L. C.; Winter, C. H. *Coord. Chem. Rev.* **2013**, *257*, 3222–3231.
19. Leskelä, M.; Ritala, M.; Nilsen, O. *MRS Bull.* **2011**, *36*, 877–884.
20. (a) Haynes, W. M. *Handbook of Chemistry and Physics*, 92nd Ed., CRC, Boca Raton, Florida, 2012, p 5–80 to 5–89. (b) p 9048.
21. Huo, J.; Solanki, R. *J. Mater. Res.* **2002**, *17*, 2394–2398. (b) Li, Z.; Gordon, R. G. *Chem. Vap. Deposition* **2006**, *12*, 435–441. (c) Waechtler, T.; Ding, S.-F.; Hofmann, L.; Mothes, R.; Xie, Q.; Oswald, S.; Detavernier, C.; Schulz, S. E.; Qu, X.-P.; Lang, H.; Gessner, T. *Microelectronic Eng.* **2011**, *88*, 684–689.
22. (a) Hsu, I. J.; McCandless, B. E.; Weiland, C.; Willis, B. G. *J. Vac. Sci. Technol., A* **2009**, *27*, 660–667. (b) Lim, B. S.; Rahtu, A.; Gordon, R.G. *Nature Mater.* **2003**, *2*, 748–754. (c) Solanki, R.; Pathangey, B. *Electrochem. Solid St. Lett.* **2000**, *3*, 479–480. (d) Mårtensson, P.; Carlsson, J.-O. *Chem. Vap. Deposition* **1997**, *3* 45–50. (e) Juppo, M.; Ritala, M.; Leskelä, M. *J. Vac. Sci. Technol., A* **1997**, *15*, 2330–2333. (f) Waechtler, T.; Ding, S.-F.; Hofmann, L.; Mothes, R.; Xie, Q.; Oswald, S.; Detavernier, C.; Schulz, S. E.; Qu, X.-P.; Lang, H.; Gessner, T.; *Microelectronic Eng.* **2011**, *88*, 684–689.
23. Lee, B. H.; Hwang, J. K.; Nam, J. W.; Lee, S. U.; Kim, J. T.; Koo, S.-M.; Baunemann, A.; Fischer, R. A.; Sung, M. M. *Angew. Chem. Int. Ed.* **2009**, *48*, 4536–4539.
24. Knisley, T. J.; Ariyasena, T. C.; Sajavaara, T.; Saly, M. J.; Winter, C. H. *Chem. Mater.* **2011**, *33*, 4417–4419.

25. Kittl, J. A.; Lauwers, A.; Chamirian, O.; Van Dal, M.; Akheyar, A.; De Potter, M.; Lindsay, R.; Maex, K. *Microelectron. Eng.* **2003**, *70*, 158–165.
26. Yang, T. S.; Cho, W.; Kim, M.; An, K.-S.; Chung, T.-M.; Kim, C. S.; Kim, Y. *J. Vac. Sci. Technol., A* **2005**, *23*, 1238–1243.
27. (a) Lindahl, E.; Ottosson, M.; Carlsson, J.-O. *Chem. Vap. Deposition* **2009**, *15*, 186–191.
(b) Lindahl, E.; Ottosson, M.; Carlsson, J.-O. *Surf. Coat. Technol.* **2010**, *205*, 710–716.
28. (a) Lu, H. L.; Wiemer, C.; Perego, M.; Spiga, S.; Fanciulli, M.; Pavia, G. *J. Electrochem. Soc.* **2008**, *155*, H807–H811. (b) Chung, T.-M.; Lee, S. S.; Cho, W.; Lee, Y. K.; Hwang, J.-H.; An, K.-S.; Kim, C. G. *Bull. Korean Chem. Soc.* **2011**, *32*, 783–784.
29. Kada, T.; Ishikawa, M.; Machida, H.; Ogura, A.; Ohshita, Y.; Soai, K. *J. Cryst. Growth* **2005**, *275*, E1115–E1119.
30. Li, Z.; Gordon, R. G.; Li H.; Shenai, D. V.; Lavoie, C. *J. Electrochem. Soc.* **2010**, *157*, H679–H683.
31. Bakovets, V. V.; Mitkin, V. N.; Gelfond, N. V. *Chem. Vap. Deposition* **2005**, *11*, 112–117.
32. Knisley, T. J.; Saly, M. J.; Heeg, M. J.; Roberts, J. L.; Winter, C. H. *Organometallics* **2011**, *30*, 5010–5017.
33. Chae, J.; Park, H.-S.; Kang, S.-W.; *Electrochem. Solid St. Lett.* **2002**, *5*, C64–C66.
34. (a) Do, K.-W.; Yang, C.-M.; Kang, I.-S.; Kim, K.-M.; Back, K.-H.; Cho, H.-I.; Lee, H.-B.; Kong, S.-H.; Hahm, S.-H.; Kwon, D.-H.; Lee, J.-H. *Jpn. J. Appl. Phys.* **2006**, *45*, 2975–2979. (b) Yang, C.-M.; Yun, S.-W.; Ha, J.-B.; Na, K.-I.; Cho, H.-I.; Lee, H.-B.; Jeong, J.-H.; Kong, S.-H.; Hahm, S.-H.; Lee, J.-H. *Jpn. J. Appl. Phys.* **2007**, *46*, 1981–1983. (c) Lee, K.-M.; Kim, C.Y.; Choi, C.K.; Yun, S.-W.; Ha, J.-B.; Lee, J.-H.;

- Lee, J. Y. *J. Korean Phys. Soc.* **2009**, *55*, 1153–1157. (d) Lee, H.-B.-R.; Bang, S.-H.; Kim, W.-H.; Gu, G. H.; Lee, Y. K.; Chung, T.-M.; Kim, C. G.; Park, C. G.; Kim, H. *Jpn. J. Appl. Phys.* **2010**, *49*, 05FA11. (e) Lee, H.-B.-R.; Gu, G. H.; Son, J. Y.; Park, C. G.; Kim, H. *Small* **2008**, *4*, 2247–2254.
35. (a) Lutsev, L. V.; Stognij, A. I.; Novitskii, N. N. *Phys. Rev. B.* **2009**, *80*, 184423. (b) Sanyal, B.; Eriksson, O.; Arvidsson, P. I. *Phys. Rev. B.* **2008**, *77*, 155407. (c) Vo-Van, Chi; Kassir-Bodon, Z.; Yang, H.; Coraux, J.; Vogel, J.; Pizzini, S.; Bayle-Guillemaud, P.; Chshiev, M.; Guisset, V.; David, P.; Salvador, V.; Fruchart, O. *New J. Phys.* **2010**, *12*, 103040.
36. (a) Burriel, M.; Garcia, G.; Santiso, J.; Abrutis, A.; Saltyte, Z.; Figueras, A. *Chem. Vap. Deposition* **2005**, *11*, 106–111. (b) Klepper, K. B.; Nilsen, O.; Fjellvåg, H. *Thin Solid Films* **2007**, *515*, 7772–7781.
37. Kim, K.; Lee, K.; Han, S.; Jeong, W.; Jeon, H. *J. Electrochem. Soc.* **2007**, *154*, H177–H181.
38. Kim, J.-M.; Lee, H.-B.-R.; Lansalot, C.; Dussarrat, C.; Gatineau, J.; Kim, H. *Jpn. J. Appl. Phys* **2010**, *49*, 05FA10.
39. Kwon, J.; Saly, J. M.; Halls, M. D.; Kanjolia, R. K.; Chabal, Y. J. *Chem. Mater.* **2012**, *24*, 1025–1030.
40. Lee, H.-B.-R.; Kim, H. *ECS Trans.* **2008**, *16*, 219–225.
41. Roule, A.; Amuntencei, M.; Deronzier, E.; Haumesser, P. H.; Da Silva, S.; Avale, X.; Pollet, O.; Baskaran, R.; Passemard, G. *Microelectron. Eng.* **2007**, *84*, 2610–2614.
42. Lie, M.; Klepper, K. B.; Nilsen, O.; Fjellvåg, H.; Kjekshus, A. *Dalton Trans.* **2008**, 253–259.

43. Mathur, S.; Sivakov, V.; Shen, H.; Barth, S.; Cavelius, C.; Nilsson, A.; Kuhn, P. *Thin Solid Films* **2006**, *502*, 88–93. (b) Lin, Y.; Xu, Y.; Mayer, M. T.; Simpson, Z. I.; McMahon, G.; Zhou, S.; Wang, D. *J. Am. Chem. Soc.* **2012**, *134*, 5508–5511.
44. (a) Scheffe, J. R.; Francés, A.; King, D. M.; Liang, X.; Branch, B. A.; Cavanagh, A. S.; George, S. M.; Weimer, A. W. *Thin Solid Films* **2009**, *517*, 1874–1879. (b) Martinson, A. B. F.; DeVries, M. J.; Libera, J. A.; Christensen, S. T.; Hupp, J. T.; Pellin, M. J.; Elam, J. W. *J. Phys. Chem. C* **2011**, *115*, 4333–4339.
45. Burton, B. B.; Fabreguette, F. H.; George, S. M. *Thin Solid Films* **2009**, *517*, 5658–5665.
46. (a) Nilsen, O.; Fjellvåg, H.; Kjekshus, A. *Thin Solid Films* **2003**, *444*, 44–51. (b) Nilsen, O.; Foss, S.; Fjellvåg, H.; Kjekshus, A. *Thin Solid Films* **2004**, *468*, 65–74.
47. (a) Sun, H.; Qin, X.; Zaera, F. *J. Phys. Chem. Lett.* **2011**, *2*, 2525–2530. (b) Zaera, F. *J. Phys. Chem. Lett.*, **2012**, *3*, 1301–1309. (c) Qin, X.; Sun, H.; Zaera, F. *J. Vac. Sci. Technol. A* **2012**, *30*, 01A112.
48. Au, Y.; Lin, Y.; Kim, H.; Beh, E.; Liu, Y.; Gordon, R. G. *J. Electrochem. Soc.* **2010**, *157*, D341–D345.
49. Goedde, D. M.; Windler, G. K.; Girolami, G. S. *Inorg. Chem.* **2007**, *46*, 2814–2823.
50. El-Kadri, O. M.; Heeg, M. J.; Winter, C. H. *Dalton Trans.* **2006**, 4506–4513.
51. Kucheyev, S. O.; Biener, J.; Baumann, T. F.; Wang, Y. M.; Hamza, A. V.; Li, Z.; Lee, D. K.; Gordon, R. G. *Langmuir* **2008**, *24*, 943–948.
52. Moon, D.-Y.; Han, D.-S.; Park, J.-H.; Shin, S.-Y.; Park, J.-W.; Kim, B. M.; Cho, J. Y. *Thin Solid Films* **2012**, *521*, 146–149.

53. C. H. Winter, T. J. Knisley, L. C. Kalutarage, M. A. Zavada, J. P. Klesko, and T. H. Perera, *Encyclopedia of Inorganic Chemistry-II*, Wiley, Chichester, **2012**, *in pres*, <http://dx.doi.org/10.1002/9781119951438.eibc0128.pub2>.
54. (a) Park, K.-H.; Bradley, A. Z.; Thompson, J. S.; Marshall, W. J. *Inorg. Chem.* **2006**, *45*, 8480–8482. (b) Thompson, J. S.; Zhang, L.; Wyre, J. P.; Brill, D. J.; Lloyd, K. G. *Thin Solid Films* **2009**, *517*, 2845–2850.
55. Sanyal, U.; Jagirdar, B. R. *Inorg. Chem.* **2012**, *51*, 13023–13033.
56. Rollison, C. L.; Bailar, J. C.; Emeleus, H. J.; Nyholm, R.; A. F. Trotman-Dickenson, Pergamon Press, *Comprehensive Inorganic Chemistry*, Oxford, 1973, vol. 3, pp. 623–769.
57. Jeong, C. W.; Lee, J. S.; Joo, S. K. *Jpn. J. Appl. Phys.* **2001**, *40*, 285.
58. Dezelah, C. L., IV; Wiedmann, M. K.; Mizohata, K.; Baird, R. J.; Niinistö, L.; Winter, C. *H. J. Am. Chem. Soc.* **2007**, *129*, 12370.
59. Buono-Core, G. E.; Cabello, G. Klahn, A. H.; Lucero, A.; Nunez, M. V.; Torrejon, B.; Castillo, C. *Polyhedron* **2010**, *29*, 1551.
60. (a) Herera, J. E.; Kwak, J. H.; Hu, J. Z.; Wang, Y.; Peden, C. H. F. *Topics in Catalysis* **2006**, *39*, 245. (b) Wittingham, M. S. *Proc. Solid State Chem.* **1978**, *12*, 41. (c) Deb, S. K. *Proc. Roy. Soc. London Ser. A* **1968**, *304*, 211. (d) Abdellaoui, A.; Leveque, G.; Donnadiou, A.; Bath, A.; Bouchikhi, B. *Thin Solid Films* **1997**, *304*, 39. (e) Guerfi, A.; Dao, L. H. *J. Electrochem. Soc.* **1989**, *136*, 2435. (f) Julien, C.; Yebka, B.; Nazari, G. A. *Mater. Sci. Eng. B* **1996**, *38*, 65. (g) Buono-Core, G. E.; Cabello, G. Klahn, A. H.; Lucero, A.; Nunez, M. V.; Torrejon, B.; Castillo, C. *Polyhedron* **2010**, *29*, 1551.

61. (a) Tagstrom, P.; Martensson, P.; jansson, U.; Carlsson, J. O, *J. Electrochem. Soc.* **1999**, *146*, 3139. (b) Herera, J. E.; Kwak, J. H.; Hu, J. Z.; Wang, Y.; Peden, C. H. F.; Macht, M.; Igslesia, E. *J. Catal.* **2006**, *239*, 200. (c) Kriss, R. U.; Meda, L. *Appl. Organometal. Chem.* **1998**, *12*, 155. (d) Tracy, C. E.; Benson, D. K. *J. Vac. Sci. Technol., A* **1986**, *4*, 2377. (e) Harding, G. L. *Thin Solid Films* **1986**, *138*, 279.
62. Dezelah, C. L., IV; El-Kadri, O. M.; Szilagyi, I. M.; Campbell, J. M.; Arstila, K.; Niinistö, L.; Winter, C. H. *J. Am. Chem. Soc.* **2006**, *128*, 9638.
63. (a) Suh, S.; Hoffman, D. M.; Atagi, L. M.; Smith, D. C.; Liu, J. R.; Chu, W. K. *Chem. Mater.* **1997**, *9*, 730. (b) Malandrino, G.; Lo Nigro, R.; Rossi, P.; Dapporto, P.; Fragala, I. L. *Inorg.Chim. Acta.* **2004**, *357*, 3927. (c) Lehn, J. S. M.; Van, H. P.; Wang, Y.; Suh, S.; Hoffman, D. M. *J. Mater. Chem.* **2004**, *14*, 3239.
64. (a) Goel, S. C.; Kramer, K. S.; Chiang, M. Y.; Buhro, W. E. *Polyhedron* **1990**, *9*, 611–613. (b) Becker, R.; Weiß, J.; Winter, M.; Merz, K.; Fischer, R. A. *J. Organomet. Chem.* **2001**, *630*, 253–262. (c) Becker, R.; Devi, A.; Weiß, J.; Weckenmann, U.; Winter, M.; Kiener, C.; Becker, H.-W.; Fischer, R. A. *Chem. Vap. Deposition* **2003**, *9*, 149–156. (d) Park, J. W.; Jan, H. S.; Kim, M.; Sung, K.; Lee, S. S.; Chung, T.-M.; Koo, S.; Kim, C. G.; Kim, Y. *Inorg. Chem. Commun.* **2004**, *7*, 463–466.
65. (a) Yoo, S. H.; Choi, H.; Kim, H.-S.; Park, B. K.; Lee, S. S.; An, K.-S.; Lee, Y. K.; Chung, T.-K.; Kim, C. G. *Eur. J. Inorg. Chem.* **2011**, 1833–1839. (b) Werndrup, P.; Gohil, S.; Kessler, V. G.; Kritikos, M.; Hubert-Pfalzgraf, L. G. *Polyhedron* **2001**, *20*, 2163–2169.
66. Bradley, D. C.; Mehrotra, R. C.; Gaur, D. P. *Metal Alkoxides*, Academic Press, New York, 1978.

67. (a) Vidjayacoumar, B.; Emslie, D. J. H.; Clendenning, S. B.; Blackwell, J. M.; Britten, J. F.; Rheingold, A. *Chem. Mater.* **2010**, *22*, 4844–4853. (b) Vidjayacoumar, B.; Emslie, D. J. H.; Blackwell, J. M.; Clendenning, S. B.; Britten, J. F. *Chem. Mater.* **2010**, *22*, 4854–4866.
68. (a) Bondi, J. F.; Oyler, K. D.; Ke, X.; Schiffer, P.; Schaak, R. E. *J. Am. Chem. Soc.* **2009**, *131*, 9144–9145. (b) Ward, M. B.; Brydson, R.; Cochrane, R. F. *J. Phys.: Conf. Ser.* **2006**, *26*, 296–299. (c) Adner, D.; Korb, M.; Schulze, S.; Hietschold, M.; Lang, H. *Chem. Commun.* **2013**, *48*, 6855–6857.
69. Karunaratne, M. C.; Knisley, T. J.; Tunstull, G. S.; Heeg, M. J.; Winter, C. H. *Polyhedron* **2013**, *52*, 820–830.
70. (a) Mane, A. U.; Shivashankar, S. A. *J. Cryst. Growth*, **2005**, *275*, e1253–e1257. (b) Zeng, L. Wu, W.; Eisenbraun, E. *ECS Trans.*, **2007**, *11*, 67. (c) Morozova, N. B.; Zherikova, K. V.; Semyannikov, P. P.; Trubin, S. V.; Igumenov, I. K. *J. Therm. Anal. Calorim.* **2009**, *98*, 395. (d) Au, H.; Lin, Y.; Kim, H.; Beh, E.; Liu, Y.; Gordon, R. G. *J. Electrochem. Soc.* **2010**, *157*, D341–D345.
71. Reedijk, J.; Marshall, W. J. *Recl. Trav. Chim. Pays-Bas* **1968**, *87*, 552–558.
72. Kwiatkowski, P.; Chaladaj, W.; Jurczak, J. *Tetrahedron* **2006**, *62*, 5116–5125.
73. Fuson, R. C.; Gray, H.; Gouza, J. J. *J. Am. Chem. Soc.* **1939**, *61*, 1937–1940.
74. Lu, C. C.; Bill, E.; Weyhermu, T.; Wieghardt, C. *Inorg. Chem.* **2007**, *46*, 7880–7889.
75. (a) Siebenlist, R.; Fruhauf, H. W.; Vrieze, K.; Smeets, W. J. J.; Spek, A. L. *Eur. J. Inorg. Chem.* **2000**, 907. (b) Binotti, B.; Carfagna, C.; Foresti, E.; Macchioni, A.; Sabatino, P.; Zuccaccia, C.; Zuccaccia, D. *J. Organomet. Chem.* **2004**, *689*, 647. (c) Spencer, L. P.; Fryzuk, M. D. *J. Organomet. Chem.* **2005**, *690*, 5788. (d) Chamberlain, L.

- R.; Durfee, L. D.; Fanwick, P. E.; Kobriger, L. M.; Latesky, S. L.; McMullen, A. K.; Steffey, B. D.; Rothwell, I. P.; Folting, K.; Huffman, J. C. *J. Am. Chem. Soc.* **1987**, *109*, 6068. (e) McMullen, A. K.; Rothwell, I. P.; Huffman, J. C. *J. Am. Chem. Soc.* **1985**, *107*, 1072. (f) Szevere'nyi, Z.; Fu'lo'p, V.; Ka'lma'n, A.; Sima'ndi, L. I. *Inorg. Chim. Acta* **1988**, *147*, 135. (f) Visentin, L. C.; Ferreira, L. C.; Bordinhã, J.; Filgueiras, C. A. L. *J. Braz. Chem. Soc.* **2010**, *7*, 1187–1194.
76. Binotti, B.; Carfagna, C.; Foresti, E.; Macchioni, A.; Sabatino, P.; Zuccaccia, D. *J. Organomet. Chem.* **2004**, 647–661.
77. Smith, A. L.; Clapp, L. A.; Hardcastle, K. I.; Soper, J. D. *Polyhedron* **2010**, *29*, 164–169.
78. (a) Vandeputte, A. G.; Reyniers, M-F.; Marin, G. B. *ChemPhysChem* **2013**, *14*, 3751–3771. (b) Wang, L.; Wen, J.; He, H.; Zhang, J. *Int. J. Quantum Chem* **2013**, *113*, 2338–2344.
79. Lim, B. S.; Rahtu, A.; Park, J.-S.; Gordon, R. G. *Inorg. Chem.* **2003**, *42*, 7951–7958.
80. Evans, D. F. *J. Chem. Soc.* **1959**, 2003.
81. (a) MacLeod-Carey, D. A.; Bustos, C.; Schott, E.; Alvarez-Thon, L.; Fuentealba, M. *Acta Crystallogr., Sect. E: Struct. Rep. Online* **2007**, *63*, m670–m672. (b) Marten, J.; Seichter, W.; Weber, E. *Z. Anorg. Allg. Chem.* **2005**, *631*, 869–877. (c) Kuzmina, N. P.; Eliseeva, S. V.; Balashov, A. M.; Trojanov, S. I. *Zh. Neorg. Khim.* **2002**, *47*, 1300–1304.
82. (a) Kopylovich, M. N.; Mahmudov, K. T.; da Silva, M. F. C. G.; Figiel, P. J.; Karabach, Y. Y.; Kuznetsov, M. L.; Luzyanin, K. V.; Pombeiro, A. J. L. *Inorg. Chem.* **2011**, *50*, 918–931. (b) Kopylovich, M. N.; MacLeod, T. C. O.; Mahmudov, K. T.; da Silva, M. F. C. G.; Pombeiro, A. J. L. *Dalton Trans.* **2011**, *40*, 5352–5361. (c) Kopylovich, M. N.; Nunes, A. C. C.; Mahmudov, K. T.; Haukka, M.; MacLeod, T. C. O.; Martins, L. M. D.

- R. S.; Kuznetsov, M. L.; Pombeiro, A. J. L. *Dalton Trans.* **2011**, *40*, 2822–2836. (d) Paira, M. K.; Mondal, T. K.; Ojha, D.; Slawin, A. M. Z.; Tiekink, E. R. T.; Samanta, A.; Sinha, C. *Inorg. Chim. Acta* **2011**, *370*, 175–185. (e) Paira, M. K.; Mondal, T. K.; López-Torres, E.; Ribas, J.; Sinha, C. *Polyhedron* **2010**, *29*, 3147–3156. (f) You, W.; Zhu, H.-Y.; Huang, W.; Hu, B.; Fan, Y.; You, X.-Z. *Dalton Trans.* **2010**, *39*, 7876–7880. (g) Mahmudov, K. T.; Kopylovich, M. N.; da Silva, M. F. C. G.; Figiel, P. J.; Karabach, Y. Y.; Pombeiro, A. J. L. *J. Mol. Catal. A: Chem.* **2010**, *318*, 44–50. (h) Emeleus, L. C.; Cupertino, D. C.; Harris, S. G.; Owens, S.; Parsons, S.; Swart, R. M.; Tasker, P. A.; White, D. J. *J. Chem. Soc., Dalton Trans.* **2001**, 1239–1245. (i) Banße, W.; Jager, N.; Ludwing, E.; Schilde, U.; Uhlemann, E.; Lehmann, A.; Mehner, H. *Z. Naturforsch., B: Anorg. Chem., Org. Chem.* **1997**, *52*, 237–242. (j) Moreno, J. M.; Ruiz, J.; Dominguez-Vera, J. M.; Colacio, E.; Galisteo, D.; Kivekäs, R. *Polyhedron* **1994**, *13*, 203–207. (k) Colacio, E.; Dominguez-Vera, J.-M.; Kivekäs, R.; Ruiz, J. *Inorg. Chim. Acta* **1994**, *218*, 109–116. (l) Colacio, E.; Ruiz, J.; Moreno, J. M.; Kivekäs, R.; Sundberg, M. R.; Dominguez-Vera, J. M.; Laurent, J. P. *J. Chem. Soc., Dalton Trans.* **1993**, 157–163. (m) Colacio, E.; Dominguez-Vera, J. M.; Costes, J.-P.; Kivekäs, R.; Laurent, J. P.; Ruiz, J.; Sundberg, M. *Inorg. Chem.* **1992**, *31*, 774–778. (n) Abraham, N.; Capon, J. M.; Nowogrocki, G.; Sueur, S.; Brémard, C. *Acta Crystallogr., Sect. C: Cryst. Struct. Commun.* **1985**, *41*, 706–709. (o) Abraham, N.; Capon, J. M.; Nowogrocki, G.; Sueur, S.; Brémard, C. *Acta Crystallogr., Sect. C: Cryst. Struct. Commun.* **1984**, *40*, 1355–1357.
83. Zhang, X.; Zhang, G.-Y.; Chen, D.; Song, Y.-J. *Acta Crystallogr., Sect. E: Struct. Rep. Online* **2008**, *64*, m642.

84. Bao, F.; Jiao, Y.-H.; Ng, S. W. *Acta Crystallogr., Sect. E: Struct. Rep. Online* **2006**, *62*, m558–m559.
85. Granum, D. M.; Riedel, P. J.; Crawford, J. A.; Mahle, T. K.; Wyss, C. M.; Begej, A. K.; Arulsamy, N.; Pierce, B. S. Mehn, M. P. *Dalton Trans.* **2011**, *40*, 5881–5890.
86. Bondi, J. F.; Oyler, K. D.; Ke, X.; Schiffer, P.; Schaak, R. E. *J. Am. Chem. Soc.* **2009**, *131*, 9144–9145. (b) Ward, M. B.; Brydson, R.; Cochrane, R. F. *J. Phys.: Conf. Ser.* **2006**, *26*, 296–299.
87. (d) Iijima, J.; Fujii, Y.; Neishi, K.; Koike, J. *J. Vac. Sci. Technol., B* **2009**, *27*, 1963–1968. (e) Chung, S.-M.; Koike, J. *J. Vac. Sci. Technol., B* **2009**, *27*, L28–L31. (f) Otsuka, Y.; Koike, J.; Sako, H.; Ishibashi, K.; Kawasaki, N.; Chung, S. M.; Tanaka, I. *Appl. Phys. Lett.* **2010**, *96*, 012101. (g) Chen, G. S.; Chen, S. T.; Lu, Y. L. *Electrochem. Commun.* **2010**, *12*, 1483–1486. (h) Lozano, J. G.; Lozano-Perez, S.; Bogan, J.; Wang, Y. C.; Brennan, B.; Nellist, P. D.; Hughes, G. *Appl. Phys. Lett.* **2011**, *98*, 123112. (i) Casey, P.; Bogan, J.; Brennan, B.; Hughes, G. *Appl. Phys. Lett.* **2011**, *98*, 113508. (j) Au, H.; Lin, Y.; Gordon, R. G. *J. Electrochem. Soc.* **2011**, *158*, D248–D253. (k) Dixit, V. K.; Neishi, K.; Akao, N.; Koike, J. *IEEE Trans. Dev. Mater. Reliab.* **2011**, *11*, 295–302.
88. Granum, D. M.; Riedel, P. J.; Crawford, J. A.; Mahle, T. K.; Wyss, C. M.; Begej, A. K.; Arulsamy, N.; Pierce, B. S. Mehn, M. P. *Dalton Trans.* **2011**, *40*, 5881–5890.
89. Bourget-Merle, L.; Lappert, M. F.; Severn, J. R. *Chem. Rev.* **2002**, *102*, 3031–3065. (b) Tsai, Y.-C. *Coord. Chem. Rev.* **2012**, *256*, 722–758.
90. Kopylovich, M. N.; Pombeiro, A. J. L. *Coord. Chem. Rev.* **2011**, *255*, 339–355.
91. (a) Bolano, T.; Gunnoe, T. B.; Sabat, M. *Dalton Trans.* **2013**, *42*, 347–350. (b) Zhou, M.; Qiao, X.; Tong, H.; Gong, T.; Fan, M.; Yang, Q.; Dong, Q.; Chao, J.; Guo, Z.; Liu, D.

- Inorg. Chem.* **2012**, *51*, 4925–4930. (c) Zhou, M.; Gong, T.; Qiao, X.; Tong, H.; Guo, J.; Liu, D. *Inorg. Chem.* **2011**, *50*, 1926. (d) Kopylovich, M. N.; Lasri, J.; da Silva, M. F. C. G.; Pombeiro, A. J. L. *Eur. J. Inorg. Chem.* **2011**, 377–383. (e) Flores, J. A.; Kobayashi, Y.; Rasika Dias, H. V. *Dalton Trans.* **2011**, *40*, 10351–10359.
92. (a) Shchegol'kov, E. V.; Burgart, Y. V.; Saloutin, V. I. *J. Fluor. Chem.* **2007**, *128*, 779–788. (b) Fomicheva, E. B.; Belskii, V. K.; Panova, G. V. *Koord. Khim.* **1989**, *15*, 937–941. (c) Fomicheva, E. B.; Belskii, V. K.; Panova, G. V. *Koord. Khim.* **1989**, *15*, 209–213. (d) Fomicheva, E. B.; Belskii, V. K.; Panova, G. V. *Zh. Obshch. Khim.* **1986**, *56*, 607–613.
93. (a) Uraev, A. I.; Korshunov, O. Y.; Nivorozhkin, A. L.; Antsyshkina, A. S.; Sadikov, G. G.; Nevodchikov, V. I.; Sergienko, V. S.; Garnovsky, A. D. *Russ. J. Inorg. Chem.* **2009**, *54*, 521–529. (b) El-Ghar, M. F. A.; El-Ghani, N. T. A.; El-Borady, O. M. *J. Coord. Chem.* **2008**, *61*, 1184–1199. (c) Moreno, J. M.; Ruiz, J.; Dominguez-Vera, J. M.; Colacio, E.; Galisteo, D.; Kivekäs, R. *Polyhedron* **1994**, *13*, 203–207. (d) Nivorozhkin, A. L.; Toftlund, H.; Nivorozhkin, L. E.; Kamenetskaya, I. A.; Antsyshkina, A. S.; Porai-Koshits, M. A. *Trans. Met. Chem.* **1994**, *19*, 319–324. (e) Krol, I. A.; Starikova, Z. A.; Makarevich, S. S.; Krasikov, A. Y.; Dziomko, V. M.; Khodas, A. V. *Kristallogr.* **1992**, *37*, 373–381.
94. (a) Sedai, B.; Heeg, M. J.; Winter, C. H. *J. Organomet. Chem.* **2008**, *693*, 3495–3503. (b) Sedai, B.; Heeg, M. J.; Winter, C. H. *Organometallics* **2009**, *28*, 1032–1038. (c) El-Kaderi, H. M.; Heeg, M. J.; Winter, C. H. *Polyhedron* **2006**, *25*, 224–234. (d) El-Kaderi, H. M.; Heeg, M. J.; Winter, C. H. *Eur. J. Inorg. Chem.* **2005**, 2081–2088. (e) El-Kaderi,

- H. M.; Heeg, M. J.; Winter, C. H. *Organometallics* **2004**, *23*, 4995–5002. (f) El-Kaderi, H. M.; Xia, A.; Heeg, M. J.; Winter, C. H. *Organometallics* **2004**, *23*, 4995–5002.
95. (a) Khusniyarov, M. M.; Bill, E.; Weyhermüller, T.; Bothe, E.; Wieghardt, K. *Angew. Chem. Int. Ed.* **2011**, *50*, 1652–1655. (b) Hitchcock, P. B.; Lappert, M. F.; Linnolahti, M.; Sablong, R.; Severn, J. R. *J. Organomet. Chem.* **2009**, *694*, 667–676. (c) Healy, P. C.; Bendall, M. R.; Doddrell, D. M.; Skelton, B. W.; White, A. H. *Aust. J. Chem.* **1979**, *32*, 727–735.
96. McNab, H. *J. Chem. Soc., Perkin Trans. 2* **1981**, 1283.
97. Severin, T.; Poehlmann, H. *Chem. Ber.* **1977**, *110*, 491.
98. Knisley, T. J.; Kalutarage, L. C.; Winter, C. H. *Coord. Chem. Rev.* **2013**, *257*, 3221–3231.
99. (a) Rollison, C. L., in *Comprehensive Inorganic Chemistry*; Bailar, J. C., Jr.; Emeleus, H. J.; Nyholm, R.; Trotman-Dickenson, A. F.; Pergamon Press: Oxford; 1973; Volume 3; pp 623–769. (b) Kemmitt, R. D. W., in *Comprehensive Inorganic Chemistry*; Bailar, J. C., Jr.; Emeleus, H. J.; Nyholm, R.; Trotman-Dickenson, A. F.; Pergamon Press: Oxford; 1973; Volume 3; pp 771–876.
100. Jaska, C. A.; Temple, K.; Lough, A. J.; Manners, I. *J. Am. Chem. Soc.* **2003**, *125*, 9424–9434.
101. *Handbook of X-ray Photoelectron Spectroscopy*; Wagner, C. D.; Riggs, W. M.; Davis, L. E.; Moulder, J. F.; Murlenberg, G. E., Eds; Perkin-Elmer Corporation: Eden Prairie, Minnesota; 1979, pp 81, 82.
102. Barnat, E. V.; Nagakura, D.; Wang, P.-I.; Lu, T.-M. *J. Appl. Phys.* **2002**, *91*, 1667–1672.

103. Zhengwen, Li.; Rahtu, A.; Gorden, R. G. *J. Electrochem. Soc.* **2006**, *153*, C787–C794.
104. Lim, B. S.; Rahtu, A.; Park, J.-S.; Gordon, R. G. *Inorg. Chem.* **2003**, *42*, 7951–7958.
105. Jaska, C. A.; Temple, K.; Lough, A. J.; Manners, I. *J. Am. Chem. Soc.* **2003**, *125*, 9424–9434.
106. Cotton, F. A.; Murillo, C. A.; Walton, R. A. *Multiple Bonds between Metal Atoms*, 3rd ed.; Springer: New York, 2005.
107. (a) Huang, Y. L.; Huanh, B. H.; Ko, B. T.; Lin, C. C. *J. Chem. Soc., Dalton Trans.* **2001**, 1359. (b) Huanh, B. H.; yu, T. L.; Huang, Y. L.; Ko, B. T.; Lin, C. C. *Inorg. Chem.* **2002**, *41*, 2987.
108. Finar, I. L. *Organic Chemistry, Vol. 1*; Pearson Education (Singapore): Delhi, India, **2003**.
109. Li, C.; Thompson, R.; Gillon, B.; Patrick, B.; Schafer, L. L. *Chem. Commun.* **2003**, 2462.
110. Lichtenberger, D. L.; Kristofzski, J. G.; Bruck, M. A. *Acta Crystallogr* **1988**, *C44*, 1523–1526.
111. Cotton, F. A.; Ilsley, W. H.; Kaim, W. *J. Am. Chem. Soc.* **1980**, *102*, 3475–3479.
112. Bino, A.; Cotton, F. A.; Kaim, W. *Inorg. Chem.* **1979**, *18*, 3030–3033.
113. Baral, S.; Cotton, F. A.; Ilsley, W. H. *Inorg. Chem.* **1981**, *20*, 2696–2703.
114. Cotton, F. A.; Ilsley, W. H.; Kaim, W. *Inorg. Chem.* **1980**, *19*, 3586–3589.
115. Sattelberger, A. P.; McLaughlin, K. W.; Huffman, J. C. *J. Am. Chem. Soc.* **1981**, *103*, 2880.
116. Baral, S.; Cotton, F. A.; Ilsley, W. H.; Kaim, W. *Inorg. Chem.* **1982**, *21*, 1644–1650.

117. (a) Gupta, S.; Paul, B. K.; Barik, A. K.; Mandal, T. N.; Roy, S.; Guchhait, N.; Butcher, R. J.; Kar, S. K. *Polyhedron* **2009**, *28*, 3577–3585. (b) Gupta, S.; Barik, A. K.; Pal, S.; Hazra, A.; Roy, S.; Butcher, R. J.; Kar, S. K. *Polyhedron* **2007**, *26*, 133–141.
118. (a) Cotton, F. A.; Niswander, R. H.; Sekutowski, J. C. *Inorg. Chem.* **1979**, *18*, 1152–1159. (b) Chisholm, M. C.; Clark, R. J. H.; Gallucci, J.; Hadad, C. M.; Patmore, N. *J. Am. Chem. Soc.* **2004**, *126*, 8303–8313.
119. Sattelberger, A. P.; McLaughlin, K. W.; Huffman, J. C. *J. Am. Chem. Soc.* **1981**, *103*, 2880.
120. (a) Hochberg, E.; Walks, P.; Abbott, E. H. *Inorg. Chem.* **1974**, *13*, 1824. (b) Brignole, A. B.; Cotton, F. A. *Inorg. Synth.* **1972**, *13*, 81. (c) Holste, G. Z. *Anorg. Allg. Chem.* **1975**, *414*, 81. (d) McCarley, R. E.; Templeton, J. L.; Colburn, T. J.; Katovic, V.; Hoxmeier, R. *J. Adv. Chem. Ser.* **1976**, *150*, 318. (e) Schafer, H.; Holste, G. Z. *Anorg. Allg. Chem.* **1972**, *391*, 263.
121. Bino, A.; Cotton, F. A.; Dori, Z.; Kosh, S.; Kuppers, H.; Millar, M.; Sekutowski, J. C. *Inorg. Chem.* **1978**, *17*, 3245.
122. Bino, A.; Hesse, K. F.; Kuppers, H. *Acta Crystallogr* **1980**, *B36*, 723.
123. Cotton, F. A.; Mott, G. N. *J. Am. Chem. Soc.* **1982**, *104*, 5978.
124. Cotton, F. A.; Hubbard, J. L.; Lichtenberger, D. L.; Shim I. *J. Am. Chem. Soc.* **1982**, *104*, 679.
125. Cotton, F. A.; Wang, W. *Inorg. Chem.* **1984**, *23*, 1604.
126. Karunarathne, M. C. PhD. Dissertation, “Synthesis and Characterization of Amidate, Carbohydrazide, and Amidrazonate Complexes of Group 4 and First Row Transition

Metals as Potential Precursors for Atomic Layer Deposition of Metal and Metal Oxide Thin Films,” Wayne State University, **2010**.

127. Cotton, F. A.; Ilsley, W. H.; Kaim, W. *Inorg. Chem.* **1979**, *18*, 2717–2719.

128. Miikkulainen, V.; Suvanto, M.; Pakkanen, T. A. *Chem. Vap. Deposition* **2008**, *14*, 71–77.

129. Rische, D.; Parala, H.; Gemel, E.; Winter, M.; Fisher, R. A. *Chem. Mater.* **2006**, *18*, 6078–6082.

130. Dezelah, C. L.; El-Kadri, O. M.; Kukli, K.; Arstila, K.; Baird, R. J.; Lu, J.; Niinistö, L.; Winter, C. H. *J. Mater. Chem.*, **2007**, *17*, 1109–1116.

ABSTRACT**PRECURSORS AND PROCESSES FOR THE GROWTH OF METALLIC FIRST ROW
TRANSITION METAL FILMS BY ATOMIC LAYER DEPOSITION**

by

LAKMAL CHARIDU KALUTARAGE**May 2014****Advisor:** Professor Charles H. Winter**Major:** Chemistry (Inorganic)**Degree:** Doctor of Philosophy

As a result of the continuous miniaturization of microelectronics devices, atomic layer deposition (ALD) has gained much attention in the recent years. ALD allows the deposition of ultra-thin conformal films with accurate thickness control due to the self-limiting growth mechanism. The microelectronics industry requires the growth of metallic first row transition metal films by ALD. Due to the positive electrochemical potentials, the ALD growth of noble metal thin films has been well developed in the past. By contrast, the ALD growth of first row transition metal films remains poorly documented. The reasons for this scarcity include the lack of suitable metal precursors and powerful reducing co-reagents that can convert precursors in positive oxidation states to the metals. In this dissertation, the development of new transition metal precursors, solution phase reaction screening for powerful reducing agents, and ALD growth of transition metal thin films are discussed.

In this dissertation, five classes of new ALD precursors for Cr, Mn, Fe, Co, Ni, and Cu are discussed, namely, α -imino alkoxides, α -imino ketonates, α -imino enolates, hydrazonates, and 1,2,5-triazapentadienyls. These precursors are volatile, thermally stable, and reactive toward reducing co-reagents, which are the key properties that ALD precursors must have. α -Imino

alkoxide, α -imino ketonate, α -imino enolate, hydrazonate, and 1,2,5-triazapentadienyl precursors have volatilities that range from 85–160, 135–145, 110–165, 100–135, and 105–175 °C at 0.05 Torr, respectively, and thermally stabilities that range from 183–270, 108–248, 190–295, 240–308, and 180–310 °C, respectively. Solution screening of these precursors with commercially available reducing agents revealed high reactivity toward reducing agents. These solution screening reactions demonstrated that $\text{BH}_3(\text{NHMe}_2)$ is a powerful reducing agent that can transfer Cr(II), Mn(II), Fe(II), Co(II), Ni(II), and Cu(II) centers to their metallic forms and, thereby, can be used in viable ALD processes.

Thermal ALD growth of late first row transition metal films was discussed. Cu ALD depositions were carried out with $\text{Cu}(\text{damp})_2$ and $\text{BH}_3(\text{NHMe}_2)$. The deposited Cu films are smooth and continuous, even at thicknesses of 2 nm, and high purity and low resistivity were achieved. The deposition of Cr, Mn, Fe, Co, and Ni films was performed with the α -imino alkoxide precursors and $\text{BH}_3(\text{NHMe}_2)$. X-ray photoelectron spectroscopy (XPS) of these films suggests that the film surfaces are oxidized, however, the bulk of the films showed metals for all except Mn. Moreover, Cr thin films have never been deposited by ALD and this dissertation reports the first ALD growth of Cr films.

Considering the fact that limited precursors are available for the deposition of metastable Mo and W oxide films, this work also discusses the synthesis and complete characterization of Mo and W complexes containing amidate and carbohydrazide ligands. These new complexes are volatile between 120 and 170 °C at 0.05 Torr, and thermally decompose temperatures between 193 °C and 355 °C, which should allow low temperature ALD of oxide films.

Ligands that are discussed herein have emerged as new classes of ligands that can form thermally stable metal precursors for ALD applications. Additionally, the selection of the ligands

with proper substituents for desired metal ions was demonstrated toward the design of ideal ALD precursors with the best possible properties. Moreover, the ALD growth of late first row transition metals was demonstrated using the metal precursors with similar ligands and same reducing co-reagent that enable the late transition metal alloy film growth.

AUTOBIOGRAPHICAL STATEMENT

LAKMAL CHARIDU KALUTARAGE

Education Ph.D., Inorganic Chemistry, Wayne State University, Detroit, MI, 2008–2014
 Advisor: Professor Charles H. Winter
 B.Sc., Chemistry Special, University of Colombo, Colombo-3, Sri Lanka
 2002–2006; Minors: Botany, Zoology

Honors and Awards

Wayne State University Graduate School 2013 Summer Dissertation Fellowship
 Wayne State University Chemistry Department 2013 Graduate Student Professional Travel Award

Publications

- 1.) “Volatile and Thermally Stable Mid to Late Transition Metal Complexes Containing α -Imino Alkoxide Ligands, a New Strongly Reducing Co-Reagent, and Thermal Atomic Layer Deposition of Ni, Co, Fe, and Cr Metal Films” **Kalutarage, L. C.**; Martin, P. D.; Heeg, M. J.; Winter, C. H. *J. Am. Chem. Soc.* **2013**, *135*, 12588–12591.
- 2.) “Synthesis, Structure, and Solution Reduction Reactions of Volatile and Thermally Stable Mid to Late First Row Transition Metal Complexes Containing Hydrazonate Ligands” **Kalutarage, L. C.**; Martin, P. D.; Heeg, M. J.; Winter, C. H. *Inorg. Chem.* **2013**, *52*, 5385–5394.
- 3.) “Volatility and High Thermal Stability in Mid-to-Late First-Row Transition-Metal Complexes Containing 1,2,5-Triazapentadienyl Ligands” **Kalutarage, L. C.**; Martin, P. D.; Heeg, M. J.; Saly, M. J.; Kuiper, D. S.; Winter, C. H. *Inorg. Chem.* **2013**, *52*, 1182–1184.
- 4.) “Precursors and Chemistry for the Atomic Layer Deposition of Metallic First Row Transition Metal Films” Knisley, T. J.; **Kalutarage, L. C.**; Winter, C. H. *Coord. Chem. Rev.* **2013**, *257*, 3221–3231.
- 5.) “Metallic Materials Deposition: Metal-Organic Precursors” Winter, C. H.; Knisley, T. J.; **Kalutarage, L. C.**; Zavada, M. A.; Klesko, J. P.; Perera, T. H. *Encyclopedia of Inorganic Chemistry-II*, Wiley: Chichester, **2012**, <http://dx.doi.org/10.1002/9781119951438.eibc0128.pub2>.

Patents

- 1) “Precursors for the Atomic Layer Deposition” **Kalutarage, L. C.**; Winter, C. H. U.S. Provisional Patent Application, Case # 61/658,064, filed June 11, 2012. (U.S. Patent Application filed June 11, 2013.)
- 2) “Synthesis and Characterization of First Row Transition Metal Complexes Containing α -Keto Hydrazonate Ligands as Potential Precursors for Atomic Layer Deposition” **Kalutarage, L. C.**; Winter, C. H. U.S. Patent Application, Case # 13709564, filed December 10, 2012.
- 3) “Synthesis and Characterization of First Row Transition Metal Complexes Containing α -Imino Alkoxide Ligands as Potential Precursors for Use in Atomic Layer Deposition” **Kalutarage, L. C.**; Winter, C. H. U.S. Patent Application, filed February 2, 2013.